Experimental Investigation of Thrust Fault Rupture Mechanics

Thesis by

Vahe Gabuchian

In Partial Fulfillment of the Requirements

for the Degree of

Doctor of Philosophy
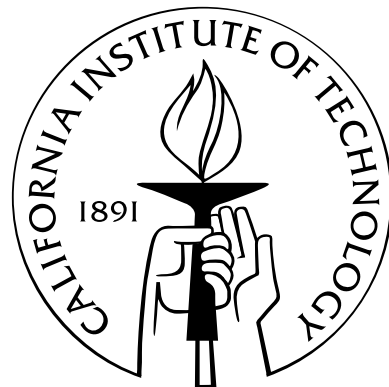
California Institute of Technology

Pasadena, California

2015

(Defended April 23, 2015)

To the reader, wherever and whenever you may be.

Acknowledgements

First and foremost, I extend my appreciation to the California Institute of Technology for fostering my scientific development and research during my graduate years, culminating in the publication of this thesis. The vibrant atmosphere of discovery and eager pursuit of knowledge was exactly the character I was looking for in an academic setting. This environment quickly revealed the seemingly infinite expanse and creativity of the human mind: I am proud to be a part of such an institute.

I thank the professors at the Graduate Aerospace Laboratories (G.A.L.C.I.T.), whose rigorous and comprehensive approach to each subject fortified theory with application and historical context. Joseph Shepherd and Guruswami Ravichandran, thank you for making fluid and solid mechanics such memorable experiences. James Polk, thank you for extending my knowledge of propulsion into space: it's my favorite topic in engineering. Many thanks to you, Niles Pierce, and your elegant approach to complex analysis that gave me a hallmark for recognizing a great lecture.

The advice, guidance, and friendship of upperclassmen at G.A.L.C.I.T. naturally established a welcoming environment, especially comforting through the more difficult times. For this, I thank Phillip Boettcher, Angie Capece, Francisco López Jiménez, Jeff LeHew, Celia Reina Romo, and Sylvain Barbot, I appreciate your support on campus and your friendship off campus.

To the incoming Aerospace and Aeronautic master classes of 2007, it was a pleasure sharing the halls and dungeons of Firestone, Guggenheim, Kármán, and Thomas with you. Francisco Montero Chacón, you helped me not only develop my problem-solving skills, but kept me at an even keel as a human being: eventually I found myself as best man at your wedding, and now I find myself writing about it here (perhaps the use of Crocco's theorem will help in this space-time anomaly?). Jason Damazo, our fuel-driven (Diet Coke$^{©}$) study sessions propelled us through the most difficult courses as we took over the basement of the Sherman Fairchild Library: it was a pleasure working with you. Ivan Szelengowics, to this day I have to check the spelling of your last name, but don't let that be the rubric with which you judge our friendship: I look forward to our next discussion of life and the infinite (see Paco's time dilemma above). Prakhar Mehrotra, I thank you for always making me feel exactly like I did my first day on campus in every one of our interactions, almost without fail. Jonathan Mihaly, my colleague, office mate, and group member, you have made everything seem manageable with friendly advice and unconditional support: thank you Jon.

Abstract

Thrust fault earthquakes are investigated in the laboratory by generating dynamic shear ruptures along pre-existing frictional faults in rectangular plates. A considerable body of evidence suggests that dip-slip earthquakes exhibit enhanced ground motions in the acute hanging wall wedge as an outcome of broken symmetry between hanging and foot wall plates with respect to the earth surface. To understand the physical behavior of thrust fault earthquakes, particularly ground motions near the earth surface, ruptures are nucleated in analog laboratory experiments and guided up-dip towards the simulated earth surface. The transient slip event and emitted radiation mimic a natural thrust earthquake. High-speed photography and laser velocimeters capture the rupture evolution, outputting a full-field view of photo-elastic fringe contours proportional to maximum shearing stresses as well as continuous ground motion velocity records at discrete points on the specimen. Earth surface-normal measurements validate selective enhancement of hanging wall ground motions for both sub-Rayleigh and super-shear rupture speeds. The earth surface breaks upon rupture tip arrival to the fault trace, generating prominent Rayleigh surface waves. A rupture wave is sensed in the hanging wall but is, however, absent from the foot wall plate: a direct consequence of proximity from fault to seismometer. Signatures in earth surface-normal records attenuate with distance from the fault trace. Super-shear earthquakes feature greater amplitudes of ground shaking profiles, as expected from the increased tectonic pressures required to induce super-shear transition. Paired stations measure fault parallel and fault normal ground motions at various depths, which yield slip and opening rates through direct subtraction of like components. Peak fault slip and opening rates associated with the rupture tip increase with proximity to the fault trace, a result of selective ground motion amplification in the hanging wall. Fault opening rates indicate that the hanging and foot walls detach near the earth surface, a phenomenon promoted by a decrease in magnitude of far-field tectonic loads. Subsequent shutting of the fault sends an opening pulse back down-dip. In case of a sub-Rayleigh earthquake, feedback from the reflected S wave re-ruptures the locked fault at super-shear speeds, providing another mechanism of super-shear transition.

Contents

List of Tables

List of Figures

xxi

Glossary of Terms

Introductory concepts

$F_{\mathrm{s,d}}$: static and dynamic frictional resistive force at the contact interface of two bodies.

$f_{\mathrm{s,d}}$: static and dynamic coefficients of friction, specific to conditions at the contact interface.

v: sliding velocity of the rigid block along an angled wedge.

Ω: control surface surrounding the material volume.

$u_i(\mathbf{x}, t)$: displacement field components ($i = 1, 2, 3$) within material surface, Ω.

$\dot{u}_i(\mathbf{x}, t)$: velocity field components ($i = 1, 2, 3$) within material surface, Ω.

$\ddot{u}_i(\mathbf{x}, t)$: acceleration field components ($i = 1, 2, 3$) within material surface, Ω.

$f_i(\mathbf{x}, t)$: field (body) forces ($i = 1, 2, 3$) acting on material volume within surface, Ω.

$\sigma_{ij}(\mathbf{x}, t)$: stress tensor components ($i, j = 1, 2, 3$) within material surface, Ω.

$\varepsilon_{ij}(\mathbf{x}, t)$: strain tensor components ($i, j = 1, 2, 3$) within material surface, Ω.

$C_{ijkl}(\mathbf{x}, t)$: material compliance tensor components ($i, j, k, l = 1, 2, 3$) within material surface, Ω.

$\omega_{ij}(\mathbf{x}, t)$: rotational (shear/skewing) tensor components ($i, j = 1, 2, 3$) within material surface, Ω.

$k(\nu)$: ratio of P to S wave speeds as a function of Poisson's ratio, ν.

$v_{\mathrm{r}}(t)$: instantaneous rupture (crack tip) speed.

K_i: static stress intensity factor for mode-I, mode-II, and mode-III loading ($i = \mathrm{I, II, III}$).

$K_i^{\mathrm{d}}(t)$: dynamic stress intensity factor for mode-I, II, and III loading ($i = \mathrm{I, II, III}$).

K_i^{c}: critical stress intensity factor for mode-I, II, and III loading ($i = \mathrm{I, II, III}$).

$L(t)$: instantaneous crack length.

L_{c}: critical crack length, a length-based criterion for the onset of crack extension.

$f_{\alpha\beta}^i(\theta)$: angular functions of the stress field ($\alpha, \beta = 1, 2$) for mode-I, II, and III loading ($i = $ I, II, III).

$G_i(v_\mathrm{r})$: energy flux into the crack tip for mode-I, II, and III loading ($i = $ I, II, III).

$\phi(\xi_1, \xi_2)$: the shear potential function.

$\psi(\xi_1, \xi_2)$: the dilatational potential function.

$\alpha_\mathrm{p}(v_\mathrm{r})$: relativistic pressure coefficient (inter-sonic regime), $\alpha_\mathrm{p} = \sqrt{1 - (v_\mathrm{r}/c_\mathrm{p})^2}$.

$\alpha_\mathrm{s}(v_\mathrm{r})$: relativistic shear coefficient (sub-shear regime), $\alpha_\mathrm{s} = \sqrt{1 - (v_\mathrm{r}/c_\mathrm{s})^2}$.

$\hat{\alpha}_\mathrm{s}(v_\mathrm{r})$: relativistic shear coefficient (inter-sonic regime), $\hat{\alpha}_\mathrm{s} = \sqrt{(v_\mathrm{r}/c_\mathrm{s})^2 - 1}$.

$\hat{\xi}_1 - \hat{\xi}_2$: moving frame whose origin is fixed to the crack tip and $\hat{\xi}_1$ aligned with crack tip directivity.

$\sigma_{\alpha\beta}^\mathrm{SR}(\xi_1, \xi_2, v_\mathrm{r})$: asymptotic steady-state stress field for a dynamic sub-Rayleigh rupture ($\alpha, \beta = 1, 2$).

$\sigma_{\alpha\beta}^\mathrm{SS}(\xi_1, \xi_2, v_\mathrm{r})$: asymptotic steady-state stress field for a dynamic super-shear rupture ($\alpha, \beta = 1, 2$).

$\varepsilon_{\alpha\beta}^\mathrm{SR}(\xi_1, \xi_2, v_\mathrm{r})$: asymptotic steady-state strain field for a dynamic sub-Rayleigh rupture ($\alpha, \beta = 1, 2$).

$\varepsilon_{\alpha\beta}^\mathrm{SS}(\xi_1, \xi_2, v_\mathrm{r})$: asymptotic steady-state strain field for a dynamic super-shear rupture ($\alpha, \beta = 1, 2$).

$\dot{\mathbf{u}}^\mathrm{SR}(\xi_1, \xi_2, v_\mathrm{r})$: asymptotic steady-state velocity field for a dynamic sub-Rayleigh rupture.

$\dot{\mathbf{u}}^\mathrm{SS}(\xi_1, \xi_2, v_\mathrm{r})$: asymptotic steady-state velocity field for a dynamic super-shear rupture.

$q(v_\mathrm{r})$: super-shear singularity strength, $q = (1/\pi) \tan^{-1} \left[4\alpha_\mathrm{p} \hat{\alpha}_\mathrm{s}/(1 - \hat{\alpha}_\mathrm{s}^2)^2 \right]$, with $q(\sqrt{2}c_\mathrm{s}) = 1/2$.

$D(v_\mathrm{r})$: Rayleigh function, $D = 4\alpha_\mathrm{p}\alpha_\mathrm{s} - (1 + \alpha_\mathrm{s}^2)^2$, where $D \to 0$ as $v_\mathrm{r} \to c_\mathrm{R}$.

$\gamma_\mathrm{p,s}(v_\mathrm{r})$: speed-scaled parameters, $\gamma_\mathrm{p,s} = \sqrt{1 - (v_\mathrm{r}\sin(\theta)/c_\mathrm{p,s})^2}$.

r_p: scaled radius of polar coordinate system, $r_\mathrm{p} = \sqrt{\xi_1^2 + (\alpha_\mathrm{p}\xi_2)^2}$ (unscaled, $r = \sqrt{\xi_1^2 + \xi_2^2}$).

$\theta_\mathrm{p,s}$: scaled angle of polar coordinate system, $\theta_\mathrm{p,s} = \tan^{-1}\left[\alpha_\mathrm{p,s}\tan(\theta)\right]$ (unscaled, $\theta = \tan^{-1}\left[\xi_2/\xi_1\right]$).

T: parameter used for predicting pulse-like ($T \approx 1$) or crack-like ($T \ll 1$) rupture modes.

L: system-dependent process zone size.

β: cohesive zone law parameter, β ($\beta > 0$ is rate-strengthening; $\beta < 0$ is rate-weakening).

D_c: material-dependent characteristic slip distance.

$\theta(t)$: state variable in the rate-and-state frictional law, e.g., total accumulated slip, u_slip.

σ_n: resolved normal stress along the fault (interface), $\sigma_\mathrm{n} = P\cos^2\alpha$.

σ_t: resolved shear stress along the fault (interface), $\sigma_\mathrm{t} = P\cos\alpha\sin\alpha$.

M_w: moment magnitude, proportional to the product of total accumulated slip and slip area.

Experimental design: reflected wave and critical load analyses

$\hat{\zeta}_1 - \hat{\zeta}_2$: coordinate system pinned to a corner of the experimental specimen (rectangular plate), where $\overline{\zeta}_1, \overline{\zeta}_2$ signifies the hypocenter location.

T_{exp}: uncorrupted experimental measurement window, $T_{\text{exp}} = 120\,\mu\text{s}$, based on previous studies.

$D_i(\zeta_1, \zeta_2, \theta_i)$: distance functions measuring total travel distance of reflected information to any point on the plate from specimen edges B, C, and D, respectively $(i = 1, 2, 3)$.

θ_i: dummy angle variables used in reflected wave analysis to determine minimum travel distance of reflected waves from edge B, C, and D $(i = 1, 2, 3)$, where $D_i^{\text{min}} = D_i(\overline{\zeta}_1, \overline{\zeta}_2, \theta_i^{\text{min}})$.

$T_i(\zeta_1, \zeta_2)$: reflected wave arrival times for edge B, C, and D $(i = 1, 2, 3)$ based on c_{p}; $T_i = D_i/c_{\text{p}}$.

$T_{\text{ref}}(\zeta_1, \zeta_2)$: minimum travel time of all reflected waves from source to any point on the specimen.

$T_{\text{inc}}(\zeta_1, \zeta_2)$: arrival time of slowest incident wave (S wave) from the hypocenter, $T_{\text{inc}}(\zeta_1, \zeta_2) = |\boldsymbol{\zeta}|/c_{\text{s}}$.

$\Delta T(\zeta_1, \zeta_2)$: difference between the arrivals of the fastest reflected and slowest direct incident wave emitted from the source, $\Delta T = T_{\text{ref}} - T_{\text{inc}}$.

$w(\zeta_1, \zeta_2)$: out-of-plane $(\pm \hat{\zeta}_3)$ displacement function for the mid-plane of the plate.

D: plate rigidity, $D = Eh^3/12(1 - \nu^2)$, where h is the plate height.

$q(\zeta_1, \zeta_2)$: lateral load applied to the plate (absent in experimental configuration).

$N_{\alpha\beta}(\zeta_1, \zeta_2)$: forces acting along the mid-plane of the plate (per unit length) $(\alpha, \beta = 1, 2)$.

h_{eff}: effective plate height, $h_{\text{eff}} = h/2$, relates analytical solutions for various boundary conditions.

σ_i^{c}: theoretical critical buckling loads for each boundary condition set considered $(i = \text{I}, \text{II}, \text{III}, \text{IV})$.

Specimen geometry and material properties

α: interface angle, measured from the laboratory horizontal (compliment of dip angle in seismology).

D: distance from the event source (hypocenter) to the free surface (fault trace) along the fault.

h: rectangular plate height, $h = 360\,\text{mm}$, determined from reflected wave and critical load analyses.

w: rectangular plate width, $w = 180\,\text{mm}$, determined from reflected wave and critical load analyses.

t: rectangular plate thickness, $t = 9.52\,\text{mm}$, avoids buckling and approximates two-dimensionality.

E: material elastic modulus, $E = 5.2\,\text{GPa}$ for Homalite H-100.

ν: material Poisson's ratio, $\nu = 0.35$ for Homalite H-100.

ρ: material density, $\rho = 1200\,\mathrm{kg/m^3}$ for Homalite H-100.

μ: material shear modulus, $\mu = 1.4\,\mathrm{GPa}$ for Homalite H-100.

$c_{\mathrm{p,s}}$: pressure/shear (P/S) wave speed, $c_{\mathrm{p}} = 2.59\,\mathrm{mm/\mu s}$ and $c_{\mathrm{s}} = 1.27\,\mathrm{mm/\mu s}$, for Homalite H-100.

c_{R}: surface Rayleigh (R) wave speed, $c_{\mathrm{R}} = 1.18\,\mathrm{mm/\mu s}$ for Homalite H-100 (plane-stress).

Experimental parameters

P: initial applied static pre-load from the hydraulic press, mimicking tectonic pressures in the earth.

$\epsilon^{\pm}$: stand-off distance between reflective tape and fault trace required for earth surface-normal measurements on paired hanging (+) and foot wall (−) stations ($\epsilon^{\pm} \approx 200 - 300\,\mathrm{\mu m}$).

$\eta^{\pm}$: stand-off distance between reflective tape and frictional interface required for fault normal measurements on paired hanging (+) and foot wall (−) stations ($\eta^{\pm} \approx 400 - 600\,\mathrm{\mu m}$).

$\theta^{\pm}$: taper angle between interface and the reflective tape edge for paired hanging (+) and foot wall (−) stations ($|\theta^{\pm}| \leq 8°$).

D_{fov}: diameter of expanded laser beam, i.e., diameter of the field-of-view, $D_{\mathrm{fov}} \approx 145\,\mathrm{mm}$.

P_{L}: laser output power, where $P_{\mathrm{L}} = 0.10 - 0.25\,\mathrm{W}$ for alignment and $P_{\mathrm{L}} = 1.00 - 1.85\,\mathrm{W}$ for imaging.

f: objective lens focal length determines image magnification according to the laws of optics.

λ: emission source wavelength, $\lambda = 532\,\mathrm{nm}$ for the green-light laser used in the experiments.

δ: offset distance ($\delta \approx 100\,\mathrm{\mu m}$) between interface surfaces and polishing rig required during polishing.

Arrival times and phase velocities

$\hat{x}_1 - \hat{x}_2$: coordinate system fixed to the fault trace, used for measurements along the simulated earth surface on the hanging wall ($x_1 > 0, x_2 = 0$) and foot wall ($x_1 < 0, x_2 = 0$) plates.

$\hat{x}'_1 - \hat{x}'_2$: coordinate system fixed to the fault trace, used for measurements at various depths, x'_1, along the fault ($x'_2 = 0$).

$t_{\mathrm{p,s}}(x_1)$: initial P and S wave arrivals to stations placed along the simulated earth surface.

$v_{\mathrm{p,s}}(x_1)$: P and S wave phase velocity for stations along the simulated earth surface.

$t_{\mathrm{R}}(x_1)$: surface Rayleigh wave arrivals to stations placed along the simulated earth surface.

$v_{\mathrm{R}}(x_1)$: surface Rayleigh disturbance phase velocity along the simulated earth surface, $v_{\mathrm{R}} = c_{\mathrm{R}}$.

$t_\mathrm{M}(x_1)$: up-dip Mach front arrivals to stations placed along the simulated earth surface.

$v_\mathrm{M}(x_1)$: up-dip Mach front phase velocity along the simulated earth surface.

$t'_\mathrm{M}(x_1)$: down-dip Mach front arrivals to stations placed along the simulated earth surface.

$v'_\mathrm{M}(x_1)$: down-dip Mach front phase velocity along the simulated earth surface.

$t_\mathrm{r}^\mathrm{SR}(x'_1)$: sub-Rayleigh rupture tip arrival time to stations at-depth during up-dip propagation towards the free surface.

$v_\mathrm{r}^\mathrm{SR}(x'_1)$: sub-Rayleigh rupture tip speed during up-dip propagation towards the free surface.

$t'^\mathrm{SR}(x'_1)$: arrival times along the fault of dynamic features (trailing-Rayleigh signature) generated by the sub-Rayleigh rupture tip interacting with the free surface.

$v'^\mathrm{SR}(x'_1)$: phase velocity along the fault of dynamic features (trailing-Rayleigh signature) generated by the sub-Rayleigh rupture tip interacting with the free surface.

$t_\mathrm{r}^\mathrm{SS}(x'_1)$: super-shear rupture tip arrival time to measurement stations at-depth during up-dip propagation to the free surface.

$v_\mathrm{r}^\mathrm{SS}(x'_1)$: super-shear rupture tip speed during up-dip propagation towards the free surface.

$t'^\mathrm{SS}(x'_1)$: arrival times along the fault of dynamic features (down-dip super-shear and trailing-Rayleigh signatures) generated by up-dip propagation of a super-shear rupture.

$v'^\mathrm{SS}(x'_1)$: phase velocities along the fault of dynamic features (down-dip super-shear and trailing-Rayleigh signatures) generated by up-dip propagation of a super-shear rupture.

$t_\mathrm{df}(x'_1)$: arrival time of the lead dilatational field associated with the up-dip super-shear rupture.

Data reduction

d: length disparity between transition lengths measured from two proposed mechanisms.

t_dyn: lag time between trigger of diagnostics and the initiation of dynamic crack growth.

ω_c: cut-off frequency used in filtering algorithm, $\omega_\mathrm{c} = 1.5\,\mathrm{MHz}$.

$\omega_\mathrm{c,n}$: normalized cut-off frequency determined from the Nyquist criterion, $\omega_\mathrm{c,n} = \omega_\mathrm{c}/(\omega_\mathrm{m}/2)$.

ω_m: sampling rate of capturing oscilloscope, $\omega_\mathrm{m} = 1.25\,\mathrm{GHz}$.

t_vib: lag time between Polytec$^\copyright$ velocimeter decoder models VD-02 and VD-09, $t_\mathrm{vib} = 4.9\,\mathrm{\mu s}$.

v_offset: constant DC velocimeter offset on the order of $\approx 0.01\,\mathrm{m/s}$.

Measurable quantities

$\dot{u}_2(x_1, t)$**:** simulated earth surface-normal velocity record, measured on the hanging ($x_1 > 0$) or foot
  wall ($x_1 < 0$) plate.

$u_2(x_1, t)$**:** cumulative free surface-normal displacement record, measured on the hanging ($x_1 > 0$) or
  foot wall ($x_1 < 0$) plate.

$\dot{u}_1^{\pm\eta}(x_1', t)$**:** fault parallel velocity record at-depth, measured on the hanging ($+$) or foot wall ($-$)
  plate on the fault at paired stations with stand-off distances, η, between station and interface.

$\dot{u}_2^{\pm\eta}(x_1', t)$**:** fault normal velocity record at-depth, measured on the hanging ($+$) or foot wall ($-$)
  plate on the fault at paired stations with stand-off distances, η, between station and interface.

$u_1^{\pm\eta}(x_1', t)$**:** fault parallel displacement records at-depth, measured on the hanging ($+$) or foot wall
  ($-$) plate at paired on-fault stations with stand-off distances, η, between station and interface.

$u_2^{\pm\eta}(x_1', t)$**:** fault normal displacement records at-depth, measured on the hanging ($+$) or foot wall
  ($-$) plate at paired on-fault stations with stand-off distances, η, between station and interface.

$\dot{u}_{\text{slip}}(x_1', t)$**:** slip rate between paired hanging and foot wall stations, $\dot{u}_{\text{slip}} = \dot{u}_1^+ - \dot{u}_1^-$.

$\dot{u}_{\text{open}}(x_1', t)$**:** opening rate between paired hanging and foot wall stations, $\dot{u}_{\text{open}} = \dot{u}_2^+ - \dot{u}_2^-$.

$u_{\text{slip}}(x_1', t)$**:** accumulated slip between paired hanging and foot wall stations, $u_{\text{slip}} = u_1^+ - u_1^-$.

$u_{\text{open}}(x_1', t)$**:** accumulated opening between paired hanging and foot wall stations, $u_{\text{open}} = u_2^+ - u_2^-$.

$\beta^{\pm}$**:** angle between up-dip hanging wall ($+$) and foot wall ($-$) Mach fronts and the interface.

$\beta'^{\pm}$**:** angle between down-dip hanging wall ($+$) and foot wall ($-$) Mach fronts and the interface.

O**:** location of the event source (hypocenter), distance $D = 74.3\,\text{mm}$ at-depth along the interface.

$x_1'^{\,\text{tr}}$**:** boundary that demarcates regions of sub-Rayleigh and super-shear rupture tip speed regimes.

ϕ**:** ratio of maximum opening to slip rate, $\phi = \dot{u}_{\text{open}}^{\max}/\dot{u}_{\text{slip}}^{\max}$, used to assess mode dominance.

$|\tau_{\max}|$**:** maximum shear stress, captured with the method of dynamic photo-elasticity.

L_{soot}**:** soot patch penetration length along the interface, measured post-experiment.

$\Delta\sigma$**:** stress drop, the difference between the final load and initial load, $\Delta\sigma = P_{\text{f}} - P$.

u_2^{offset}**:** final free surface-normal offset measured at the fault trace, $u_2^{\text{offset}} = u_2^+ - u_2^-$.

l_{tr}**:** rupture speed transition length from sub-Rayleigh to super-shear regime, measured from source.

l_{patch}**:** length of polished patch heterogeneity located along the interface from the fault trace.

Chapter 1

Introduction

The following thesis is an investigation of earthquake rupture mechanics by means of surrogate laboratory experiments. A rupture is nucleated and guided along a frictionally locked weak plane mating two half-plates of a homogeneous, linear-elastic, isotopic polymer. The propagating crack tip emits waves into the specimen, inducing ground motions. The metrics of laser velocimetry and dynamic photo-elastic interferometry are used synergistically in the correlation of ground motion signatures to arrivals of various rupture features. Of interest is the local mechanical behavior when the rupture is forced to interact with a free surface boundary. The specimen geometry and loading conditions are specifically tailored to model a thrust fault configuration as a thin, two-dimensional slice of earth. In this chapter, analogy is drawn between a sliding block and tectonic plates, introducing the fundamental principles of tectonophysics and orienting the reader to the study. Chapter 2 introduces the laboratory and provides a detailed overview of experimental design and procedures. Chapter 3 describes the reduction and synchronization of the two diagnostic outputs. Chapter 4 presents results and provides a discussion of salient observations, namely asymmetry in ground motion magnitudes between the hanging and foot wall plates and the possibility of fault opening near the free surface for both sub-Rayleigh and super-shear rupture speed regimes. Experimental reproducibility is assessed in Chapter 5, followed by a summary of research findings and concluding remarks in Chapter 6. Thoughts on future research directions are shared in Chapter 7.

Friction is a resistive force confined at the interface of two contacting surfaces. According to classical rigid body mechanics, a block resting on an incline under the action of a gravity field remains at rest if the friction force F_s can match the resolved weight force along the direction of the incline, $F_\mathrm{s} \geq W \sin \alpha$ (Figure 1.1, left panel). Increasing the inclination angle, α, such that the driving force outweighs the available frictional resistance accelerates the block down the incline. Continuous resistance during sliding is supplied by a dynamic friction force, F_d. Coulomb proposed a simple functional form for F_s and F_d as the product of resolved normal forces present at the contact interface and an appropriate frictional coefficient: this gives, for the block, the simple relation $F_\mathrm{s,d} = f_\mathrm{s,d} W \cos \alpha$ [1]. In the absence of motion ($v = 0$) the coefficient assumes the static value,
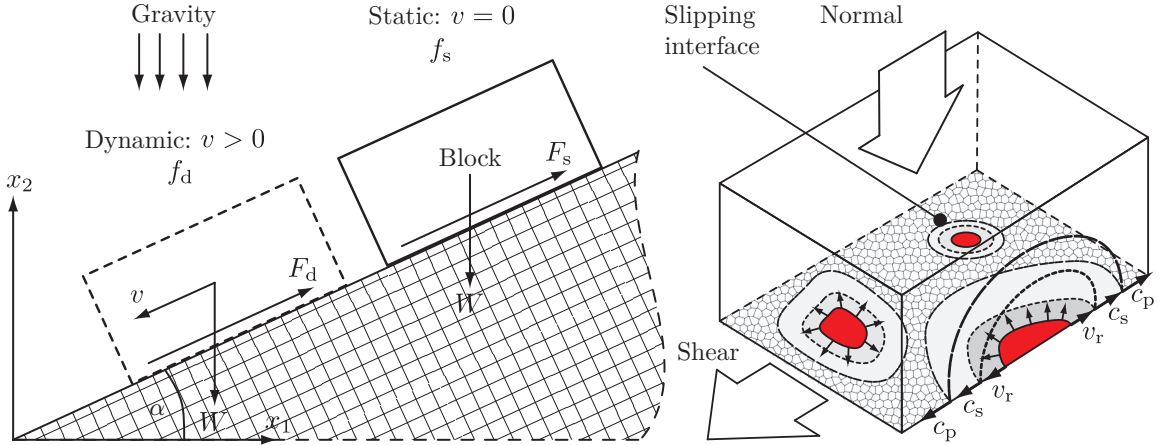
Figure 1.1: Coulomb friction model in the framework of rigid body Netwonian mechanics (left panel). Nucleation of local slip events at the contact interface of a deformable body (right panel). Analogy of the sliding block to earthquake mechanics is the basis of the experimental work in this thesis.

f_s, while during sliding ($v > 0$) the coefficient assumes the dynamic value, f_d. Whether $f_\mathrm{s} > f_\mathrm{d}$ or $f_\mathrm{d} > f_\mathrm{s}$ depends on the evolution of frictional resistance along the slipping interface: such changes in traction are tangible to anyone who has tried to move a refrigerator across the kitchen floor. Non-dimensional coefficients f_s and f_d are determined experimentally for each specific system and provide an excellent predictive method for rigid body dynamics where friction is a dominant force. However, the assumptions of rigid body motion and the discontinuous jump in friction coefficient shroud the underlying physical mechanisms. Any imperfection in the contact surface would yield normal stress gradients, and, in turn, gradients of driving conditions, implying that slip will initiate at a given point rather than uniformly along the interface (red patches in Figure 1.1, right panel), in direct contradiction of the rigid body assumption. Finite times are required to communicate the onset of local sliding to the remainder of the interface. Continuum mechanics provides a theoretical basis for investigating the physical mechanism governing material deformations and consequent slip events at the contact interface of such sliding systems as the block.

The governing equations of continuum mechanics identify characteristic speeds with which information propagates by relating forces to deformations at every point in the material body. The main assumptions in the framework are that field values such as displacement, $u_i(\mathbf{x}, t)$, velocity, $\dot{u}_i(\mathbf{x}, t)$, accelerations, $\ddot{u}_i(\mathbf{x}, t)$, stresses, $\sigma_{ij}(\mathbf{x}, t)$, and strains, $\varepsilon_{ij}(\mathbf{x}, t)$, to name a few, exist and are appropriately differentiable in space and time coordinates within the applicable material volume defined by the control surface Ω (Figure 1.2) [2, 3]. Thus the field equations will more accurately describe the motions of a dense solid than the rarefied gas of the upper atmosphere, as the latter challenges the approximation of a continuum. Assuming a linear-elastic material response $\sigma_{ij}(\mathbf{x}, t) = C_{ijkl}(\mathbf{x}, t)\varepsilon_{ij}(\mathbf{x}, t)$, the governing set of equations for a homogeneous, isotropic solid for a Cartesian frame are expressed in indicial notation as [4]:

$$\sigma_{ij,j} + \rho f_i = \rho \ddot{u}_i,$$

$$\sigma_{ij} = \lambda \varepsilon_{kk} \delta_{ij} + 2\mu \varepsilon_{ij},$$

$$\varepsilon_{ij} = \frac{1}{2}(u_{i,j} + u_{j,i}),$$

$$\omega_{ij} = \frac{1}{2}(u_{i,j} - u_{j,i}),$$

(1.1)

where $i, j, k = 1, 2, 3$. The first relates Cauchy stress tensor components $\sigma_{ij}(\mathbf{x}, t)$ and field forces $f_i(\mathbf{x}, t)$ to accelerations $\ddot{u}_i(\mathbf{x}, t)$ with the material density ρ, the second relates stresses to strains $\varepsilon_{ij}(\mathbf{x}, t)$ with the Lamé material constants λ and μ, the third relates the strain tensor (symmetric) to the sum of displacement gradients $u_{i,j}(\mathbf{x}, t)$ and $u_{j,i}(\mathbf{x}, t)$, and the fourth relates the rotational tensor (anti-symmetric) $\omega(\mathbf{x}, t)$ to the difference of said displacement gradients. Substituting ε_{ij} into the constitutive relation and then into the equation of motion yields the Navier form in terms of u_i:

$$(\lambda + \mu)u_{j,ji} + \mu u_{i,jj} + \rho f_i = \rho \ddot{u}_i. \tag{1.2}$$

The vector identity $\nabla^2 \mathbf{u} = \nabla \nabla \cdot \mathbf{u} - \nabla \times \nabla \times \mathbf{u}$ recasts Navier's equation, separating dilatational ($\nabla \cdot \mathbf{u}$, compressive/expansive) and rotational ($\nabla \times \mathbf{u}$, skewing/shear) terms, giving the expression

$$(\lambda + 2\mu)\nabla \nabla \cdot \mathbf{u} - \mu \nabla \times \nabla \times \mathbf{u} + \rho \mathbf{f} = \rho \ddot{\mathbf{u}}. \tag{1.3}$$

In the absence of body forces, $\mathbf{f} = \mathbf{0}$, the divergence of Equation 1.3 gives

$$\nabla^2 \Delta = \frac{1}{c_\mathrm{p}^2} \frac{\partial^2 \Delta}{\partial t^2}. \tag{1.4}$$

This is recognized as the wave equation, where dilatational information encapsulated in $\Delta = \nabla \cdot \mathbf{u}$ propagates at a characteristic wave speed, $c_\mathrm{p} = \sqrt{(\lambda + 2\mu)/\rho}$. This is the P (pressure) wave velocity of the material, appropriately named as the disturbance is dilatational in nature. Taking the divergence of Equation 1.3 followed by the curl yields yet another wave equation,

$$\nabla^2 \boldsymbol{\omega} = \frac{1}{c_\mathrm{s}^2} \frac{\partial \boldsymbol{\omega}}{\partial t^2}, \tag{1.5}$$

where the propagation velocity, $c_\mathrm{s} = \sqrt{\mu/\rho}$, is called the S (shear) wave speed due to the rotational nature of the propagating disturbance, $\boldsymbol{\omega}$. These characteristic wave speeds are dependent on intrinsic material properties, ρ, μ, and λ. The ratio of P to S wave speeds may be written as the function $k(\nu) = \sqrt{2(1 - \nu)/(1 - 2\nu)}$, where ν is the Poisson's ratio. Due to limits of Poisson's ratio, $0 \leq \nu \leq 1/2$, the dilatational speed is necessarily greater than the shear speed, $c_\mathrm{p} > c_\mathrm{s}$, and is usually twice so in brittle solids [5]. Equilibrium configurations require time-dependent displacement $u_i(\mathbf{x} = \Omega, t)$ and/or stressing $\sigma_{ij}(\mathbf{x} = \Omega, t)$ boundary conditions to generate these dynamic waves.
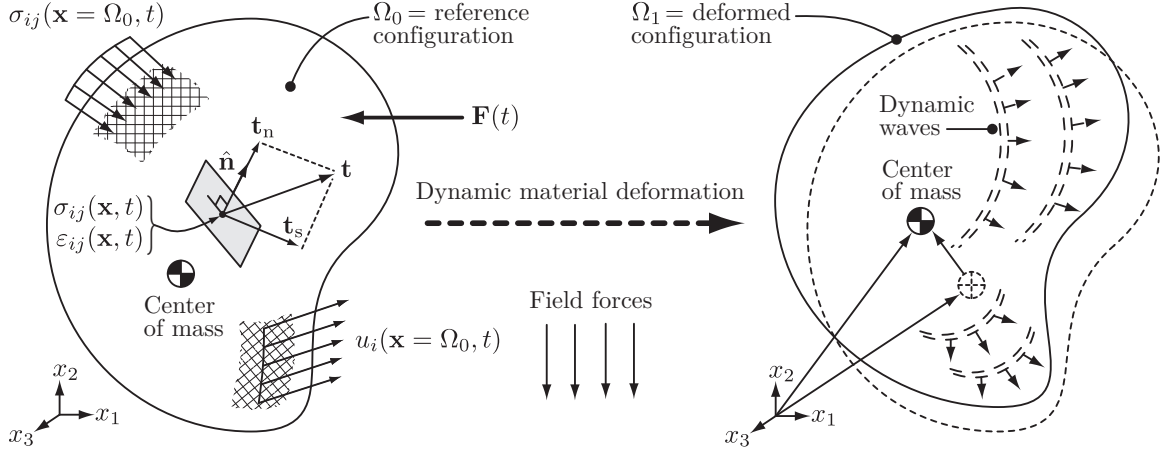
Figure 1.2: Description of motion for an arbitrarily shaped, deformable body within the continuum mechanics framework (Equation 1.1). An imbalance of static and dynamic loads applied on the system causes the body to translate, rotate, and deform through the transmission of stress waves.

Loading rates and amplitudes of dynamic inputs determine the character of field value distributions. Wave speeds increase with the ease a particle can transfer dynamic deformations to its adjacent neighbors, e.g., solids typically have greater wave speeds than gases [6]. A hammer strike at the end of a long, slender table will generate both dilatational (volumetric) and shear (distortional) waves in the solid due to the coupling of stress components via the Poisson effect. An observer with an ear at the opposite end of the table will first sense the P wave followed by the S wave. Finally, the sound of the hammer strike will reach the remaining ear, carried by acoustic pressure waves in the air. Figure 1.3 shows dilatational and shear point sources propagating at various constant velocities, v_r, along a linear path, analogous to dragging the hammer across the table length. The moving source simultaneously emits P and S wavelets whose relative displacement magnitudes and directions are represented by arrows (shown independently in the top and bottom panels for clarity) [7]. Doppler effects compress and expand these waves upstream and downstream of the moving source, respectively. Once v_r surpasses a given wave speed, characteristic lines emanate from the source. These characteristics are called Mach fronts and are spatial discontinuities across which drastic, sudden changes of field values occur [8]. A source traveling in the inter-sonic regime, $c_s < v_r < c_p$, emits shear Mach fronts since $c_s < v_r$; in the super-sonic regime, $c_p < v_r$, the source emits shear as well as dilatational Mach fronts; in the sub-sonic regime, $0 < v_r < c_s$, no Mach fronts may be formed. Sources traveling faster than a characteristic speed force dynamic information to trail behind, bounding the influence of the emitted waves within a Mach cone; for this reason, a super-sonic aircraft is silent to the upstream observer [9]. Much like a shock wave is the physical mechanism with which a super-sonic flow decelerates to sub-sonic values, these bulk waves are the physical mechanism with which a solid reacts to dynamic loads in order to redistribute forces within the body in accord with the fundamental principles of nature: the conservation law of

Sub-sonic regime: $0 < v_r < c_p$

Super-sonic regime: $c_p < v_r$

v_r

β

v_r

Pressure discontinuities
normal to Mach front

$+$ $-$
$-$ $+$

P wavelets

Sub-Rayleigh regime: $0 < v_r < c_R$

At shear wave speed: $v_r = c_s$

v_r

v_r

S wavelets

Super-shear regime: $c_s < v_r < c_p$

Nodal Mach $(\beta = 45°)$: $v_r = \sqrt{2}c_s$

β

v_r

Shear discontinuities
parallel to Mach front

β

v_r
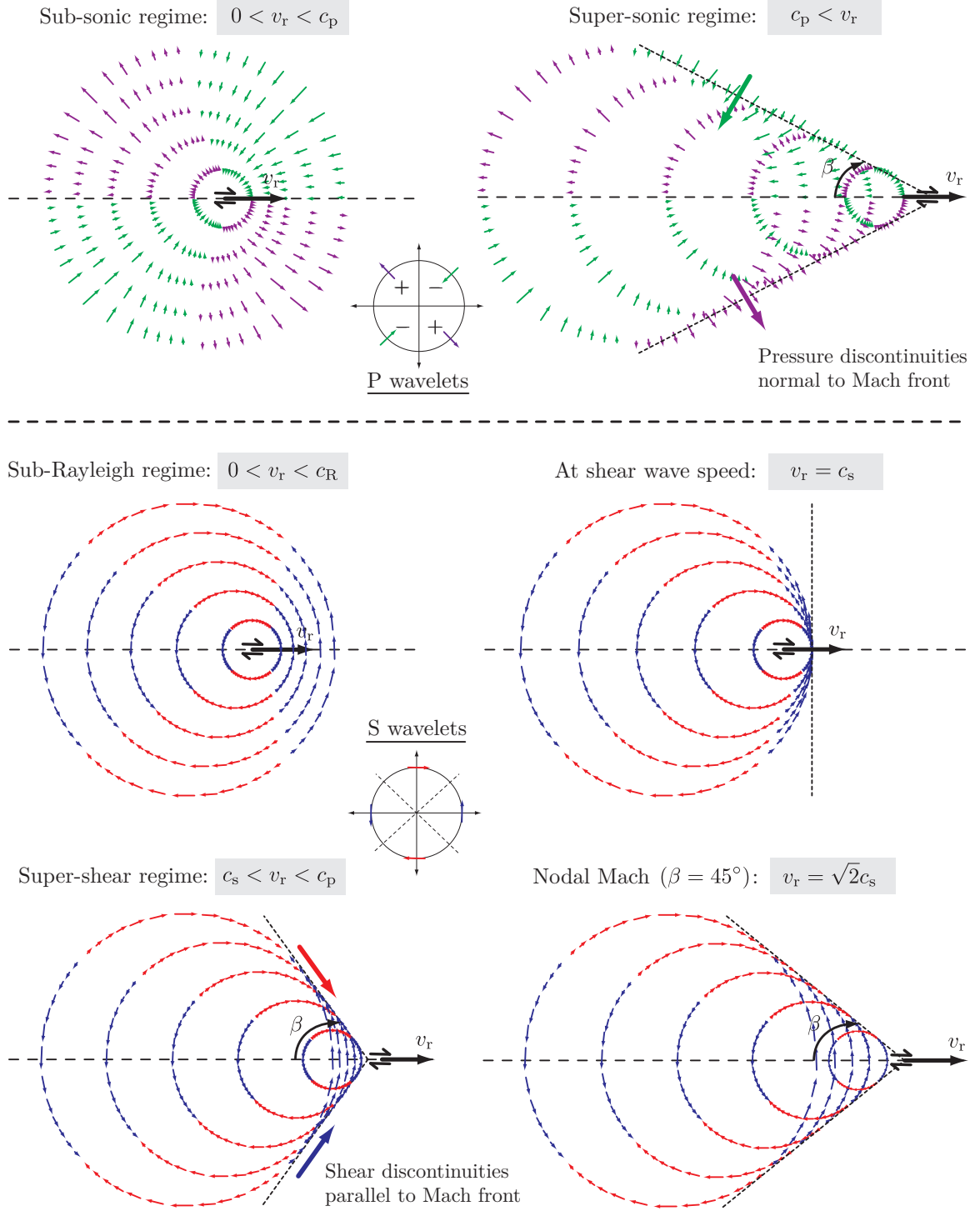
Figure 1.3: Pressure (c_p) and shear (c_s) wavelets emitted from point sources moving at constant velocities, v_r. Particle motion direction and magnitude are represented by arrows of varying lengths. Mach cones are formed when the source speed, v_r, surpasses a characteristic wave speed, c_p or c_s.

mass, momentum, the minimization of internal energy, and maximization of universal entropy. In fact, a moving crack tip is an in situ emission source of both P and S waves during fracture [10].
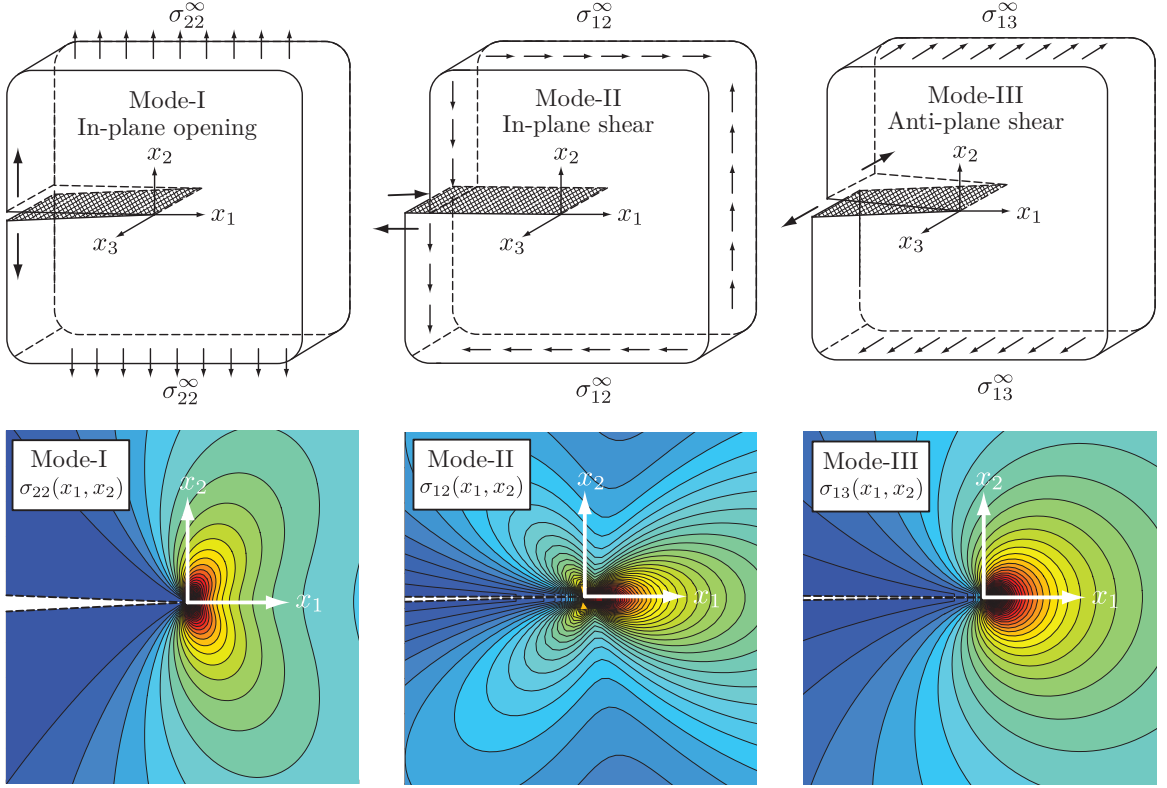
Figure 1.4: Schematic representation of mode-I, mode-II, and mode-III loading configurations (top panels) and the resulting static, singular stress field near the crack tip (bottom panels). The crack tip is a stress concentration, amplifying far-field stresses and driving the mechanical response.

Fracture mechanics is the study of flawed materials and their response to various driving conditions. A crack is one such flaw in a continuum, encompassing the collective boundaries of de-bonded material. Presence of the flaw introduces an additional length scale into the problem, as well as requires additional boundary conditions for the flaw surfaces. While the material properties remain homogeneous, the fracture response is expected to be quite different than a monolithic analogue. A canonical problem of fracture mechanics is that of a linear edge crack in a semi-infinite plate subject to constant far-field loads, as shown in Figure 1.4. Far-field, in-plane tensile loads are called mode-I ($\sigma_{22}^{\infty}, u_1^{\infty}$, left column); in-plane shear loads are called mode-II ($\sigma_{12}^{\infty}, u_2^{\infty}$, middle column); anti-plane shear loads are called mode-III ($\sigma_{13}^{\infty}, u_3^{\infty}$, right column) [11]. The crack has zero thickness and is traction free, $\sigma_{ij} = 0$. Equations 1.1, with no loss of generality, may be reduced to two-dimensions under the assumptions of plane-stress ($\sigma_{i3} = 0$) or plane-strain ($\varepsilon_{i3} = 0$), which are particularly valid for a material configuration whose third dimension is less capable of sustaining stress or strain gradients than the remaining two, $h, w \gg t$; this approximation is the geometric definition of a plate. A static solution in the absence of body forces, $\ddot{u}_i = f_i = 0$, reduces the problem to solving the bi-harmonic equation $\nabla^4 \Phi(r, \theta) = 0$ for the scalar potential $\Phi(r, \theta)$ with an arbitrary mixture of boundary conditions [12]. The scalar potential is in turn related to stresses; thus the solution for

$\Phi(r,\theta)$ determines all mechanical field data within the material body, Ω. The general solution for an arbitrary mixture of loads is given by [13]:

$$\sigma_{\alpha\beta}(r,\theta) = \frac{K_{\text{I}}}{\sqrt{2\pi r}} f_{\alpha\beta}^{\text{I}}(\theta) + \frac{K_{\text{II}}}{\sqrt{2\pi r}} f_{\alpha\beta}^{\text{II}}(\theta) + \frac{K_{\text{III}}}{\sqrt{2\pi r}} f_{\alpha\beta}^{\text{III}}(\theta), \tag{1.6}$$

where $r = \sqrt{x_1^2 + x_2^2}$ and $\theta = \tan^{-1}(x_2/x_1)$ are coordinates of a local polar frame fixed at the crack tip, $f_{\alpha\beta}^{i}(\theta)$ are mode-specific angular functions, and constants K_i are the mode-specific stress intensity factors. Indices $i, j, k = 1, 2, 3$ are reduced to $\alpha, \beta = 1, 2$ after loss of one spatial dimension. The stress intensity factors, K_i are functions of geometry and loading conditions whose relative magnitudes provide a quantitative measure of mode-mixture present in the system configuration [14]. The singular solutions for each mode are plotted in the bottom panels of Figure 1.4 for arbitrary values of K_i [15]. Stress magnitudes tend to infinite values in the limit $r \to 0^+$: the crack tip is a mathematical singularity of order $\mathcal{O} = 1/2$ in the stress field, amplifying the far-field stresses in the local vicinity of the crack tip. In the complex plane, the crack faces ($x_1 < 0, x_2 = \pm\eta$ with $\eta \to 0$) lie along a branch cut for an arbitrary Riemann surface, allowing discontinuous values across the crack face [16]. Infinite stresses are physically unsustainable; plastic effects are thus activated near the crack tip at points where the material proportional limit is surpassed [17]. If the plastic zone size remains small with respect to the K-dominant region of the singular elastic solution (Equation 1.6), mechanical behavior is accurately predicted by the current linear analysis [18]; this is usually the case for stiff, brittle materials. De-bonding, if any, is expected to initiate at these stress concentrations. Indeed, the crack tip accelerates once local amplified driving stresses outweigh the resistive material bond strength. Fracture criteria determine the onset of quasi-static crack growth. One such criterion compares the configuration stress intensity factors, $K_i(t)$, to tabulated critical values, K_i^{c}; growth commences once $K_i(t) > K_i^{\text{c}}$ [19]. The scalars $K_i(t)$, in effect, communicate far-field loads to local fields near the crack tips, which determine and dominate the mechanical response. Another criterion makes use of a critical crack length, L_{c}: similarly, growth commences once $L(t) > L_{\text{c}}$ [20]. Transition from quasi-static to dynamic crack growth rates is the culprit of most catastrophic failures in engineering systems, occurring abruptly, with little warning, and typically at high rupture speeds. The de Havilland DH 106 Comet airliner was constructed with square windows, which significantly amplified the hoop stresses induced by repeated cabin pressurization cycles; the crack tips transitioned to dynamic rates and de-bonded the fuselage, resulting in three unfortunate mid-air accidents in 1953 and a re-design to rounded corners [21]. Introduction of flaws alters the fracture behavior of the material, at best maintaining the value of its monolithic analogue, yet usually falling significantly short. Note that changes in crack length are strictly not permitted in the static analysis: a dynamic analysis is required to provide insight into the nature of radiation since the crack tip is a translating source of both dilatational and shear waves.
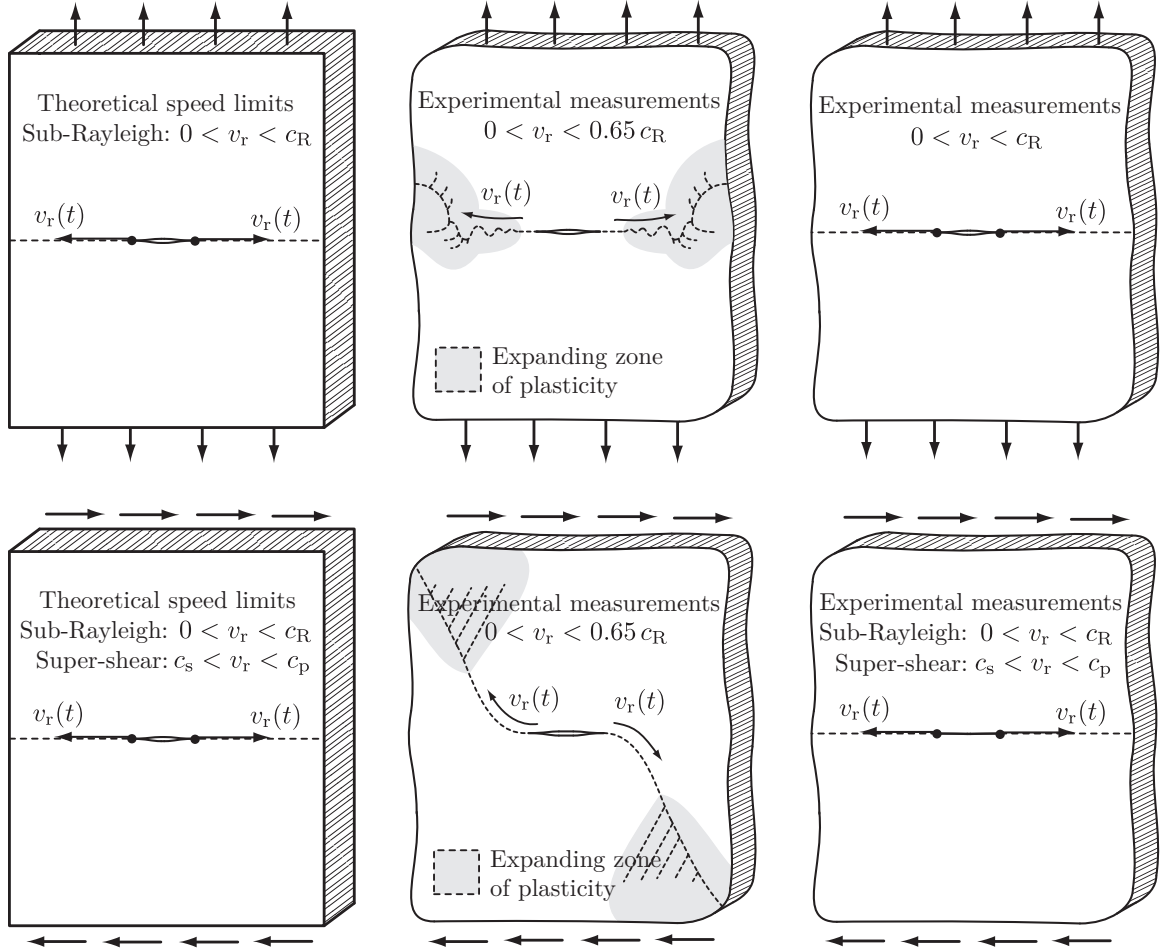
Figure 1.5: Crack speeds and directionality for far-field mode-I (top) and mode-II loads (bottom).

Rupture speed limits are predicted through the full dynamic solution of the governing equations and bounding arguments from energetics. Once inertial terms attain magnitudes on the order of the stress tensor components, $|\rho \ddot{u}_\alpha| \approx |\sigma_{\alpha\beta}|$, the crack propagates dynamically into the medium [22]; this typically occurs when the crack tip speed is a large fraction of c_s. A semi-infinite crack, subject to arbitrary far-field loading, is confined to the $\hat{x}_1 - \hat{x}_3$ plane. For convenience of extracting local values near the crack, the origin of a moving Cartesian frame, $\hat{\xi}_1 - \hat{\xi}_2 - \hat{\xi}_3$, is fixed to the crack tip with its unit normal $\hat{\xi}_1$ always parallel to the instantaneous crack tip directivity. The crack tip is a structureless point whose boundary is co-linear with $\hat{\xi}_3$. Galilean invariance draws equivalencies between the inertial and moving frames with relations $\xi_1 = x_1 - v_r t$, $\xi_2 = x_2$, and $\xi_3 = x_3$. The general stress field solution in the local vicinity of a steady-state crack tip ($v_r = $ constant) confined to the intersection of two half-spaces is given by [23]:

$$\sigma_{\alpha\beta}^{\mathrm{SR}}(r,\theta,t) = \frac{K_{\mathrm{I}}^{\mathrm{d}}(t)}{\sqrt{2\pi r}} f_{\alpha\beta}^{\mathrm{I}}(\theta, \alpha_{\mathrm{p}}, \alpha_{\mathrm{s}}) + \frac{K_{\mathrm{II}}^{\mathrm{d}}(t)}{\sqrt{2\pi r}} f_{\alpha\beta}^{\mathrm{II}}(\theta, \alpha_{\mathrm{p}}, \alpha_{\mathrm{s}}) + \frac{K_{\mathrm{III}}^{\mathrm{d}}(t)}{\sqrt{2\pi r}} f_{\alpha\beta}^{\mathrm{III}}(\theta, \alpha_{\mathrm{p}}, \alpha_{\mathrm{s}}), \qquad (1.7)$$

a form similar to the static case (Equation 1.6), except to account for the motion of the singularity, relativistic terms $\alpha_{\mathrm{p,s}} = \sqrt{1 - (v_{\mathrm{r}}/c_{\mathrm{p,s}})^2}$ enter in the angular functions $f^i_{\alpha\beta}(\theta, \alpha_{\mathrm{p}}, \alpha_{\mathrm{s}})$, and the static stress intensity factors are replaced by their dynamic analogues related through universal functions $k_i(v_{\mathrm{r}})$ as $K^{\mathrm{d}}_i(v_{\mathrm{r}}) = k_i(v_{\mathrm{r}})K_i(v_{\mathrm{r}})$. The superscript in Equation 1.7 signifies the sub-Rayleigh (SR) speed regime, $0 < v_{\mathrm{r}} < c_{\mathrm{R}}$, a subset of the domain $0 < v_{\mathrm{r}} < c_{\mathrm{s}}$; significance of the Rayleigh wave speed, c_{R}, will soon be elucidated. The dynamic energy release rate, $G(v_{\mathrm{r}})$, is the energy flux from the surrogate body into the crack tip per unit area of new crack surface generated from the action of material de-bonding. A contour integral encompassing the crack tip is used to evaluate $G(v_{\mathrm{r}})$ [13]:

$$G(v_{\mathrm{r}}) = A_{\mathrm{I}}(v_{\mathrm{r}})\frac{K^{\mathrm{d}}_{\mathrm{I}}(v_{\mathrm{r}})^2}{E'} + A_{\mathrm{II}}(v_{\mathrm{r}})\frac{K^{\mathrm{d}}_{\mathrm{II}}(v_{\mathrm{r}})^2}{E'} + A_{\mathrm{III}}(v_{\mathrm{r}})\frac{K^{\mathrm{d}}_{\mathrm{III}}(v_{\mathrm{r}})^2}{E'}, \tag{1.8}$$

where $E' = E$ for plane-stress and $E' = E/(1 - \nu^2)$ for plane-strain, and $A_i(v_{\mathrm{r}})$ are functions of rupture speed, v_{r}. Thermodynamic arguments mandate that the crack tip remains a sink and never becomes a source of energy, as the breaking of bonds is naturally an energy consuming process, requiring a constant supply from the surrounding material [24]; permissible rupture speeds v_{r} for each individual mode must therefore satisfy the inequality $G_i(v_{\mathrm{r}}) > 0$.

Figure 1.5 depicts bi-lateral mode-I (top panels) and mode-II ruptures (bottom panels) as theoretical models (left column) and schematic representations of experimental results for unbounded (middle column) as well as confined crack growth (right column). For a mode-I rupture ($K^{\mathrm{d}}_{\mathrm{II}} = K^{\mathrm{d}}_{\mathrm{III}} = 0$), the function $G_{\mathrm{I}}(v_{\mathrm{r}})$ is finite and positive for values $0 < v_{\mathrm{r}} < c_{\mathrm{R}}$, yet becomes negative and monotonically decays when $c_{\mathrm{R}} < v_{\mathrm{r}}$; steady-state mode-I de-bonding is thus predicted to propagate at a maximum speed of c_{R} [23, 24]. Experiments on a monolithic plate with a prescribed crack subject to mode-I loading show that the rupture initially propagates in a linear fashion; however, the rupture soon incurs an instability and begins to undulate about the crack plane, accelerating and decelerating as it turns [25, 26, 27]. Significant micro-damage is observed at the onset of instability, showing the desire for the crack to branch off into different directions. The zone of plastic effects and micro-damage drastically grows in size as the rupture tip speed increases (shaded regions in Figure 1.5), demanding greater fracture energy and eventually branching off into secondary ruptures [28, 29, 30]: maximum speeds attained are $v^{\mathrm{max}}_{\mathrm{r}} \approx 0.65 c_{\mathrm{R}}$ [31]. Similar mode-I experiments are conducted with two half-plates cohesively bound at the mid-plane, $\hat{x}_1 - \hat{x}_3$, in hopes of guiding the crack along the prescribed path [32]: weld points in structures, glued interfaces, composites, or atomic weak planes in an anisotropic crystal exemplify this situation. In the limit of vanishing bond strength, the measured rupture speeds indeed approach the Rayleigh wave speed, $v_{\mathrm{r}} \to c_{\mathrm{R}}$, validating the upper limit predictions of the theoretical model: the weak path guides the rupture and suppresses branching. Similar arguments with $G_{\mathrm{II}}(v_{\mathrm{r}})$ and $G_{\mathrm{III}}(v_{\mathrm{r}})$ reveal that mode-II and III ruptures have speed limits of c_{R} and c_{s} in the sub-sonic regime [33]. The function $G_{\mathrm{II}}(v_{\mathrm{r}})$ has
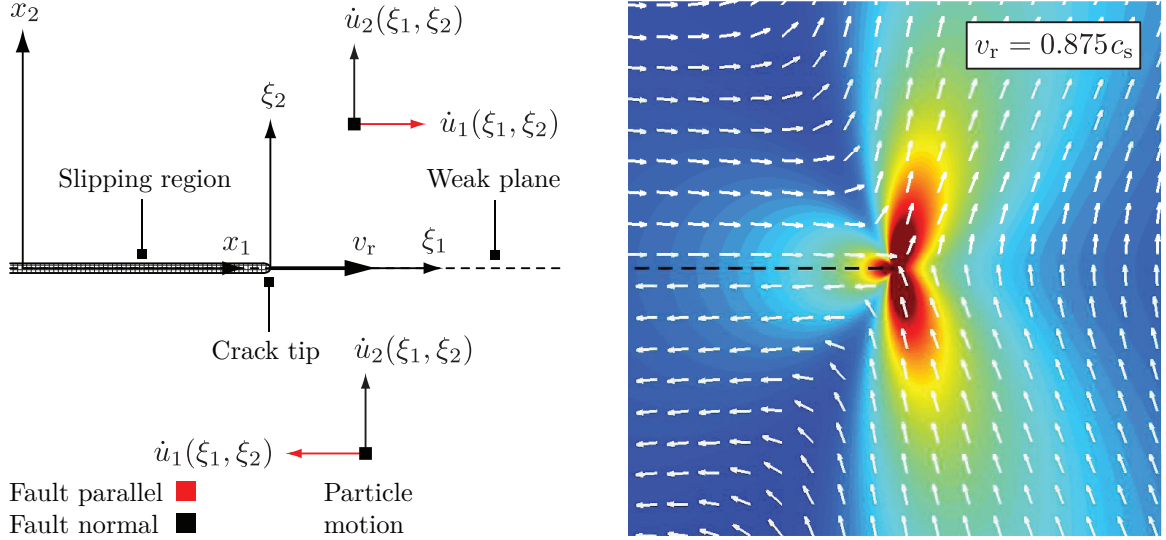
Figure 1.6: Schematic setup and resulting contour plot of the asymptotic velocity field for a steady-state mode-II rupture in the sub-Rayleigh regime $(0 < v_{\rm r} < c_{\rm R})$ at speed $v_{\rm r} = 0.875c_{\rm s}$. Unit vectors and contour levels indicate the direction and magnitude of velocity, $\mathbf{u}(\xi_1, \xi_2)$, respectively. [37]

a more nuanced behavior, with finite positive values in the SR domain, $0 < v_{\rm r} < c_{\rm R}$, zero at the Rayleigh speed, $G_{\rm II}(c_{\rm R}) = 0$, negative values for the sub-domain, $c_{\rm R} < v_{\rm r} < c_{\rm s}$, and zero values for all inter-sonic speeds except for $v_{\rm r} = \sqrt{2}c_{\rm s}$: ruptures in the super-shear (SS) domain, $c_{\rm s} < v_{\rm r} < c_{\rm p}$, are predicted to propagate at the particular speed $v_{\rm r} = \sqrt{2}c_{\rm s}$. The energy barrier $G_{\rm II} < (c_{\rm R}, c_{\rm s})$, however, demarcates the SR and SS regimes, raising the question of whether mode-II SS speeds are physically attainable. Mode-II experiments of unconstrained ruptures consistently observe the crack tip initially kinking to an angle of approximately $\pm 72°$ with respect to the crack plane; local crack tip directivity is selected to maximize mode-I tensile de-bonding [34, 35, 36]. For this reason, the crack speed in an unconstrained mode-II rupture is again limited to mode-I values, $0 < v_{\rm r} < c_{\rm R}$ [13]. Confining the rupture to a weak plane, however, enforces shear-dominant de-bonding, restricting rupture directivity and perhaps extending the physically permissible speeds to the SS regime.

Mechanical field values of mode-II SR and SS ruptures have unique characters. Dilatational and shear elastic potentials, ϕ and ψ, are governed by a set of partial differential equations [23]:

$$
\begin{aligned}
\phi_{,11}\,(\xi_1, \xi_2) + \frac{1}{\alpha_{\rm p}^2}\phi_{,22}\,(\xi_1, \xi_2) &= 0, && 0 < v_{\rm r} < c_{\rm p}, \\
\psi_{,11}\,(\xi_1, \xi_2) + \frac{1}{\alpha_{\rm s}^2}\psi_{,22}\,(\xi_1, \xi_2) &= 0, && 0 < v_{\rm r} < c_{\rm s}, \\
\psi_{,11}\,(\xi_1, \xi_2) - \frac{1}{\hat{\alpha}_{\rm s}^2}\psi_{,22}\,(\xi_1, \xi_2) &= 0, && c_{\rm s} < v_{\rm r} < c_{\rm p},
\end{aligned}
\tag{1.9}
$$

where $\hat{\alpha}_{\rm s} = \sqrt{(v_{\rm r}/c_{\rm s})^2 - 1}$ is the inter-sonic relativistic shear parameter. Motion in the SR regime is governed by a set of elliptical equations; in the SS regime, a change in coefficient sign transforms

the set to an elliptical and hyperbolic pair [38]. Analytical solutions for both SR (Equation 1.7) and SS regimes for a steady-state mode-II rupture propagating along a linear weak plane are [13]:

$$\sigma_{\alpha\beta}^{\mathrm{SR}}(\xi_1, \xi_2, v_{\mathrm{r}}) = \frac{K_{\mathrm{II}}^{\mathrm{d}}(t)}{\sqrt{2\pi r}} f_{\alpha\beta}(\theta, \alpha_{\mathrm{p}}, \alpha_{\mathrm{s}}), \tag{1.10}$$

$$\sigma_{\alpha\beta}^{\mathrm{SS}}(\xi_1, \xi_2, v_{\mathrm{r}}) = K_{\mathrm{II}}^{*}(t) \left[\frac{l_{\alpha\beta}(\theta, \alpha_{\mathrm{p}}, \hat{\alpha}_{\mathrm{s}})}{r^q} - \frac{m_{\alpha\beta}(\alpha_{\mathrm{p}}, \hat{\alpha}_{\mathrm{s}})}{(-\xi_1 - \hat{\alpha}_{\mathrm{s}}|\xi_2|)^q} H(-\xi_1 - \hat{\alpha}_{\mathrm{s}}|\xi_2|) \right], \tag{1.11}$$

where $r = \sqrt{\xi_1^2 + \xi_2^2}$, $\theta = \tan^{-1}(\xi_2/\xi_1)$, $l_{\alpha\beta}(v_{\mathrm{r}})$, and $m_{\alpha\beta}(v_{\mathrm{r}})$ are scaled functions of speed, v_{r}, $q(v_{\mathrm{r}}) = (1/\pi) \tan^{-1} \left[4\alpha_{\mathrm{p}}\hat{\alpha}_{\mathrm{s}}/(1 - \hat{\alpha}_{\mathrm{s}}^2)^2 \right]$ is the singularity strength, K_{II}^{*} is the inter-sonic mode-II stress intensity factor, and $H(\cdot)$ is the Heaviside unit-step function. Inspection of Equations 1.10 and 1.11 shows the unique features of SS ruptures, namely the variable singularity strength with rupture speed, $q(v_{\mathrm{r}})$, and the emergence of the Heaviside step function, $H(\cdot)$. Once $c_{\mathrm{s}} < v_{\mathrm{r}}$, shear waves are forced to trail behind the emission source and may not extend their influence outside of a cone whose bounds are defined by the argument of the Heaviside function, $-\xi_1 - \hat{\alpha}_{\mathrm{s}}|\xi_2|$ (Figure 1.3, bottom panels). When $v_{\mathrm{r}} = \sqrt{2}c_{\mathrm{s}}$, the square-root singularity of the SR field is recovered, $q = 1/2$, and the shear discontinuities disappear as the Mach fronts become nodal in shear [37]. The stress solutions of Equations 1.10 and 1.11 are used to determine the SR and SS strain fields, $\varepsilon_{\alpha\beta}^{\mathrm{SR/SS}}(\xi_1, \xi_2, v_{\mathrm{r}})$, which in turn are integrated in space to determine the displacement fields, $u_{\alpha}^{\mathrm{SR/SS}}(\xi_1, \xi_2, v_{\mathrm{r}})$, then differentiated in time to obtain the velocity fields, $\dot{u}_{\alpha}^{\mathrm{SR/SS}}(\xi_1, \xi_2, v_{\mathrm{r}})$ [39]:

$$\dot{\mathbf{u}}^{\mathrm{SR}}(\xi_1, \xi_2, v_{\mathrm{r}}) = \begin{cases} -\left(\dfrac{\mathrm{sgn}(\xi_2)v_{\mathrm{r}}\alpha_{\mathrm{s}}K_{\mathrm{II}}(t)}{\mu D(v_{\mathrm{r}})\sqrt{2\pi r}} \right) \left[\dfrac{2\sin(\theta_{\mathrm{p}}/2)}{\sqrt{\gamma_{\mathrm{p}}}} - (1 + \alpha_{\mathrm{s}}^2)\dfrac{\sin(\theta_{\mathrm{s}}/2)}{\sqrt{\gamma_{\mathrm{s}}}} \right] \hat{\xi}_1, \\ -\left(\dfrac{v_{\mathrm{r}}K_{\mathrm{II}}(t)}{\mu D(v_{\mathrm{r}})\sqrt{2\pi r}} \right) \left[2\alpha_{\mathrm{p}}\alpha_{\mathrm{s}}\dfrac{\cos(\theta_{\mathrm{p}}/2)}{\sqrt{\gamma_{\mathrm{p}}}} - (1 + \alpha_{\mathrm{s}}^2)\dfrac{\cos(\theta_{\mathrm{s}}/2)}{\sqrt{\gamma_{\mathrm{s}}}} \right] \hat{\xi}_2, \end{cases} \tag{1.12}$$

$$\dot{\mathbf{u}}^{\mathrm{SS}}(\xi_1, \xi_2, v_{\mathrm{r}}) = \begin{cases} Av_{\mathrm{r}} \left[\dfrac{\sin(q\theta_{\mathrm{p}})}{r_{\mathrm{p}}^q} - \left(\dfrac{\mathrm{sgn}(\xi_2)\hat{\alpha}_{\mathrm{s}}^2 \left(2 - \frac{v_{\mathrm{r}}^2}{c_{\mathrm{s}}^2} \right) \sin(\pi q)}{2\hat{\alpha}_{\mathrm{s}} \left(|\xi_1 + \hat{\alpha}_{\mathrm{s}}\xi_2| \right)^q} \right) H(-\xi_1 - \hat{\alpha}_{\mathrm{s}}|\xi_2|) \right] \hat{\xi}_1, \\ Av_{\mathrm{r}} \left[-\dfrac{\alpha_{\mathrm{p}} \cos(q\theta_{\mathrm{p}})}{r_{\mathrm{p}}^q} + \left(\dfrac{\left(2 - \frac{v_{\mathrm{r}}^2}{c_{\mathrm{s}}^2} \right) \sin(\pi q)}{2\hat{\alpha}_{\mathrm{s}} \left(|\xi_1 + \hat{\alpha}_{\mathrm{s}}\xi_2| \right)^q} \right) H(-\xi_1 - \hat{\alpha}_{\mathrm{s}}|\xi_2|) \right] \hat{\xi}_2, \end{cases} \tag{1.13}$$

where $\gamma_{\mathrm{p,s}} = \sqrt{1 - (v_{\mathrm{r}}\sin(\theta)/c_{\mathrm{p,s}})^2}$, $r_{\mathrm{p}} = \sqrt{\xi_1^2 + (\alpha_{\mathrm{p}}\xi_2)^2}$, and $\theta_{\mathrm{p,s}} = \tan^{-1}\left[\alpha_{\mathrm{p,s}}\tan(\theta)\right]$ are speed-scaled parameters, and $D(v_{\mathrm{r}}) = 4\alpha_{\mathrm{p}}\alpha_{\mathrm{s}} - (1 + \alpha_{\mathrm{s}}^2)^2$ is the Rayleigh function ($D \to 0$ as $v_{\mathrm{r}} \to c_{\mathrm{R}}$) [40]. Figures 1.6 and 1.7 show the local mode-II crack tip velocity field for SR and SS ruptures, respectively. The contour levels represent velocity magnitudes $|\dot{\mathbf{u}}(\xi_1, \xi_2)|$ and normalized arrows indicate direction of particle motion. As v_{r} is increased throughout the entire permissible domain, $(0, c_{\mathrm{R}}) \cup (c_{\mathrm{s}}, c_{\mathrm{p}})$, relativistic effects are amplified in the velocity field distribution. Emitted P and S waves are compressed and expanded upstream and downstream of the moving crack tip, respectively, much like the moving point source of Figure 1.3. The most drastic change in field character occurs
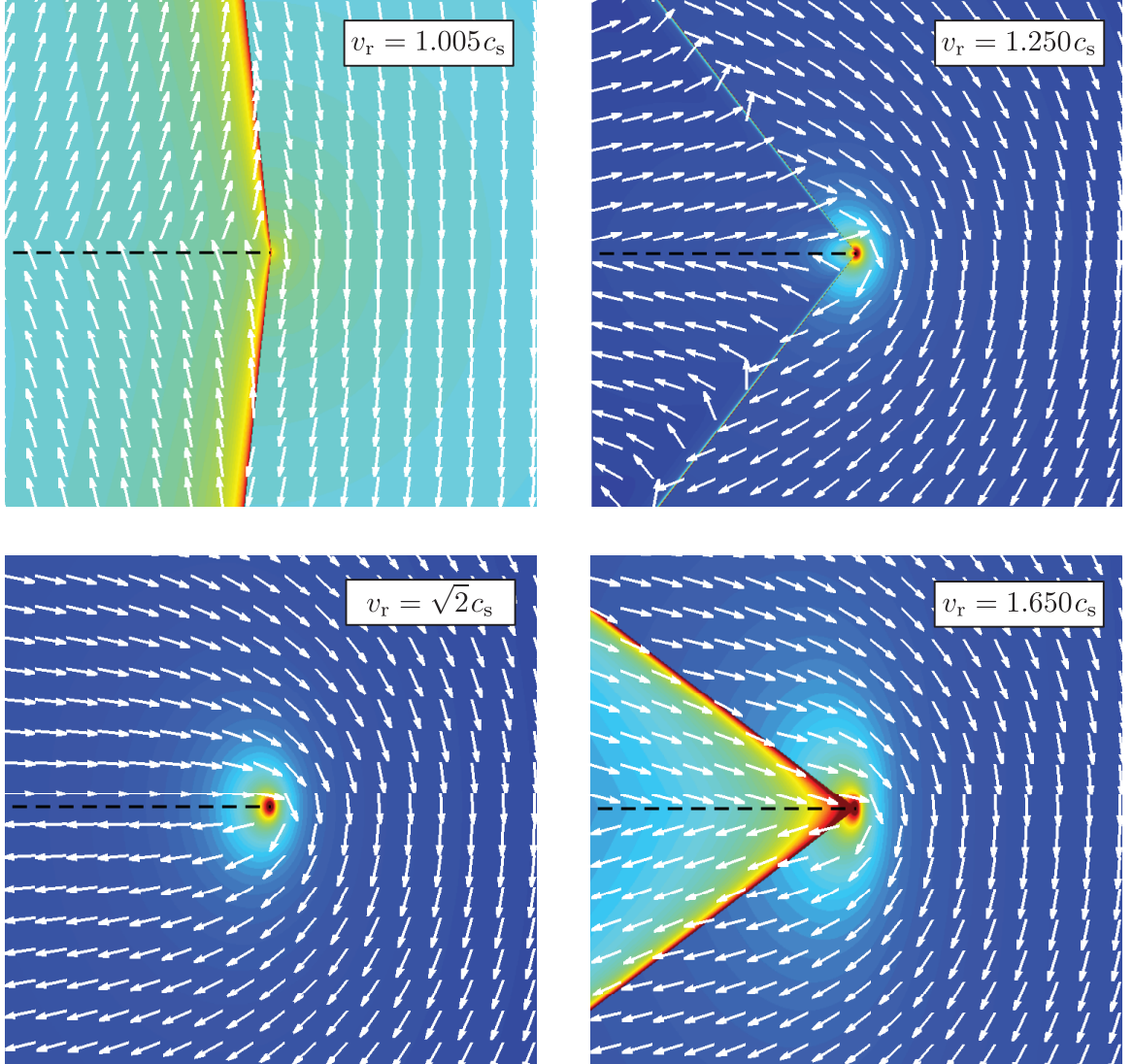
Figure 1.7: Asymptotic velocity field for a mode-II rupture in the super-shear regime ($c_\mathrm{s} < v_\mathrm{r} < c_\mathrm{p}$) at speeds $v_\mathrm{r} = c_\mathrm{s}^+$, $v_\mathrm{r} = 1.250c_\mathrm{s}$, $v_\mathrm{r} = \sqrt{2}c_\mathrm{s}$, and $v_\mathrm{r} = 1.650c_\mathrm{s}$. Unit vectors and contour levels indicate the direction and magnitude of $\mathbf{u}(\xi_1, \xi_2)$, respectively. Mach angle β decreases with an increase in rupture speed, v_r. Note the disappearance of the Mach front characteristics for $v_\mathrm{r} = \sqrt{2}c_\mathrm{s}$. [37]

with the emergence of Mach fronts in the transition from SR to SS speeds. The angle the Mach front makes with the weak plane, β, is geometrically related to the rupture speed through the Mach-angle formula, $\beta = \sin^{-1}(c_\mathrm{s}/v_\mathrm{r})$ [41]. Figure 1.7 shows the effects of v_r on β as well as highlights the particular speed $v_\mathrm{r} = \sqrt{2}c_\mathrm{s}$, where $\beta = 45°$ and the Mach cone vanishes: at this angle, the SR-like singular field is recovered ($q = 1/2$) and the Mach front characteristics become nodal in shear, as expected [37]. Slip rate is defined as $\dot{u}_\mathrm{slip}(\xi_1, \xi_2) = \dot{u}_1(\xi_1, +\eta) - \dot{u}_1(\xi_1, -\eta)$, where the limit $\eta \to 0$ indicates paired particles just above and below the weak plane: for brevity, $\dot{u}_\mathrm{slip} = \dot{u}_1^+ - \dot{u}_1^-$. Because $\xi_1 < 0, \xi_2 = 0$ is a branch cut in the complex plane, no solutions are allowed along the

zero-thickness crack surface. For the same reason, discontinuous values are permitted across the $-\hat{\xi}_1$-axis. The $\hat{\xi}_1$ component of Equations 1.12 and 1.13 are discontinuous and anti-symmetric across the crack surface, $\dot{u}_1^+ = -\dot{u}_1^-$, enforced by the sign function, $\mathrm{sgn}(\cdot)$. Slip rate may thus also be written as $\dot{u}_{\mathrm{slip}} = 2\dot{u}_1^+ = -2\dot{u}_1^-$. The $\hat{\xi}_2$ velocity component, however, is continuous across the crack surface, $\dot{u}_2^+ = \dot{u}_2^-$: crack opening rate, $\dot{u}_2 = \dot{u}_2^+ - \dot{u}_2^-$, is identically zero for all time. For a SR rupture, maximum velocity swings of the $\hat{\xi}_2$ component are greater than those of $\hat{\xi}_1$, $|\dot{u}_2^{\max} - \dot{u}_2^{\min}| > |\dot{u}_1^{\max} - \dot{u}_1^{\min}|$. For a SS rupture, $|\dot{u}_2^{\max} - \dot{u}_2^{\min}| > |\dot{u}_1^{\max} - \dot{u}_1^{\min}|$ when $v_{\mathrm{r}} = (c_{\mathrm{s}}, \sqrt{2}c_{\mathrm{s}})$ and $|\dot{u}_2^{\max} - \dot{u}_2^{\min}| > |\dot{u}_1^{\max} - \dot{u}_1^{\min}|$ when $v_{\mathrm{r}} = (\sqrt{2}c_{\mathrm{s}}, c_{\mathrm{p}})$, the reversal occurring at the S wave nodal speed of $v_{\mathrm{r}} = \sqrt{2}c_{\mathrm{s}}$. Knowledge of the rupture tip speed provides insight into the expected ground motions and stress distributions, and vice versa.

Low-speed impact experiments successfully capture the first evidence of a mode-II SS rupture (Figure 1.8). Two half-plates are cohesively bound and a notch is introduced at one edge of the interface. A projectile impacts the bottom half-plate, driving a shear rupture along the weak plane. Dynamic photo-elastic interferometry is used to capture in-plane contours of maximum shear stress magnitude, $|\tau_{\max}|$ (Appendix B) [44, 45], generating a sequence of images with information about shear stress evolution. Figure 1.8 shows an experimental photograph of a shear Mach cone emanating from the crack tip (left panel) and the history of crack tip speed, $v_{\mathrm{r}}(t)$ (right panel), indicating that the shear de-bonding process is born and remains SS for the entire experimental window (excluding a few points within the duration of the impact loading cycle) [13]. The rupture speed, though initially varying, exhibits the asymptotic behavior $v_{\mathrm{r}} \to +\sqrt{2}c_{\mathrm{s}}$. Future experiments alter the initiation condition from impact loading to the discharge of a capacitor bank across a wire embedded along a pre-fabricated, angled interface in a rectangular plate (Figure 1.9) [43]. A hydraulic press loads the rectangular plate, introducing uniform resolved compressive and driving shear forces along the frictionally resistive weak plane. Upon capacitor discharge, the wire transforms to plasma and induces local opening and slip of the interface from the pressure increase of the phase transformation [46]; once dynamic criteria are met, shear-dominant cracks are driven bi-directionally away from the nucleation site along the interface. Figure 1.9 shows a sequence of photographs representing a single experiment where a crack tip accelerates from rest in the SR regime then transitions to SS speeds, confirming the existence of a physical transition mechanism [47]. A stress concentration remnant from the original SR rupture trails behind the S wave (trailing-Rayleigh signature at t_3). Moreover, once in the SS domain, the rupture speed tends to $v_{\mathrm{r}} \to +\sqrt{2}c_{\mathrm{s}}$, further elucidating the importance of the value $v_{\mathrm{r}} = \sqrt{2}c_{\mathrm{s}}$ [48]. Diagnostics capable of measuring particle velocity components extend the capability to study mode-II ruptures within the same experimental setup [49]. Measurements of slip rates are conducted for various rupture tip speeds by controlling the initial conditions along the frictional interface and the projectile impact speed; two basic categories of ruptures are discovered through slip rate measurements, namely, the pulse-like and crack-like modes [50, 51]. In a pulse-
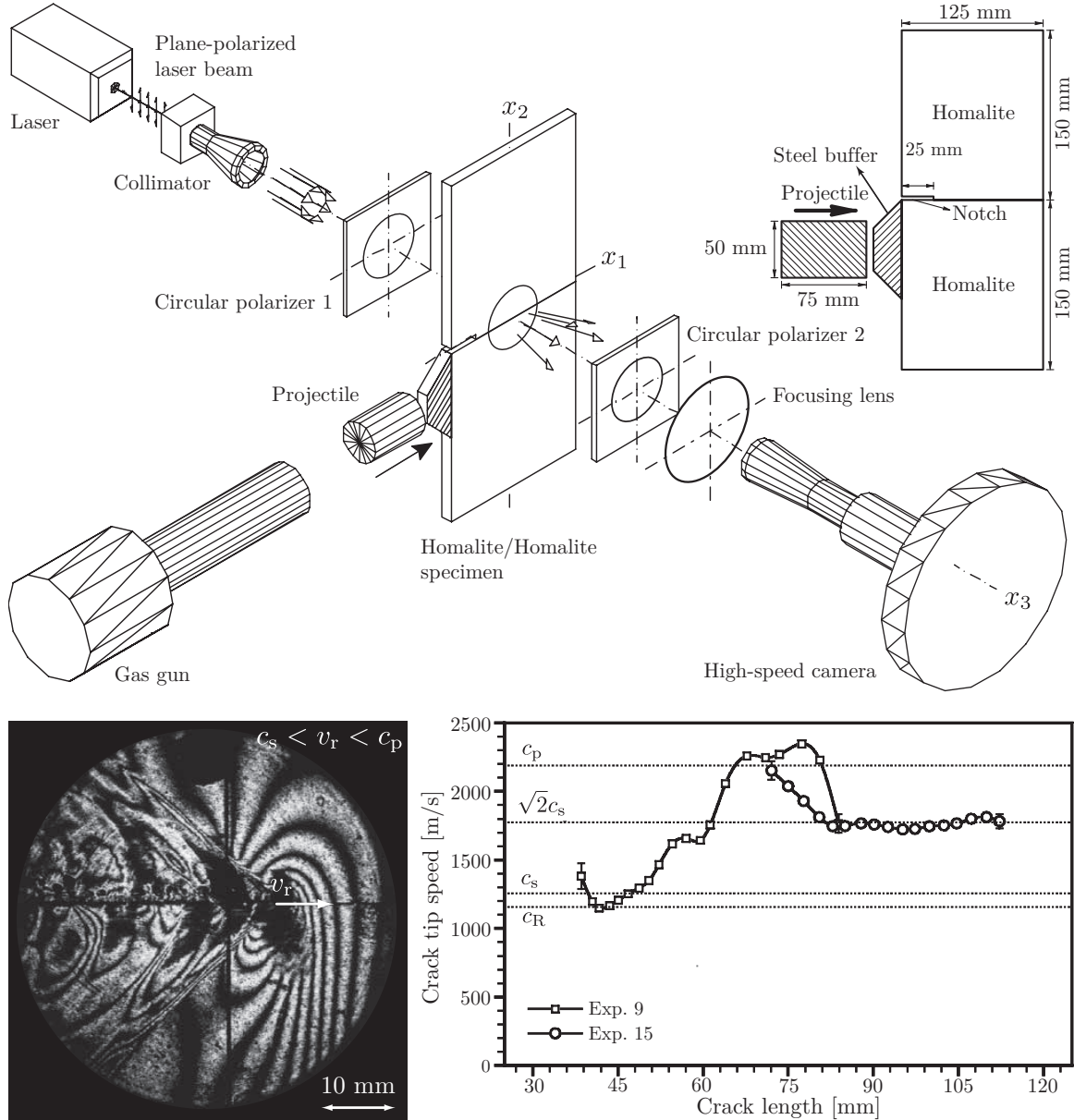
Figure 1.8: First experimental evidence of a shear-dominant rupture propagating along a weak plane at super-shear (SS) speeds, $c_s < v_r < c_p$. The experimental schematic shows the impact mechanism and dynamic photo-elasticity setup. Photograph of a SS rupture captures a shear Mach front of finite thickness. Crack speed history shows the rupture is born and remains SS, settling to $v_r = \sqrt{2}c_s$. [42]

like rupture, the slipping zone eventually re-locks behind the crack tip, creating a finite slip patch; in a crack-like rupture, the region behind the crack tip continues to slip indefinitely within the experimental observation window. A parameter T is introduced to judge the crack-like ($T \approx 0$) or pulse-like ($T \approx 1$) rupture mode, with excellent correlation to experiments [52, 53]. The transition length, l_{tr}, defined as the distance from rupture nucleation to SS transition, is another controllable rupture parameter; parametric study of interface angle, α, and static pre-load, P, generates criteria
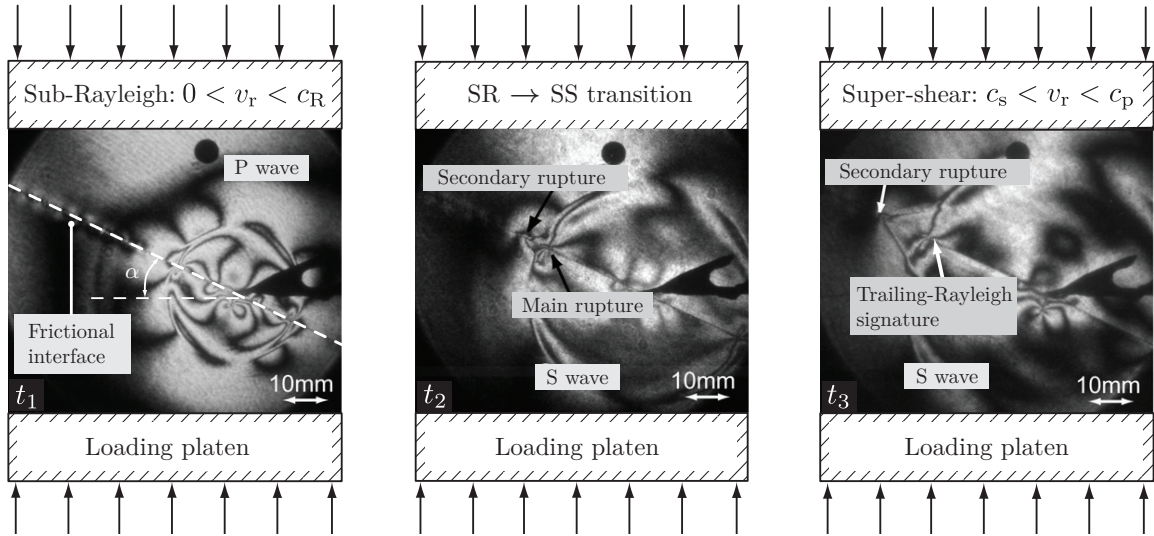
Figure 1.9: Experimental evidence of transition from SR to SS regimes for a rupture along a frictional weak plane. A bi-directional rupture is nucleated by discharging a capacitor across an embedded wire; the remnant stresses of the original rupture trails behind the S wave (trailing-Rayleigh). [43]

to determine whether transition would occur, and if so, at what distance [54]. Measurements away from the interface along $\hat{\xi}_2$ investigate spatial attenuation of the dilatational and shear radiation fields emitted by the propagating rupture tip, concluding that slip information carried by the Mach fronts decays slower with distance from the interface than the local field effects near the crack tip, an expected outcome from the characteristic nature of the Mach fronts [55]. While experiments yield a wealth of information about sliding systems, several unsettling contradictions between measurements and theory remain; Mach fronts are of finite widths, rather than infinitesimally thin characteristics; theory predicts a single possible SS speed, $v_r = \sqrt{2}c_s$, yet experiments show the entire inter-sonic regime is permissible; the existence of pulse and crack-like modes implies healing of the interface in the rupture tip wake, a phenomenon absent in the current solution. Further investigations show that non-zero $G_{II}(v_r)$ are possible in the inter-sonic regime for all speeds $v_r = (c_s, c_p)$ under the condition that the stress state evolves continuously across the crack tip, rather than abruptly across the structureless crack tip of this model [56]. A continuous evolution requires finite distances, thus proposing the existence of process zones associated with the rupture tips.

The inclusion of a process zone in the crack tip model energetically reconciles mode-II rupture propagation in the entire SS regime. Experiments are conducted where a block is subject to stepwise changes in sliding rate, $\dot{\delta}$, under constant normal stressing conditions; the measured shear response shows characteristic dependencies on normal stress, sliding rate, and contact time for a diverse range of materials, leading to the development of empirical friction laws which encapsulate the observed behavior [58, 59, 60, 61]. During step changes in sliding rate, abrupt jumps in shear resistance are followed by stabilization towards a steady-state value, τ_{ss} [62]; a state variable, θ, which may be
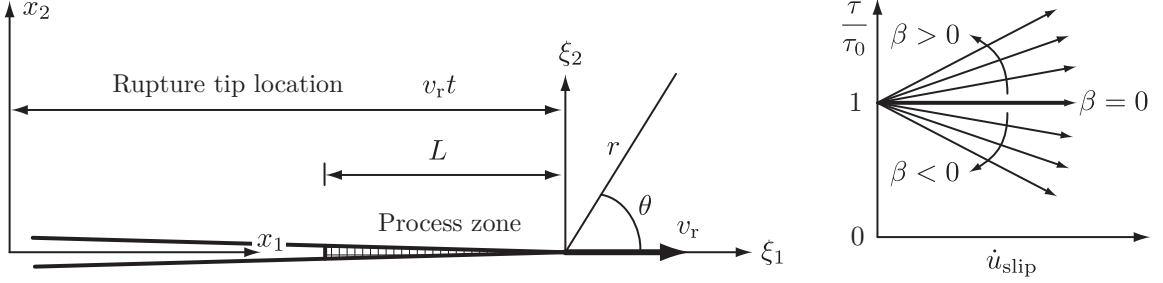
Figure 1.10: Process zone schematic; the crack tip ($\xi_1 = -L, \xi_2 = 0$) moves at a speed v_r, carrying with it a process zone of length L. Stress evolution occurs within the process zone based on material-specific values β (rate-weakening, $\beta < 0$; rate-strengthening, $\beta > 0$). Standard Coulomb resistance, $\tau(\xi_1/L) = \sigma_0 f_0$, is recovered in the process zone when $\beta = 0$, eliminating rate-dependence. [57]

interpreted as the age of contacting regions along the frictional interface, is introduced to account for time-dependent strengthening during stationary contact. The commonly implemented form for the rate-and-state law with a single state variable is given by [63]:

$$\tau(\dot{\delta}, \theta) = \sigma_0 \left(f_0 + a \ln \frac{\dot{\delta}(t)}{\dot{\delta}^*} + b \ln \frac{\theta(t)\dot{\delta}^*}{D_\mathrm{c}} \right), \tag{1.14}$$

$$\frac{\mathrm{d}\theta(t)}{\mathrm{d}t} = 1 - \frac{\dot{\delta}(t)}{D_\mathrm{c}}, \tag{1.15}$$

where σ_0 is the effective normal stress ($\tau_0 = f_0 \sigma_0$, from the Coulomb model), $\dot{\delta}^*$ is a reference sliding rate, constants a and b are material specific parameters, and D_c is the characteristic slip distance. The rate-and-state formulation allows sliding surfaces to heal over time due to the evolution of state variable within D_c, allowing strengthening during stationary contact ($\dot{\delta} = 0$) and healing behind the crack tip, i.e., pulse-like ruptures [64]. Measurements of slip rate, $\dot{u}_\mathrm{slip}$, during mode-II rupture along an incoherent plane show an abrupt increase and subsequent decay in slip rates near the vicinity of the advancing crack tip, suggesting the use of a rate-and-state frictional law to model the shear response within a finite process zone near the crack tip. Figure 1.10 schematically represents a process zone (hashed region) just ahead of the crack tip located at $\xi_1 = -L$, $\xi_2 = 0$; ignoring effects of the state variable for steady crack propagation and implementing a simple rate-dependent frictional law yields the shear tractions within the process zone as [57]:

$$\tau(\xi_1/L) = \tau_0 \left[1 + \beta \frac{\mu}{2\tau_0} \frac{|\dot{u}_\mathrm{slip}(\xi_1/L)|}{c_\mathrm{s}} \right], \qquad -1 < \xi_1/L < 0, \tag{1.16}$$

with β as the constitutive parameter (Figure 1.10, right panel). The governing equations are re-solved and the non-dimensional energy flux G/G_0 is plotted for $v_\mathrm{r} = (0, c_\mathrm{p})$ in Figure 1.11, where G_0 is the energy release rate for a quasi-static crack with the identical far-field loads [65]. While the sub-domain $(c_\mathrm{R}, c_\mathrm{s})$ is still forbidden, the function is continuous in the SR and SS regimes: the
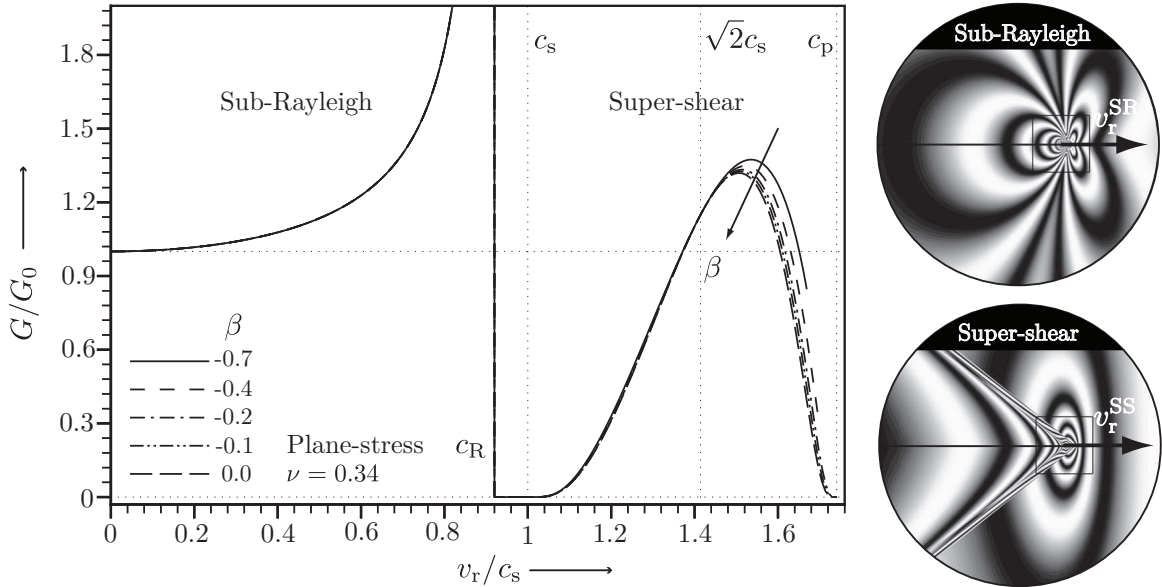
Figure 1.11: Non-dimensional crack tip energy release rate, $G(v_r)/G_0$ for various values of constitutive parameter, β. Energy flux is continuous in the SR, $(0, c_R)$, and SS regime, (c_s, c_p). Synthetic Mach fronts have finite thickness after inclusion of a process zone. [65]

process zone thus permits mode-II rupture propagation at all inter-sonic speeds, unlike the singular value $v_r = \sqrt{2}c_s$ predicted by the structureless crack tip model. As the parameter β is decreased, the inter-sonic energy maximum shifts away from $\sqrt{2}c_s$ towards increasingly higher rupture speeds (arrow): when $\beta = 0$, the process zone vanishes and the singular crack tip solution is recovered. A stability analysis of crack tip speeds shows that the entire SR regime $(0, v_r)$ is unstable, while the SS regime is unstable for $(c_s, \sqrt{2}c_s)$ and stable for $(\sqrt{2}c_s, c_p)$ [42]. A mode-II rupture along a weak plane will consequently accelerate towards c_R, transition to SS speeds (if conditions permit), then stabilize just above $v_r = \sqrt{2}c_s$, corroborated remarkably well by the experimentally measured crack speeds of Figure 1.8. Principle stresses σ_1 and σ_2 are used to determine the maximum in-plane shear stress, $\tau_{max}(\xi_1, \xi_2) = (\sigma_1 - \sigma_2)/2$. Synthetic contour plots of $|\tau_{max}|$ for SR and SS rupture speeds are plotted near the crack tip in Figure 1.11 [65]. Synthetic isochromats show that the Mach front has structure whose width is bound by the extent of the process zone, much like the experimentally captured isochromats. Inspection of the stress field around the crack tip reveals a local maxima of driving shear stresses ahead of the crack tip [66, 67]: under appropriate conditions where the shear resistance of the interface is insufficient, these local maxima may induce secondary ruptures ahead of the original crack. These secondary slip regions may be born at SS speeds, by-passing the forbidden energy barrier, (c_R, c_s), and permitting a SR to SS transition.

Dynamics of the sliding block and wedge are analogous to those of ruptures in the earth, i.e., natural earthquakes [68]. Revisiting the sliding problem of Figure 1.1, a slow increase in wedge angle, α, increases the resolved shear stress along the contact interface. The act of sliding nucleates
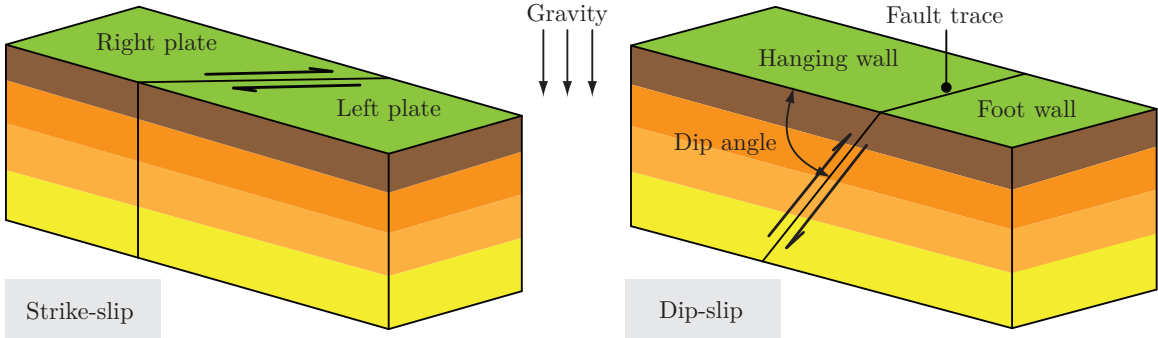
Figure 1.12: Fault configurations in the earth; a strike-slip configuration describes relative lateral motion of left and right tectonic plates (left panel); a dip-slip configuration describes relative vertical motion of the hanging and foot wall tectonic plates (right panel).

at local points along the contact interface where the driving shear force surpasses the available frictional resistance according to critical criteria (Figure 1.1, boundaries of red patches). These nucleation sites grow as the ruptures propagate dynamically, leaving in their wakes slipped regions of processed interface. The rupture front continuously emits dilatational and shear waves into the bulk and generates Rayleigh surface waves at the crack intersection with the block edges. Acoustic waves are driven in the air by surface Rayleigh waves and the bulk wave interactions with the fluid-solid interfaces. The rupture fronts reach the edges of the contact surface and reflect back into the material, continuously accumulating slip and moving the center of mass of the block down the incline. The total accumulated slip from the transient behavior should place the block in its final static position. Once at rest, a further increase in wedge angle is required to generate a subsequent slip event by nucleating fresh failure sites according to updated critical criteria. Replacing the surface of the incline with a similar block models two tectonic plates mating along a frictional interface, i.e., the fault. Two common fault configurations in the earth are schematically presented in Figure 1.12; a strike-slip configuration describes left or right-lateral motion of the plates with respect to each other (left panel); a dip-slip configuration describes relative vertical motion of the hanging wall and foot wall plates (right panel). By minimizing the block thickness, experimental investigations on sliding plate systems provide direct insight into the fields of seismology, geology, and tectonophysics.

Seismic activity is the earth's transient response in order to redistribute accumulated stresses along the fault through the emission of dynamic waves into the surrounding medium. Relative displacements of the tectonic plates quasi-statically increase the stored elastic energy in the bulk and consequently load the locked fault plane with increasing compressive and shear stresses [70]: this is equivalent to slowly increasing the wedge angle, α. The available frictional resistance along the fault continuously sustains the tectonic loading during relatively long aseismic periods. A dynamic rupture nucleates locally along the fault plane once the accumulated driving forces surpass the available resistance: in seismology, these failure sites are called hypocenters and are akin to the
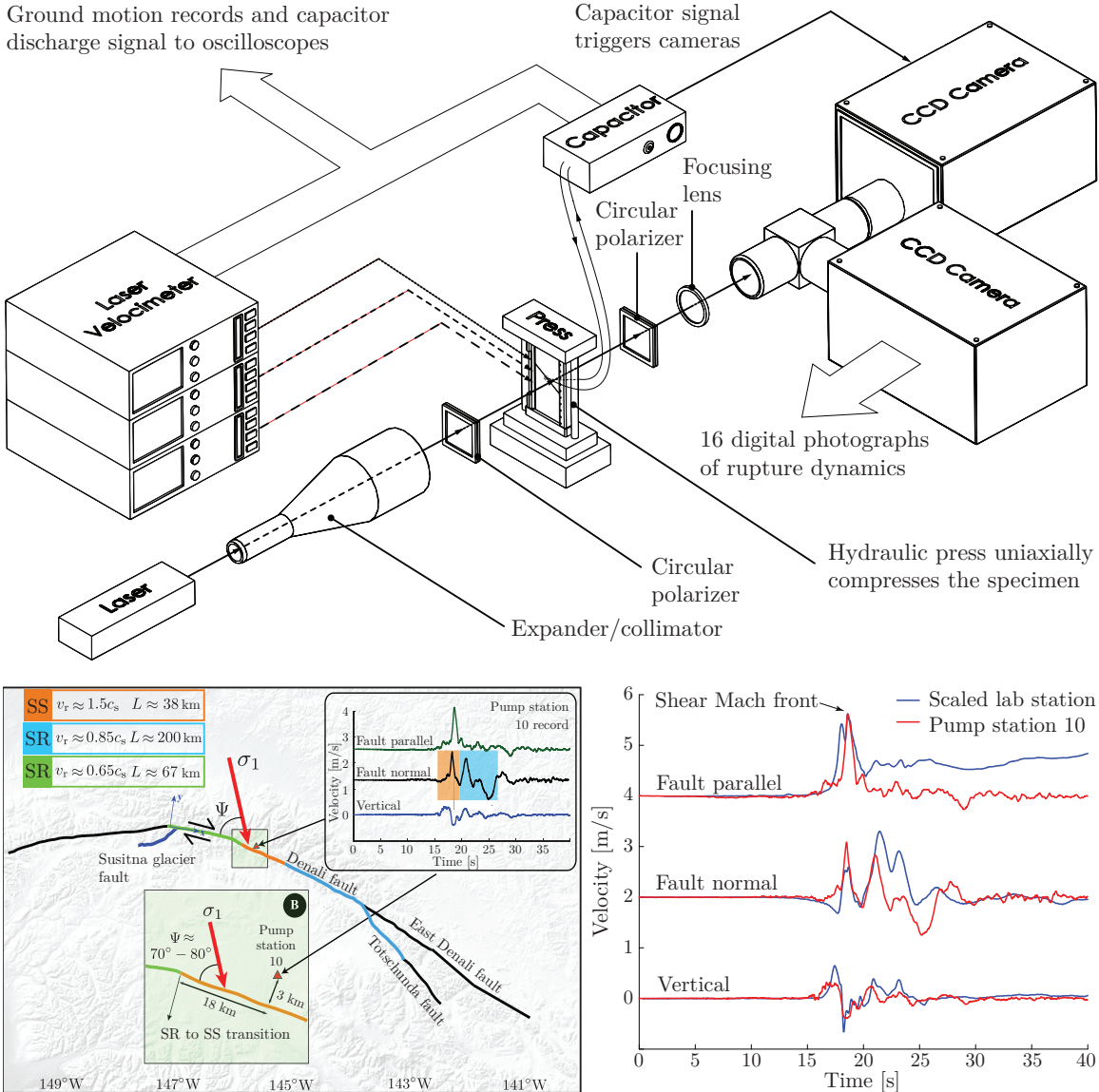
Figure 1.13: Analogue experiment simulating the 2002 $M_w = 7.9$ Denali, Alaska earthquake. A block diagram of the experimental setup shows the laser velocimeter and dynamic photo-elasticity setups interacting with the specimen loaded in the hydraulic press. The Denali fault system is schematically represented along with velocity records derived from seismogram measurements (left panel). Scaling of laboratory results yields remarkable similarity with field data (right panel). [69]

origins of rupture in the sliding block problem. An earthquake is the necessary intermediate transient towards a new system equilibrium. Ruptures propagate along the weak plane, unzipping the locked material ahead and emitting stress waves in transit, equivalent to the sliding phase of the block. Once a new static equilibrium is established, the subsequent seismic event would occur when the driving force overcomes the new values of frictional resistance along the fault. Accelerometers placed along the earth surface record time histories of ground motions driven by the various rupture features. Inversion techniques use these records to determine the event hypocenter, slip history,

etc., through wave arrival times. More recently, global positioning systems (G.P.S.) and satellite images aid in constraining inversion results [71]. Experiments attempt to reproduce seismometer records of the 2002 $M_w = 7.9$ Denali, Alaska earthquake (Figure 1.13) through similar sliding plates designed for the study of strike-slip configurations [69]; mismatch in specimen and earth properties are used to specify the measurement point in the plate along with scaling between pulse-widths and amplitudes. Inversions of the 2002 Denali event show evidence of mode-II dominant SS ruptures along certain portions of the fault [72]. A SS rupture is generated in the laboratory and off-fault measurements mimicking the placement of Pump Station 10 (seismometer) are recorded with the additional diagnostic of laser velocimetry (Section 2.2.3): experimentally measured fault parallel, normal, and vertical components of ground motion exhibit astonishing resemblance to the earthquake records (Figure 1.13, right panel). This result verifies previously suspect SS earthquakes which were originally thought to be dual-events, but in fact are distinct arrivals of the SS rupture tip followed by the trailing-Rayleigh (TR) signature within a single event (Figure 1.9). SS rupture has been inferred in a growing number of earthquakes, including the 1979 Imperial Valley event [73], the 2001 Kunlunshan event [74], and the 2002 Denali Fault event [72], causing particularly greater damage due to the dominance of fault parallel and fault normal ground motion directions associated with the arrivals of the SS rupture tip followed by the TR signature [75, 76]; this rotation of dominant ground motion directivity sequentially shakes structures in alternating directions within a single seismic event, inducing un-reinforced torsional loading and promoting failure in tall structures [77]. Such rupture propagation has been observed and modeled almost entirely in the context of long strike-slip earthquakes [78]; there is little literature on its effect on dip-slip faults, largely because with the exception of mega-thrust events, there may not be sufficient fault length up-dip for transition to occur, prohibiting SS rupture propagation along strike on a thrust fault. However, there is no reason to rule such propagation speeds out in the case of natural thrust faults. For example, data from the 1906 $M_w = 7.8$ San Francisco earthquake, one of the most catastrophic along the San Andreas Fault in record history (Figure 1.14, panels A and C), shows evidence of SS speeds [79]. The major limitation in predicting earthquakes lies in the lack of mechanical, material, and geometric field data of the complex, multi-layered structure of the earth at a resolution sufficient to satisfy the continuum assumption. With appropriate scaling, the study of ground motions in laboratory earthquake experiments can bound and guide the development of building safety codes according to new discoveries in rupture phenomena. While long-term, quasi-static loading is impossible to perceive with human senses alone (aseismic plate motion is on the order of $1\,\mathrm{m/yr}$), the short-term dynamic response (on the order of $10\,\mathrm{m/s}$ for several minutes) is responsible for the devastation typically associated with natural earthquakes and in itself merits investigation.

The severe effects of recent thrust earthquakes, e.g., the 1999 Chi-Chi earthquake, the 2004 Indian Ocean earthquake, the 2008 Wenchuan earthquake, and the 2011 Tohoku-Oki earthquake,

Figure 1.14: Unfortunate repercussions of earthquakes, requiring rethinking of building safety codes. A: the 1906 $M_w = 7.8$ San Francisco earthquake, a suspect super-shear event caused city-wide fires. [80] B: 2011 $M_w = 9.0$ Tohoku-Oki earthquake, an undersea thrust fault event generated a devastating tsunami. [81] C: aerial view of the San Andreas Fault, circa 2008. [82] D: the 1999 $M_w = 7.4$ Izmit, Turkey earthquake. [83] E: 1988 $M_w = 6.8$ Leninakan, Armenia earthquake. [84]

emphasize the special risks that earthquakes on thrust or reverse faults pose: mega-thrust faults line the Pacific Rim, and intra-plate thrust faults lie near many major metropolitan centers around the globe. Furthermore, the tsunamis generated from thrust faults threaten millions of people in
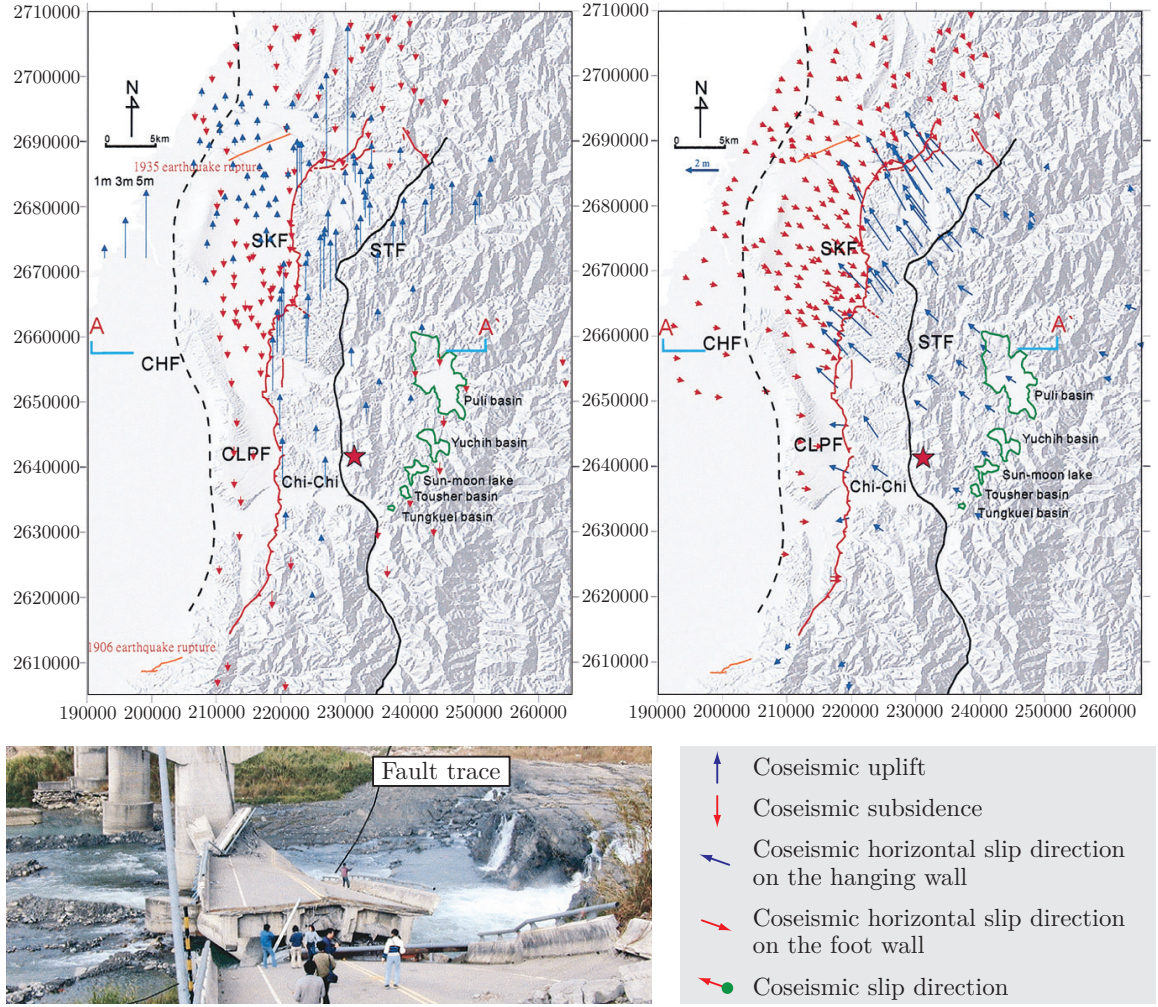
Figure 1.15: Inversion results of the 1999 Chi-Chi $M_w = 6.3$ earthquake shows the enhanced ground motions along the hanging wall plate in comparison to those of the foot wall (top panels). Field observations show total accumulated vertical offset of $\approx 10\,\mathrm{m}$ at the fault trace (photograph). [85]

fast-growing coastal cities (Figure 1.14, panel B). Therefore it is crucial to understand the physical behavior of thrust faults, the ground motion they produce, and how these features differ from simpler, more commonly-studied vertical strike-slip faults. There is considerable evidence that dip-slip faults (thrust faults in particular) display many behaviors that arise from their asymmetric geometry with respect to the earth surface. Observational studies have indicated that ground motion on the hanging wall is typically larger than the ground motion on the foot wall [86, 87, 88, 89]. Inversion results of the 1999 Chi-Chi earthquake are shown in Figure 1.15 [85]; vertical and horizontal arrows indicate the uplift and lateral displacements between the hanging (blue arrows) and foot wall plates (red arrows), respectively, making the enhanced ground motions on the hanging wall self-evident. Geological observations, particularly near the intersection of the fault with the earth surface (fault trace), corroborate conclusions of the inversion results, at times measuring displacements on the
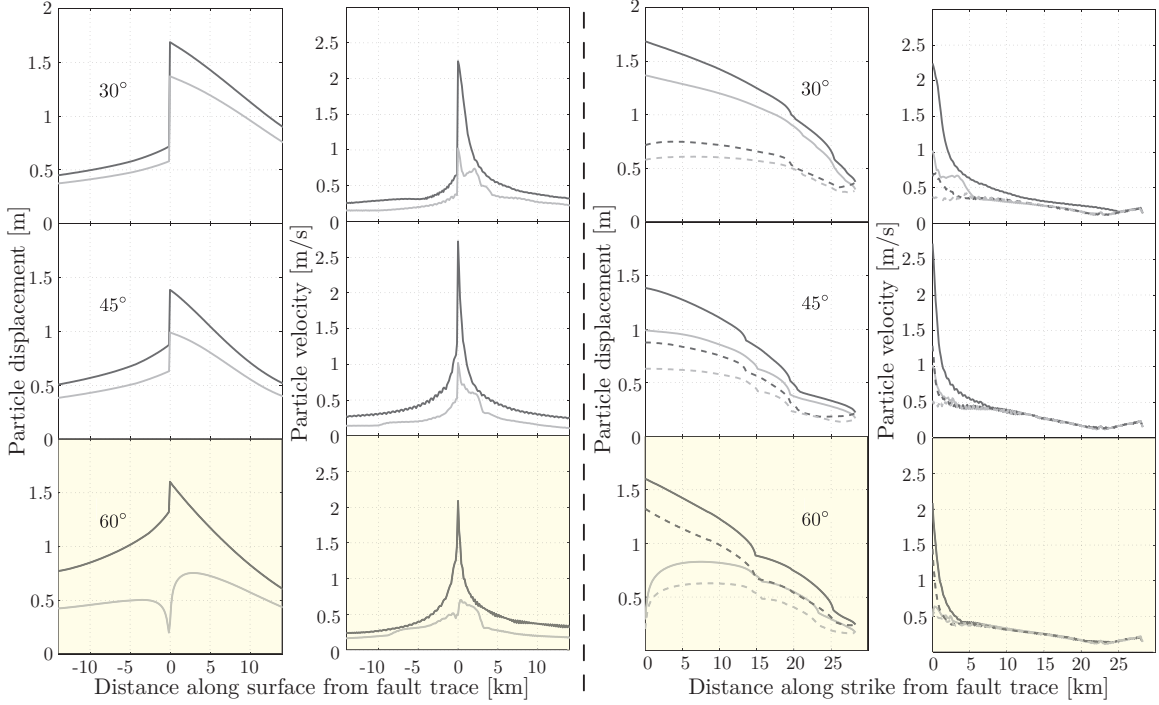
Figure 1.16: Numerical results of sub-Rayleigh peak particle displacements and velocities in thrust (black) and normal (grey) earthquake simulations for various dip angles. Peak displacements and velocities along the simulated earth surface (left panel) and along the fault at-depth (right panel) are plotted as functions of distance from the fault trace. Enhanced ground motions are noted in the hanging wall in all cases. Shaded panels represent the thesis specimen geometry within 1°. [93]

order of ≈ 10 m at the fault trace (Figure 1.15, photograph insert). Analog and numerical models of thrust faults also display this asymmetry in ground motions [90, 91, 92, 93, 94]; it can be partly ascribed to the closer proximity of hanging wall seismic stations to the fault and partly to waves trapped in the hanging wall during slip. The latter is shown by asymmetric displacements at the fault trace [90, 91, 92]. Furthermore, waves radiated by the up-dip rupture reflect from the free surface onto the fault, leading to time-dependent stresses which affect the dynamics [91, 95].

While numerical models may shed a great deal of light on the active physical processes during thrust earthquakes, such models must be compared to real-world observations and measurements. The advent of modern computing and the ever-increasing processor capabilities allow full three-dimensional simulations of the governing equations for any given complex fault system with boundary conditions best matching geological observations and measurements. For example, a very simple model of the 1999 Chi-Chi event could explain the significantly higher ground motion amplitudes on the hanging wall [97, 98]; ground motion asymmetry was an inevitable outgrowth of the dipping fault geometry. Likewise, dynamic models of the 2008 Wenchaun earthquake correctly reproduce the asymmetric ground motion of this event [99]. Computational capabilities of modern processors are suitable for performing parametric studies of physical variables and their effect on the system
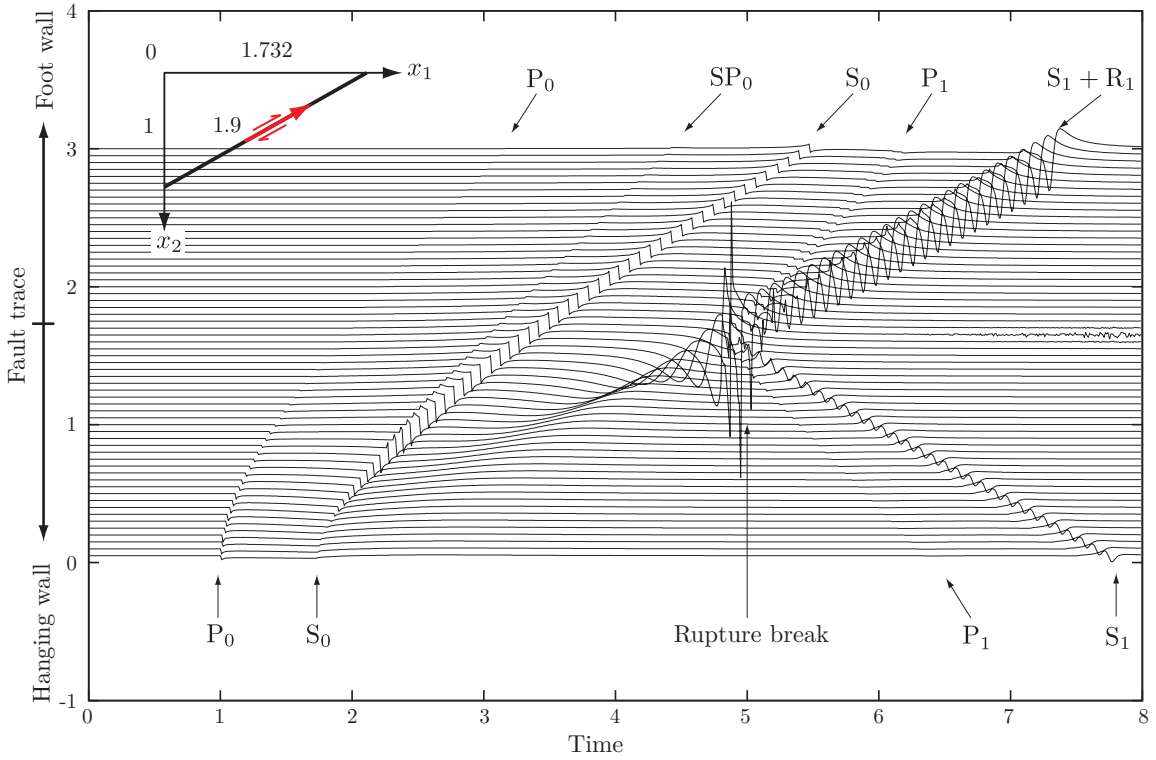
Figure 1.17: Synthetic earth surface-normal ground motion records for a thrust fault of the geometry shown in the schematic insert. Up-dip and down-dip information are marked with subscripts 0 and 1, respectively. Peak values are associated with the rupture. [96]

response. Kinematic simulations of SR ruptures along dip-slip faults study the dip-angle dependency on peak displacements and velocities along the earth surface (Figure 1.16, left panel) and the fault at-depth (Figure 1.16, right panel) as functions of distance from the fault trace [93]. In both thrust (black curves) and normal (grey curves) loading configurations, symmetry about the ordinate for earth-surface results shows larger peak magnitudes of both displacements and velocities along the hanging wall. Amplification of asymmetry is observed along the fault in both thrust and normal configurations between paired stations on the hanging (solid) and foot wall (dashed) plates as the free surface is approached. The rows in Figure 1.16 show that asymmetries in hanging and foot wall ground motions decrease with an increase of dip angle; this is expected, as a dip angle of $90°$ implies a vertical fault, recovering expected symmetries which are immediately broken by any other angle. Synthetic earth surface-normal velocity traces are produced from kinematic simulations of a SR rupture along a fault of dip-angle $30°$ (Figure 1.17) [96]. Signatures in the records correspond to arrivals of up-dip P waves (P_0), S waves (S_0), converted SP waves (SP_0), followed by the arrival of the rupture tip to the fault trace, $(t, x_1) = (5, 1.732)$, generation of a surface Rayleigh wave (R_1), and the effects of reflected P (P_1) and S waves (S_1). Peak magnitudes of ground motions are associated with the arrival of the rupture tip to the free surface. A rupture wave is also observed just prior to

$t = 5$ along the hanging wall $(-\infty, 1.732)$, but is absent along the foot wall plate $(1.732, +\infty)$. To run the simulation, frictional parameters must be defined along the entire fault surface, mandating the condition that the crack surfaces must be in contact at all times during slip. This assumption may restrict numerical modeling by omitting a key aspect of rupture interactions with a free surface, namely, the possibility of fault opening at the fault trace.

Even with a growing body of seismological data and numerical models of dip-slip faults, it is crucial to have more laboratory data on the dynamics of ruptures in such configurations. Laboratory models can help to indicate how important certain features of the numerical models (such as the asymmetry between hanging and foot wall) are in the real world. Many of the effects of dip-slip faults noted above, e.g., the asymmetry between hanging wall and foot wall motion and amplified motion from thrust faults, were predicted by analog foam rubber models [90]. Experiments can help to validate numerical results, providing more confidence in predictions made from the deterministic models. Perhaps most importantly, though, laboratory experiments can reveal fresh observations that can then be investigated in numerical models and seismological data, such as conclusive evidence of SS ruptures. With this framework in mind, we enter the laboratory.

Chapter 2

Simulating an Earthquake

Earthquakes are simulated in a laboratory setting by nucleating a rupture along a prescribed weak plane in Homalite$^{\text{TM}}$ H-100, a high density, brittle, transparent polymer. High-speed camera and laser velocimeter diagnostics capture rupture propagation towards the simulated earth surface and
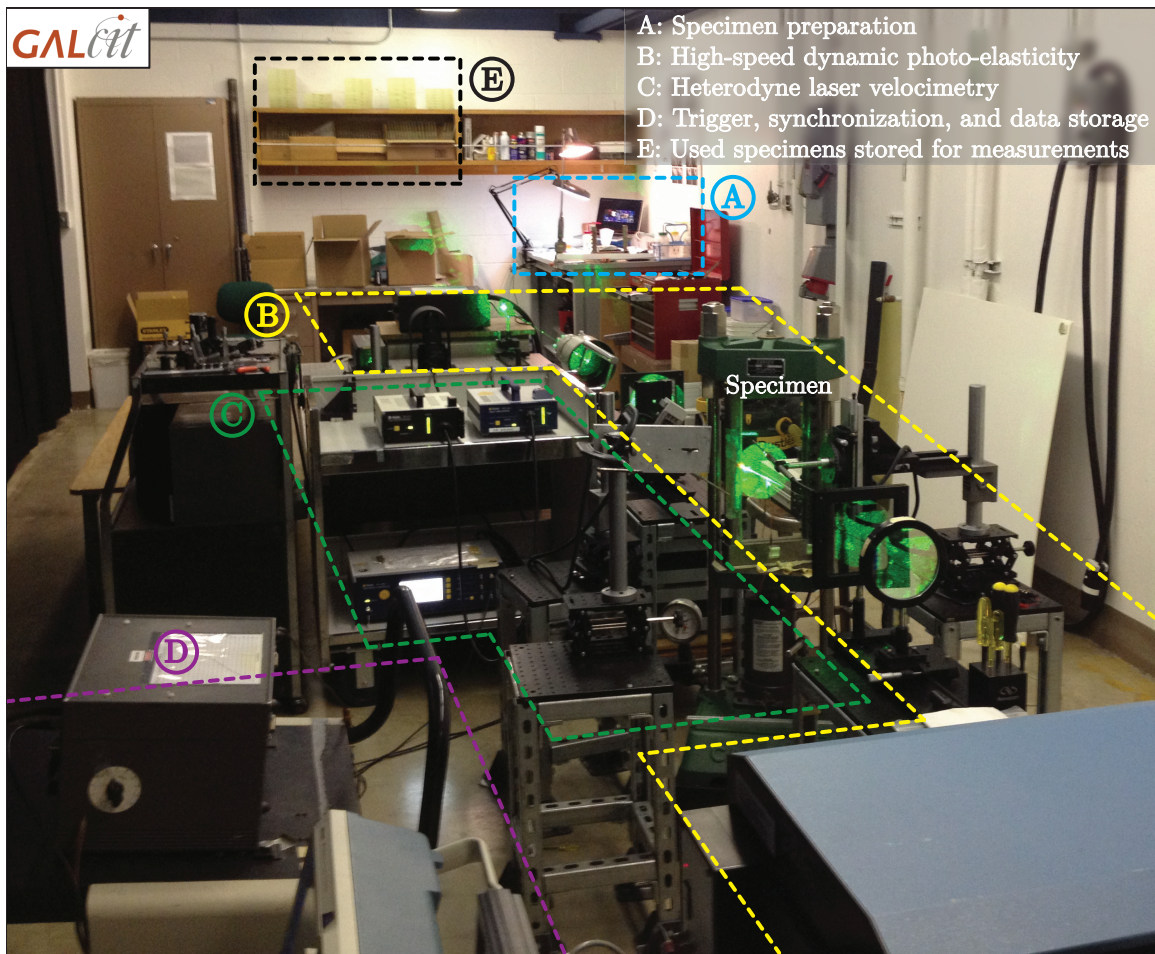
Figure 2.1: Photograph of the earthquake simulation laboratory. The experiment is segmented into interacting sub-systems A-E. The specimen can be seen resting in the hydraulic press.

the resulting radiated fields and ground motions, following the developments of previous studies: these diagnostics have been utilized to record the first experimental evidence of a super-shear rupture [43, 100] and in other fundamental studies within the field of mechanics, such as bi-material effects [49, 101], ground motions in a strike-slip configuration [37, 43, 69], off-fault damage [102, 103], three-dimensional effects [55], pulse-like versus crack-like rupture modes [51, 53, 104], and a parametric study of super-shear transition lengths [47, 54]. Figure 2.1 shows a photograph of the workspace, segmented into interacting parts including the specimen preparation, A, the photo-elasticity setup, B (first diagnostic), laser velocimeter systems, C (second diagnostic), and the control station, D, which triggers the dynamic event as well as synchronizes the diagnostics. Specimens are stored for various post-experiment measurements, E. The current chapter provides full details on the experimental design (Section 2.1), testing procedure (Section 2.2), and diagnostics (Sections 2.2.2 and 2.2.3).

2.1 Experimental design

In the present study, the experimental setup is modified from previous research configurations to facilitate the modeling of thrust faults in two important ways. First, the specimen size has been increased to avoid measuring the ground motion response of reflected mechanical waves from the remaining three specimen edges at stations near the experimental free surface, and second, the specimen holder has been redesigned to prevent buckling of the enlarged plate.

2.1.1 Modeling a thrust fault in the laboratory

The fundamental problem of a dynamic rupture propagating along a weak plane immediately lends itself to analogy with earthquake mechanics. A thrust fault in the earth is modeled in the laboratory with a rectangular plate ($w = 180\,\mathrm{mm}$, $h = 360\,\mathrm{mm}$, $t = 9.52\,\mathrm{mm}$) divided into two pieces at a prescribed angle, as shown in Figure 2.2. The geometry of the specimen is related to elements of a natural fault in the earth while the experimental diagnostics mimic both seismological measurements and numerical inversions of geological field data for information within the surface of the earth.

The experimental specimen models an idealized slice of earth. The mating pieces of the specimen represent the hanging and foot wall plates in a thrust fault, A_1 and A_2 in Figure 2.2, respectively. The simulated earth surface is represented by the hashed region, B. The interface where the hanging and foot wall plates mate is analogous to a fault extending down-dip into the earth at a constant interface angle, α (Figure 2.2, C). The dip-angle, a term more familiar in the field of seismology, is the complement of the interface angle. The intersection of the interface plane and the experimental free surface is called the fault trace, located at the origin of coordinate systems $\hat{x}_1 - \hat{x}_2$ and $\hat{x}'_1 - \hat{x}'_2$. The hypocenter is modeled by a through-thickness notch fabricated at a predetermined location at-depth along the interface (Figure 2.2, D). The uniaxial compression of the specimen in the lab
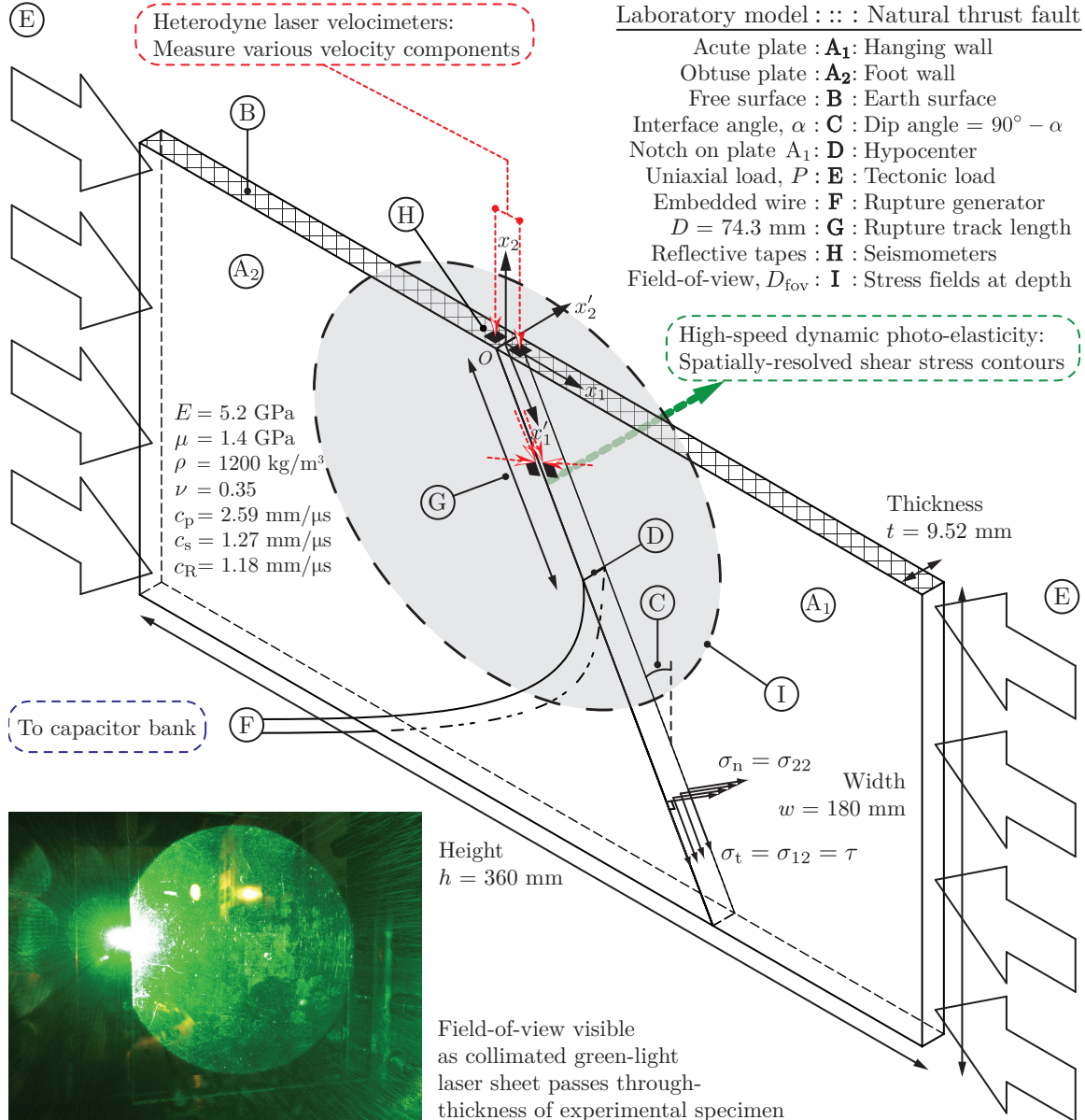
Figure 2.2: Experimental specimen configuration modeling a thrust fault in a slice of earth. Analogies are drawn between the simulated and real earth thrust fault features (A-I). The photograph insert shows the field-of-view as the expanded laser beam passes through the transparent specimen. Note: though the hydraulic press requires the specimen to be loaded vertically in the lab frame, the schematics are rotated to align the simulated earth surface in customary orientation.

represents the far-field tectonic load in the earth (Figure 2.2, E), which is resolved into normal and shear stress components along the interface as $\sigma_\mathrm{n} = P\cos^2\alpha$ and $\sigma_\mathrm{t} = P\sin\alpha\cos\alpha$. A shear-dominant, mixed-mode rupture is generated by discharging a capacitor bank across a wire embedded in the pre-fabricated notch (Figure 2.2, F). Discharge of the capacitor bank converts the filament to plasma, locally decreasing the fault strength such that the driving shear stress is sufficient to initiate slip. At the same time, a low-Voltage signal from the capacitor triggers the two available diagnostics,

synchronizing the entire experiment. This mechanism nucleates the dynamic slip event, generating a bi-directional rupture propagating symmetrically away from the hypocenter. Confined to the fault plane, the rupture tips unzip the fault in transit, continuously emitting pressure (P) and shear (S) stress waves into the bulk which later reflect from the free surface and feed back onto the fault. The radiation process and resulting slip redistribute accumulated stresses along the fault towards a new static equilibrium: this transient simulates an earthquake. The up-dip rupture propagates a distance $D = 74.3$ mm from the hypocenter to the fault trace (Figure 2.2, G), interacting with the free surface and feeding back stress waves towards the bulk of the material.

Laser velocimetry and the opto-mechanical method of dynamic photo-elasticity yield experimental data that are analogous to seismogram records and inversion results. Retro-reflective tapes (Figure 2.2, H) are placed at designated points on the specimen and mark the locations of the seismometers. Doppler-shifted light from the moving tape is diffusively reflected back into the velocimeter systems and decoded to output a single component of velocity at a given station, defined by the focal point and orientation of the incident beams [105]. Focusing the beams normal to the simulated earth surface records vertical velocity components, $\dot{u}_2(x_1, 0, t)$, while focusing the beams on tapes placed at-depth along the interface records fault parallel and fault normal velocity components just above and below the interface, $\dot{u}_1(x_1', x_2' = \pm\eta, t)$ and $\dot{u}_2(x_1', x_2' = \pm\eta, t)$, respectively, with offset distances $\eta \approx 400 - 600\,\mu$m. Contours of maximum shear stress magnitude, $|\tau_{\max}(x_1, x_2, t)|$, are recorded with standard methods of photo-elasticity (Appendix B) [106, 107, 108]. Laser light is expanded to a diameter of $D_{\text{fov}} \approx 145$ mm, collimated, and transmitted through the specimen: intersection of the beam with the specimen mid-plane defines the field-of-view (Figure 2.2, I), bounding the region captured by the high-speed digital cameras. These contours are two-dimensional analogues of field data inversion results for mechanical quantities below the earth surface.

The surrogate material used in all experimentation is Homalite H-100. Homalite is a transparent, brittle polyester resin with elastic modulus $E = 5.2$ GPa, shear modulus $\mu = 1.4$ GPa, density $\rho = 1200$ kg/m^3 and Poisson's ratio $\nu = 0.35$ [43]. The dilatational, shear, and plane-stress Rayleigh wave speeds are $c_{\text{p}} = 2.59$ mm/μs, $c_{\text{s}} = 1.27$ mm/μs, and $c_{\text{R}} = 1.18$ mm/μs, respectively [65]. Homalite H-100 is optically-birefringent with a stress-optic coefficient $C = 23.1 \times 10^{-12}$ m^2/N [109], thus sensitive to the methods of photo-elastic interferometry, and is a well-documented material in experiments utilizing opto-mechanical techniques [110, 111]. Past research on dynamic ruptures with Homalite H-100 have shown that the material behaves like crustal rock in the upper strata of the earth, in the sense that the response is linearly elastic within the strain rates of the experiment [55]. Furthermore, estimates of SS transition lengths yield $l_{\text{tr}} \approx 10 - 100$ mm (Section 3.1.4); transition lengths scale with the critical crack length, L_{c}, which in turn scales with the shear modulus of the material, μ [37]. Crustal rock moduli are approximately 30 times greater than that of Homalite H-100, requiring specimen dimensions beyond the current laboratory capability to capture transition.

2.1.2 Reflected wave analysis

Measurements near the simulated earth surface must record the effects of incident waves from the up-dip propagating rupture and continuing motion after the rupture reaches the free surface, before reflected waves arrive from the loading platens and the opposite specimen boundary. Waves reflected off the specimen edges other than the simulated earth surface (edges B, C, and D in Figure 2.3) are eventually expected to corrupt the measured signals, in the sense that such boundaries are absent for natural faults. One goal is to avoid such potential contamination in ground motion signals; a reflected wave calculation is performed to determined appropriate plate dimensions w, h, t and hypocenter location $(\bar{\zeta}_1, \bar{\zeta}_2)$ that would satisfy a suitable uncorrupted experimental window of T_{exp}.
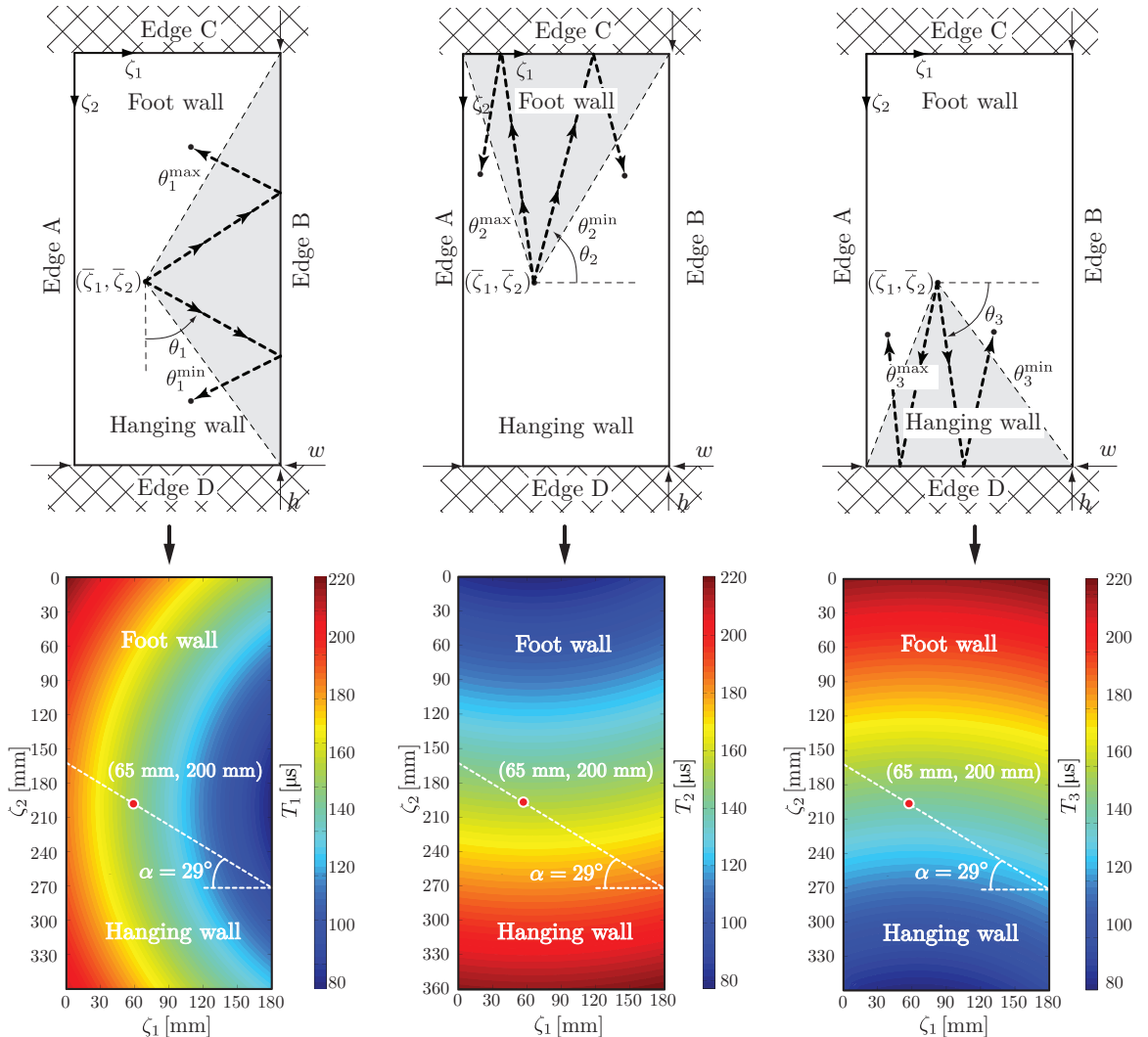
Figure 2.3: Reflected wave analysis setup; an uncorrupted measurement window of $T_{\text{exp}} \approx 120\,\mu\text{s}$ is desired near the experimental free surface, edge A. Each sub-problem corresponds to reflections from one of three problematic specimen edges. Variables θ_i ($i = 1, 2, 3$) are spanned across appropriate sectors (shaded regions) to determine minimum paths, D_i, for a given hypocenter location $\bar{\zeta}_1, \bar{\zeta}_2$. Contour plots show arrival times of the first reflected wave from each edge $T_i = D_i/c_{\text{p}}$.

Physical constraints and previous studies of rupture dynamics in similar configurations suggest a choice of $T_{\mathrm{exp}} = 120\,\mu\mathrm{s}$, seeding the initial plate dimensions used in the reflected wave analysis. The average experimentally measured sub-Rayleigh (SR) and super-shear (SS) rupture speeds are $v_{\mathrm{r}}^{\mathrm{SR}} = 1.14\,\mathrm{mm/\mu s}$ and $v_{\mathrm{r}}^{\mathrm{SS}} = 2.10\,\mathrm{mm/\mu s}$, respectively (Section 3.1.2 further discusses rupture speeds). Previous studies with similar frictional surface preparation methodologies verify these values for a range of applied loads up to $P = 25\,\mathrm{MPa}$ and interface angles $\alpha = 20 - 30°$ [37, 47, 53]. Said studies also report the transition length of SR to SS ruptures occurs well within $\approx 70\,\mathrm{mm}$. This bounds the minimum rupture track length $D > 70\,\mathrm{mm}$ (Figure 2.2:G), sufficient to capture rupture propagation in both speed regimes. The travel time of the slowest rupture feature to the simulated earth surface is $\approx 60\,\mu\mathrm{s}$. A doubling of this time suggests a minimum experimental window $T_{\mathrm{exp}} = 120\,\mu\mathrm{s}$, allowing the study of reflected and generated information due to the presence of the free surface. To assure uniform compression at the loading surfaces, the specimen width must be less than the width of the hydraulic press platen, bounding the plate width to $w \leq 180\,\mathrm{mm}$. In addition, the plate height is limited by critical buckling loads, an issue for the high-load experiments required to generate SS transition within the available rupture track length, $l_{\mathrm{tr}} < D$.

The numerical calculation is split into three problems as shown in Figure 2.3, one for each plate edge in consideration. Since P and S waves are continuously generated during the rupture, the problem is to find the shortest path that a reflected wave travels for a given hypocenter location and plate dimensions, $(\overline{\zeta}_1, \overline{\zeta}_2)$ and (w, h), respectively. P and S waves are idealized as circles, thus reducing the problem to a ray analysis. Examples of such paths are shown as bold dashed lines in Figure 2.3 (top panels). For set plate dimensions and hypocenter location, distance functions are defined for any given point (ζ_1, ζ_2) on the plate as functions of θ_i $(i = 1, 2, 3)$:

$$D_1(\zeta_1, \zeta_2, \theta_1) = \frac{w - \overline{\zeta}_1}{\sin\theta_1} + \sqrt{\left(\zeta_2 - \overline{\zeta}_2 - \frac{w - \overline{\zeta}_1}{\tan\theta_1}\right)^2 + (w - \zeta_1)^2}, \tag{2.1}$$

$$D_2(\zeta_1, \zeta_2, \theta_2) = \frac{\overline{\zeta}_2}{\sin\theta_2} + \sqrt{\left(\zeta_1 - \overline{\zeta}_1 - \frac{\overline{\zeta}_2}{\tan\theta_2}\right)^2 + (\zeta_2)^2}, \tag{2.2}$$

$$D_3(\zeta_1, \zeta_2, \theta_3) = \frac{h - \overline{\zeta}_2}{\sin\theta_3} + \sqrt{\left(\overline{\zeta}_1 - \zeta_1 + \frac{h - \overline{\zeta}_2}{\tan\theta_3}\right)^2 + (h - \zeta_2)^2}. \tag{2.3}$$

These three distance functions are minimized for every point by spanning variable θ_i, finding the shortest travel path for the reflected waves. The shortest travel times are obtained using the P wave speed, $T_i^{\mathrm{min}}(\zeta_1, \zeta_2) = D_i^{\mathrm{min}}(\zeta_1, \zeta_2)/c_{\mathrm{p}}$. The three problems are then unified by determining the global minimum arrival time of reflections over all such paths, $T_{\mathrm{ref}}(\zeta_1, \zeta_2)$, defining all suitable measurement points (ζ_1, ζ_2) as those satisfying the criteria $T_{\mathrm{exp}} \leq T_{\mathrm{ref}}(\zeta_1, \zeta_2)$:

$$T_{\mathrm{ref}}(\zeta_1, \zeta_2) = \min\left[T_1^{\mathrm{min}}(\zeta_1, \zeta_2), T_2^{\mathrm{min}}(\zeta_1, \zeta_2), T_3^{\mathrm{min}}(\zeta_1, \zeta_2)\right]. \tag{2.4}$$
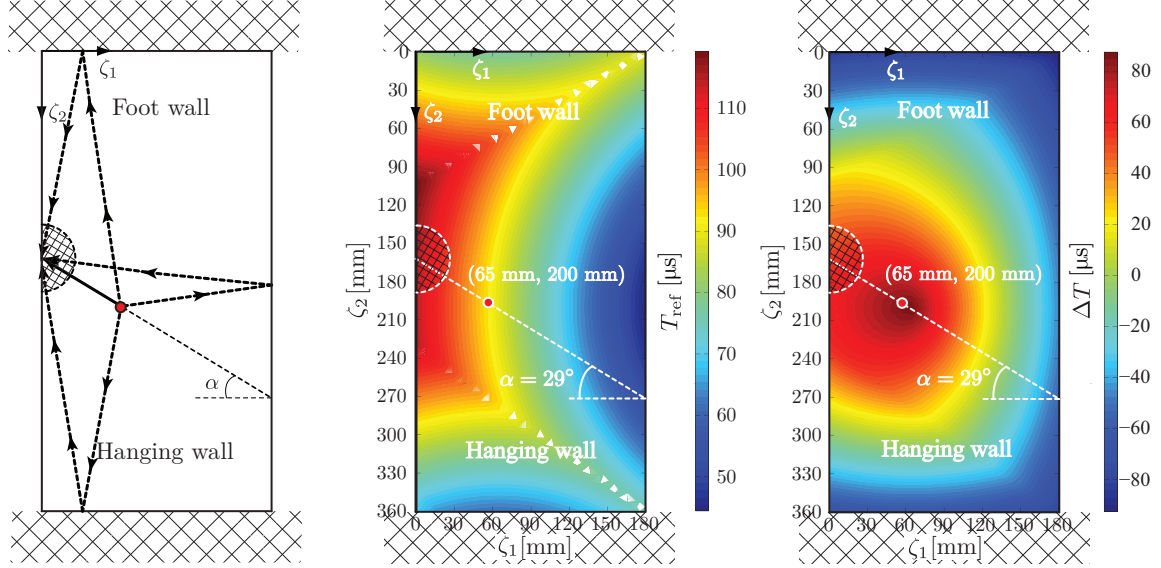
Figure 2.4: Reflected wave analysis results for a plate with dimensions $w = 180\,\text{mm}$, $h = 360\,\text{mm}$, $t = 9.52\,\text{mm}$ and hypocenter location $(\overline{\zeta}_1, \overline{\zeta}_2) = (65, 200)\,\text{mm}$. Contour plots show values of $T_{\text{ref}} = \min[T_1, T_2, T_3]$ and $\Delta T = T_{\text{ref}} - T_{\text{inc}}$, where $T_{\text{inc}}(\zeta_1, \zeta_2)$ is the incident S wave arrival time. Shaded regions at the fault trace satisfy $T_{\text{ref}} \leq T_{\text{exp}}$ and evade unwanted reflections up to $\approx 120\,\text{μs}$.

Contour plots of each independent problem's solution are given in the bottom panel of Figure 2.3 for plate dimensions $(w, h) = (180, 360)\,\text{mm}$ and a hypocenter location of $(\overline{\zeta}_1, \overline{\zeta}_2) = (65, 200)\,\text{mm}$. These results satisfy physical constraints $w \leq 180\,\text{mm}$ (press platen) and $D \approx 70\,\text{mm}$ (rupture track length). For plate heights $h \leq 300\,\text{mm}$, no choice of hypocenter location would give $T_{\text{exp}} \leq T_{\text{ref}}$ for any measurement location, thus a convenient ratio of 2:1 plate height to width is chosen, giving $h = 360\,\text{mm}$. The three problems are combined (Equation 2.4) and a contour plot of T_{ref} is presented in Figure 2.4, showing that points within $\approx 40\,\text{mm}$ of the fault trace are suitable measurement locations (hashed semi-circles). It is noted that the asymmetry of the inclined interface forces the hypocenter to drop below the vertical mid-plane, making the hanging wall plate slightly shorter than the foot wall. The hypocenter is placed closer to edge A than edge B, deduced from the contour plot of T_1. To better visualize the hypocenter location, $\Delta T = T_{\text{ref}} - T_{\text{inc}}$ is defined, where $T_{\text{inc}}(\zeta_1, \zeta_2) = c_{\text{s}}^{-1} \sqrt{(\zeta_1 - \overline{\zeta}_1)^2 + (\zeta_2 - \overline{\zeta}_2)^2}$ is the arrival time of the first S wave from the hypocenter. Note that the SR rupture tip speed is about $89 - 92\,\%$ of the S wave speed.

The reflected wave analysis proposes plate dimensions of $w = 180\,\text{mm}$, $h = 360\,\text{mm}$ and a hypocenter location of $(\overline{\zeta}_1, \overline{\zeta}_2) = (65, 200)\,\text{mm}$. The calculations are repeated for the angle range $\alpha = 20 - 30°$ with little change in T_{ref} (average values of $100\,\text{μs}$ for $\alpha = 20°$). Ruptures are heavily influenced by the resolved shear and normal stresses along the fault, σ_{n} and σ_{t}, thus a wide range of dynamics may be studied with minimum change in geometry [54]. In previous studies, the specimen sizes were $\approx 150\,\text{mm} \times 150\,\text{mm}$ with the hypocenter placed at the center. The experiment avoids unwanted reflections by design; however, the enlarged plate is more susceptible to buckling failure.

2.1.3 Critical load analysis

A buckling analysis of the enlarged plate is conducted to assure that the specimen will not fail under larger compressive loads ($P \approx 15\,\text{MPa}$), which favor the transition of ruptures to SS speeds. The buckling loads are first calculated theoretically with various mixtures of boundary conditions for the proposed specimen dimensions $w = 180\,\text{mm}$, $h = 360\,\text{mm}$, $t = 9.52\,\text{mm}$ (approximated as $10\,\text{mm}$), as shown in Figure 2.5. Small-scale experiments are conducted to verify the calculations.

Homalite H-100 properties and specimen geometry
$E = 5.2$ GPa $v = 0.35$
$w = 180$ mm, $h = 360$ mm, $t = 10$ (≈ 9.52) mm

Case I:
A - free
B - free
C - simply-supported
D - simply-supported

Case III:
A - free
B - free
C - elastically built-in
D - elastically built-in

Case II:
A - free
B - simply-supported
C - simply-supported
D - simply-supported

Case IV:
A - free
B - simply-supported
C - elastically built-in
D - elastically built-in
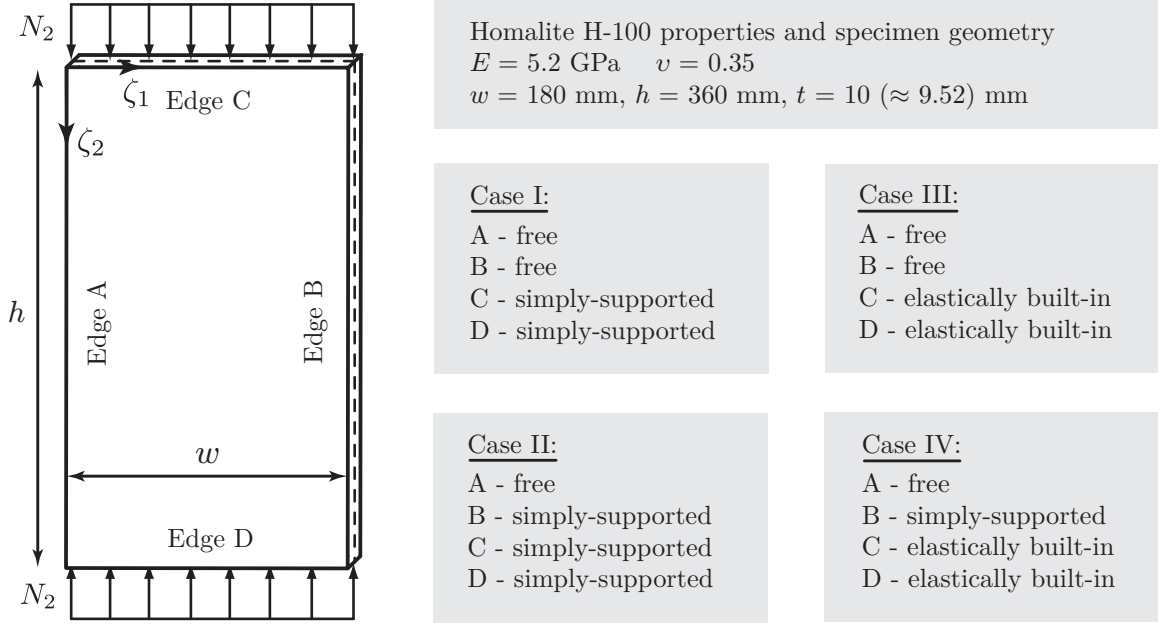
Figure 2.5: Theoretical buckling analysis determines the critical loads of the Homalite H-100 specimen with various mixtures of boundary conditions listed in cases I, II, III, and IV.

In accord with the theory of plates and shells, deflection of plates under the combined actions of lateral loads and forces acting along the mid-plane are governed by the plate equation [112]:

$$\frac{\partial^4 g}{\partial \zeta_2^4} + 2\frac{\partial^4 g}{\partial \zeta_2^2 \partial \zeta_1^2} + \frac{\partial^4 g}{\partial \zeta_1^4} = \frac{1}{D}\left(q + N_2\frac{\partial^2 g}{\partial \zeta_2^2} + N_1\frac{\partial^2 g}{\partial \zeta_1^2} + 2N_{12}\frac{\partial^2 g}{\partial \zeta_1 \partial \zeta_2}\right), \tag{2.5}$$

where $g(\zeta_1, \zeta_2)$ is the out-of-plane deflection from the mid-plane, $D = Eh^3/12(1 - \nu^2)$ is the plate stiffness, $q(\zeta_1, \zeta_2)$ is a lateral load, and $N_1(\zeta_1, \zeta_2)$, $N_2(\zeta_1, \zeta_2)$, and $N_{12}(\zeta_1, \zeta_2)$ are forces acting along the $\hat{\zeta}_1$, $\hat{\zeta}_2$, and $\hat{\zeta}_1 - \hat{\zeta}_2$ axes (per unit length), respectively.

There are two methods of obtaining critical buckling loads for a plate. The first directly integrates Equation 2.5 with the appropriate boundary conditions, then solves for the null-space of the coefficient matrix to determine the non-trivial solution for the deflection curve (trivial solution describes the stable flat-form configuration). The energy method may also be used to determine critical loads by comparing the work done by the applied forces to the mid-plane's strain energy of bending: buckling occurs when the work done by these external forces surpasses the strain energy

of bending for all possible deflection functions, $g(\zeta_1, \zeta_2)$. The energy method is most useful when approximate bounding calculations are needed for complex plate systems, such as reinforcements with stiffeners. For simpler geometries, a more direct method is to integrate Equation 2.5. Using the method of integration with appropriate boundary conditions, an analytical solution is found for the plate deflection surface, $g(\zeta_1, \zeta_2)$, which in turn is used to determine the critical buckling load [113]. Panels in Figure 2.5 summarize the four sets of boundary conditions considered.

Case I

In the absence of lateral loads ($q = 0$) and forces in the $\hat{\zeta}_1$ ($N_1 = 0$) and $\hat{\zeta}_1 - \hat{\zeta}_2$ ($N_{12} = 0$) directions, Equation 2.5 reduces to

$$\frac{\partial^4 g}{\partial \zeta_2^4} + 2\frac{\partial^4 g}{\partial \zeta_2^2 \partial \zeta_1^2} + \frac{\partial^4 g}{\partial \zeta_1^4} = -\frac{N_2}{D}\frac{\partial^2 g}{\partial \zeta_2^2}. \tag{2.6}$$

The simply-supported boundary condition along edges C and D prohibits deflections and moment-bearing capabilities of the loading surfaces:

$$(g)|_{\zeta_2 = 0, \zeta_2 = h} = 0, \qquad \left(\frac{\partial^2 g}{\partial \zeta_1^2} + \nu\frac{\partial^2 g}{\partial \zeta_2^2}\right)\Bigg|_{\zeta_2 = 0, \zeta_2 = h} = 0. \tag{2.7}$$

A solution for the deflection curve which satisfies the simply-supported boundary conditions is:

$$g(\zeta_1, \zeta_2) = f(\zeta_1)\sin\frac{m\pi\zeta_2}{h}, \qquad m = 1, 2, 3, ..., \tag{2.8}$$

where m is the number of deflection half-waves at the buckling load ($m = 1$ is the first mode). The proposed solution of Equation 2.8 is substituted into Equation 2.6 to give

$$\frac{d^4 f}{d\zeta_1^4} - \frac{2m^2\pi^2}{h^2}\frac{d^2 f}{d\zeta_1^2} + \left(\frac{m^4\pi^4}{h^4} - \frac{N_2}{D}\frac{m^2\pi^2}{h^2}\right)f = 0, \tag{2.9}$$

a fourth order, homogeneous, ordinary differential equation subject to the additional constraint

$$\frac{N_2}{D} > \frac{m^2\pi^2}{h^2}, \tag{2.10}$$

due to limiting physical conditions on edges A and B. The general solution to Equation 2.9 is:

$$f(\zeta_1) = C_1 e^{-\alpha\zeta_1} + C_2 e^{\alpha\zeta_1} + C_3\cos\beta\zeta_1 + C_4\sin\beta\zeta_1, \tag{2.11}$$

where $\alpha = \sqrt{\frac{m^2\pi^2}{h^2} + \sqrt{\frac{N_2}{D}\frac{m^2\pi^2}{h^2}}}$ and $\beta = \sqrt{\frac{-m^2\pi^2}{h^2} + \sqrt{\frac{N_2}{D}\frac{m^2\pi^2}{h^2}}}$. Edge A (experimental surface) and edge B sustain no forces or moments and are thus considered free:

$$\left(\frac{\partial^2 g}{\partial \zeta_1^2} + \nu\frac{\partial^2 g}{\partial \zeta_2^2}\right)\Bigg|_{\zeta_1 = 0, \zeta_1 = w} = 0, \qquad \left(\frac{\partial^3 g}{\partial \zeta_1^3} + (2 - \nu)\frac{\partial^3 g}{\partial \zeta_2^2 \partial \zeta_1}\right)\Bigg|_{\zeta_1 = 0, \zeta_1 = w} = 0. \tag{2.12}$$

Applying the boundary condition along edge A ($\zeta_1 = 0$) and B ($\zeta_1 = w$) gives the coefficient matrix $[\mathbf{A_I}]$ of the matrix equation $A_{ij}C_j = 0$:

$$[\mathbf{A_I}] = \begin{bmatrix} \alpha^2 - \nu\frac{m^2\pi^2}{h^2} & \alpha^2 - \nu\frac{m^2\pi^2}{h^2} & \cdots \\ -\alpha^3 + \alpha(2-\nu)\frac{m^2\pi^2}{h^2} & \alpha^3 - \alpha(2-\nu)\frac{m^2\pi^2}{h^2} & \cdots \\ e^{\alpha w}\left(\alpha^2 - \nu\frac{m^2\pi^2}{h^2}\right) & e^{\alpha w}\left(\alpha^2 - \nu\frac{m^2\pi^2}{h^2}\right) & \cdots \\ e^{-\alpha w}\left(-\alpha^3 + \alpha\frac{m^2\pi^2(2-\nu)}{h^2}\right) & e^{\alpha w}\left(\alpha^3 - \alpha\frac{m^2\pi^2(2-\nu)}{h^2}\right) & \cdots \end{bmatrix}$$

$$\begin{bmatrix} \cdots & -\nu\frac{m^2\pi^2}{h^2} & 0 \\ \cdots & 0 & -\beta^3 - \beta\frac{m^2\pi^2(2-\nu)}{h^2} \\ \cdots & \cos\beta w\left(-\beta^2 - \nu\frac{m^2\pi^2}{h^2}\right) & \sin\beta w\left(-\beta^2 - \nu\frac{m^2\pi^2}{h^2}\right) \\ \cdots & \sin\beta w\left(\beta^3 + \beta\frac{m^2\pi^2(2-\nu)}{h^2}\right) & \cos\beta w\left(-\beta^3 - \beta\frac{m^2\pi^2}{h^2}\right) \end{bmatrix} . \quad (2.13)$$

The minimum zero of function $D_\text{I}(N_2\colon w, h, D, \nu) = \det[\mathbf{A_I}]$, satisfying the additional constraint of Equation 2.10, determines the force N_2 required to generate the unstable plate deflection surface, and in turn the critical buckling load of $\sigma_\text{I}^\text{c} = 3.4\,\text{MPa}$.

Case II

The loading surface boundary conditions are maintained as simply-supported (edges C and D); however, edge B is now considered as simply-supported rather than free as it was in case I. With the altered boundary condition, the coefficient matrix $[\mathbf{A_{II}}]$ is:

$$[\mathbf{A_{II}}] = \begin{bmatrix} \left(\alpha^2 - \nu\frac{m^2\pi^2}{h^2}\right)\sinh\alpha w & \left(\beta^2 + \nu\frac{m^2\pi^2}{h^2}\right)\sin\beta w \\ \alpha\left(\alpha^2 - (2-\nu)\frac{m^2\pi^2}{h^2}\right)\cosh\alpha w & -\beta\left(\beta^2 + (2-\nu)\frac{m^2\pi^2}{h^2}\right)\cos\beta w \end{bmatrix}, \quad (2.14)$$

where the reduction of coefficients from four to two gives a 2×2 matrix. As in case I, solution for the critical buckling load is reduced to finding the minimum root of function $D_\text{II}(N_2\colon w, h, D, \nu) = \det[\mathbf{A_{II}}]$ subject to the constraint in Equation 2.10. This method yields $\sigma_\text{II}^\text{c} = 8.7\,\text{MPa}$. By merely changing the boundary condition along edge B from free to simply-supported, the critical buckling load of the system is expected to increase more than two-fold.

Case III

Load-bearing surfaces (edges C and D) in contact with the press platens will carry a moment due to the finite thickness of the plate. The built-in boundary condition,

$$(g)|_{\zeta_2=0, \zeta_2=h} = 0, \qquad \left(\frac{\partial g}{\partial \zeta_2}\right)\Big|_{\zeta_2=0, \zeta_2=h} = 0, \quad (2.15)$$
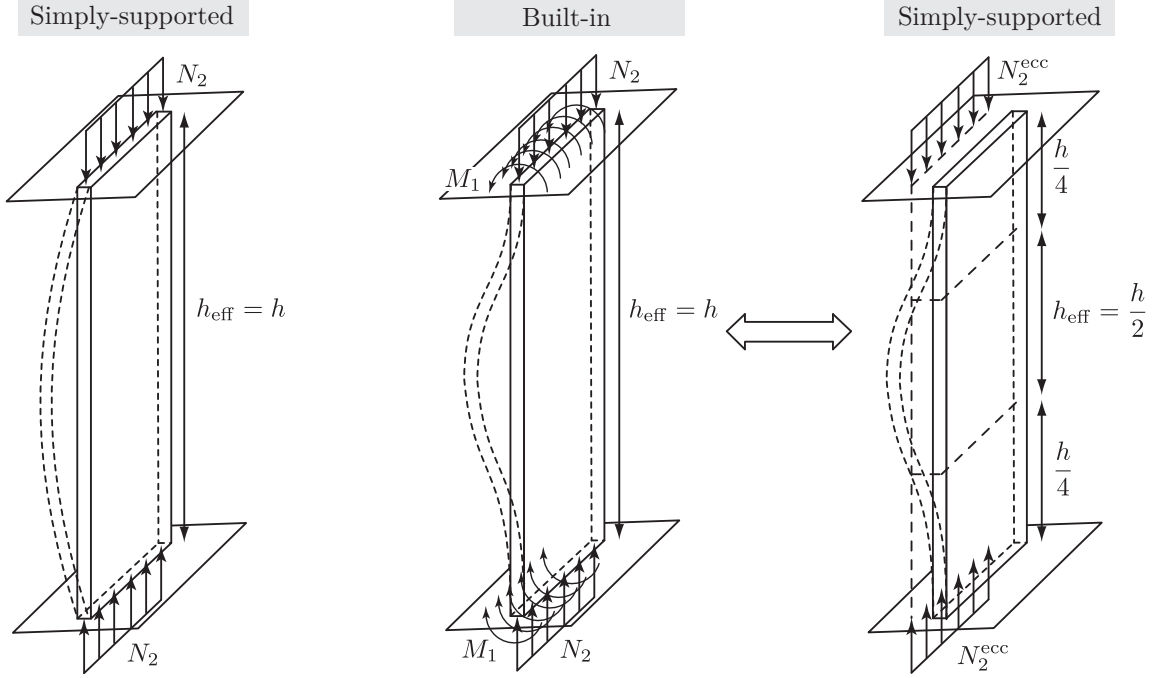
Figure 2.6: Analytical equivalence is drawn between simply-supported and built-in boundary condition configuration solutions with the use of an effective plate height, $h_{\text{eff}} = h/2$.

must be used to re-solve the plate equation (Equation 2.5) with a new functional form for the deflection curve, $g(\zeta_1, \zeta_2)$. The force-couple system at the loading surface, however, can be transformed to a force applied eccentrically to the plate (Figure 2.6). Intersections of the eccentric force's action and the deflection curve define nodal lines with zero moment. The nodal lines mimic simply-supported conditions, effectively reducing the solution to that of case I with an effective plate height, $h_{\text{eff}} = h/2$. The critical buckling load with this solution technique gives $\sigma_{\text{III}}^{\text{c}} = 13.5\,\text{MPa}$.

Case IV

In the same manner as extending the simply-supported boundary conditions of the loading surfaces to built-in from cases I to III, the same logic applies when extending case II to IV by transforming the plate height to $h_{\text{eff}} = h/2$ and using the same solution technique to determine $\sigma_{\text{IV}}^{\text{c}} = 18.5\,\text{MPa}$.

According to the analysis, the addition of constraints that limit plate deflection tends to increase the failure loads. The theoretical critical loads are $\sigma_{\text{I}}^{\text{c}} = 3.4\,\text{MPa}$, $\sigma_{\text{II}}^{\text{c}} = 8.7\,\text{MPa}$, $\sigma_{\text{III}}^{\text{c}} = 13.5\,\text{MPa}$, and $\sigma_{\text{IV}}^{\text{c}} = 18.5\,\text{MPa}$. An increase from case I to case II occurs from simply-supporting the free edge B. Case III and IV treat the load bearing surfaces as built-in rather than simply-supported, decreasing plate deflections, consequently increasing critical loads. Simply-supporting the free edge B similarly increases the critical load from case III to case IV. Limiting the plate deflection forces the material to deform under compression rather than bending. Theory predicts that a Homalite
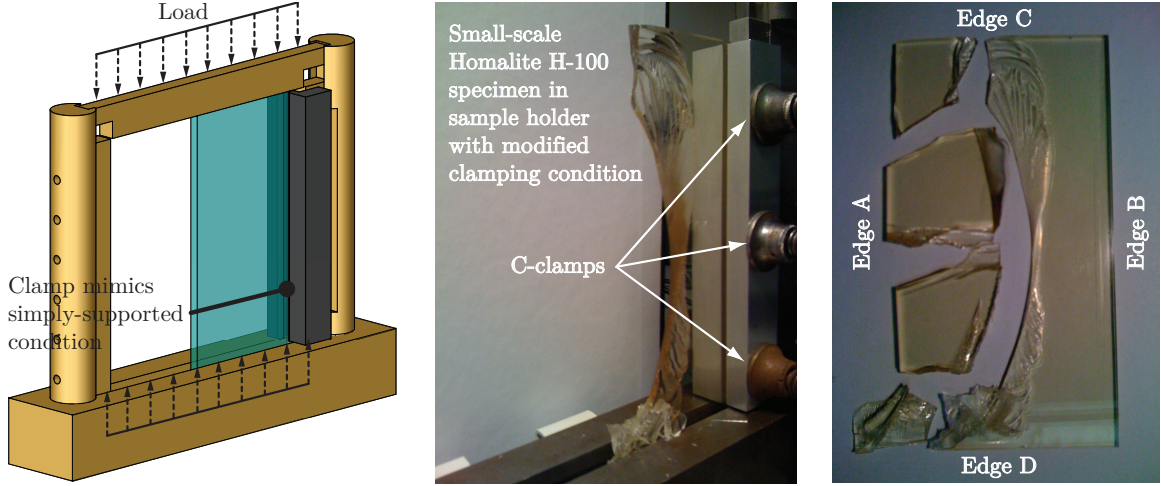
Figure 2.7: Experimental buckling setup and post-fracture damage pattern of the small-scale plate; $w' = 75\,\text{mm}$, $h' = 150\,\text{mm}$, and $t' = 5\,\text{mm}$. Supporting the plate with an additional clamp increases the buckling load from $\sigma_{\text{I}}'^{\text{exp}} = 4.7\,\text{MPa}$ to $\sigma_{\text{II}}'^{\text{exp}} = 10.4\,\text{MPa}$.

H-100 specimen with dimensions $w = 180\,\text{mm}$, $h = 360\,\text{mm}$, and $t = 9.52\,\text{mm}$ will not buckle under increased uniaxial loads ($P \approx 15\,\text{MPa}$) if the plate can be simply-supported along edge B.

Small-scale buckling tests are conducted on Homalite H-100 plates of roughly half the optimized specimen dimensions: $w' = 75\,\text{mm}$, $h' = 150\,\text{mm}$, and $t' = 5\,\text{mm}$. It is clear that the thinner plate will less effectively bear a moment, and it is for this reason that only the boundary conditions of case I and II are considered. The functions $D_{\text{I}}(N_2 \colon w', h', D, \nu)$ and $D_{\text{II}}(N_2 \colon w', h', D, \nu)$ are used to determine the small-scale critical loads $\sigma_{\text{I}}'^{\text{c}} = 5.4\,\text{MPa}$ and $\sigma_{\text{II}}'^{\text{c}} = 13.8\,\text{MPa}$. These two cases are tested by a slow increase in press load until the plate fractures (Figure 2.7). Measured failure loads are given as an average of two values, $\sigma_{\text{I}}'^{\text{exp}} = 4.7\,\text{MPa}$ and $\sigma_{\text{II}}'^{\text{exp}} = 10.4\,\text{MPa}$, closely matching the theoretical values of 5.4 MPa and 13.8 MPa, respectively. The post-mortem specimens for case II are shown in Figure 2.7; the fracture pattern matches the proposed half-wave deflection profile, where failure occurs at the maximum deflection point mid-height along the lateral free edge. On any constant ζ_2, the deflection curve must attenuate to zero traversing across the plate from $\zeta_1 = 0$ to $\zeta_1 = w$. The clamps enforce a simply-supported condition at $\zeta = w$, and thus the absence of cracks along edge B. These small scale results fortify the theoretical calculations for the optimized plate.

2.1.4 Specimen holder design

The specimen dimensions drive the design of the specimen holder. To prevent buckling, the specimen holder must supply a simply-supported condition for edge B, much like the clamps in the small-scale buckling experiments. Previous specimen holders do not allow velocimeter measurements to be taken on any lateral free surface (edges A and B), since these are masked by the presence of specimen holder columns; the current design also incorporates removable material to expose these surfaces.
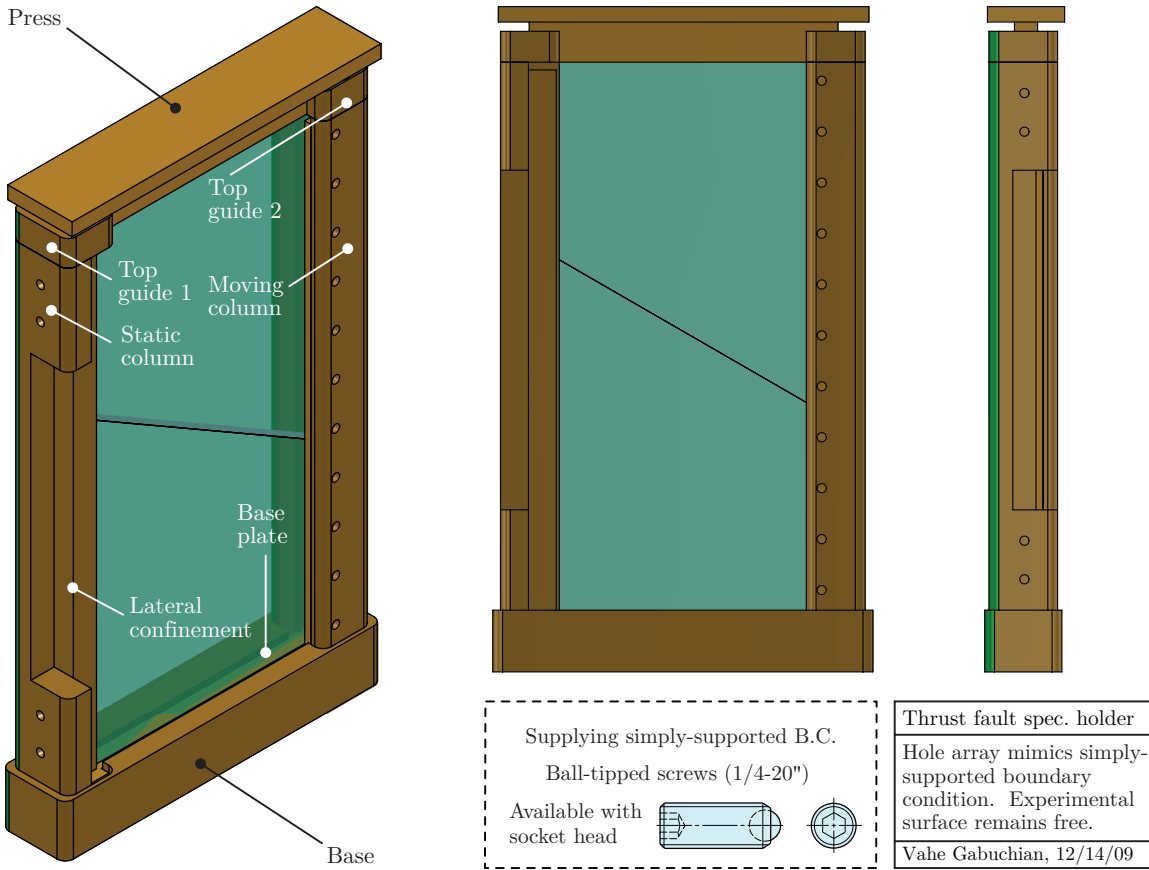
Figure 2.8: Specimen holder design. An array of ball-tipped screws on both sides of the moving column mimic the simply-supported boundary condition necessary to prevent buckling.

The specimen holder design is shown in Figure 2.8 and addresses all requirements of the experiment (drawing files are included in Appendix C). The holder accepts specimens of $h = 360\,\mathrm{mm}$ and $w = 180\,\mathrm{mm}$ with thicknesses up to $t = 15\,\mathrm{mm}$. Shorter specimens are accommodated with metal spacers. The entire holder is manufactured from steel alloy to increase the rigidity as much as possible. Impedance matching of Homalite H-100 and steel was un-necessary at the loading surfaces since these reflected waves do not interfere with measurements by design. The base of the holder is low enough so that the laser field-of-view can be centered about the interface and the fault trace. The moving column has an array of threaded thru-holes on both sides where ball-tipped screws are used to mimic the simply-supported boundary condition necessary to prevent buckling. The press is removable so the specimen can be inserted from the top. A confinement bar supports and stabilizes the plates during initial load application, but is removed before increasing to the final desired value. The static column has material removed in the mid-section such that when the lateral confinement bar is removed, measurements are possible on the exposed surface of edge A. Various other extrusions are used to mate and align the hanging and foot wall plates within the holder (Section 2.2.1.7): success of an experiment relies heavily on proper specimen alignment within the holder.

2.2 Testing procedure

The earthquake visualization experiment is segmented into four parts, as shown in Figure 2.9. This section describes in detail how an experiment is conducted, from specimen preparation to data acquisition. The specimen preparation process (A, shaded blue) describes how the Homalite H-100 sheets are treated and placed in the test section; the photo-elasticity setup (B_1, B_2, B_3, shaded yellow) outputs a sequence of full-field, spatially-resolved digital photographs of $|\tau_{\max}|$ contours; the laser velocimeters (C, shaded green) record various components of ground motion records on the specimen; the intersection of these two diagnostics is the test section (hashed region) where the specimen rests and measurements are conducted; the experiment is controlled with a single trigger that initiates the dynamic rupture as well as synchronizes the two diagnostics (D, shaded magenta). To accurately represent the laboratory space, all figures in this section are to scale and maintain proper orientation of the system components, e.g., in reference to Figure 2.1. For exact replication of experimental conditions, a full bill of materials used is included in Table D.3 (Appendix D).

A : Specimen preparation
B_1: Photo-elasticity: light source
B_2: Photo-elasticity: test section
B_3: Photo-elasticity: imaging
C : Heterodyne laser velocimetry
D : Trigger, sync, and storage

Capacitor triggers oscilloscopes which capture velocity time series

Oscilloscope triggers cameras

Data stored for processing
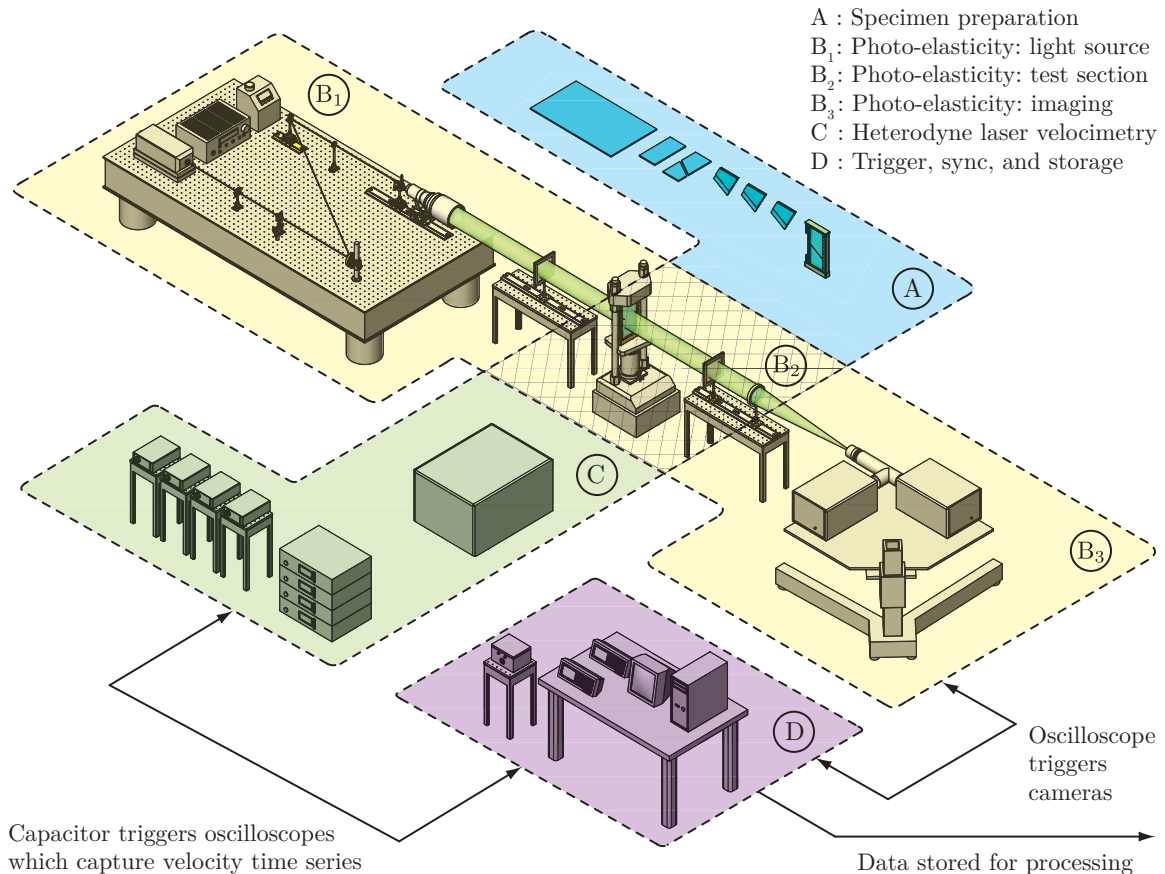
Figure 2.9: Overview of the experimental procedure. Specimen preparation workflow (A) culminates with the specimen statically pre-loaded in the test section (B_2), which is the intersection of the photo-elasticity diagnostic (B_1, B_2, B_3) and the laser velocimetry diagnostic (C). Dynamic rupture nucleation and experimental diagnostics are synchronized with a single trigger (D).

2.2.1 Specimen preparation

As part of any experimental science, a careful specimen preparation workflow is established for repeatability such that results from one set may be compared to those of another. This workflow is summarized in Figure 2.10. Sheets are CNC milled to rectangles which are later separated by an angled cut. The angled surfaces are polished until optically-reflective and then bead-blasted to increase the surface roughness. A notch is placed along the interface on the hanging wall plate. The specimen is marked up for measurement and aligned in the specimen holder, which gets placed in the test section. Manufacturing and mark-up effects on reproducibility are discussed in Chapter 5.

A: Sheets of Homalite H-100 (21" x 31" x 3/8")
B: Outer perimeter of specimen is CNC machined
C: Interface is machined at the appropriate fault angle, α
D: Mating interface surfaces polished until optically reflective
E: Mating interface surfaces roughened with controlled bead blasting
F: Notch placed on hanging wall plate to house NiCr wire at nucleation site
G: Reflective tapes and NiCr wire placed on specimen and plates are aligned in holder

Figure 2.10: Specimen preparation workflow. Manufacturing and mark-up processes are summarized from A-G, starting with the Homalite H-100 sheet stock and culminating with the hanging and foot wall plates aligned in the specimen holder. The photograph shows the specimen ready for trigger.

2.2.1.1 Manufacturing specimens

Homalite H-100 sheets of thickness $t = 9.52\,\mathrm{mm}$ are first machined to rectangles of width $w = 180\,\mathrm{mm}$ and height $h = 360\,\mathrm{mm}$ and then separated into hanging and foot wall plates with an angled cut. The machine order is shown in Figure 2.11. The specimen is carefully clamped to avoid damaging the imaging surfaces and to avoid elastic unloading of the material during the cutting process.

Stock sheets of Homalite$^{\mathrm{TM}}$ H-100 (Brandywine Investment Group #375 000 1000) with approximate dimensions $h = 31$ inch, $w = 21$ inch, and $t = 3/8$ inch are shipped in wooden crates. In contrast to a standard box, a crate minimizes shipping damage to the large sheets, as cracks in the
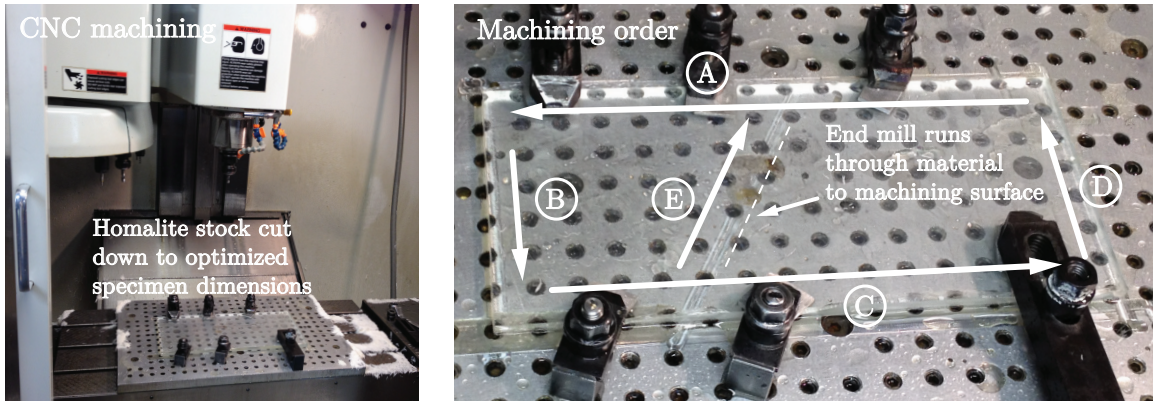
Figure 2.11: The plates are CNC machine manufactured into the hanging and foot wall plates. Most critical to successful manufacturing is the clamping pressure on the plates, end mill speeds, and constant lubrication, due to the material's brittle nature. (Appendix C, detailed drawing files).

brittle polymer can render large portions of the material defunct. The material flows over a long period of time, much like glass, introducing non-manufacturing related thickness variations across the plate. The sheets themselves have a reported thickness error of $\pm 15\,\%$ along their lengths, a fact inherent in the mold pouring manufacturing method. At times there is visible curvature in the sheet; these sheets should not be used since the plate will bow during loading. Extended periods of light exposure during storage turns the material an opaque yellow. Experiments are initially organized into groups according to material shipment batch to maximize reproducibility across experiments; however, no identifiable scatter in measurements is observed across different batches.

The Homaite sheet is first cut into rectangles and then the interface is cut at an angle $\alpha = 29°$, separating the hanging and foot wall plates. The plates are marked to avoid thickness mismatch along the interface during mating. A CNC machine (Fadal$^{©}$ VCM 40) is used to perform these precision cuts, maintaining accuracy within $5 \times 10^{-6}\,\mathrm{m}$. The protective film is kept on to prevent damage to the imaging surfaces. Over-tightening the clamps damages the imaging surfaces and introduces appreciable elastic unloading near the end mill, making the freshly-cut edges non-parallel, and eventually leading to bowing under load. To prevent chipping of the brittle material, appropriate end mil speeds are selected and constant lubrication is provided to the tool. In particular, the translational speed of the end mil is decreased when the tool reaches a free surface to prevent material damage at the fault trace (e.g., acute wedge of the hanging wall plate, Figure 2.11, arrowhead E).

2.2.1.2 Polishing interfacial surfaces

The polishing process removes machine-induced surface effects on the hanging and foot wall interface surfaces. The purpose is to achieve a baseline standard for all specimen interfacial conditions. By positioning the mating plates in a steel rig (Figure 2.12) and then following standard polishing techniques (Figure 2.13), uniform, optically-reflective mating surfaces are obtained.
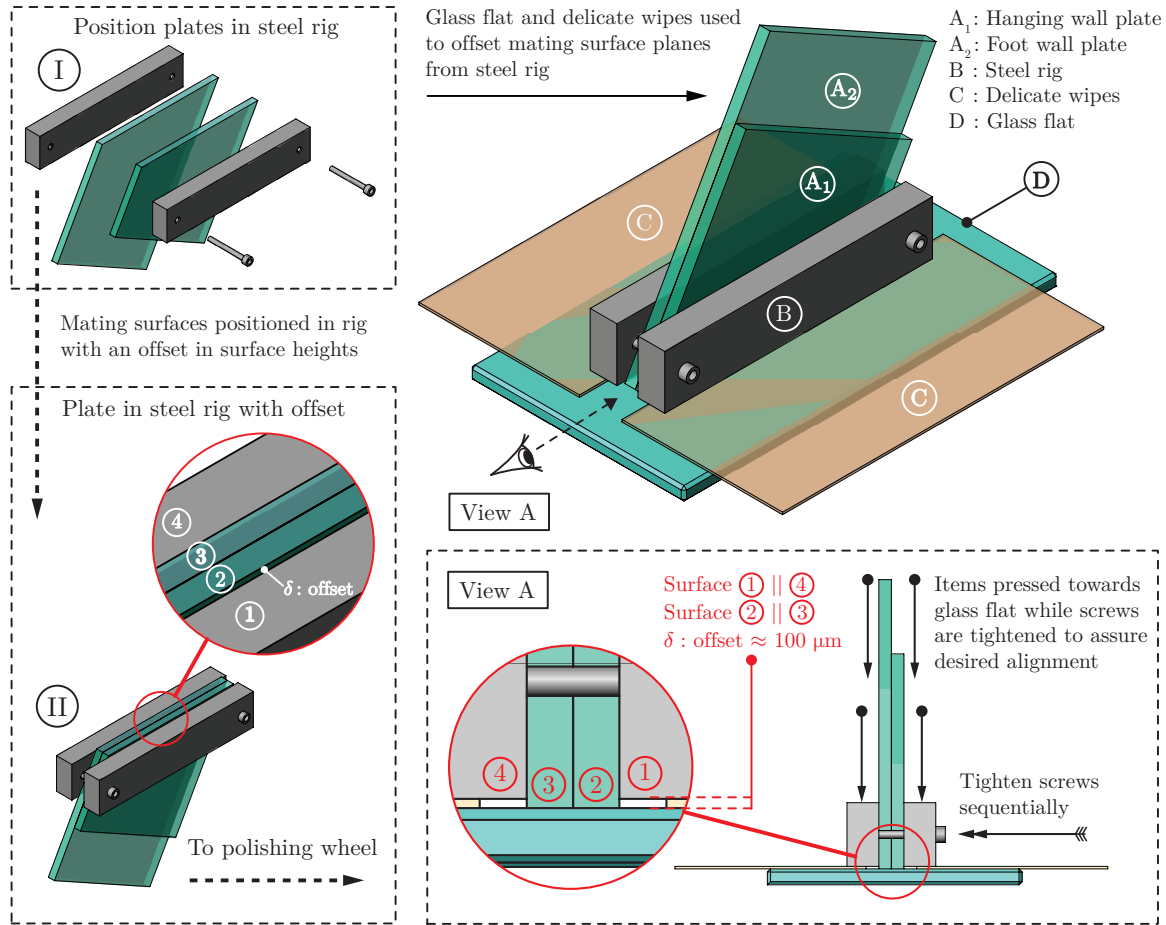
Figure 2.12: Successful and rapid polishing of the hanging and foot wall interface surfaces requires careful alignment of the hanging and foot wall plates in the steel rig. The top right schematic shows the hanging (A_1) and foot (A_2) wall plates placed in the steel rig (B). The rig rests on delicate task wipes (C) which in turn sit on a glass flat (D). The bottom left and right inserts show the offsets between the interfacial planes (surfaces 2 and 3) and the bottom of the steel rig (surfaces 1 and 4).

The quality and rate of polish is mostly dependent on the initial placement of the mating plates in the steel rig. Figure 2.12 (panel I) shows the placement of the plates in the steel rig. The protective film is kept on the material to prevent damage to the imaging surfaces. The final placement of the plates in the rig must have an offset, δ, between the interface surface planes (surfaces 2 and 3, panel II) and those of the steel rig (surfaces 1 and 4, panel II); this offset is achieved by placing two folded task wipes (KimTech$^{©}$ #34133) in between a glass flat and the steel rig. The Homalite plates are placed in the rig, resting the interfacial surfaces against the glass flat. The set screws are sequentially tightened as constant downward pressure is applied to both plates and the steel rig; the result should be offsets of $\delta \approx 100\,\mu\text{m}$, as shown in view A of Figure 2.12. Values of δ on the order of $\approx 1\,\text{mm}$ are undesirable, as the rig may catch on the polishing cloth, or worse yet, introduce uneven polishing effects to the mating surfaces. The steps in between the planes should be constant throughout the lengths of the interface, and checked with the use of the greatest tool: a finger.

1) Polishing cloth attached to wheel
2) Cloth initially wet with water
3) CeO applied to cloth
4) Wheel again wet with water
5) Wheel kept hydrated (3-4)

1:2 ratio CeO polishing
compound to H_2O

View A

Ⓒ

Ⓑ

Ⓓ

Ⓐ

A: Steel polishing wheel
B: Variac adjusts wheel rpm
C: Mating plates arranged in steel rig
D: Adhesive polishing cloth

View A (x4)   Motion of steel rig on wheel
Interface edges
stay on wheel
Steel rig and plates
Pressure applied
for uniform contact   Maximum
radius which still
maintains full
interface contact
Steel rig rotates clockwise
Wheel rotates counterclockwise

Figure 2.13: Standard polishing procedures are used to achieve optically-reflective interface surface conditions. A 12 inch steel polishing wheel (A) rotates at a set rate adjusted by a Variac (B). The steel rig holding the hanging and foot wall plates (C) rests on a polishing cloth treated with CeO polishing compound and water (D). The photograph describes motion of the rig during polishing.

The steel rig and plates are counter-rotated against the spinning polishing wheel until optically-reflective surfaces are achieved. Offset δ pushes the interface surfaces against the polishing cloth (Buehler$^{©}$ 12 inch Microcloth #407222) as shown in Figure 2.12. A Variac sets the polishing wheel spin rate, which is kept constant at $\approx$ 100 r.p.m. Air pockets formed during initial adhesion of the polishing cloth on the steel wheel must be avoided, as they may cause the steel rig to catch. The cloth is initially wet with a 2:1 ratio of water and cerium oxide polishing compound (Buehler$^{©}$ MicroMet #406355006). Uniform pressure is applied onto the steel rig to maintain contact with the polishing cloth. The rig is rotated at the outermost possible radius from the center to increase the relative velocity between the specimen and cloth without falling off the wheel edges (Figure 2.13, view A). To avoid a bias in polishing, the orientation of the rig is periodically changed. Surfaces are checked by reflections of light at grazing angles against the interface surfaces; a uniform reflective surface must be achieved, otherwise the process should be repeated. The wheel must constantly be wet with a 2:1 ratio of water to polishing compound to hinder the wearing of the cloth, which may cause spotted irregularities on the polished surfaces if not monitored. Two distinct surface features are eliminated with the polishing process, as discussed in terms of experimental reproducibility in Section 5.1. Surface profile measurements conducted along the mid-thickness of the plate generate a height function $z(x)$ which is used to determine the average surface roughness $R = 1/L \int_0^L |z(x)| \mathrm{d}x$ within a distance L [55]: reported values of $R = 0.502 \, \mu m$ and $R = 0.016 \, \mu m$ for the as-machined and polished surfaces indicate an order of magnitude decrease in average roughness after polishing.

2.2.1.3   Bead blasting interfacial surfaces

The polished interface surfaces are systematically roughened with the bead blasting procedure. Glass beads are ejected from a nozzle, impacting the mating surfaces, and removing material in the process.

A$_1$: Bead blasting chamber
A$_2$: Pedal throttles bead release
A$_3$: Comp. air accelerates beads
A$_4$: Nozzle (view A) ejects beads
B : Mating plates put in chamber
C : Metal spacers for extra height
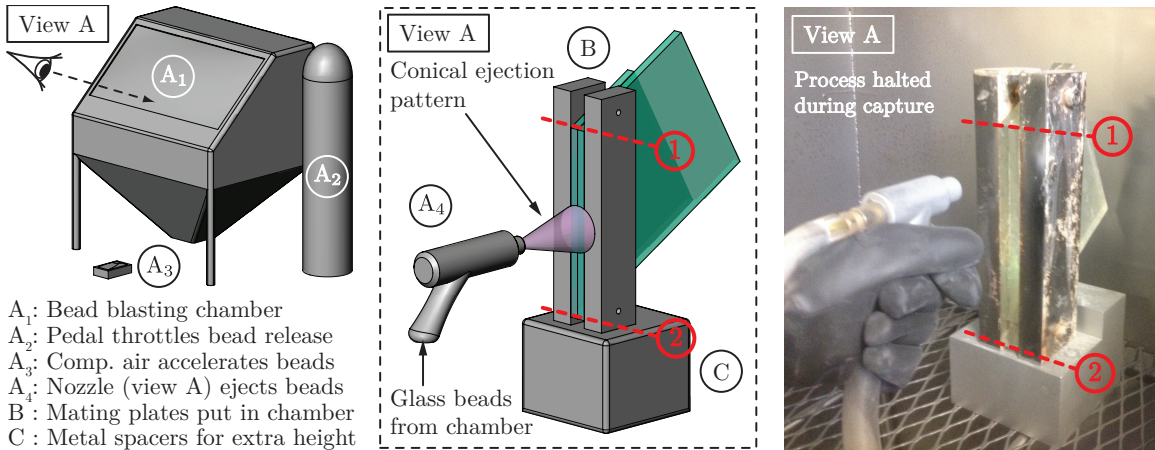
Figure 2.14: Bead blasting techniques roughen the polished interface surfaces. The steel rig (B) holding the hanging and foot wall plates is placed inside the bead blasting chamber (A$_1$). A compressor (A$_2$), throttled by a pedal (A$_3$), accelerates the glass beads out of a nozzle towards the polished interface surfaces (view A). Systematic procedures are followed to minimize spread in data.

The polished interface surfaces are repositioned into the steel rig and placed into the bead blasting chamber, where a systematic process is followed to uniformly roughen the surfaces (Figure 2.14). The plates are first washed, dried, and then replaced into the steel rig. Unlike during polishing, the steel rig and interface surface planes are coincident, $\delta = 0$, to assure through-thickness uniformity. Prior to use, the blasting chamber (Econoline$^{\copyright}$ DP 36-1) is cleaned from residual blast material by purging the hose and striking the chamber walls. A fresh batch of glass beads with diameters in the range of $104 - 211 \, \mu m$ are used in all experiments (McMaster Carr$^{\copyright}$ 70-140 mesh #3386K73). Surface profilometer measurements of the final bead-blasted interfaces obtained by similar surface treatment methodologies report an average roughness of about $R = 1.157 \, \mu m$ [55], as measured along the length of the interface. The steel rig is placed in the bead blasting chamber. A compressor is throttled by a pedal, accelerating and ejecting the glass beads towards the steel rig. The nozzle is maintained at an average distance of $\approx 5 - 7 \, cm$ from the steel rig and is always kept perpendicular. The nozzle moves up and down a total of 20 times, with each vertical stroke lasting a $5 \, s$ count. Edge effects of the interface are minimized by tilting the nozzle up/down during an up/down stroke to prevent prolonged blasting at any given edge; metal spacers help to achieve this rhythm. The steel rig is removed and washed with water to remove excess beads from the plates. Qualitatively, the surfaces are now opaque and feel rough to the touch (Figure 4.40 in Section 4.3). The study of Section 4.3 requires a minor procedural modification to leave a polished patch heterogeneity near the fault trace in attempts to arrest the up-dip rupture by increasing the frictional resistance.

2.2.1.4 Notch placement along interface

A square profile notch is machined through-thickness along the hanging wall frictional surface at a predetermined location $D = 74.3$ mm from the fault trace along dip (Figure 2.15). The notch is the origin of the ruptures and is representative of the event hypocenter in a natural earthquake.
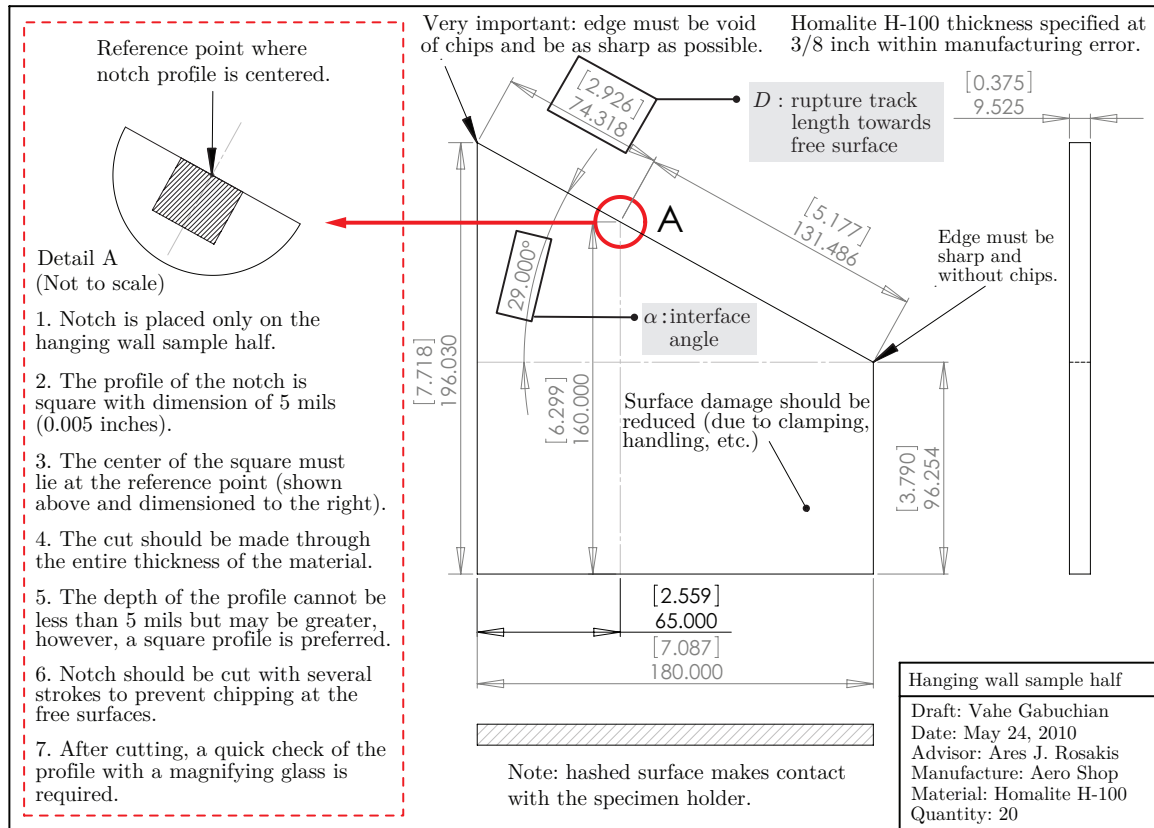
Figure 2.15: A square profile notch is machined through-thickness along the hanging wall interface surface at the location $(\bar{\zeta}_1, \bar{\zeta}_2) = (65, 200)$ mm, or $D = 74.3$ mm for an angle $\alpha = 29°$.

A hand-driven mill (Lagun Engineering$^{©}$ FTV-2 vertical mill) is used to remove material to create the notch, as shown in Figure 2.16. Contact with the interface surfaces is minimized to avoid damage. The protective coating is taken off during plate alignment with the instrument. A square profile notch of side length 127 µm is cut out through-thickness of the hanging wall interface surface at a distance $D = 74.3$ mm from the fault trace, as determined from the reflective wave calculations (Section 2.1.2). Right angles are maintained with the imaging surface, as shown in the photographs of Figure 2.16; oblique angles of the notch may cause significant three-dimensional effects of the rupture tip, especially at the nucleation site. The entry and exit rates of the mill should be sufficiently slow ($\approx 1/20$ m/s) to prevent chipping near the free surfaces (edges A and B, circled white). Previous tests were conducted where an identical paired notch was machined into the foot wall plate as well; however, matching the engravings on both plates is unpredictable and may be
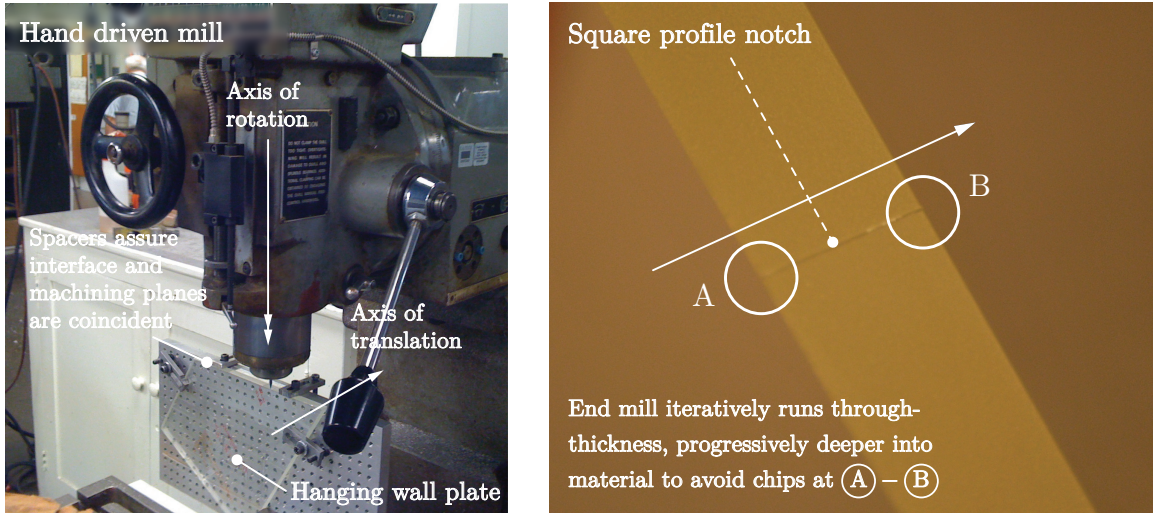
Figure 2.16: A hand-driven mill engraves the notch with decreased speeds near corners A and B.

more disruptive to repeatability of experiments since initial-time and near-source regions suffer the largest pressure gradients. The rupture nucleation process is discussed in Section 5.2.

2.2.1.5 Wire nucleation mechanism

A nickel chromium wire is embedded in the machined notch on the hanging wall plate. This wire bridges a high-Voltage capacitor bank which, when discharged, converts the filament to plasma and nucleates the rupture. The wire must be fully embedded in the channel to assure static stability.

The hanging and foot wall interfaces are thoroughly cleaned since no more machine processes remain. All protective covers are removed and all surfaces of the plates are washed with acetone and task wipes. Glass beads or other particles may have lodged themselves along the roughened interface surfaces, especially the notch engraving, requiring multiple wipes. Problematic spots can be removed with other solvents such as methanol, but acetone should be the final solvent used due to its hydrophilic nature and high vapor pressure. It is good practice to work with large soft task wipes to avoid introducing scratches to the imaging surfaces of the specimen.

A long piece of NiCr wire of diameter $79\,\mu\mathrm{m}$ (McMaster Carr$^{©}$ #8880K87) is stretched over the channel and held in place with tape on both sides of the plate. A gimbal arm is used to fix the plate's position during wire placement. A piece of tape is partially attached on each side of the plate, leaving portions of the tape unfastened. The wire is stretched over the channel and secured in place by fastening the remaining portions of the two tapes on each side of the plate over the wire; Figure 2.18 shows the tapes holding the wire in place (left and right panels). The wire must be fully embedded and not protruding above the interface surface to assure the hanging and foot wall plates statically hold; a fact simply ascertained with a magnifying glass. Pliers are used to pull the wire edges taught across the channel if adjustments are necessary; the excess wire will soon be helpful.

2.2.1.6 Retro-reflective tape markers

Retro-reflective tapes are placed on desired specimen locations and reflect Doppler-shifted light back to the velocimeter systems, which in turn decode the information and output a single component of ground motion velocity. The velocimeter systems and reflective tapes are robust at normal beam incidence onto the tape surface; however, grazing angle configurations require careful cutting and placement of the tapes onto the specimen for successful, uncorrupted measurements for $T_{\exp} = 120\,\mu s$.
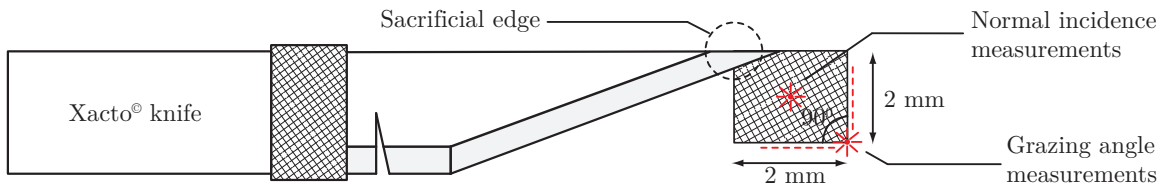
Figure 2.17: Normal incidence measurements occur at the large exposed area of the tape. Grazing angle measurements utilize the tape thickness and require an undamaged 90° corner.

A large sheet of reflective tape is cut down to smaller strips and then rectangles of $2\,mm \times 2\,mm$. The reflective tape (Polytec© #A-RET-S001) is made of glass beads with average radius on the order of $10\,\mu m$ attached to an adhesive backing. Cutting the surface removes these glass beads, reducing the reflective property of the tape and thus success of at-depth grazing angle measurement, which utilizes the thickness of the tape for back-reflections (Section 4.2); measurements made at normal incidence to the tape surface (Sections 4.1 and 4.3) are insensitive to the cutting method. Strips of width $\approx 2\,mm$ are cut by a single swipe of a razor edge; squares with side $\approx 2\,mm$ are then cut by placing the blade on top of the strip and firmly pushing down. Fresh, sharp blades are used to minimize damage to the reflective tape edges; it's best to restart from a fresh segment than to make fine adjustments which ultimately further damage that edge. Reflective tapes are taken off their backing and placed onto the specimen at marked locations. Measurement locations are determined with the use of a micrometer (Mitutoyo© calipers #500-465) and are marked on the specimen. Normal incidence measurements require tape placement at the marked location and enough surface exposed for the incident normal beam. Grazing angle measurements are more demanding and require a selection of a tape corner. An Xacto© knife is used to lift the corner of the tape while the razor holds down the tape backing (Figure 2.17). A corner is selected by holding up the $2\,mm \times 2\,mm$ square against light and selecting a 90° corner with perpendicular and straight edges, while avoiding the sacrificial regions of the tape used for positioning; this corner is placed on the marking.

The tapes must be firmly placed to avoid any dynamics caused by de-bonding of the tape. This must be carefully done by applying normal pressure onto the tape through a task wipe while avoiding any shearing motion. The sacrificial tape regions may be used for minor adjustments to the tape position and orientation. Beam focusing techniques are described in Section 2.2.3.2 and a discussion of possible measurement errors from tape placement are discussed in Section 5.5.

2.2.1.7 Specimen alignment in holder

The success and validity of experimental results hinge on the proper alignment of the hanging and foot wall plates within the specimen holder. Various alignment criteria are met to assure the specimen is vertical and the loading surfaces are parallel to prevent bowing under load.
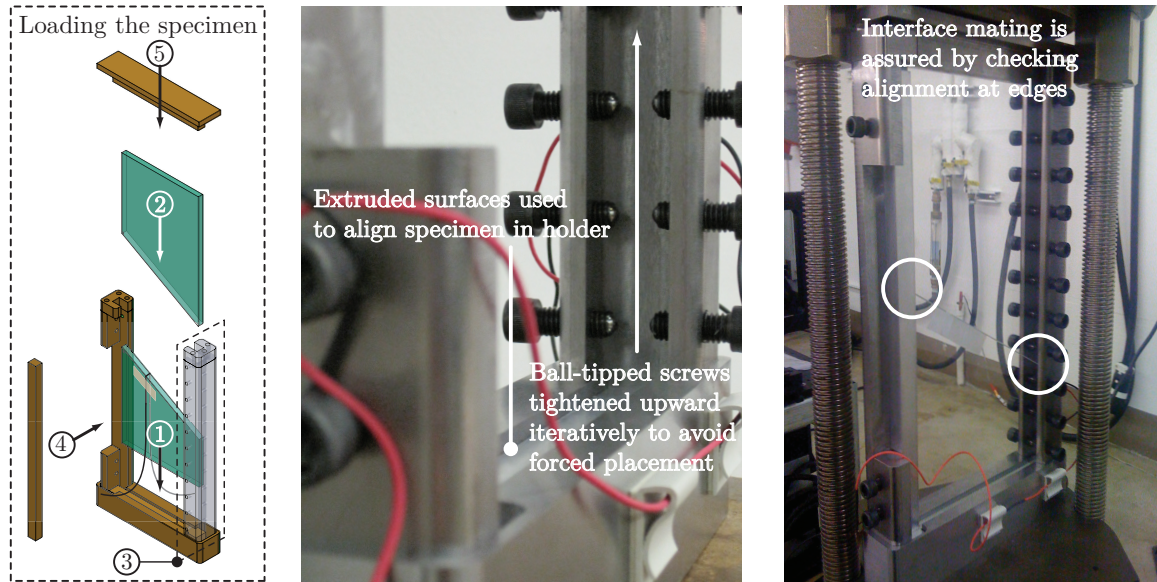
Figure 2.18: Various specimen holder features are used to align the hanging and foot wall plates in the holder. The left panel shows the loading order of the plates into the holder; the middle panel highlights holder features used for specimen alignment; the right panel shows the holder in the press with markers identifying key check points for alignment.

The hanging wall is inserted first into the holder, aligned, followed by the foot wall. The loading order of the plates into the holder is visually summarized in Figure 2.18 (left panel). Hanging and foot wall interface surfaces are wiped several times with acetone prior to mating. The ball-tipped screws are loosened to allow the hanging wall plate to be inserted from the top (number 1) and rested against the extruded portion of the specimen holder's base (callout in Figure 2.18, middle photograph). The ball-tipped screws are sequentially tightened from both sides just to the point of tangency with the hanging wall plate; the natural rest position of the plate should not be altered by the screws. The foot wall plate is inserted next, making sure the specimen edges match at the interface (number 2), which is best checked at the mating edges (white circles in the photograph). The simulated earth surfaces of the hanging and foot wall plates must be coplanar to assure no initial offset at the fault trace, a condition enforced during plate alignment. The remainder of the ball-tipped screws are tightened, fixing both the hanging and foot wall plates (number 3). The lateral confinement bar is inserted and its set screws are adjusted to stabilize the plates and maintain the zero offset at the fault trace (number 4); this bar is used during initial loading and is removed prior to measurement. The press is inserted on top of the foot wall, completing the assembly (number 5).

2.2.2 High-speed dynamic photo-elastic interferometry

The method of dynamic photo-elastic interferometry is used to generate a sequence of digital images that contain full-field information of maximum shear stress contour magnitudes, $|\tau_{\max}|$, as they evolve within the plate due to the rupture process. Laser light is treated and expanded to a collimated sheet of diameter $D_{\mathrm{fov}} \approx 145\,\mathrm{mm}$ (Figure 2.19), passed through the transparent specimen in the test section (Figure 2.20), and finally collected and captured with high-speed digital cameras (Figure 2.21). Chronologically ordering the images yields a movie of $|\tau_{\max}|$ evolution, as described in Section 3. The fundamental theory of photo-elasticity, summarized in Appendix B, shows how isochromatic fringe patterns are related to contours of $|\tau_{\max}|$, averaged through-thickness of the specimen. Initial alignment of the optics is discussed in Section 5.6, as it factors heavily in the quality of the images.

2.2.2.1 Photo-elasticity: light source

The light source table (Figure 2.19) generates a $D_{\mathrm{fov}} \approx 145\,\mathrm{mm}$ diameter collimated sheet of $532\,\mathrm{nm}$, in-phase, linear-polarized green laser light which passes through the specimen in the test section. Various optical components guide and control beam quality to achieve a uniformly expanded beam.

Photograph of source table in the laboratory

A$_1$: Laser head emits beam
A$_2$: Laser controller sets power output
A$_3$: Heat exchanger maintains temperature
B$_1$: Auxiliary power control: linear polarizer
B$_2$: Auxiliary power control: Glan-laser polarizer
C$_1$: Guiding optics: mirror elevates beam height
C$_2$: Guiding optics: mirror aligns beam to horizontal
C$_3$: Guiding optics: iris for initial beam alignment/check
D$_1$: Spatial filter cleans up the beam wave front (uniform)
D$_2$: Lens expands/collimates beam to $D_{\mathrm{fov}} \approx 145$ mm diameter

Expanded/collimated beam sent to the test section

Figure 2.19: Photo-elasticity; light source table. Laser light is guided and cleaned up prior to exiting the aperture of a telephoto lens as an expanded and collimated beam of light which is directed towards the test section (Figure 2.20). The optical components used to treat the beam are summarized from A-D and are pictured in the photograph insert.

A Coherent$^{\circledR}$ Verdi V-5 solid-state, continuous-wave, vertically polarized, 532 nm green-light laser is the emission source for the photo-elastic setup. It is composed of three components: the pump medium (Figure 2.19, A_1), the control deck (A_2), and the cooling system (A_3). Laser emission power settings up to $P_L = 0.25$ W are used for alignment, while the power range $P_L = 1.00 - 1.85$ W is used for image capture. Though most experiments are conducted at $P_L = 1.5$ W, deviations in alignment may require increased power output. To prevent damage to the camera CCDs, a maximum of $P_L = 1.85$ W is not exceeded. To stabilize the emitted beam, a chiller maintains a constant 293.15 K temperature of the laser head by recirculating fluid through a cooling block.

An auxiliary power control and guiding mirrors elevate the beam and direct it towards the cameras. A half-wave plate (Figure 2.19, B_1) paired with a Glan-laser polarizer/beam-dump assembly (B_2) provide a secondary control of the power output. A pair of optical-grade guiding mirrors (C_1 and C_2) elevate and angle the beam along the camera axis, directed towards the imaging table where the high-speed cameras rest and capture the collected light (Figure 2.21).

The spatial filter and lens clean the beam and expand it to a collimated sheet of $D_{\text{fov}} \approx 145$ mm. The spatial filter has a 15 μm pinhole with a 60× microscope objective lens that filters out higher spatial frequencies caused by optical component aberrations or source variations [114]. A white piece of paper is used to check the beam quality as it exits the telephoto lens (Canon$^{\circledR}$ 400 mm f/2). The degrees-of-freedom within the spatial filter and between the filter and lens are set such that a planar, linear-polarized, coherent light of uniform intensity is output from the lens. This condition is enforced to assure the polarization state and intensity is uniformly sensed by the specimen at every material point within the field-of-view. Section 5.6 discusses the initial alignment of source optics.

2.2.2.2 Photo-elasticity: test section

Photo-elastic interferometry is accomplished by passing the expanded and collimated laser beam through an arrangement of polarizers and the transparent test specimen aligned in the holder (Section 2.2.1.7). Figure 2.20 shows the laser beam and the following section describes the elements required to generate and image contours of $|\tau_{\text{max}}|$ within the field-of-view.

The collimated light enters a circular polarizer, a 150 mm × 150 mm sandwich structure of linear-polarizer and quarter-wave-plate (Figure 2.20, A), to produce circularly polarized light. The circularly polarized light passes through the compressed Homalite H-100 specimen in the press (B) and emerges as a distorted light field due to the anisotropic response of the material index refraction to applied stresses, e.g., optical birefringence. The perturbed light field is interfered by passing through the analyzer (C, an oppositely-oriented circular-polarizer) and collected to a point with a plano-convex lens of focal length $f = 1000$ mm (D). Convergence point of the beam is centered at the aperture of the field lens on the imaging table during initial setup of optics: this condition is maintained as needed to optimize the image quality (Figure 2.21). Decreasing the focal length of the
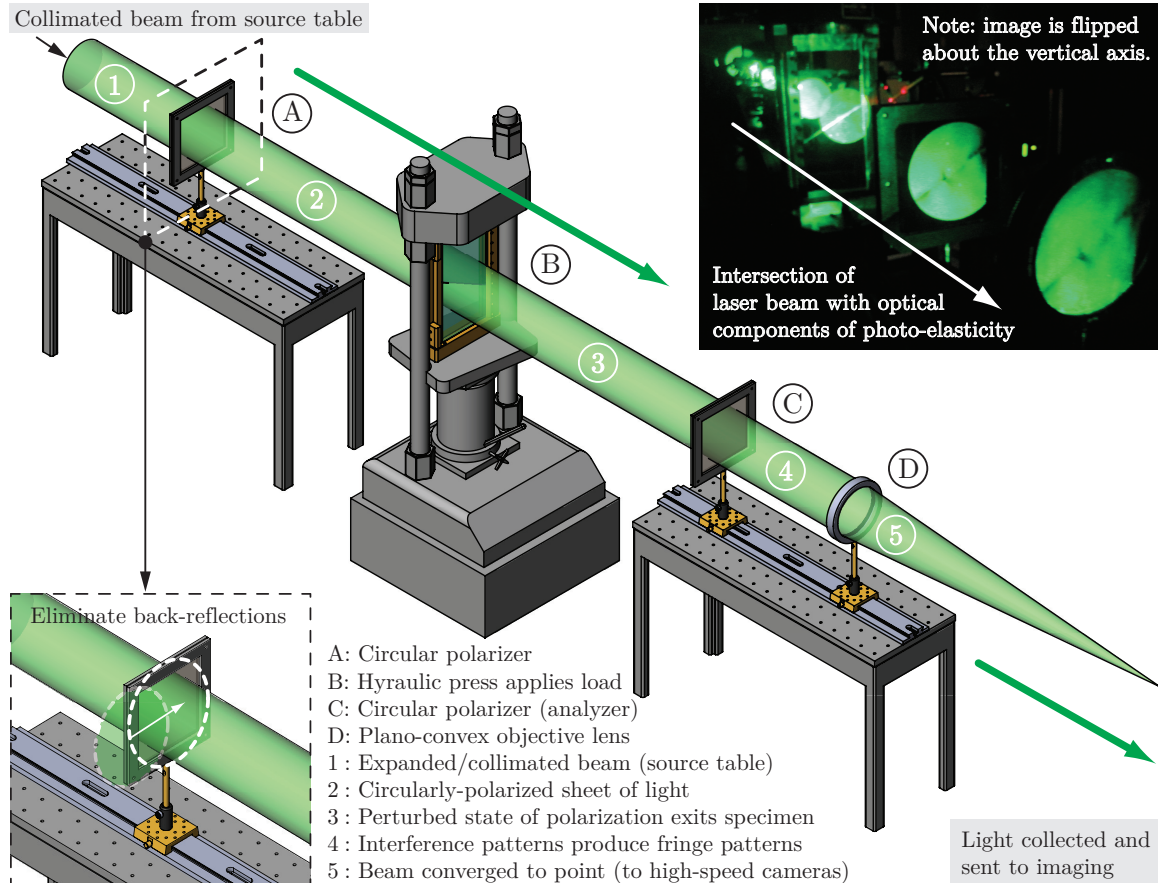
Figure 2.20: Photo-elasticity; test section. The specimen holder and specimen assembly is placed in a hydraulic press, aligned, and compressed to the desired initial static load, P. The expanded beam from the light source table (Figure 2.19) passes through the various optics of the photo-elasticity setup, including the transparent specimen, and is sent to the imaging station (Figure 2.21). Back reflections are eliminated to avoid horizontal skewing of images (left insert). The expanded beam is seen interacting with the various optical components of the setup (photograph insert).

objective lens increases the magnification of the imaging plane (co-planar with the specimen plate mid-plane), effectively zooming into a smaller region of interest on the plate.

The specimen holder is positioned in the hydraulic press (Carver$^{©}$ model #3925) such that the desired imaging region on the specimen is illuminated by the laser sheet: the field-of-view encompasses the entire up-dip portion of the fault from the hypocenter to the simulated earth surface. To avoid horizontal skewing of the images, the specimen holder is rotated in place until the back-reflections are eliminated on the upstream circular-polarizer (Figure 2.20, left insert). The focal distance from the imaging plane must match the mid-plane of the specimen for a well-defined, focused interface; this may require iterative imaging and re-positioning of the holder in the press. Once aligned, the specimen is loaded quasi-statically to a load of $\approx 1\,\mathrm{MPa}$. The lateral confinement bar is removed and the specimen is slowly loaded to its desired static initial value, P. A shadow test checks if the loading platen and holder press surfaces are parallel during loading; the orientation of

the hydraulic press top platen is adjusted until light disappears at the same time along the loading surfaces. For a successful experiment, it is important to check the alignment criteria of the hanging and foot wall plates within the holder (Section 2.2.1.7) as well as the alignment of the holder within the press. Several loading/unloading iterations may be needed to achieve uniform compression of the plates with no bowing; once in proper position, task wipes and acetone remove any fingerprints.

The electrodes of a capacitor bank bridge the embedded wire with two alligator clips. Once the specimen is under full load, one of the tapes holding the wire in place is removed and an alligator clip built into the holder is attached to the wire as close as possible to the specimen surface. The second tape is removed and the remaining alligator clip is similarly attached on the opposite side of the specimen. All excess wire is removed to prevent long-duration phase transformations that will illuminate and over-expose large portions of the images. The alligator clips are sanded down thoroughly to remove wire deposits before gripping the wire. A BNC cable delivers a high-Voltage signal across the two alligator clips, triggering the dynamic rupture (Section 2.2.4).

2.2.2.3 Photo-elasticity: imaging

High-speed digital cameras capture a total of 16 frames at user-defined inter-frame times. Collected light information is split and sent to each camera with an array of field lenses and a non-polarizing beamsplitter. The cameras rest on vertical stages which in turn rest on an adjustable table (Figure 2.21). These degrees-of-freedom with appropriately resolved actuation are integral to quality images.

A_1: High-speed digital camera (frames 1-8)
A_2: High-speed digital camera (frames 9-16)
B_1: Field lenses (x3) direct light into cameras
B_2: Non-polarizing (50/50) beamsplitter cube
C : Table with multiple degrees-of-freedom
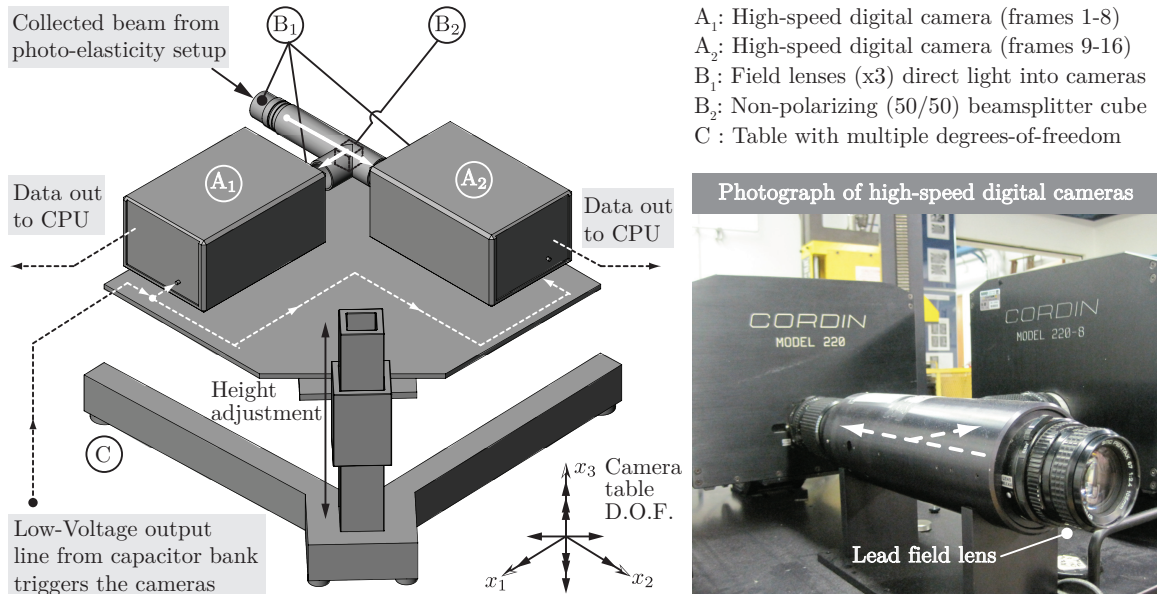
Figure 2.21: Photo-elasticity; imaging. Two high-speed cameras capture 16 frames of $|\tau_{\max}|$ contours averaged through the specimen thickness at user defined inter-frame times up to 100 million f.p.s. Degrees-of-freedom built into the optical table allow for fine adjustments in the leading field lens orientation (right panel); centering the collected light onto the lens at normal incidence is key to quality imaging. A Voltage signal from the control table (Figure 2.26) triggers the camera system.

Two Cordin$^{\copyright}$ model 220 gated-intensified digital cameras (Figure 2.21, B_1 and B_2) capable of frame rates up to 100 million f.p.s. are used to image $|\tau_{\mathrm{max}}|$ in the field-of-view during the dynamic event. The cameras are capable of such high frame rates because of the gated-intensified technology. Photons are first captured on an intermediate plane which emits electrons; the electrons are accelerated in a micro-channel-plate (MCP), and strike another plane which emits photons, and these photons are captured by CCDs, one per frame. The nanosecond switch capability of these devices allows the system to operate at nanosecond shutter speeds with minimal light. Each camera gives a total of 8 images, which together make a total of 16 monochrome digital images at user-defined inter-frame times. The low frame count is a cost paid for the high shutter speed. The cameras are set to 50 ns exposure times, more than sufficient to prevent motion blur for experimental speeds on the order of 1 mm/µs. Fringe patterns from a statically loaded specimen are used to optimize the quality of each frame and increase the contrast as much as possible prior to running an experiment. For a given laser power, the gains of each CCD are adjusted with a control program until uniform-quality images are obtained. The cameras are triggered by an oscilloscope, as discussed in Section 2.2.4.

Adjustments of appropriate degrees-of-freedom provide the best quality images. The camera table has four degrees-of-freedom that are used to place the converged laser light at the center of the lead field lens (Figure 2.21, A_1, photographed in the right panel). A removable reflective lens cap is used while the table is lifted vertically, tilted, and rotated to center the focused beam on the leading field lens. The beam axis and the lens array axis must also be collinear. The focused beam is split by a 50/50 non-polarizing beamsplitter cube and sent to each camera, which has its own field lens. Test images showing acceptable images in one camera but unacceptable ones in the other can be improved by adjusting the height of the problematic camera independently. Vignetting of the circular field-of-view occurs during extreme vertical adjustments and should be avoided. Quality images stem from proper initial alignment of the optics, as discussed in Section 5.6.

2.2.3   Laser velocimeter traces

Heterodyne laser velocimeter systems are used to record velocity components at various points on the specimen. Each system consists of a controller (Figure 2.22, A_1), which decodes and records a velocity series, as well as a sensor head (A_2), which houses the interferometer optics. Fiber-optic wires from the sensor heads are held in position with an appropriate combination of manual actuators (B), orienting and focusing the beams to record the desired velocity components (see Section 2.2.3.2).

2.2.3.1   Heterodyne laser velocimetry

Polytec$^{\copyright}$ heterodyne laser velocimeter systems are used to measure the particle velocity signals. A block diagram of the system is shown in Figure 2.23. The components are segmented into the sensor head (Polytec$^{\copyright}$ OFV-511 and OFV-551, top panel) and the controller (Polytec$^{\copyright}$ OFV-5000
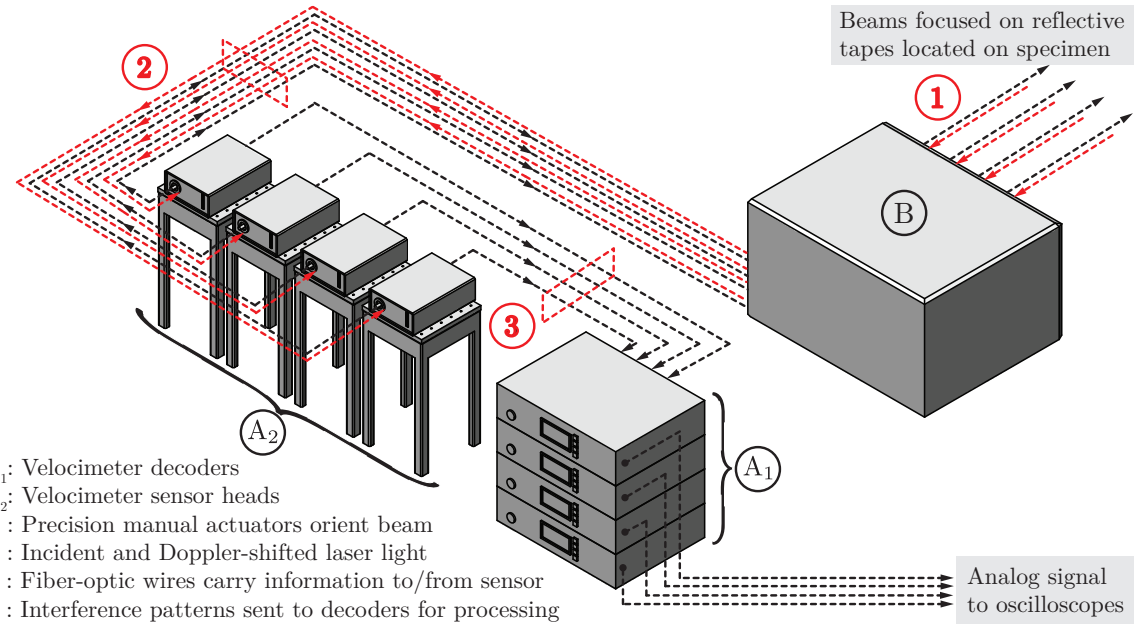
Figure 2.22: Heterodyne laser velocimeters are used to record a time series for a single component of velocity. Each system consists of a controller (A_1) and a paired sensor head (A_2). Various configurations of manual actuators and adjustment screws (B) (minimum of 100 t.p.i.) orient the fiber-optic heads in space for the desired measurement. Doppler-shifted light reflects back from a moving surface and is sent to the system for processing/conversion to a velocity-time series in Volts.

VD-02 and VD-09, bottom panel). The optical components in the sensor head operate on the light and record intensities on a detector. These intensities are sent to the decoder, which converts the intensity signal and outputs an analog Voltage signal for measurement.

The interference of a reference beam and Doppler-shifted reflected light in the sensor head produces a time-varying intensity signal (Figure 2.23, top panel) that is recorded and sent to a decoder for processing [105]. A HeNe laser is split into a reference beam and the test beam. The test beam gets sent through a fiber-optic cable attached to a coupler. This cable emits light onto the reflective tapes and receives Doppler-shifted light depending on the motions of the object being measured. The reference beam path contains a Bragg cell to remove ambiguity in motion directionality, since a fringe count in itself does not yield information about direction [115]. The Doppler-shifted and reference beams are interfered and recorded on a detector. Misalignment of the system optics can cause erroneous measurements, therefore the system should be calibrated and static during operation.

The controller (Figure 2.23, bottom panel) receives an intensity signal from the senor head and converts the signal to a velocity time series [116], which is sent to an oscilloscope (Tektronix$^{©}$ DPO-3034). The signals are immediately passed through a high-frequency signal conditioning block. A choice of decoder in the controller settings can either output velocity or displacements directly; however, the former is chosen for all experiments. A low-pass analog filter with a cut-off frequency of 1.5 MHz removes most of the noise in the signals and sends the Voltage data to the oscilloscopes.
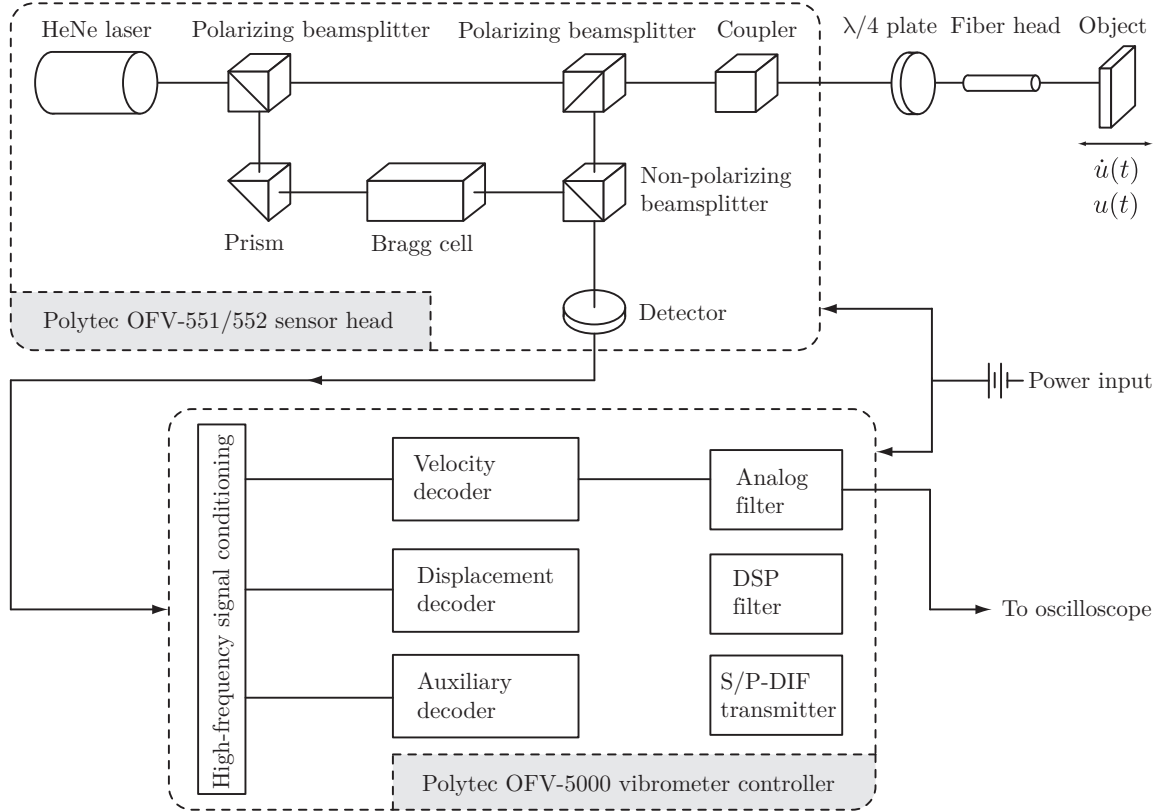
Figure 2.23: Block diagram of the velocimeter sensor head and controller. The sensor head components interfere a reference beam with the Doppler-shifted light reflected from a moving surface. A built-in Bragg cell eliminates directional ambiguity during fringe counting. A detector converts the intensity signal to digital information that is processed in the controller. Data is converted to an analog signal and recorded in time as a Voltage.

The receiving ports of the oscilloscopes should have a $1\,\text{M}\Omega$ impedance for proper data acquisition. The velocimeter systems provide velocity measurements up to $\pm 10\,\text{m/s}$ (positive towards sensor, negative away from the sensor) with resolution limits of $0.15\,\mu\text{m/s}$ and $0.02\,\mu\text{m/s}$ for VD-02 and VD-09 decoders, respectively [117]. Conversion factors at these sampling rates are $1\,\text{V} = 1\,\text{m/s}$.

2.2.3.2   Beam focusing onto reflective tapes

The success of ground motion measurements relies on the quantity, arrangement, and resolution of various degrees-of-freedom that must be used collectively to position and orient the beam appropriately onto the reflective tape. Spatial restrictions due to setup introduce cosine errors in beam approach angles, which are maintained under $\approx 5°$ across all measurements.

The logic of beam placement is summarized in Figure 2.24. Progressing from the fixed laboratory frame, A, to the fiber-optic terminus, D, translational and rotational degrees-of-freedom are sequentially added to the system with various stages and posts. Both coarse and fine resolutions of motion allow initial placement of structure in the test section as well as final adjustments of

A: Mounting point to optics table with coarse and fine degrees of freedom
B: Vertical and horizontal extensions for coarse placement
C: Fine adjustments with multiple degrees-of-freedom
D: Fiber-optic terminus and beam focus

Coarse adjustments
Fine adjustments

Beam focus

Corner turn

Normal measurements use main tape surface

Retro-reflective tape has glass beads on adhesive backing

Grazing angle measurements utilize tape thickness

Figure 2.24: Coarse and fine adjustments of multiple degrees-of-freedom focus and orient the laser beam onto the reflective tape (models courtesy of Newport Corporation); beam end-effector may be the fiber-optic terminus or a 90° corner; the insert describes normal and grazing angle measurements.

beam termini with actuators of at least 100 t.p.i. specifications (a full turn results in displacement of about 250 μm). Multi-point measurements confined to a small region on the specimen pose arrangement issues due to the size of the stages, and thus various horizontal and vertical extensions are required to place the fiber-optic termini yet closer to the measurement surface. A three-beam setup utilized in earth surface-normal measurements (Section 4.1 and 4.3) exemplifies the spatial restrictions (Figure 2.25). Mounting the fiber-optic termini on multi-axis optical stages with translation and tilt control positions and orients the velocimeter beams onto the reflective tapes. Angled (90°) termini are utilized to place the beam emission points as close as possible to minimize cosine errors. The right photograph in Figure 2.24 is from the specimen point-of-view, showing vertical and horizontal offsets between the emission points. Stand-off distances and vertical/horizontal offsets estimate the grazing angles to about $\approx 5°$. Cosine errors are constrained to within this value for all measurements, thus rendering these errors negligible. In practice, setup is most easily accomplished by working backwards from the desired beam position to the required positioning components.

Reflective tape edges and corners are used to maximize accuracy of station location. Once the orientation of the beam is appropriately set for the desired measurement, independent axes of motion with fine control are used to approach the beam towards an edge or a corner of the tape. Edges and corners of tapes are utilized since reflected laser light from the tape makes it difficult to determine the spot location on the tape, and furthermore, corners are used to mark and check the placement with a micrometer during specimen mark-up. Stand-off distances from the emitted beams to the tapes never surpass 300 mm, giving spot sizes ≈ 150 μm for a well-focused beam as per manufacturer specifications [118]. Gages on the velocimeter systems measuring back-reflectance indicate when the
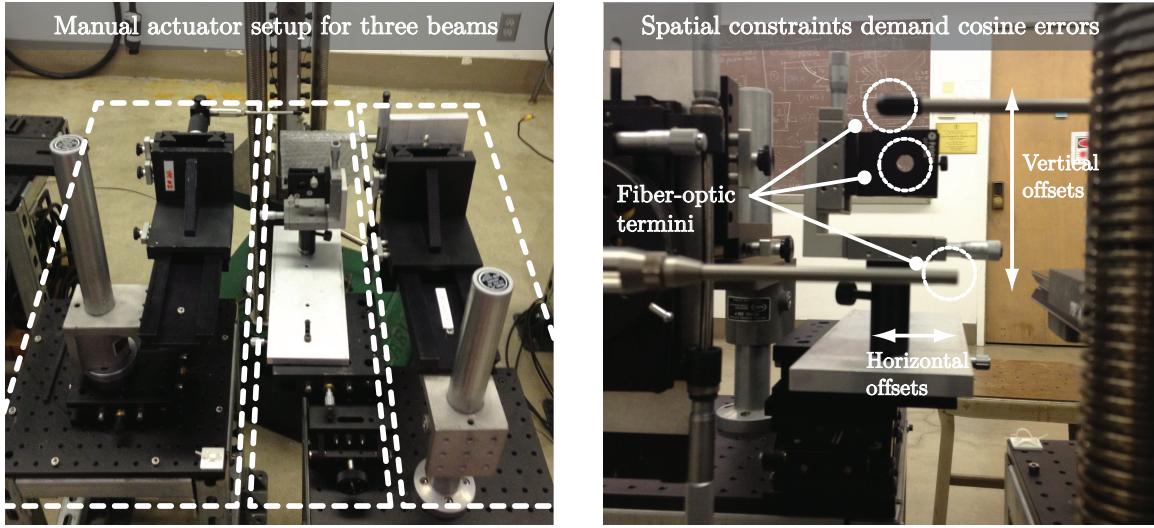
Figure 2.25: Photographs of a three-beam setup showing tandem use of coarse and fine adjustments to orient beam termini. The specimen's perspective (right photograph) shows that spatial restrictions require cosine errors, maintained within $\approx 5°$ across all data.

spot hits the edge or corner of the tape, thus fixing the beam termini for measurements with highest possible accuracy of station location. The Eulerian nature of the measurements requires certain additional caveats (Appendix A), such as stand-off distances between the tape and specimen edges for fault trace and on-fault measurements at-depth, as discussed in Section 4.1 and 4.2, respectively.

2.2.4   Trigger of dynamic event and diagnostics

Trigger of the dynamic rupture, synchronization of both experimental diagnostics, and data storage are shown in Figure 2.26 and are discussed in the following section. Discharging a capacitor bank sends a high-Voltage signal to the embedded wire in the notch as well as an attenuated signal to trigger the diagnostics. Oscilloscopes capture the velocity time series from the velocimeters while a computer stores the photo-elastic images from the cameras.

2.2.4.1   High-voltage capacitor bank

Upon discharge, the capacitor bank sends a high-Voltage signal to the wire embedded in the notch of the mated specimens and an attenuated signal to the oscilloscopes, triggering the dynamic rupture and both diagnostics, synchronizing the entire experiment.

The high-Voltage line from the capacitor converts the wire embedded in the notch into plasma and triggers the dynamic event. The capacitor is an RLC circuit with a calibrated potentiometer that allows the output discharge Voltage to be selected; a setting of 42 outputs 1.6 kV. The capacitor is charged for 5 minutes. Upon discharge, a BNC cable sends 1.6 kV through the embedded NiCr wire, immediately converting the filament to plasma. Local large pressure gradients develop at the

A: High-voltage
  to NiCr on specimen
B: Low-voltage to oscilloscopes
  (triggers capture of velocity data)
C: Output from velocimeters (x4)
D: Scope triggers digital cameras
E: High-speed digital camera data
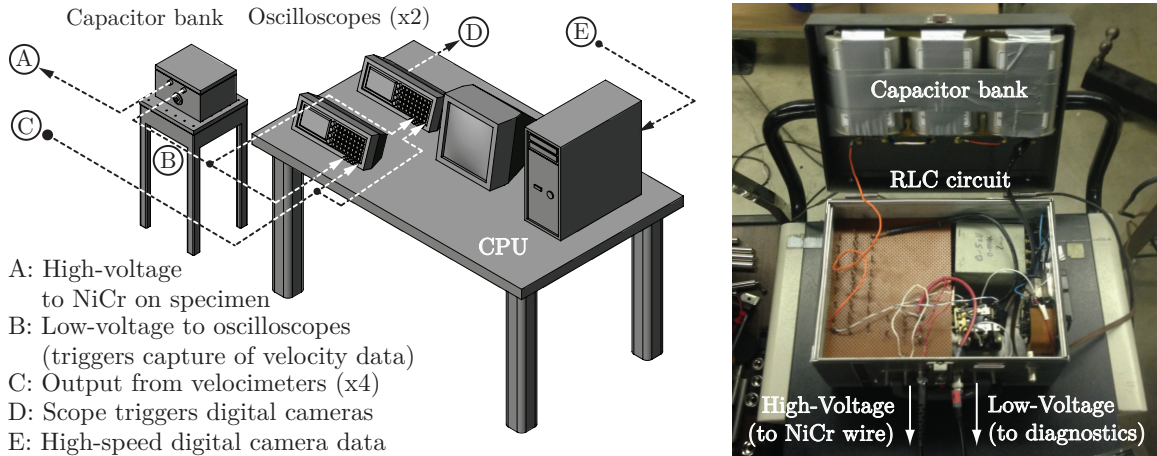
Figure 2.26: The control table triggers the dynamic event as well as synchronizes the digital camera and velocimeter diagnostics. A capacitor bank discharges $1.6\,\mathrm{kV}$ across the embedded wire between the pre-loaded hanging and foot wall plates, initiating the dynamic event. An attenuated low-Voltage signal triggers the oscilloscopes, which in turn trigger the digital camera system.

notch and push against the compressive normal stresses holding the interface closed. This temporary local opening extends bi-directionally along the interface away from the notch, depositing soot along the interface. The total length of this soot pattern, L_{soot}, is measured post-experiment. Together with soot deposits, on-fault measurements near the hypocenter imply a complex mixture of local fault opening and shear strength reduction during nucleation (further described in Section 5.2).

An attenuated signal line from the capacitor bank triggers both velocimeter and digital camera diagnostics. The low-Voltage signal triggers the oscilloscope with a sharp peak corresponding to the delivery time of $1.6\,\mathrm{kV}$ to the wire. The trigger channel on the oscilloscope is set to an $8\,\mathrm{V}$ edge-rise criteria with an impedance of $50\,\Omega$. These settings assure that erratic signal behavior prior to the trigger peak does not accidentally trigger the diagnostics and miss the dynamic event (levels below $2\,\mathrm{V}$ are avoided). Up to four channels of velocity components are recorded in a given experiment ($1\,\mathrm{M\Omega}$ impedance). At the same time, the oscilloscope triggers the digital cameras. The low and high-Voltage lines zero the experimental time and induce the mechanical event. The difference between these times, t_{dyn}, is accounted for in the timing calculations of Sections 4.1.1 and 4.2.1.

Dynamic waves cease in several seconds after experiment trigger. Velocity series and camera images are recorded and processed up to $T_{\mathrm{exp}} = 120\,\mu\mathrm{s}$ as the primary data of the experiment. The final load, P_{f}, is recorded to determine stress drop, $\Delta\sigma = P_{\mathrm{f}} - P$. The final free surface-normal offset between the hanging and foot wall plates is measured at the fault trace, $u_2^{\mathrm{offset}} = u_2(+\epsilon, 0, t) - u_2(-\epsilon, 0, t)$, where $\epsilon \to 0$ and $t \to \infty$. The wire soot deposit length, L_{soot}, is also recorded. A set of post-experiment static images are taken with an object of known dimensions attached to the specimen for a conversion factor between logical length to pixels. The camera and laser shutter are kept closed and the capacitor is disengaged to prevent accidental electric shock.

Chapter 3

Data Reduction and Analysis

The spatially-resolved photo-elastic images and the temporally-resolved velocity time series are used synergistically in the study of thrust faults. Merging these two data types yields an image/trace sequence that shows how various features within the material bulk affect ground motions measured at various points on the plate. The left and right paths in Figure 3.1 summarize the post-processing of images and velocimeter traces, respectively; spread in values is discussed in Chapter 5.
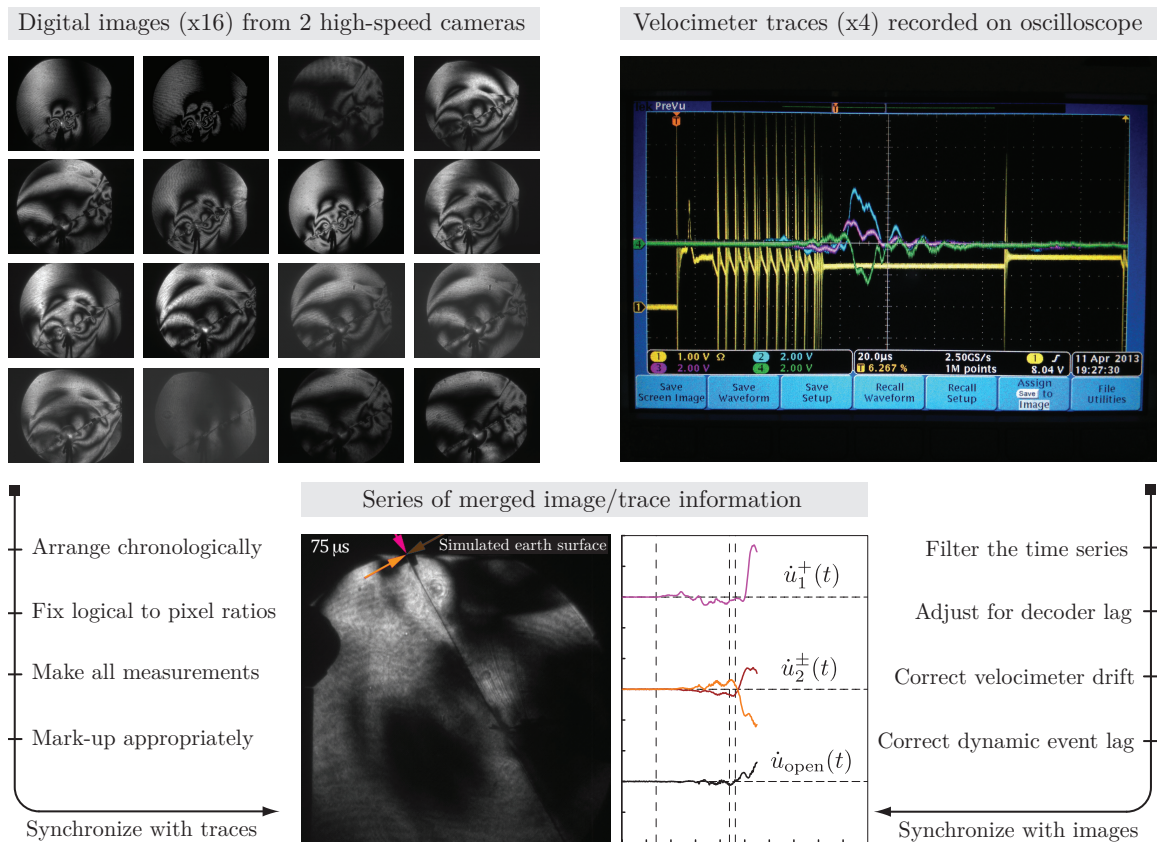
Figure 3.1: Data analysis summary; processing steps of the digital photographs and the velocimeter data are shown in the left and right paths, respectively. Each experimental data set follows the same reduction procedures and generates an image/trace sequence used to study the dynamic event.

3.1 Measurements from images
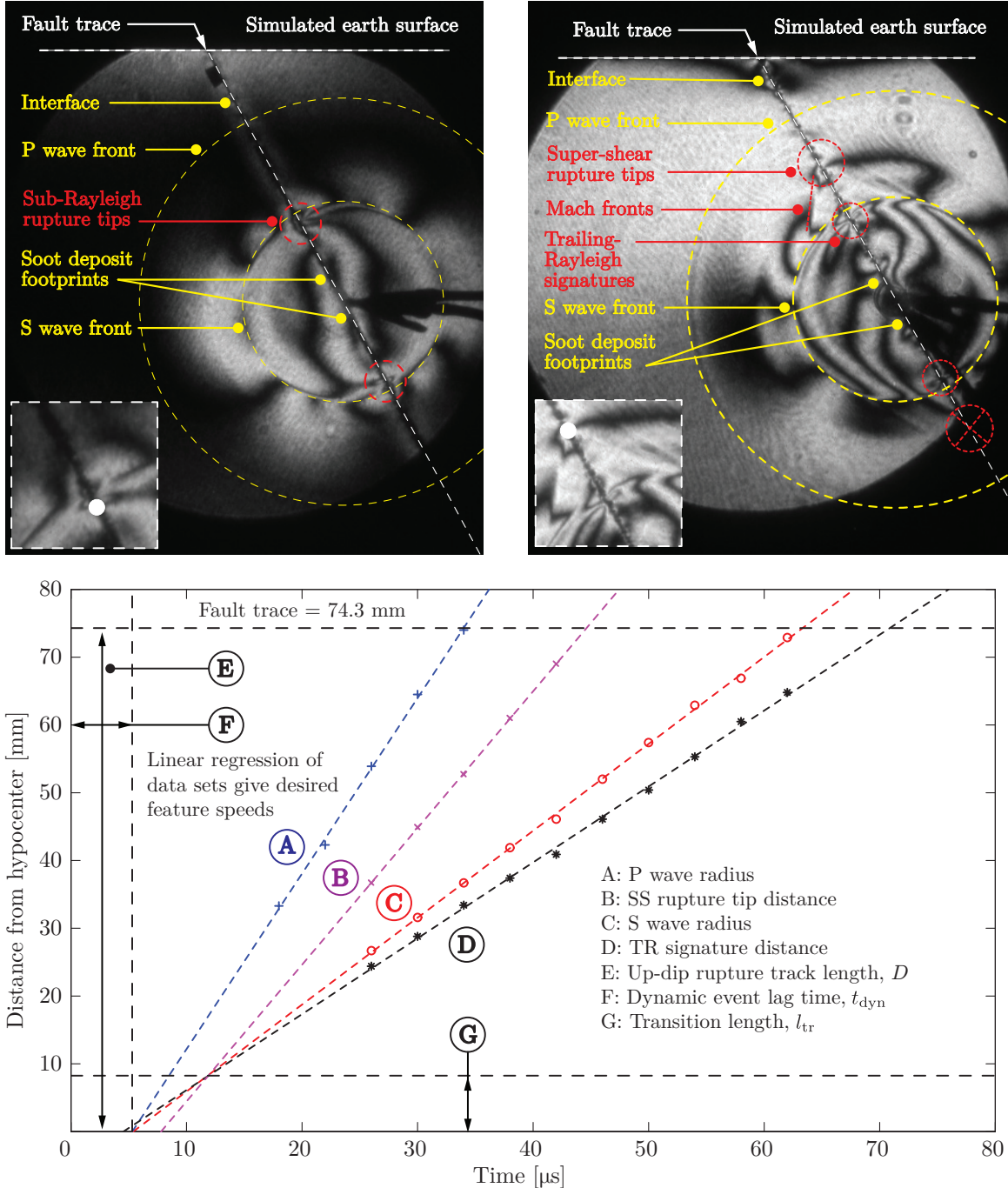
Figure 3.2: Direct measurements from photo-elastic images. A photograph during a sub-Rayleigh (SR) and a super-shear (SS) event are shown in the left and right panels, respectively. Inserts identify the fringe patterns associated with the SR and SS rupture tips. Markers identify various features of the rupture. The bottom figure summarizes all direct and derived measurements obtained from the images, including the P wave speed, c_{p}, S wave speed, c_{s}, SR rupture speed, $v_{\mathrm{r}}^{\mathrm{SR}}$ (or the trailing-Rayleigh signature in case of SS ruptures, v^{TR}), and the SS rupture speed, $v_{\mathrm{r}}^{\mathrm{SS}}$. Intersection of various waves graphically determines the dynamic event lag time, t_{dyn}, and transition length, l_{tr}.

Figure 3.2 summarizes the various photo-elastic signatures that are directly measured from the images, namely the wave speeds, c_p and c_s, and the sub-Rayleigh (SR) and super-shear (SS) rupture tip speeds, v_r^{SR} and v_r^{SS}. The bottom panel of Figure 3.2 plots the distance from the hypocenter along $\hat{x}_1'$ against time for the P wave (A), SS rupture tip speed (B), S wave (C), and the trailing-Rayleigh (TR) signature (D, a feature with nearly identical speeds as the SR rupture present only in SS ruptures as remnants of the initial crack tip). The isochromatic fringe patterns are related to $|\tau_{max}|$, as averaged through-thickness of the material (see Appendix B). The transition length to SS speeds is calculated using multiple appropriate images; Section 3.1.4 describes this method.

Prior to making measurements, the images are arranged in chronological order and given a pixel to logical length conversion ratio. A sequence of images is taken post-experiment with a reference length marker; this marker is used to determine a pixel to logical length ratio for each frame, since minor variations in the placement of optics within the cameras gives slight scale mismatch across frames. The measurement reference point is the notch (hypocenter) which is found by reducing best-fit circles around the S wave front to zero radius. Several iterations are performed until the reference point is set. The images are marked up appropriately by placing timing as well as station markers and component directions for cross-referencing with velocimeter data.

3.1.1 P and S wave velocity

The P and S wave radii are measured from the hypocenter by finding the best fit circle about the wave fronts. Since the technique of photo-elasticity is sensitive to shear, S wave fronts are well defined while P wave fronts are usually faint. A best-fit circle is drawn around the initial S wave front in every image to determine the hypocenter of the rupture. Several iterations make sure this center is accurately determined since all other measurements are referenced from here. The initial P wave is only visible for short times up to $\approx 40\,\mu s$, usually with a faint fringe front since the particle motion is dilatational; three-dimensional effects of the specimen apply transverse shear components through-thickness of the plate with the arrival of the P wave front and allows visualization with photo-elasticity. A linear regression of P and S wave data gives the wave speeds (slopes), which are reported to be $c_p = 2.59(8)\,\mathrm{mm/\mu s}$ and $c_s = 1.27(2)\,\mathrm{mm/\mu s}$ from a set of experiments (Section 5.1). P and S wave best-fit lines converge and cross the ordinate at nearly the same point when extrapolated towards the hypocenter. The zero of the S wave line graphically defines the time, t_{dyn}.

The P and S wave speeds are verified using dilatational and shear transducers (Figure 3.3). A signal generator in pulse/echo mode sends a periodic signal to either dilatational or shear transducers pressed against the surface of the Homalite H-100 plate (photograph insert). The surface contact quality determines the quality of measurement, and thus acetone is used to wipe the surface and honey is used to mate the transducer and Homalite plates. Measuring the difference in incident and reflected arrival times for P and S waves, $\Delta t_{p,s}$, and using $c_{p,s} = 2t/\Delta t_{p,s}$ with $t = 9.52\,\mathrm{mm}$
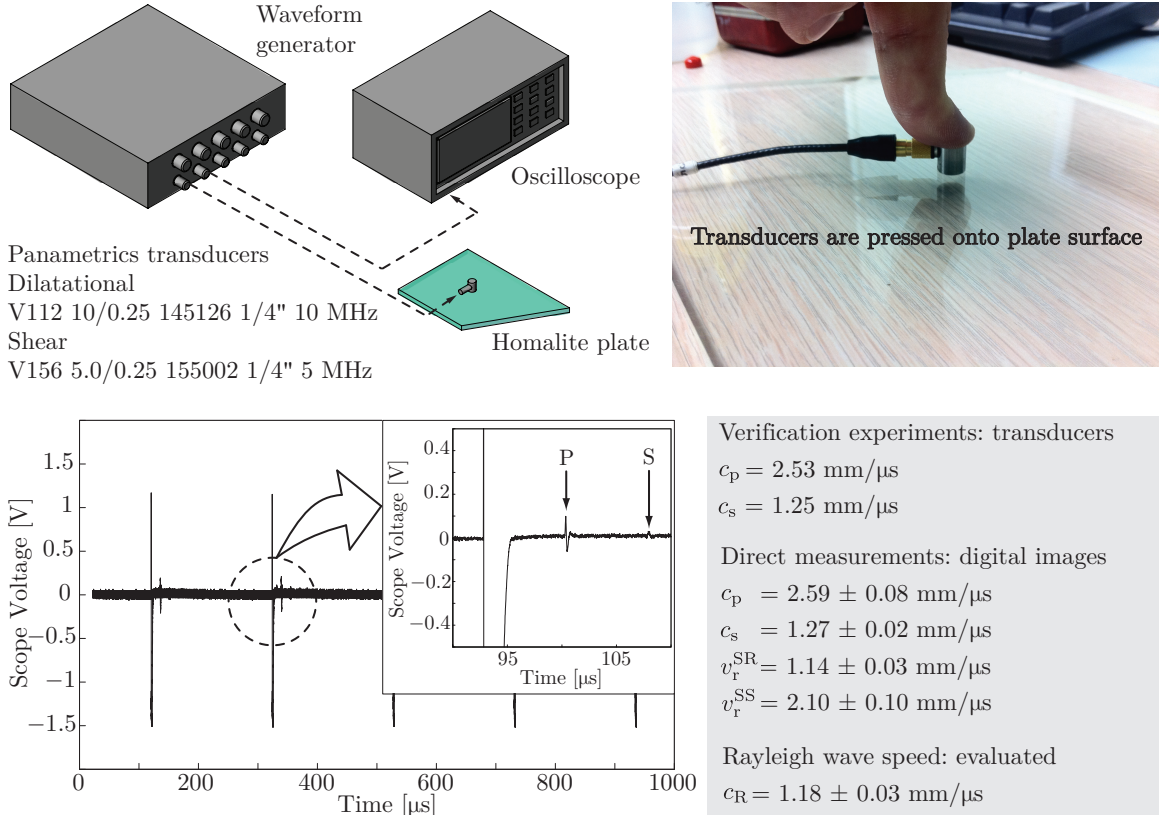
Figure 3.3: Homalite wave speed verification tests using dilatational and shear transducers. A waveform generator operating in pulse/echo mode sends dilatational and shear waves through the thickness of the specimen and captures motions of the reflected information from the opposing surface. Measured wave speeds are within $0.05\,\text{mm/µs}$ of those obtained from photo-elastic images.

yields speeds $c_\text{p} = 2.53\,\text{mm/µs}$ and $c_\text{s} = 1.25\,\text{mm/µs}$. Measurement with the transducers are within $0.05\,\text{mm/µs}$ of values measured from the photo-elastic images. As expected, the verification tests underestimate the wave speeds since inertial effects are relatively absent in the transducer tests.

3.1.2 Sub-Rayleigh and super-shear rupture tip speeds

The SR and SS rupture tip speeds are measured as they propagate along the interface causing the locked material ahead to slip. In the case of a SR rupture, a double-lobed fringe pattern crossing the interface represents the stress concentration associated with the rupture tip (Figure 3.2, left photograph insert). The intersection width of this feature with the interface is on the order of $\approx 2\,\text{mm}$, and is usually distinct and easy to identify. The rupture tip location is measured mid-thickness of this feature. A linear regression of the data gives the SR rupture tip speed as $v_\text{r}^\text{SR} = 1.14(3)\,\text{mm/µs}$ averaged over 50 experiments. These values are about $89\,to\,92\%$ of the Rayleigh wave speed of the material, calculated for plane-stress to be $c_\text{R} = 1.18(3)\,\text{mm/µs}$. In case of SS transition, this double-lobed fringe pattern is still present as the remnant of the original rupture;

this is called the trailing-Rayleigh (TR) signature, v^{TR}, since it is not a rupture tip but a stress concentration. Extrapolating this line towards the hypocenter (Figure 3.2, bottom panel) shows that the P wave, S wave, and the SR rupture tip all converge to the same point; this is to be expected, since these features are generated simultaneously at the hypocenter during nucleation.

The SS rupture tips are located at the vertices of Mach cones. The Mach cone in Homalite is analogous to a shock wave in a fluid. The superposition of shear waves emitted during rupture propagation at SS speeds ($c_{\mathrm{s}} \leq v_{\mathrm{r}}^{\mathrm{SS}} \leq c_{\mathrm{p}}$) results in the shear Mach cone. The Mach fronts in the hanging and foot wall plates converge to a point intersecting the interface, defining the SS rupture tip position (Figure 3.2, right photograph insert). These values are similarly plotted and a linear regression shows the speeds to be in the range $v_{\mathrm{r}}^{\mathrm{SS}} = 2.10(10)\,\mathrm{mm/\mu s}$. SS rupture tip speeds can also be determined by the Mach-angle relationship, $v_{\mathrm{r}}^{\mathrm{SS}} = c_{\mathrm{s}}/\sin\beta$, where β is the angle between the interface and Mach fronts. Speeds based on angles β are close to those measured with the regression and do not show much asymmetry between the hanging (+) and foot wall (−) plates ($\beta^{+} \approx \beta^{-}$). The distance at which the S wave and SS rupture tip best-fit lines intersect defines the transition length, l_{tr}, which is the distance along the interface where transition to SS occurs (Section 3.1.4).

3.1.3 Dynamic event lag time

The time delay between the trigger of the diagnostics and the commencement of dynamic rupture propagation is defined as t_{dyn} and must be factored into the data reduction. This value is determined by the intersection of the ordinate and the best-fit curve for the S wave (Figure 3.2, bottom panel).

The discharge of the capacitor marks the zero time for the diagnostics; however, it takes an average of $\approx 5\,\mathrm{\mu s}$ for wire nucleation to act on the surrounding material and induce dynamic propagation of the rupture tip. The duration of pressure increase on the material until a mixed-mode rupture may dynamically propagate is defined as t_{dyn}, and graphically represented by the vertical line F in Figure 3.2. Finite time is required to generate a mechanical response from an electrical signal. The nucleation process and its effects are discussed in terms of soot length, L_{soot}, and dynamic event lag time, t_{dyn}, in Section 5.2. These values are taken into account when generating timing curves for various waves to measurement stations and provide insight into the rupture nucleation process.

3.1.4 Transition length

Photo-elastic images provide information about the transition lengths of SS ruptures; however, the low frame count of the digital cameras make it difficult to capture an image when the rupture is exactly at the transition point. The following derives a method to estimate the transition length given any image at a time T_1 after the time of transition, T_0, where $T_1 > T_0$. Performing this calculation for every image captured after transition and averaging the results determines l_{tr}.
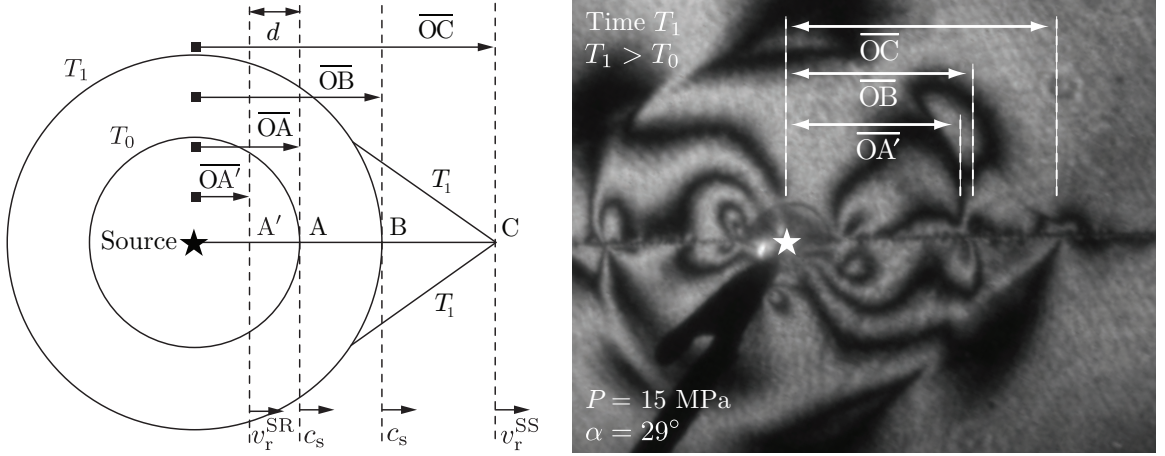
Figure 3.4: Transition length calculations from photo-elastic images. The paired schematic and photograph show the various distances required to determine the transition length, l_{tr}, as an averaged value across all applicable images at times $T_1 > T_0$, where T_0 signifies the rupture transition time.

The geometry in Figure 3.4 sets up the problem. Two shear wave fronts, one at time T_0 and the other at T_1, are marked by the S wave speed, c_{s}. The rupture tip speed prior to transition is given by v_{r}^{SR} and the rupture speed after transition is given by v_{r}^{SS}. The derivation uses the various lengths defined in the figure to solve for the time when transition occurs, T_0. Multiplying T_0 by an appropriate speed yields the transition length, l_{tr}. Two cases of transition location are considered following two proposed physical transition mechanisms.

Case I: transition occurs at pile up of shear waves

In the first mechanism, it is assumed that transition happens as described by the Burridge-Andrews mechanism [66, 67]. In this mechanism, the pile up of shear waves just ahead of the original SR crack become strong enough to outweigh frictional strength and nucleate a secondary micro-rupture ahead of the original rupture tip. The new rupture is born SS (point A in Figure 3.4) and marks the onset of transition irrespective of the current location of the SR mother. To find this point of transition, first lengths $\overline{\text{OA}}$ and $\overline{\text{OB}}$ are defined as,

$$\overline{\text{OA}} = c_{\text{s}} T_0, \tag{3.1}$$

$$\overline{\text{OB}} = c_{\text{s}} T_1, \tag{3.2}$$

then lengths $\overline{\text{AB}}$ and $\overline{\text{AC}}$ are determined and rearranged to obtain $\overline{\text{OC}}$:

$$\overline{\text{AB}} = \overline{\text{OB}} - \overline{\text{OA}} = c_{\text{s}} T_1 - c_{\text{s}} T_0 = c_{\text{s}}(T_1 - T_0), \tag{3.3}$$

$$\overline{\text{AC}} = \overline{\text{OC}} - \overline{\text{OA}} = v_{\text{r}}^{\text{SS}}(T_1 - T_0) \qquad \Rightarrow \qquad \overline{\text{OC}} = v_{\text{r}}^{\text{SS}}(T_1 - T_0) + c_{\text{s}} T_0. \tag{3.4}$$

The difference between lengths $\overline{OC}$ and $\overline{OB}$ is taken and the expression is solved for T_0:

$$\overline{OC} - \overline{OB} = v_r^{SS}(T_1 - T_0) + c_s T_0 - c_s T_1, \tag{3.5}$$

$$T_0 = T_1 - \left(\frac{\overline{OC} - \overline{OB}}{v_r^{SS} - c_s}\right). \tag{3.6}$$

To obtain the transition length, T_0 is multiplied by the wave speed of point A, giving l_{tr} as:

$$l_{tr} = c_s \left[T_1 - \left(\frac{\overline{OC} - \overline{OB}}{v_r^{SS} - c_s}\right)\right]. \tag{3.7}$$

Case II: transition occurs directly at the sub-Rayleigh rupture tip

The case of a seamless transition of an originally SR rupture to SS speeds was analyzed in previous numerical investigations [119]. This transition occurs behind the shear wave front, thus introducing a new length, d. As in case I, various lengths are first defined:

$$\overline{OA'} = v_r^{SR} T_0, \tag{3.8}$$

$$\overline{OA} = c_s T_0, \tag{3.9}$$

$$\overline{OB} = c_s T_1, \tag{3.10}$$

$$\overline{OA} = \overline{OA'} + d. \tag{3.11}$$

Similarly, distances $\overline{A'B}$ and $\overline{A'C}$ are defined and solved for $\overline{OC}$:

$$\overline{A'B} = \overline{OB} - \overline{OA'}, \tag{3.12}$$

$$\overline{A'C} = \overline{OC} - \overline{OA'} = v_r^{SS}(T_1 - T_0) \quad \Rightarrow \quad \overline{OC} = v_r^{SS}(T_1 - T_0) + v_r^{SR} T_0. \tag{3.13}$$

Taking the difference between $\overline{OC}$ and $\overline{OB}$ and solving for T_0 gives:

$$\overline{OC} - \overline{OB} = v_r^{SS} T_1 - v_r^{SS} T_0 - c_s T_1 + v_r^{SR} T_0, \tag{3.14}$$

$$T_0 = T_1 \left(\frac{v_r^{SS} - c_s}{v_r^{SS} - v_r^{SR}}\right) - \left(\frac{\overline{OC} - \overline{OB}}{v_r^{SS} - v_r^{SR}}\right). \tag{3.15}$$

To obtain the transition length, T_0 is multiplied by the rupture tip speed at point A', giving l_{tr} as:

$$l_{tr} = v_r^{SR} \left[T_1 \left(\frac{v_r^{SS} - c_s}{v_r^{SS} - v_r^{SR}}\right) - \left(\frac{\overline{OC} - \overline{OB}}{v_r^{SS} - v_r^{SR}}\right)\right]. \tag{3.16}$$

Direct comparison of Equation 3.7 and 3.16 shows that for practical purposes these two analyses give very similar transition lengths; this is because the rupture tip speed, v_r^{SR}, is close to c_s. Once the transition length is determined (or the value T_0) the distance d can be estimated as:

$$d = T_0(c_\text{s} - v_\text{r}^\text{SR}), \tag{3.17}$$

and gives values on the order of $d = 3 - 6\,\text{mm}$, as verified from photo-elastic image measurements.

The dynamic event lag time, t_dyn, must be taken into account when using the expressions in Equations 3.7 or 3.16. The transition length expressions are modified as:

$$l_\text{tr} = c_\text{s} \left[(T_1 - t_\text{dyn}) - \left(\frac{\overline{\text{OC}} - \overline{\text{OB}}}{v_\text{r}^\text{SS} - c_\text{s}} \right) \right], \tag{3.18}$$

$$l_\text{tr} = v_\text{r}^\text{SR} \left[(T_1 - t_\text{dyn}) \left(\frac{v_\text{r}^\text{SS} - c_\text{s}}{v_\text{r}^\text{SS} - v_\text{r}^\text{SR}} \right) - \left(\frac{\overline{\text{OC}} - \overline{\text{OB}}}{v_\text{r}^\text{SS} - v_\text{r}^\text{SR}} \right) \right]. \tag{3.19}$$

Equation 3.19 is applied to every frame with both measurement points in the field-of-view. The transition length is then determined by averaging these values across all viable frames. Most significant spread in measured values for nominally identical experiments occurs in l_tr (Section 5.1).

3.2 Velocimeter trace processing

The second data output of the experiment are ground motion velocity signals on the plate measured with heterodyne laser velocimeters. All time series are filtered and corrected prior to presentation (Figure 3.1, right path): these steps are described in the sections below. Additional configuration-specific corrections are described in each specific set measurement set (Sections 4.1, 4.2, and 4.3).

3.2.1 Filtering data output from the oscilloscope

A 3rd order Butterworth low-pass filter removes measurement noise from all velocity signals. The Butterworth filter is notable for its monotonic roll-off at the cut-off frequency and controls the decay rate as prescribed by the filter order [120]. Effects of cut-off frequencies (normalized by the sampling rate of the oscilloscope) on the raw output are summarized in Figure 3.5. The cut-off frequency is chosen to be $\omega_\text{c} = 1.5\,\text{MHz}$ to match the velocimeter pre-processing low-pass filter cut-off. Applying the Nyquist theorem, the normalized cut-off frequency is found by halving the sampling rate of the discrete system, i.e., laser velocimeters [121]:

$$\omega_\text{c,n} = \frac{\omega_\text{c}}{\omega_\text{m}/2}, \tag{3.20}$$

where $\omega_\text{m} = 1.25\,\text{GHz}$ is the sampling rate of the oscilloscope(s). Application of the Nyquist theorem determines the normalized cut-off frequency to be $w_\text{c,n} = 2.4 \times 10^{-3}$ (cyan curves). Filtering with this cut-off frequency does not affect the arrival time or amplitude of the signatures with the highest frequency content nor does it distort the waveforms when the cut-off frequency is too low.
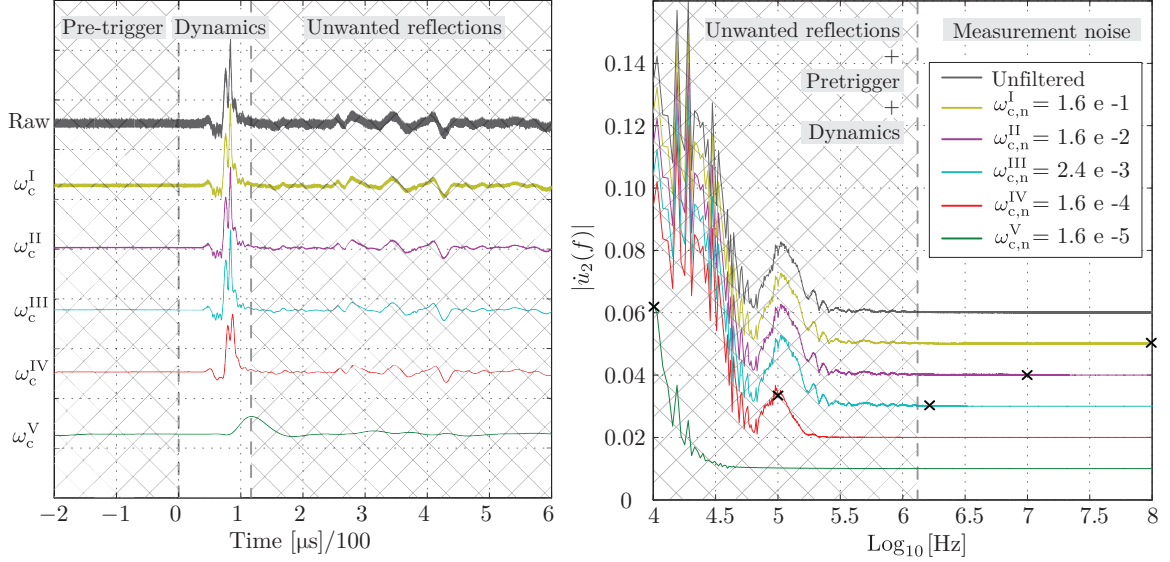
Figure 3.5: Filtering cut-off frequency effects on velocimeter data. Effects of cut-off frequency on a typical velocity series (left panel). Corresponding power spectra aid in determining the cut-off frequency to eliminate measurement noise in the spectrum (right panel).

3.2.2 Decoder based velocimeter lag time

An instrument-specific timing correction must be made based on the different decoder cards installed in the Polytec$^©$ velocimeter controllers. The decoders in the various Polytec$^©$ velocimeter systems have a certain constant built-in lag time due to differences in the circuit design. The Polytec$^©$ VD-09 digital decoder lags behind the Polytec$^©$ VD-02 analog decoders by a manufacturer-verified constant velocimeter-based time lag of $t_{\mathrm{vib}} = 4.9\,\mu$s, which must be taken into account when measurements are processed with differing decoders within the same experiment.

3.2.3 Constant velocity offset correction

The velocimeters are capable of resolving measurements in the micron scale, making them suitable candidates for this experiment. Minor offsets in the velocity signals yield non-physical results in the numerically integrated displacement curves. These long-wavelength effects are easily removed for each velocimeter trace by finding a constant velocimeter offset, $\dot{u}_{\mathrm{offset}}$.

Figure 3.6 graphically summarizes the determination and application of $\dot{u}_{\mathrm{offset}}$. The velocimeter traces are plotted in time and numerically integrated with the cumulative trapezoid method to give the uncorrected displacements. Non-zero displacements are observed at zero time before the arrival of any mechanical information; this is of course a non-physical result for ground motion. Each velocimeter offset is determined by the area under its displacement curve from the first data point to $t = 0\,\mu$s (hashed regions, middle panel). Corrected velocity signals are obtained by shifting each signal appropriately towards zero and reintegrating to obtain the corrected displacements as shown in
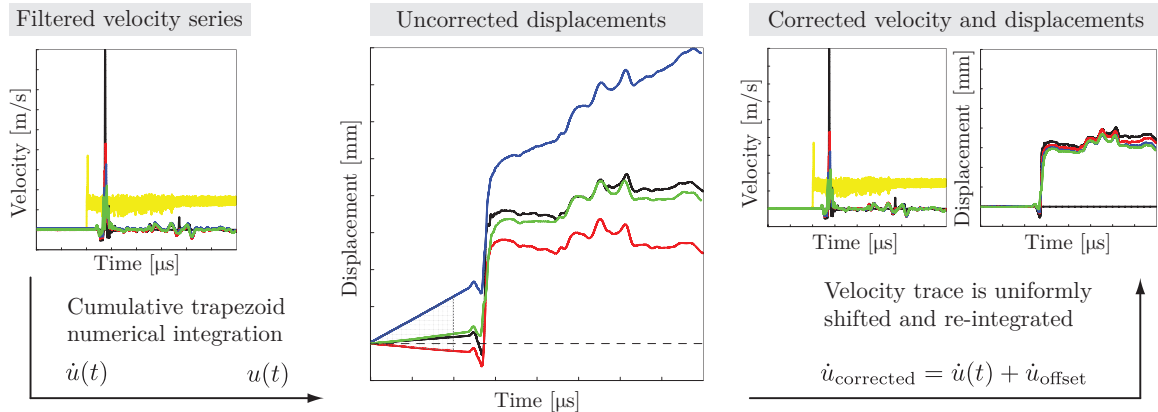
Figure 3.6: Correcting constant offset in the velocity time series using integrated displacements. Offsets $\dot{u}_{\mathrm{offset}}$ are determined from displacement curves prior to mechanical information arrival (hashed regions). Adjusted velocity series are re-integrated for displacements.

Figure 3.6 (right panel). Typical values are on the order of $\dot{u}_{\mathrm{offset}} \approx 0.01\,\mathrm{m/s}$; moreover, these values are nearly constant across all experiments, suggesting that this effect is instrument-driven. These adjustments are important for displacement more so than velocity signals. Since the magnitudes $|\dot{u}_{\mathrm{offset}}|$ are minor fractions of peak velocity amplitudes measured in experiments ($\approx 1 - 10\,\mathrm{m/s}$), interpretation of velocity data is not skewed by offset errors. Accumulated error during integration, however, is on the order of the measured displacements ($\approx 1 - 100\,\mu\mathrm{m}$) for experimental times $T_{\mathrm{exp}} \leq 120\,\mu\mathrm{s}$, rendering the interpretation of displacement data useless without this correction.

3.3 Synchronizing and merging the two data outputs

A geometrical timing analysis merges the photo-elastic images and the velocimeter data into an image/trace sequence. This pairing allows a connection to be drawn amongst various signatures in the ground motion records to photo-elastic fringe patterns associated with rupture features within the hanging and foot wall plates.

Data analysis for every experiment culminates in an image/trace sequence of digital photographs of photo-elastic fringes and velocimeter traces as shown in Figure 3.1. The two diagnostics are unified with the mechanical event by accounting for the dynamic event lag time, t_{dyn}, into the arrival timing expressions (Equations 4.1, 4.4, 4.6, 4.7, 4.10, 4.13, and 4.17). Merged data are used for initial observations of thrust fault experiment results. These sequences consistently show that specific signatures in the velocimeter traces coincide with specific rupture features arriving at the measurement stations, thus providing insight into thrust fault rupture dynamics. Representative experiments will initially be presented like so, followed by a global overview of each data set with an $x - t$ plot, as is customary in the field of seismology. A timing analysis specific to the first two configurations supersedes each presented data set (Sections 4.1.1 and 4.2.1).

Chapter 4

Experimental Results

Three thrust fault configurations are investigated, as shown in Figure 4.1. The first configuration records the surface-normal ground motions at various stations, x_1, along the simulated earth surface, $\dot{u}_2(x_1, 0, t)$ and $u_2(x_1, 0, t)$ (left panel); next, down-dip grazing angle measurements investigate rupture propagation towards the simulated earth surface and the resulting down-dip phase by recording on-fault fault parallel and fault normal ground motions, $\dot{u}_1(x_1', \pm\eta, t)$, $u_1(x_1', \pm\eta, t)$ and $\dot{u}_2(x_1', \pm\eta, t)$, $u_2(x_1', \pm\eta, t)$, where $\eta \approx 400 - 600 \, \mu m$ (middle panel); the final configuration leaves a polished patch of various lengths, l_{patch}, near the fault trace and studies the effects of the interface heterogeneity on earth surface-normal ground motions, $\dot{u}_2(l_{\text{patch}} : x_1, 0, t)$ and $u_2(l_{\text{patch}} : x_1, 0, t)$ (right panel).
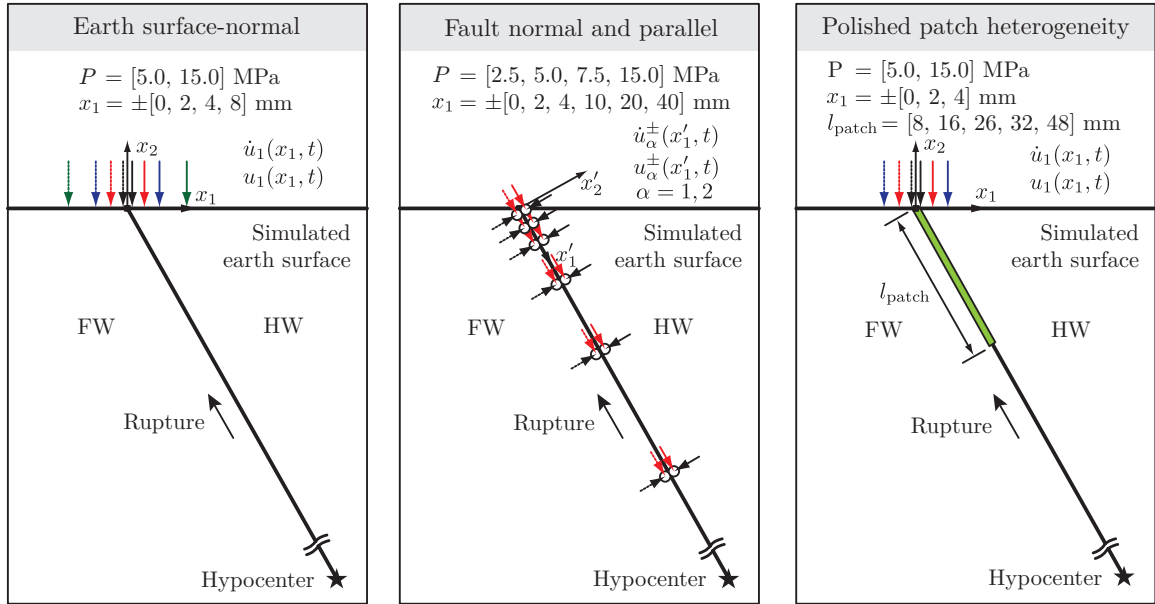
Figure 4.1: Summary of the three experimental configurations. Left panel: earth surface-normal measurements are conducted for various distances x_1 from the fault trace (Section 4.1). Middle panel: fault parallel and fault normal measurements are conducted at paired hanging and foot wall stations for various depths x_1' along the fault (Section 4.2). Right panel: earth surface-normal measurements are conducted with a polished patch heterogeneity introduced along the interface near the fault trace in attempts to arrest the rupture prior to reaching the free surface (Section 4.3).

All experiments presented follow the methodologies of previous sections; the same specimen geometry is used in all results, with dimensions $w = 180 \, \text{mm}$, $h = 360 \, \text{mm}$, and $t = 9.52 \, \text{mm}$ and an interface angle $\alpha = 29°$ cut about the notch located at $(\bar{\zeta}_1, \bar{\zeta}_2) = (65, 200) \, \text{mm}$ (Appendix C). Configuration specific analyses are presented in each respective section. The laboratory nomenclature is herein abandoned and replaced with that of natural faults for brevity (in reference to Figure 2.2).

4.1 Earth surface-normal ground motions

Velocimeter beams focused normal to the earth surface measure vertical components of velocity; a two-beam example of such a setup is shown in Figure 4.2. Due to the Eulerian nature of the measurements, stand-off distances between the reflective tape placement and the fault trace, ϵ^+ and ϵ^-, are required to prevent cross-measurement of the two fault trace velocimeter beams, $\dot{u}_2(x_1 = \epsilon^{\pm}, t)$ (Appendix A). The largest accumulated slips occur for the highest tested loads $P = 15 \, \text{MPa}$ at the fault trace and are about $u_{\text{slip}}^{\max} \approx 380 \, \mu\text{m}$ within the experimental time window $T_{\exp} = 120 \, \mu\text{s}$. The hanging wall plate covers the foot wall material once the surface is broken; an offset of $\epsilon^{\pm} \approx 200 - 300 \, \mu\text{m}$ is enforced for hanging $(+)$ and foot wall $(-)$ fault trace measurements based on an estimated beam diameter of $150 \, \mu\text{m}$ [118]. Lateral motions of the glass beads on the reflective tapes are not sensed in the records due to the diffuse nature of the reflections [122]. To minimize three-dimensional effects, all beams are aligned mid-thickness of the plate along the earth surface.
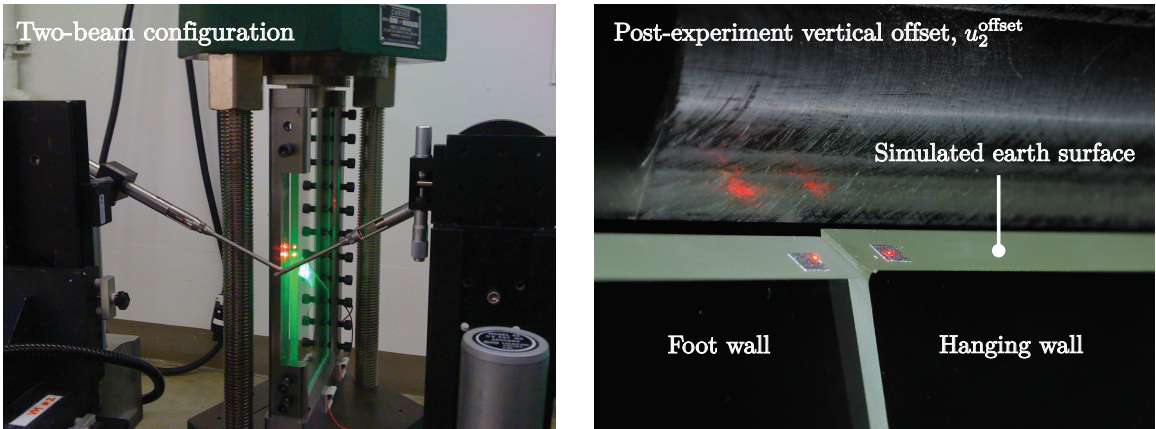
Figure 4.2: Velocimeter beam arrangement for a two-point measurement, $\dot{u}_2(x_1 = \pm 4 \, \text{mm})$. Right panel: total accumulated vertical offset at the fault trace between the hanging and foot walls, u_2^{offset}.

4.1.1 Timing analysis: earth surface arrivals

A geometrical timing analysis is conducted in order to identify the arrivals of various rupture features to stations placed along the earth surface as well as the phase velocities of the resulting surface features. The procedure followed is illustrated in Figure 4.3 in both schematic and photographic
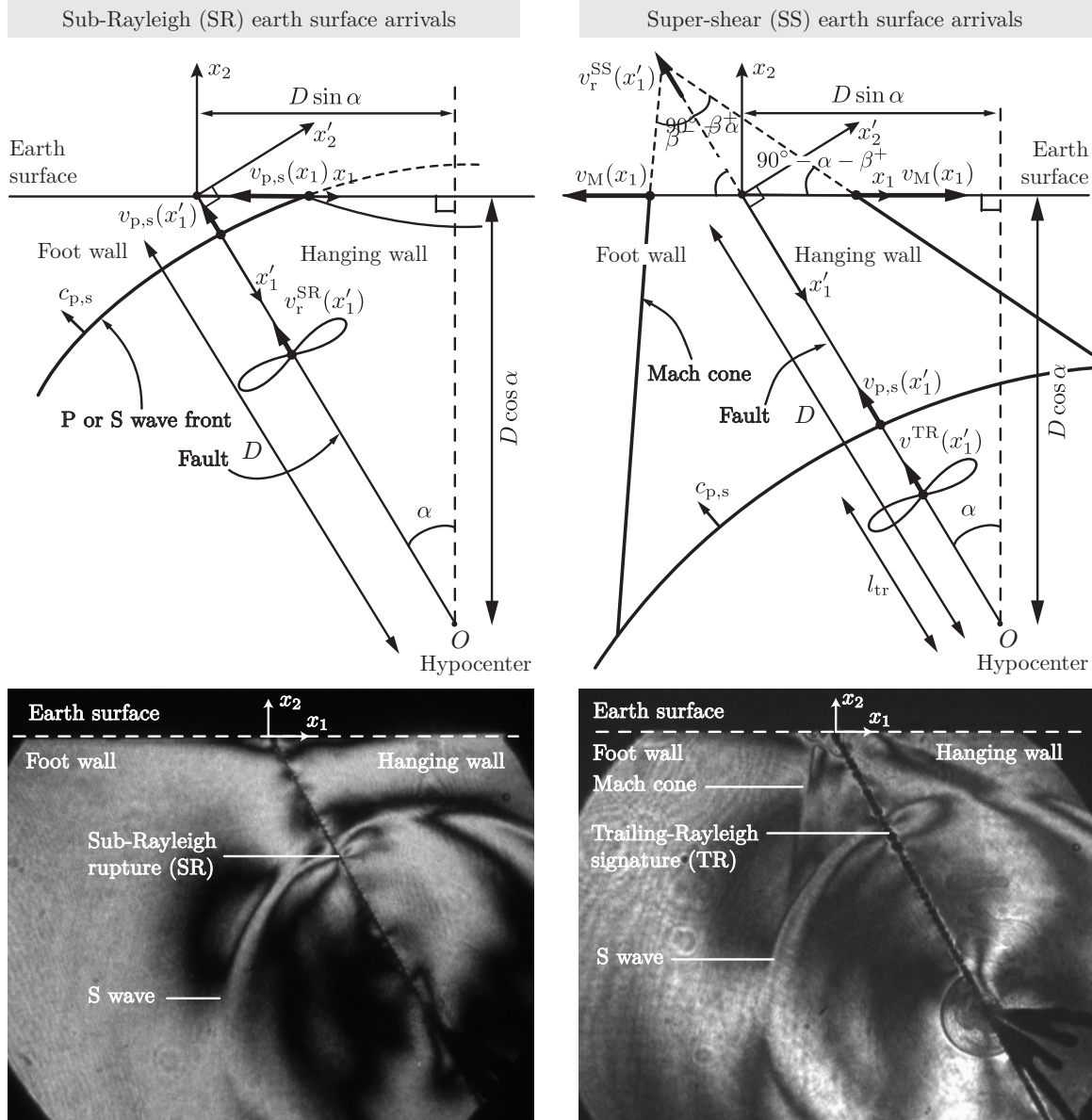
Figure 4.3: A timing analysis determines the arrival times and phase velocities of rupture features along the earth surface. Schematics and paired photographs present the various rupture features for a SR (left column) and SS rupture (right column). The P wave has outrun the S wave in both cases and it is absent in both images; however, the initial S wave, the SR rupture, the trailing-Rayleigh (TR) signature, and the Mach cone are clearly discerned by the isochromatic fringe patterns.

representations. The photo-elastic image to the bottom left of Figure 4.3 corresponds to a sub-Rayleigh (SR) rupture moving towards the earth surface with a nearly constant speed of $v_{\mathrm{r}}^{\mathrm{SR}} = 1.14(3)\,\mathrm{mm/\mu s}$. The SR rupture tip, identified by a double-lobe fringe pattern, trails just behind the circular S wave trace emitted at the time of nucleation; P and S wave speeds are $c_{\mathrm{p}} = 2.59(8)\,\mathrm{mm/\mu s}$ and $c_{\mathrm{s}} = 1.27(2)\,\mathrm{mm/\mu s}$; the initial P wave has outrun the S wave and is not visible anymore in the photographs. The photo-elastic image to the bottom right of Figure 4.3 corresponds to a rupture

which was nucleated as SR and has transitioned to super-shear speeds (SS) as evidenced by the presence of a shear Mach cone. The SS rupture tip has already reached the earth surface and rupture-induced reflections are just visible at the free surface. The circular trace of the S wave, similar to the one present in the left photograph, is also visible. Behind this circular trace is the double-lobe fringe pattern of the trailing-Rayleigh (TR) signature, propagating at a velocity v^{TR}: this signature is related to the stresses of a now extinct SR rupture that has transitioned to SS at an earlier time during the event. The TR signature has been previously studied in relation to a strike-slip configuration of a similar experimental setup [37]. In a range of experiments where transition was observed, the SS rupture tip speeds are found to be $v_{\mathrm{r}}^{\mathrm{SS}} = 2.00 - 2.20\,\mathrm{mm/\mu s}$, this $10\,\%$ variation being attributed to uncontrollable variations in the interface preparation methodology (discussed in Chapter 5). The speed of the TR signature, however, was always found to be very close to the plane-stress Rayleigh wave speed of Homalite H-100, which is $c_{\mathrm{R}} = 1.18(3)\,\mathrm{mm/\mu s}$. In fact, no measurable difference exists between the SR rupture tip and TR signature speeds ($v_{\mathrm{r}}^{\mathrm{SR}} = v^{\mathrm{TR}}$).

Idealizing the S wave and P wave fronts as concentric circles originating from the hypocenter, it is clear from the top left schematic of Figure 4.3 that these circular disturbances travel from $+\hat{x}_1$ to $-\hat{x}_1$ along the earth surface, meaning the excitation order of the stations along the hanging wall ($x_1 > 0$) are reversed in sense from those of the foot wall ($x_1 < 0$). The earliest arrival times of these circular waves, $t_{\mathrm{p,s}}(x_1)$, as well as the phase velocities of the surface disturbances created when the P (or S) wave(s) intersect with the earth surface, $v_{\mathrm{p,s}}(x_1)$, are functionally identical, the only difference being the magnitude of the wave speeds marked by subscripts "p" and "s". From the top left schematic of Figure 4.3, the arrival times of these circular disturbances are directly determined from geometry to be:

$$t_{\mathrm{p,s}}(x_1) = \frac{\sqrt{(D\sin\alpha - x_1)^2 + (D\cos\alpha)^2}}{c_{\mathrm{p,s}}}. \tag{4.1}$$

Due to the curvature of the P and S waves, the velocity of the resulting disturbance depends on station coordinate, x_1. By using the relation between the wave radius and time, $r_{\mathrm{p,s}}(t) = c_{\mathrm{p,s}}t$, the geometry of the dashed right triangle, and the chain rule, the phase velocity $v_{\mathrm{p,s}}$ at any point along the earth surface is determined to be:

$$v_{\mathrm{p,s}}(x_1) = c_{\mathrm{p,s}}\frac{\sqrt{(D\sin\alpha + x_1)^2 + (D\cos\alpha)^2}}{D\sin\alpha + x_1}. \tag{4.2}$$

The arrival times $t_{\mathrm{p,s}}(x_1)$ and velocities $v_{\mathrm{p,s}}(x_1)$ depend parametrically on the interface angle α as well as the length D, which are characteristics of the fault geometry; when $\alpha = 0°$ (vertical fault) at station $x_1 = 0$ the velocity $v_{\mathrm{p,s}} \to \infty$ as expected (circular wave front is tangent to the earth surface); for a very deep hypocenter ($D \to \infty$) the expression reduces to a simple x_1-independent relation, $v_{\mathrm{p,s}} \to c_{\mathrm{p,s}}/\sin\alpha$, which corresponds to a linear disturbance intersecting the surface (a direct consequence of increasing the wavefront radius of curvature to infinity).

Similar calculations can be performed for the case of a rupture which has transitioned to SS, as shown on the right column of Figure 4.3. The appearance of Mach cones is a distinct feature accompanying dynamic SS ruptures. The rupture tip at the vertex of the Mach cone travels at a speed v_r^{SS}, which must lie in the domain $c_s < v_r^{SS} < c_p$ [39, 57]. The rupture speed is a function of the Mach cone angle, $\beta^\pm$, through the relation $v_r^{SS} = c_s / \sin \beta^\pm$. The geometry of the dashed triangle in the top right schematic of Figure 4.3 yields arrival times of the Mach fronts to any given station, $t_M(x_1)$, as well as the resulting phase velocity, $v_M(x_1)$, along the earth surface. The Mach fronts are idealized as characteristic lines which initially appear at a distance l_{tr} from the hypocenter. The transition length, l_{tr}, is the distance from the hypocenter, traveled by the rupture the instant before the rupture tip speed changes from the SR to SS domain [47, 66, 67, 123]. The time it takes for the SS rupture tip to arrive at the fault trace ($x_1 = 0$) depends on l_{tr} and v_r^{SS} as:

$$t_r^{SS}(x_1 = 0) = \frac{l_{tr}}{c_s} + \frac{D - l_{tr}}{v_r^{SS}}. \tag{4.3}$$

The law of sines allows the above equation to be expressed as a function of measurement station as:

$$t_M(x_1) = t_r^{SS}(0) + \frac{1}{v_r^{SS}} \left[\frac{\sqrt{(x_1)^2 - (x_1 \sin \alpha)^2}}{\tan \beta^\pm} - x_1 \sin \alpha \right]. \tag{4.4}$$

Considering two stations placed equidistant from the fault trace on the hanging and foot wall surfaces, the above expression shows that it takes longer for a Mach front to arrive at the foot wall station, an obvious result from inspection of Figure 4.3.

Assuming a constant v_r^{SS}, the Mach cones form self-similar triangles at all times. Under steady-state conditions, the phase velocity $v_M(x_1)$ is related to v_r^{SS} through the law of sines as:

$$v_M(x_1) = v_r^{SS} \frac{\text{sgn}(x_1) \sin \beta^\pm}{\sin \left[90° - \beta^\pm - \alpha \right]} = \frac{\text{sgn}(x_1) c_s}{\sin \left[90° - \beta^\pm - \alpha \right]}, \tag{4.5}$$

where the signum function, $\text{sgn}(\cdot)$, appears to account for directionality between the surface velocities on the hanging and foot wall plates. The expression for $v_M(x_1)$ immediately shows that the surface velocities $v_M(x_1 > 0)$ and $v_M(x_1 < 0)$ are constants with $|v_M(x_1 > 0)| > |v_M(x_1 < 0)|$ and $v_M(x_1 > 0) > 0 > v_M(x_1 < 0)$, for all physically allowed Mach angles, β. The signum function here shows that the order of station excitations is nearest to the fault trace to furthest from the fault trace on both the hanging and foot wall plates. This is in contrast to the station excitation order for circular disturbances. For the hanging wall, in the case where $\beta^+ = 90° - \alpha$, the velocity $v_M(x_1)$ becomes infinite: this corresponds to the right-hand Mach front impinging parallel to the earth surface on the hanging wall. For $\beta^\pm \to 90°$ ($v_r^{SS} \to c_s^+$) the Mach cone degenerates to a single straight line perpendicular to the interface, traveling towards the earth surface at an angle α. In this case, $v_M(x_1) < 0$ for all x_1, with only one intersection with the free surface.

Rupture tip arrival to the fault trace is expected to generate Rayleigh waves propagating bi-laterally away from the fault trace on the earth surface. SR and SS Rayleigh wave arrivals are

$$t_{\mathrm{R}}(x_1) = \begin{cases} t_{\mathrm{r}}^{\mathrm{SR}}(0) + \dfrac{|x_1|}{c_{\mathrm{R}}} & \text{if} \quad v_{\mathrm{r}}\colon (0, c_{\mathrm{R}}) \cup (c_{\mathrm{s}}, c_{\mathrm{p}}), \\[2ex] t_{\mathrm{r}}^{\mathrm{SS}}(0) + \dfrac{|x_1|}{c_{\mathrm{R}}} & \text{if} \quad v_{\mathrm{r}}\colon (c_{\mathrm{s}}, c_{\mathrm{p}}), \end{cases} \tag{4.6}$$

where $t_{\mathrm{r}}^{\mathrm{SR}}(x_1 = 0) = D/v_{\mathrm{r}}^{\mathrm{SR}}$ and $t_{\mathrm{r}}^{\mathrm{SS}}(x_1 = 0)$ (Equation 4.3) are arrival times of the SR and SS ruptures to the fault trace, respectively. The phase velocities are by definition the Rayleigh wave speed, $v_{\mathrm{R}}(x_1) = c_{\mathrm{R}}$. For SS events, both the rupture tip and the TR signature arrivals generate Rayleigh waves, thus both timing expressions in Equation 4.6 are required with $v^{\mathrm{TR}} = v_{\mathrm{r}}^{\mathrm{SR}}$.

4.1.2 Earth surface-normal records: sub-Rayleigh event

Two representative experiments of nominally identical conditions with a static initial load $P = 5\,\mathrm{MPa}$ are presented in the image/trace sequence of Figures 4.4 and 4.5. The left columns correspond to an experiment measuring vertical velocities of hanging wall stations $x_1 = (2, 4, 8)\,\mathrm{mm}$ while the right column shows the analogous foot wall experiment with measurement stations $x_1 = (-2, -4, -8)\,\mathrm{mm}$.

The shaded bands in the velocimeter traces represent the range of theoretically computed arrival times for the P wave, S wave, and SR rupture to the measurement locations: the finite width of these arrivals is due to the fact that the stations span a finite distance. The arrival times have been calculated through the methods presented in Section 4.1.1. As predicted by theoretical calculations of l_{tr}, it is possible to have a SS transition with $P = 5\,\mathrm{MPa}$; however, this does not occur in the experiments because the fault length, D, is shorter than the estimates on l_{tr}, and a SR rupture is observed for the entire duration of the up-dip rupture propagation. The photo-elastic images in each figure represent nominally the same rupture obtained in two experimental instances with the same conditions, and hence can be used to assess the experimental repeatability. Furthermore, the stress drops for the hanging and foot wall experiments are $\Delta\sigma = 0.5\,\mathrm{MPa}$ and $\Delta\sigma = 1.0\,\mathrm{MPa}$, respectively, yet another rubric used to judge experimental reproducibility (Section 5.2).

At time $t = 30\,\mu\mathrm{s}$, the rupture tips can be seen traveling bi-directionally away from the hypocenter as the lobed-fringe patterns in the photo-elastic images (Figure 4.4, top panel). Just ahead of the rupture tip is the S wave front generated at nucleation. Though faint, the P wave from nucleation is visible in the photographs. Mechanical information has not yet arrived to any station.

At time $t = 50\,\mu\mathrm{s}$, the initial P wave has reached the measurement stations at the free surface and has induced upward vertical ground motions $\approx 0.2\,\mathrm{m/s}$ (Figure 4.4, bottom panel inserts). Measurements at depth (Section 4.2) confirm that the surface does not break with the arrival of P waves, and thus P wave arrivals are surface perturbations due to the P wave reflecting from the earth surface. The rupture tip continues to propagate up-dip, unzipping the locked fault ahead.
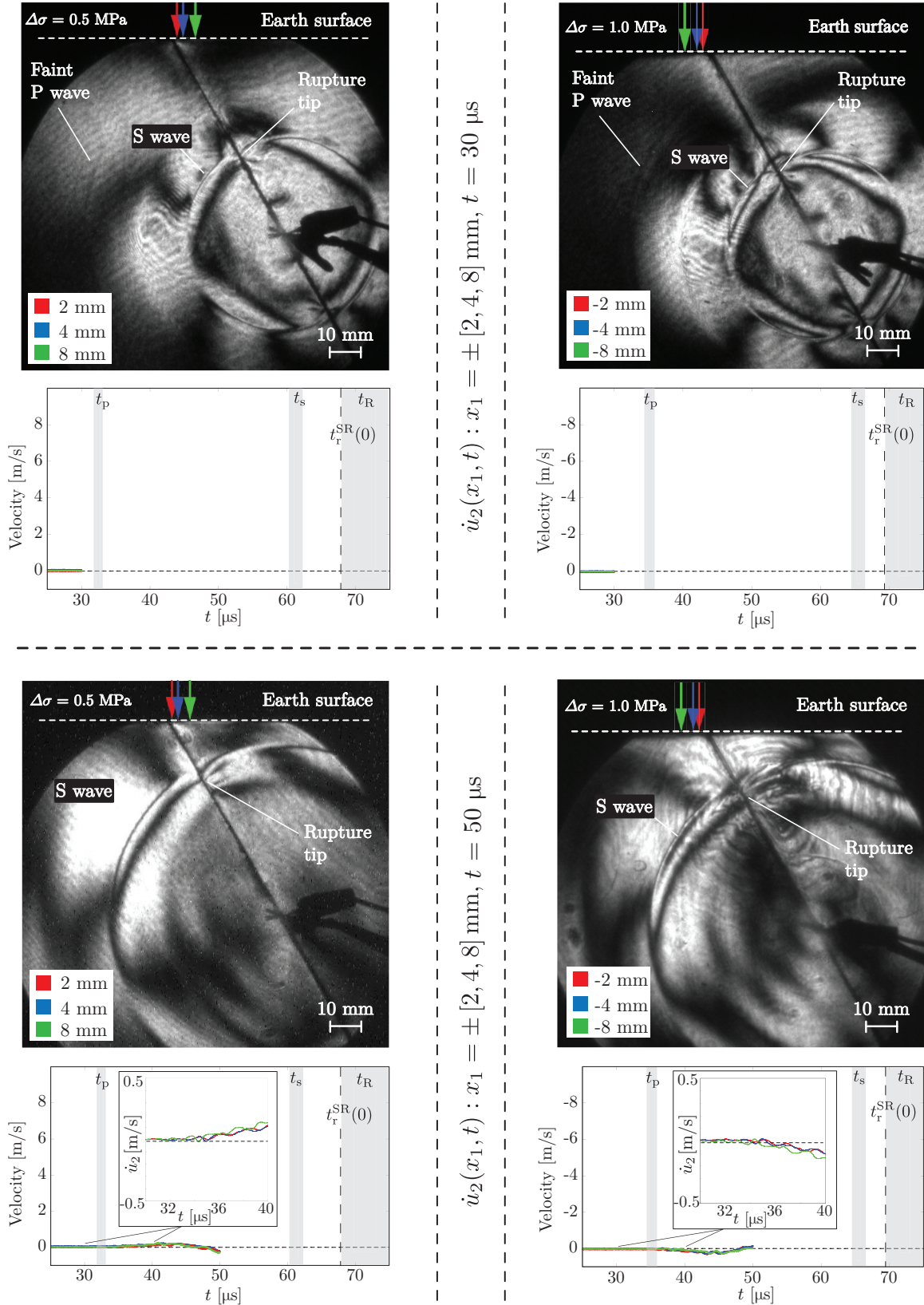
Figure 4.4: Sub-Rayleigh earth surface-normal ($\dot{u}_2$) image/trace sequence at $t = 30$ and $t = 50\,\mu$s.
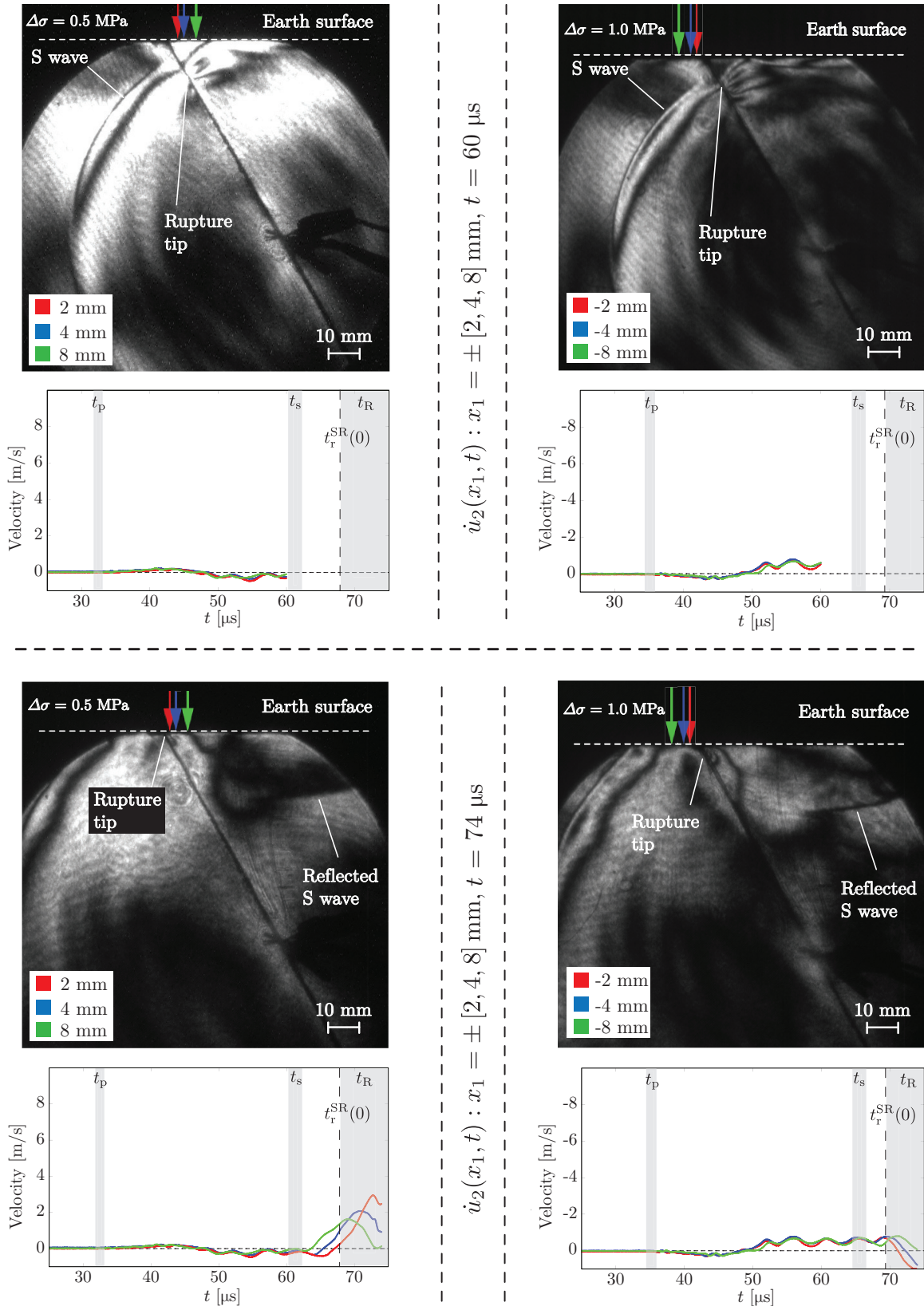
Figure 4.5: Sub-Rayleigh earth surface-normal ($\dot{u}_2$) image/trace sequence at $t = 60$ and $t = 74\,\mu$s.

The first clearly observable free surface reflection is that of the S wave at time $t = 60\,\mu$s, as can be seen on the hanging wall plate (Figure 4.5, top panel). The P wave effects continue to vertically move the stations; however, there is a direction change around $t = 50\,\mu$s from positive to negative velocities; the earth surface begins to move away from the sensors across all stations (note the ordinate for foot wall records have been inverted to aid in comparing to hanging wall magnitudes).

At time $t = 74\,\mu$s, the S wave has swept across the hanging and foot wall stations, inducing positive ground motions on the order of $1\,$m/s. The SR rupture tip has just arrived at the fault trace and begins to interact with the free surface.

The collection of records from the two experiments of the image/trace sequence are summarized in Figure 4.6 for the experimental window $T_{\text{exp}} = 120\,\mu$s. Measurements at the fault trace on the hanging and foot walls are also included in the plot (black curves). For a SR rupture, earth surface-normal ground motions are within $1\,$m/s between timing lines t_{p} and t_{s}. The arrival of the P wave commences a $\approx 15\,\mu$s upward swing of about $0.2\,$m/s across all measurement stations. At around $50\,\mu$s, oscillations with nearly constant period $\approx 5\,\mu$s commence and persist across all measurement stations until the S wave timing mark, t_{s}: these ground motions must be due to dilatational waves continuously impinging and reflecting from the free surface; furthermore, their proximity to the rupture tip suggests that the period is related to a characteristic rupture time scale. It is only after the arrival of the SR rupture tip at the fault trace, $t_{\text{r}}^{\text{SR}}(x_1 = 0)$ (marked by a star), that peak vertical ground motion velocities are observed, first at $x_1 = +0\,$mm and $x_1 = -0\,$mm locations, and subsequently at other stations. In other words, the SR tip arrives at the fault trace and breaks the surface, jutting the hanging wall plate over the foot wall and generating significant surface disturbances that spread bi-laterally away from the fault trace with speeds approximately equal to c_{R} (Figure 4.6, t_{R}); these measurements are strong evidence of generated surface Rayleigh waves. Oscillations persist after the rupture tip arrival across all stations; however, the well-defined $\approx 5\,\mu$s pre-rupture periods have increased and range from $6 - 10\,\mu$s with an average of $8\,\mu$s.

Two distinct peaks are observed on the hanging wall stations near the t_{s} and t_{R} timing lines, which coalesce into a single peak at the fault trace as $x_1 \to 0\,$mm. The double-peak behavior is absent, however, in the foot wall, suggesting its origin to be a rupture front wave. These ground motions result from the rupture tip field interacting with stations directly above the fault on the hanging wall plate; such interactions are, by nature of geometry, absent in the foot wall plate. This situation is schematically represented in the left column of Figure 4.3, showing that direct rupture field effects, represented by the double-lobed structure, may only be sensed above the fault. Numerical work for a finite surface-breaking thrust fault generates synthetic velocity traces and shows the absence of these rupture front waves on the foot wall plate (Figure 1.17) [96].

Hanging wall vertical ground motions are enhanced with the arrival of the SR rupture tip to the earth surface. For stations placed a symmetric distance from the fault trace on the hanging and foot
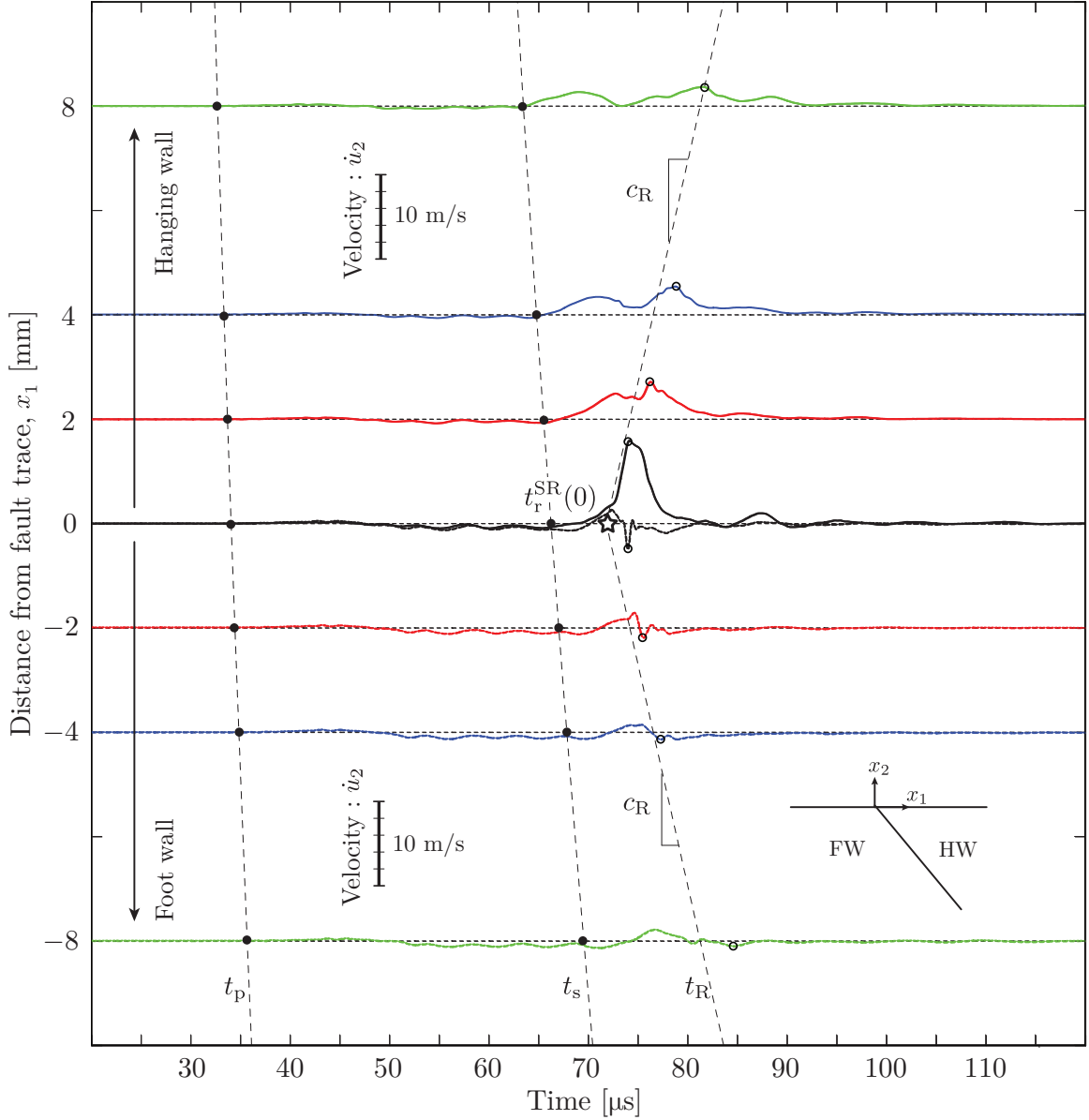
Figure 4.6: Summary of earth surface-normal velocity records for sub-Rayleigh (SR) experiments with an applied load of $P = 5\,\mathrm{MPa}$. Records from two nominally identical experiments are presented for symmetric stations $x_1 = \pm(0, 2, 4, 8)\,\mathrm{mm}$. Initial P and S wave arrival times are given by the dashed curves $t_{\mathrm{p,s}}$; arrival of the SR rupture at the fault trace is marked by a star $t_{\mathrm{r}}^{\mathrm{SR}}(x_1 = 0\,\mathrm{mm})$; arrivals of Rayleigh disturbances along the earth surface are marked by lines t_{R}.

walls, the peak velocity magnitudes are always greater for the hanging wall station. This asymmetry seems to result from the presence of the free surface and the wedge geometry of the hanging wall, a configuration prone to trapping waves if the fault surfaces detach near the free surface; further measurements are necessary to understand the underlying mechanics at the fault trace. Numerical work on the effects of fault angle on earth surface-normal ground motions shows that peak amplitude disparities between hanging and foot wall plates increase with α (Figure 1.16) [91, 93, 124].

4.1.3 Earth surface-normal records: super-shear event

Increasing the compressive load from $P = 5\,\text{MPa}$ to $P = 15\,\text{MPa}$ generates super-shear (SS) earthquake in the experimental setup [54, 104, 125]. As in the sub-Rayleigh (SR) case of the previous section, the sequence of photo-elastic images and velocimeter traces presented in Figures 4.7-4.8 describes two different experiments performed at nominally identical conditions; the left and right columns represent hanging and foot wall earth surface-normal measurement at stations $x_1 = (2, 4, 8)\,\text{mm}$ and $x_1 = (-2, -4, -8)\,\text{mm}$, respectively. The stress drops are also comparable, with values $\Delta\sigma = 8.2\,\text{MPa}$ and $\Delta\sigma = 6.8\,\text{MPa}$ for hanging and foot wall experiments, respectively; the photo-elastic images from both experiments look quite similar throughout the event.

The first pair of images at time $t = 40\,\mu\text{s}$ (Figure 4.7, top panel) are taken just after transition to SS from SR speeds and show the formation of the Mach cone. The transition lengths are measured to be $l_{\text{tr}} = 23.7\,\text{mm}$ in the experiment with the hanging wall measurements (left column) and $l_{\text{tr}} = 20.9\,\text{mm}$ in the experiment with the foot wall measurements (right column); l_{tr} is the most difficult parameter to control, and for this reason, both stress drop and transition lengths are matched when comparing nominally identical SS experiments. After transition, the remnants of the SR rupture tip persist and are identified by the lobe-like fringe pattern trailing behind the S wave front along the fault, a feature called the trailing-Rayleigh (TR) signature propagating with speeds $v^{\text{TR}} = v_{\text{r}}^{\text{SR}}$. The SS rupture tips propagate bi-laterally with speeds v_{r}^{SS} of $2.05\,\text{mm}/\mu\text{s}$ and $2.15\,\text{mm}/\mu\text{s}$ for the experiments with the hanging and foot wall measurements, respectively. Since photo-elasticity is predominantly sensitive to shear stress information, the P wave front generated at nucleation is not well resolved and it is not visible at $t = 40\,\mu\text{s}$. An up-dip fringe pattern just ahead of the Mach cone is the leading dilatational field associated with the pile-up of P waves ahead of the rupture [55, 126].

Soon thereafter ($t = 50\,\mu\text{s}$), the rupture tip reaches the earth surface (Figure 4.7, bottom panel). The dilatational field has swept across all hanging wall stations, with its endpoint marked by the inflections in the hanging wall traces. The Mach fronts have swept across all the hanging wall stations, but have not yet swept across all foot wall stations; this is due to the offset in arrival times between symmetrically placed hanging and foot wall stations. The arrival of substantial motion at the measurement stations before the arrival of the S wave is a clear indication that the earthquake has indeed transitioned to SS. The effects of the dilatational field and the Mach fronts are sequentially felt in large surface-normal motions. The hanging wall has an upward motion and the foot wall has a downward motion, as indicated by the negative signs on the vertical axis for the foot wall measurements. The arrival of the SS features has already introduced a large relative velocity between symmetrically placed stations along the hanging and foot walls.

In the top panel of Figure 4.8 ($t = 60\,\mu\text{s}$), the effects of the dilatational fields and Mach cones have been sensed throughout the stations. The asymmetry of the ground motions between the hanging and foot walls is enhanced, with the hanging wall stations having larger maximum velocity
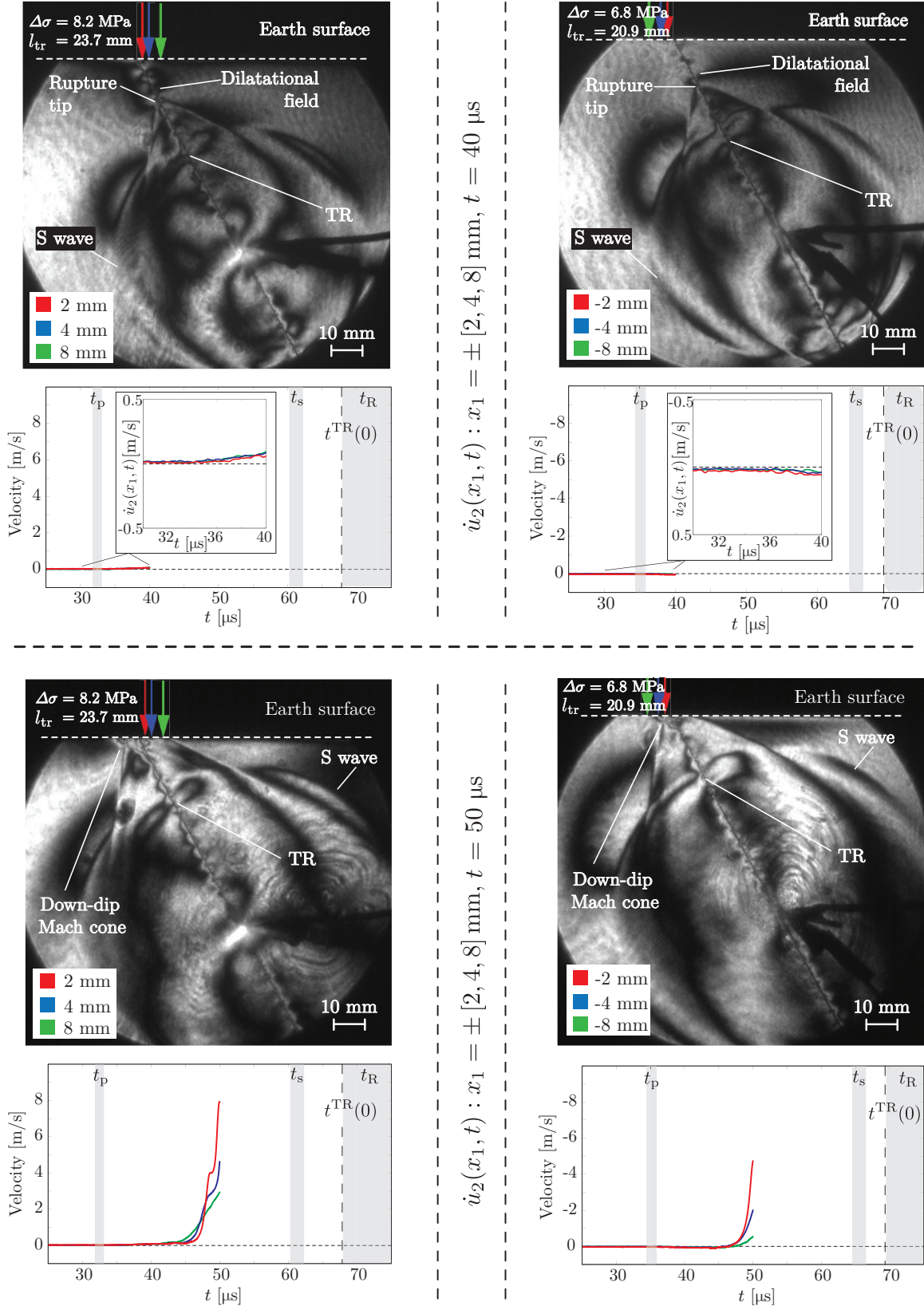
Figure 4.7: Super-shear earth surface-normal ($\dot{u}_2$) image/trace sequence at $t = 40$ and $t = 50\,\mu\text{s}$.
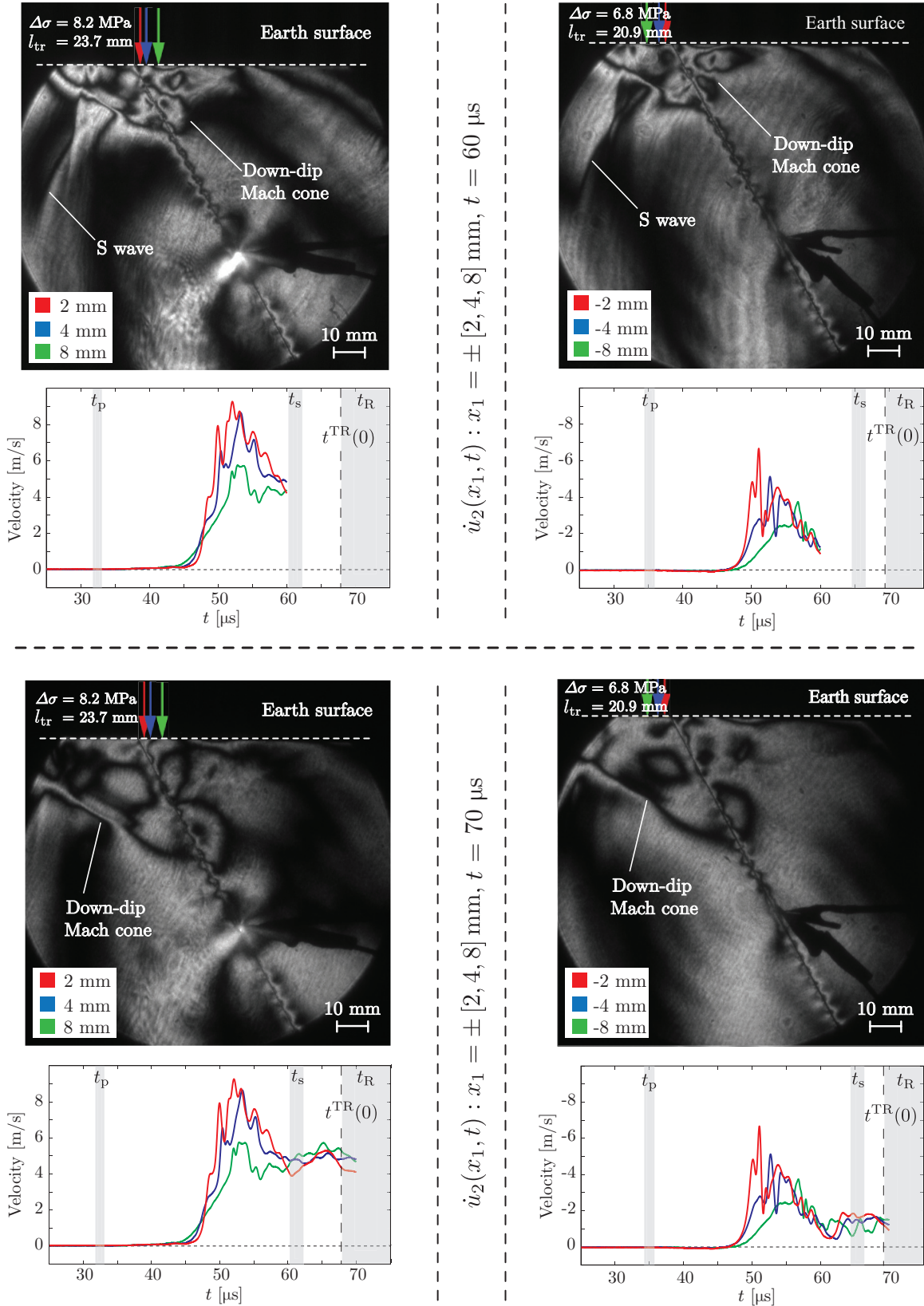
Figure 4.8: Super-shear earth surface-normal ($\dot{u}_2$) image/trace sequence at $t = 60$ and $t = 70\,\mu\text{s}$.

magnitudes than those of the corresponding foot wall stations. The time to reach the peak of the velocity traces increases with increasing distance from the fault trace, resulting in broader peaks for all Mach features; the signatures in the recorded traces also attenuate with distance from the fault trace. The photographs show a Mach-cone-like feature propagating back down-dip, mixing fringes with the incident S wave and TR signature; this feature is further discussed in Sections 4.2.3 and 4.2.8. The photographs also show the S wave about to impinge on the furthest station, $x_1 = 8$ mm.

At a later time $t = 70$ μs (Figure 4.8, bottom panel), the down-dip Mach cone feature has traveled more than halfway back down-dip towards the hypocenter. The up-dip TR signature, the remnant of the original SR rupture tip, is just about to arrive at the fault trace, similar in timing to the SR rupture in the absence of transition to SS speeds (Figure 4.6).

To visualize the temporal evolution of earth surface-normal ground motions, the velocity traces for all stations are plotted in Figure 4.9. The plotted traces include measurements at stations $x_1 = (-8, -4, -2, 2, 4, 8)$ mm shown in Figures 4.7-4.8, plus two additional measurements just to the left and right of the fault trace at $x_1 = +\epsilon$ and $x_1 = -\epsilon$ obtained in a separate experiment. The theoretically computed P and S wave arrival times at various locations, x_1, are given by the dashed curves marked t_p and t_s, respectively (Equation 4.1). The Mach front arrivals are designated by the dashed black lines, t_M (Equation 4.4). The red dashed curves, t'_M, are the arrival times of the Mach fronts from the down-dip super-shear feature, a discussion of which is deferred to Section 4.1.5. A star and triangle mark the arrivals of the SS rupture tip and the TR signature to the fault trace, $t_\mathrm{r}^{\mathrm{SS}}(0)$ and $t^{\mathrm{TR}}(0)$, respectively. Note: the triangle in Figure 4.6 is positioned based on an average value of transition length from the three experiments: $l_\mathrm{tr} = 23.7$ mm, $l_\mathrm{tr} = 20.9$ mm (Figures 4.4-4.5), and $l_\mathrm{tr} = 20.5$ mm (black curves). The closed dark circles mark the times of the various wave front arrivals at each station location, while open circles mark significant maxima on the traces themselves; comparing closed and open circles identifies various signatures in the records.

In the time intervals between t_p and t_M, the traces reflect the effects of the initial P wave arrival and the continuous arrivals of P waves emitted during the rupture process, including the dilatational field ahead of the Mach cone. P wave arrival initiates motion throughout all the stations (not visible on the scale of Figure 4.9, see insert in Figure 4.8). The dilatational field that precedes the Mach cone causes substantial motion as relativistic effects compress emitted P waves ahead of the inter-sonic rupture tip (Figure 4.9, t_df); its effects are much more prominent for stations above the fault, i.e., hanging wall records ($x_1 > 0$). The rupture tip and the associated Mach fronts reach the stations next. The rupture causes strong upward/downward velocities next to the fault trace on the hanging/foot walls. The Mach fronts arriving at the off-fault stations amplify the effect of the preceding dilatational field. Because of the dip angle asymmetry, the velocities recorded at symmetrically placed stations on the hanging and foot walls are different in magnitude, with amplified ground motions in the hanging wall. An exception to this asymmetry occurs for a brief

moment upon rupture tip arrival in the fault trace records, $x_1 = \pm 0 \, \text{mm}$ (discussion deferred to Section 4.2.8). As Figure 4.9 clearly indicates, the calculated times of the Mach cone arrivals, t_M (black dots indicate arrivals) correspond remarkably well to the rapid velocity changes in the traces. The velocity maxima for each trace (open circles) shortly follows. The red dashed lines, also shown on the plot, represent arrivals of the Mach fronts caused by a down-dip propagating SS signature (discussed in Section 4.2.1). The global maxima of earth surface-normal velocity at each station is attributed to the effects of this paired set of up and down-dip Mach cones.

The arrival of the SS rupture at the surface is expected to generate surface Rayleigh waves that would start at the fault trace and spread bi-laterally across the stations, much like the arrival of the SR rupture tip. Projected arrivals of such waves are marked by timing lines t_R ($v_\text{R} = c_\text{R}$); relative changes are indeed observed in the traces corresponding to those times. However, these changes are superimposed with other rupture effects and do not appear prominently in the records. Photographs in Figure 4.18 (Section 4.2.3) show the characteristic fringes patterns of surface Rayleigh waves.

Following the ground-shaking signatures associated with the arrival of the dilatational field and the Mach fronts, the traces decrease in magnitude at all stations until the arrival of the S wave generated at nucleation (Figure 4.9, t_s). The effect of the S wave is to once again increase the ground shaking amplitude as it sweeps the stations. Next, the TR signature arrives at the fault trace (Figure 4.6, triangle). This arrival is also expected to generate Rayleigh waves, and their projected arrival at the other stations is marked by two straight dashed-dotted lines emanating from the TR signature arrival. Indeed, the velocity traces near the projected arrival times of the Rayleigh wave consistently show an increase of the velocity magnitude. The local maxima of the traces (marked by open circles at times $t > 70 \, \mu\text{s}$) also seem to propagate with the Rayleigh wave speed along the hanging and foot wall plates. The measurements right next to the fault trace have the TR arrival slightly delayed; this is attributed to the shorter transition length of the experiment.

The traces show that the asymmetry of the motions between hanging and foot walls persists throughout the observation window. At the time of $85 \, \mu\text{s}$, all stations on the hanging wall continue to move with the vertical velocity of about $4 \, \text{m/s}$. On the foot wall, a much smaller velocity amplitude of $1-2 \, \text{m/s}$ is observed. After all significant features of the SS earthquake rupture are done interacting with the earth surface within the measurement station span, the motion at the earth surface is expected to settle to the near-constant velocity values, at least until artificial reflections arrive from the other specimen boundaries. These near-constant values would be caused by the continuous sliding of the specimen interface behind the TR signature, a behavior typical for crack-like shear-dominant ruptures. Consistent with this expectation, at the end of the observation window shown in Figure 4.9, velocities for all the stations on the hanging wall approach a similar value; the same phenomenon occurs on the foot wall. Note that the end-of-the-window velocity amplitudes at stations $x_1 = +8 \, \text{mm}$ and $x_1 = -8 \, \text{mm}$ appear to be slightly higher than those at $x_1 = \pm 0 \, \text{mm}$; this is because the effects
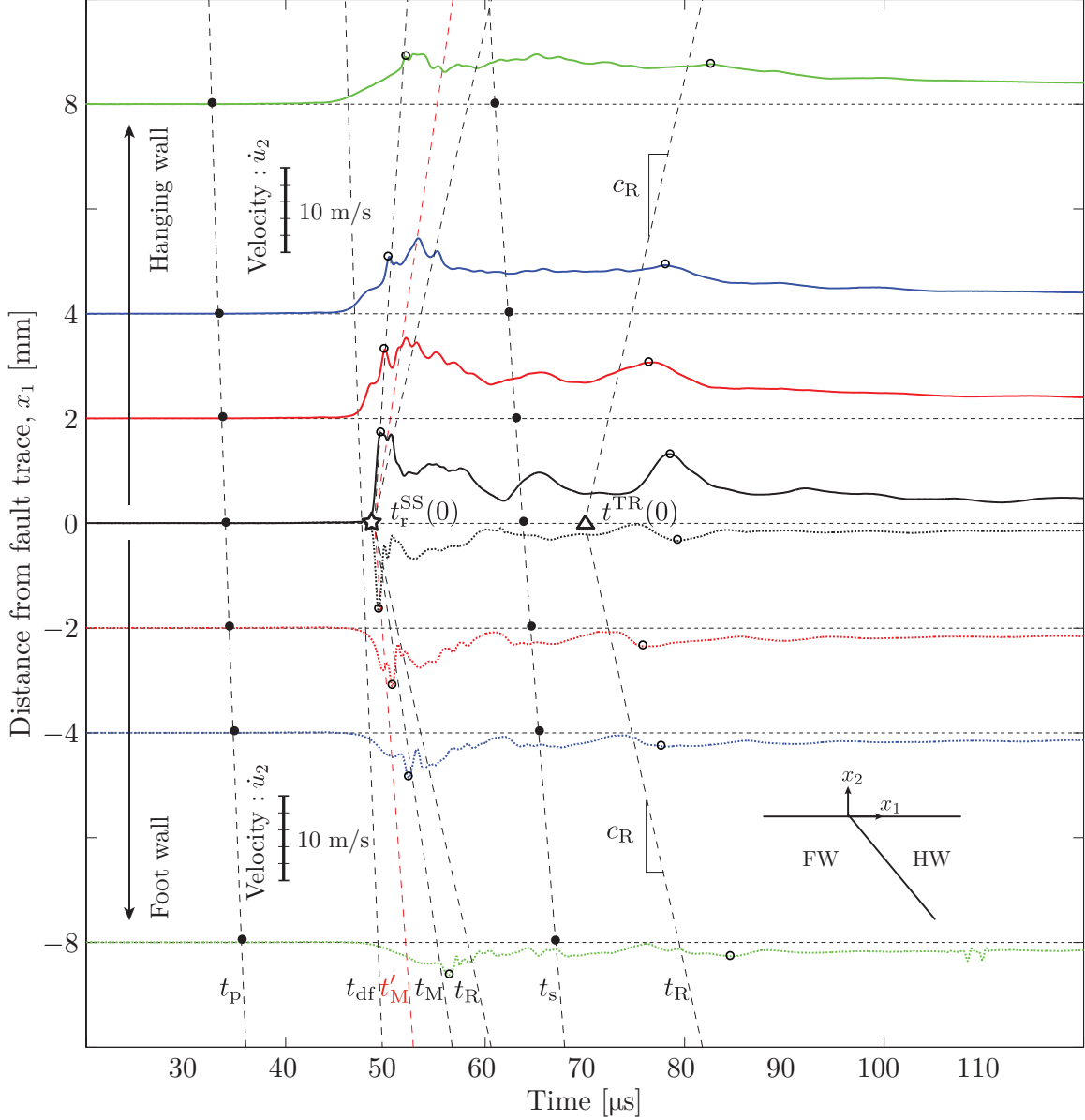
Figure 4.9: Summary of earth surface-normal velocity records for super-shear (SS) experiments with an applied load of $P = 15.0$ MPa, including traces from Figures 4.7-4.8 as well as additional measurements right next to the fault trace at $x_1 = \pm 0$ mm, recorded in a separate experiment (black curves). Initial P and S wave arrival times are given by the dashed curves labeled t_p and t_s, respectively. Arrival of the up-dip Mach fronts are given by the pair of dashed lines, t_M (Equation 4.4). Red dashed lines t'_M represent arrivals of down-dip propagating Mach fronts (discussed in Section 4.1.5). A star and triangle mark the rupture tip and TR arrivals to the fault trace, $t_r^{SS}(0)$ and $t^{TR}(0)$. Rupture tip and TR arrivals generate surface waves, requiring two Rayleigh lines, t_R.

of the surface Rayleigh waves discussed above have not yet had a chance to decay for the stations farthest from the fault trace. Since stations closer to the fault trace have higher peak amplitudes, the near-constant velocities at the end of the observation window imply that the amplitude decays more for stations closer to the fault trace. The behavior of points closer to the fault trace is also richer and

more "dynamic," with higher amplitudes alternating with near-zero values, indicating frequent and abrupt up-and-down motions, while stations away from the fault move with near-constant velocity amplitudes; this is perhaps to be expected as rupture interactions are more direct at the fault trace.

4.1.4   Signature attenuation with distance: comparing SR and SS

There are obvious qualitative differences in the surface motion records corresponding to the SR and the SS set of experiments (e.g., Figures 4.6 and 4.9). Here, the absolute maximum vertical velocity values at all stations are compared for SR and SS simulated earthquakes (Figure 4.10).
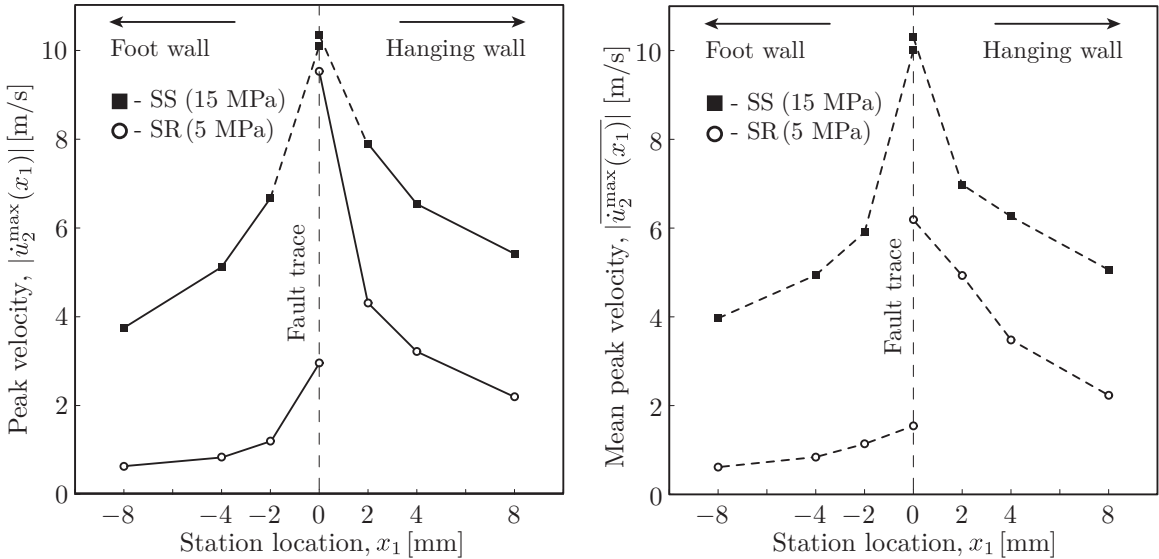
Figure 4.10: Attenuation of earth surface-normal velocity maxima in SR (open circles) and SS experiments (solid squares) with distance from the fault trace, x_1. Left panel: measurements from the 6 presented experiments with solid lines linking a single experiment and dashed lines linking results of nominally identical experiments. Right panel: mean value of maxima from all experiments, non-dimensionalized by the average value of each set measured at a distance $|x_1| = 2\,\text{mm}$.

At the fault trace, SS experiments feature peak velocity magnitudes of about $10\,\text{m/s}$ on both hanging and foot walls; however, surface velocities for SR events are about $6\,\text{m/s}$ on the hanging wall and only $1.5\,\text{m/s}$ on the foot wall, exhibiting much higher asymmetry. A discussion of this peculiar characteristic is deferred to Section 4.2.9. Higher stresses and hence higher stress drops in SS events account for the observation of overall higher levels of surface velocity [37]. The maximum surface velocity magnitudes for the SS experiments at the fault trace are just at the instrument saturation level of $\pm 10\,\text{m/s}$. While a strong conclusion may not be drawn from these measurements, peak widths for the hanging and foot wall traces at the saturation level are $0.46\,\mu\text{s}$ and $0.10\,\mu\text{s}$, respectively, suggesting that the signals have nearly peaked. The SR results for peak vertical velocity are qualitatively quite comparable to numerical models (Figure 1.16) [127]. For measurements at $|x_1| = (2, 4, 8)\,\text{mm}$ stations (solid lines), the peak values of SS cases attenuate slower than the peak

values of SR cases, as expected due to slower decay of motion along Mach front characteristics [37]. Within a distance $|x_1| \leq 2\,\mathrm{mm}$, it appears that peaks for SS experiments attenuate faster.

4.1.5 Free-surface effects in earth surface-normal records

An interesting finding from the photo-elastic images is a Mach cone propagating back down-dip after the SS rupture tip has reached the fault trace, as seen in the image/trace sequence of Figures 4.7-4.8. The down-dip Mach front is readily visible on the foot wall, but obscured on the hanging wall because of reflected radiation and the associated complex photo-elastic fringe pattern (Figure 4.11). The down-dip propagating Mach cone must be associated with a rupture-tip-like radiating feature propagating back towards the hypocenter. It is yet unclear whether this feature is actually a rupture tip, separating locked and slipping regions of the interface, or a slip feature (Section 4.2.8).
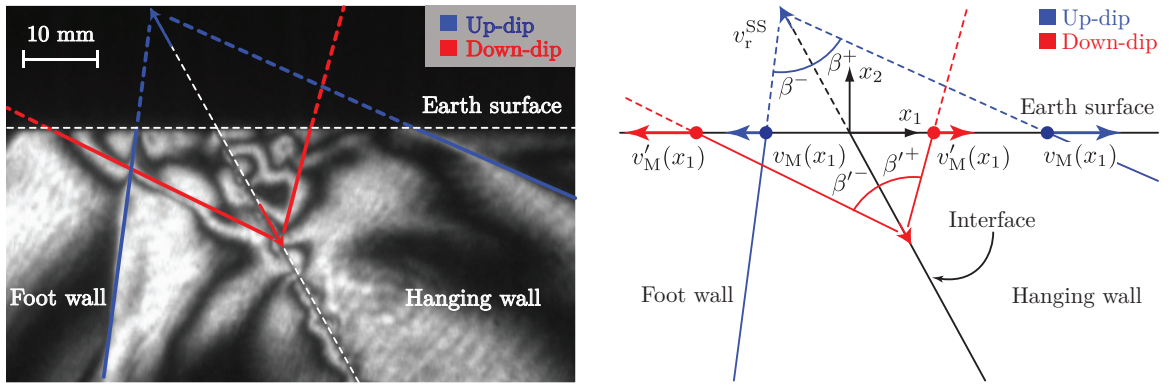
Figure 4.11: The down-dip propagating Mach front is captured in the enlarged photograph on the left and schematically illustrated on the right. Fringes from the down-dip propagating shear feature are clearly visible in the foot wall, but are obscured in the hanging wall.

The photo-elastic images are used to determine the angle of the down-dip propagating Mach front with respect to the fault $(\beta'^{\pm})$ and hence the associated SS signature speed, v'^{SS}. Based on the down-dip Mach cone angles on the foot wall, the average down-dip SS signature speed is $v'^{\mathrm{SS}} = 2.45\,\mathrm{mm/\mu s}$; this is $\approx 17\,\%$ greater than the up-dip SS rupture speed, $v_{\mathrm{r}}^{\mathrm{SS}} = 2.10\,\mathrm{mm/\mu s}$. Note: some parts of the Mach front appear curved in the later images; however, the entire assembly of fringes moves down at SS speeds (see Figure 4.8, Section 4.1.3). The curved nature of the Mach front may be a consequence of complex wave front superpositions from the incident up-dip rupture and the down-dip propagating disturbance, leading to the deceleration of the down-dip SS signature.

To see whether the arrival of the down-dip propagating Mach cone affects the surface motion, a timing analysis is done similar to the one in Section 4.1.1, using the schematic in the right panel of Figure 4.11. Assuming that the down-dip propagating slip feature is generated at the same instant as the incident Mach cone hits the fault trace, $t'_{\mathrm{M}}(x_1 = 0) = t_{\mathrm{r}}^{\mathrm{SS}}(x_1 = 0)$, a simple change $x_1 \to -x_1$ and $\beta^{\pm} \to \beta'^{\mp}$ in Equations 4.4 and 4.5 gives the arrival timing, $t'_{\mathrm{M}}(x_1)$, of the down-dip propagating

Mach fronts to any station, x_1 and the earth surface phase velocity, $v'_M(x_1)$ as:

$$t'_M(x_1) = t_r^{SS}(0) + \frac{1}{v'^{SS}} \left[\frac{\sqrt{(x_1)^2 - (x_1 \sin \alpha)^2}}{\tan \beta'^{\pm}} + x_1 \sin \alpha \right], \tag{4.7}$$

$$v'_M(x_1) = v'^{SS} \frac{\text{sgn}(-x_1) \sin \beta'^{\pm}}{\sin \left[90° - \beta'^{\pm} - \alpha \right]} = \frac{-\text{sgn}(x_1) c_s}{\sin \left[90° - \beta'^{\pm} - \alpha \right]}. \tag{4.8}$$

Note that on the foot wall, according to calculation, the signature of the down-dip slip feature travels ahead of, and faster than, the incident Mach front. In contrast, on the hanging wall, the signature of the down-dip slip feature travels behind, and slower than, the incident Mach front. These conclusions are consistent with the experimental observations (see left panel of Figure 4.11) and this agreement between calculations and observation strengthens the assertion that the down-dip propagating structures are Mach fronts of a down-dip moving disturbance rather than reflected Mach fronts of the initial, up-dip moving rupture fringe structure.

On the surface of both walls, the theoretically predicted arrival times of the down-dip propagating Mach cone match the beginning of surface velocity increase (Figure 4.9, red dashed lines marked t'_M). On the hanging wall, this effect is added to the preceding effect of the incident Mach front, resulting in the global maximum for the traces at $x_1 = 2\,\text{mm}$ and $x_1 = 4\,\text{mm}$. Signatures of the down-dip Mach cone on the foot wall are less pronounced, as it is superimposed with the dilatational field preceding the rupture. SS free-surface phenomena is further studied in Sections 4.2.3 and 4.2.8.

4.2 On-fault measurements at depth

Measurements of on-fault fault parallel and fault normal velocities are conducted at various depths along the fault to study free-surface effects on rupture dynamics, namely, whether the fault opens and if an up-dip SR rupture may transition to SS down-dip speeds. Six measurement locations, $x'_1 = (0, 2, 4, 10, 20, 40)\,\text{mm}$, are sampled for three different loads, $P = (2.5, 5.0, 7.5)\,\text{MPa}$, and locations $x'_1 = (0, 2, 4, 19, 34)\,\text{mm}$ for load $P = 15.0\,\text{MPa}$. A detailed schematic of such a configuration is shown in Figure 4.12. Four velocimeter beams approach the corners of two paired retro-reflective tapes at grazing angles within $\approx 5°$ in a single experiment (Figure 4.12, bottom photographs): two measure fault parallel components of particle velocity just above and below the fault, $\dot{u}_1^+(x'_1, \eta^+, t)$ and $\dot{u}_1^-(x'_1, \eta^-, t)$, while the remaining two beams measure paired fault normal velocities just above and below the fault, $\dot{u}_2^+(x'_1, \eta^+, t)$ and $\dot{u}_2^-(x'_1, \eta^-, t)$. Minor stand-off distances $\eta^{\pm} \approx 400 - 600\,\mu\text{m}$ are required between the tape edges and the interface to utilize reflective tape thickness for fault normal measurements. Beam orientations are checked with internal reflections within the specimen to assure accuracy of ground motion components. Appendix A discusses configuration details, including taper angle effects ($\theta_{\text{taper}}^{\pm}$) and corrections due to the Eulerian nature of the measurements.
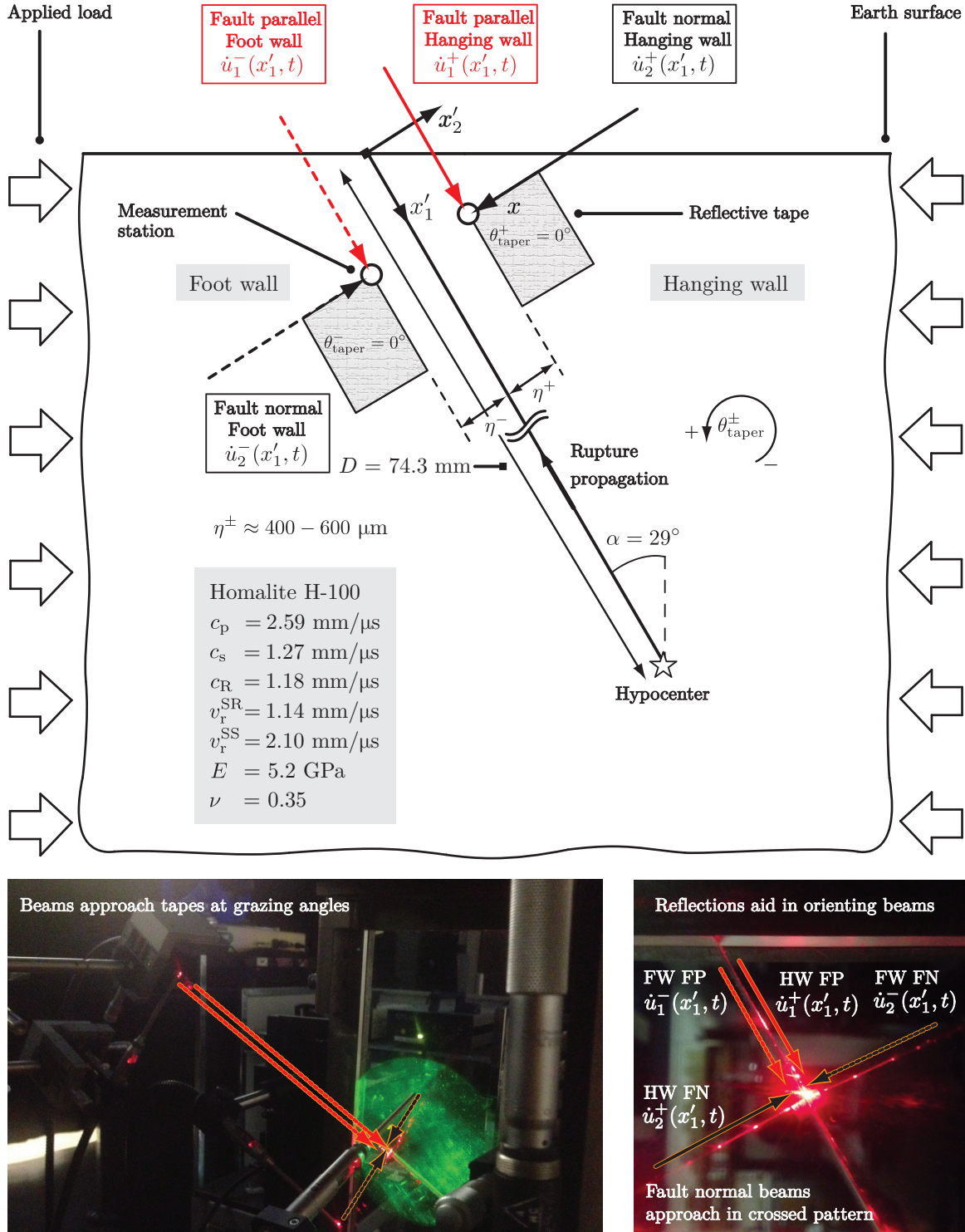
Figure 4.12: Velocimeter configuration details for fault parallel and normal measurements at-depth along the fault line. Two velocimeter beams (red arrows) approach parallel to the interface to measure on-fault fault parallel records. Another two velocimeter beams (black arrows) approach in a cross-pattern to measure on-fault fault normal velocities. Stand-off distances η^+ and η^- are required to achieve these measurements. Beam orientation is checked with internal reflections.

4.2.1 Timing analysis: arrivals at depth

A geometrical timing analysis, similar to that of Section 4.1.1, determines arrival times of various rupture features to on-fault stations placed at-depth along the fault. The photographs in the top panel of Figure 4.13 show the up-dip propagation of a sub-Rayleigh (SR, left photograph) and a super-shear (SS, right photograph) earthquake prior to the rupture tip reaching the fault trace, $(x_1', x_2') = (0, 0)$ mm. The schematics and paired photographs in the remaining panels of Figure 4.13 represent experimental times after the rupture tip has reached the fault trace, $t > t_r^{\text{SR}}(x_1' = 0)$ for the SR rupture (left column) and $t > t_r^{\text{SS}}(x_1' = 0)$ for the SS rupture (right column), respectively. Key features are marked with stars in the photographs. Sections 4.1.1 and 4.1.5 have discussed arrival times and phase velocities along the earth surface: $t_{\text{p,s}}(x_1)$, $v_{\text{p,s}}(x_1)$ are arrival times and phase velocities of P and S waves along the earth surface; $t_{\text{M}}(x_1)$, $v_{\text{M}}(x_1)$ and $t_{\text{M}}'(x_1)$, $v_{\text{M}}'(x_1)$ are the arrival times and phase velocities of the up-dip and down-dip Mach fronts along the earth surface; $t_{\text{R}}(x_1)$, $v_{\text{R}}(x_1)$ are arrival times and phase velocities of Rayleigh waves along the earth surface. Arrivals and phase velocities along the angled fault at-depth are distinguished from those of the earth surface with the use of the primed coordinate system, $\hat{x}_1' - \hat{x}_2'$: $t_{\text{p,s}}(x_1')$, $v_{\text{p,s}}(x_1')$ and $t_{\text{p,s}}'(x_1')$, $v_{\text{p,s}}'(x_1')$ are arrival times and phase velocities of up-dip and reflected P and S waves along the angled interface; $t_r^{\text{SR}}(x_1')$, $v_r^{\text{SR}}(x_1')$ and $t'^{\text{TR}}(x_1')$, $v'^{\text{TR}}(x_1')$ are arrival times and phase velocities of the up-dip SR rupture and rupture-induced down-dip features; similarly, $t_r^{\text{SS}}(x_1')$, $v_r^{\text{SS}}(x_1')$ and $t'^{\text{SS}}(x_1')$, $v'^{\text{SS}}(x_1')$ are arrivals of the up-dip SS rupture and rupture-induced down-dip features. For events which transition from SR to SS speeds, the remnant photo-elastic signature associated with the original SR rupture tip is called the trailing-Rayleigh (TR) signature, v^{TR}, as it is uncertain a priori whether this is indeed a rupture tip or merely a stress concentration. Down-dip rupture-induced features for SR events consist of a TR signature, v'^{TR}, generated when the SR rupture arrives at the fault trace. The rupture-induced features for SS events, however, are two-fold; first, SS rupture tip interaction with the earth surface generates a Mach-front emitting shear feature propagating down-dip at SS speeds, v'^{SS}, and second, arrival of the up-dip TR signature in turn generates a down-dip TR signature propagating at a speed v'^{TR}.

Phase velocities of P and S waves along the fault are determined using the geometry of Figure 4.13. P and S wave arrivals to stations at-depth during their up-dip propagation is trivially obtained. The earth surface causes geometrical reflections of the P and S wave fronts which intersect the fault as they propagate down-dip. The up and down-dip expressions are:

$$t_{\text{p,s}}(x_1') = \frac{D - x_1'}{c_{\text{p,s}}} \qquad \text{if} \quad t \leq \frac{D}{c_{\text{p,s}}}, \tag{4.9}$$

$$t_{\text{p,s}}'(x_1') = \frac{\sqrt{D^2 + 2D(1 - \cos^2 \alpha)x_1' + x_1'^2}}{c_{\text{p,s}}} \qquad \text{if} \quad t > \frac{D}{c_{\text{p,s}}}, \tag{4.10}$$
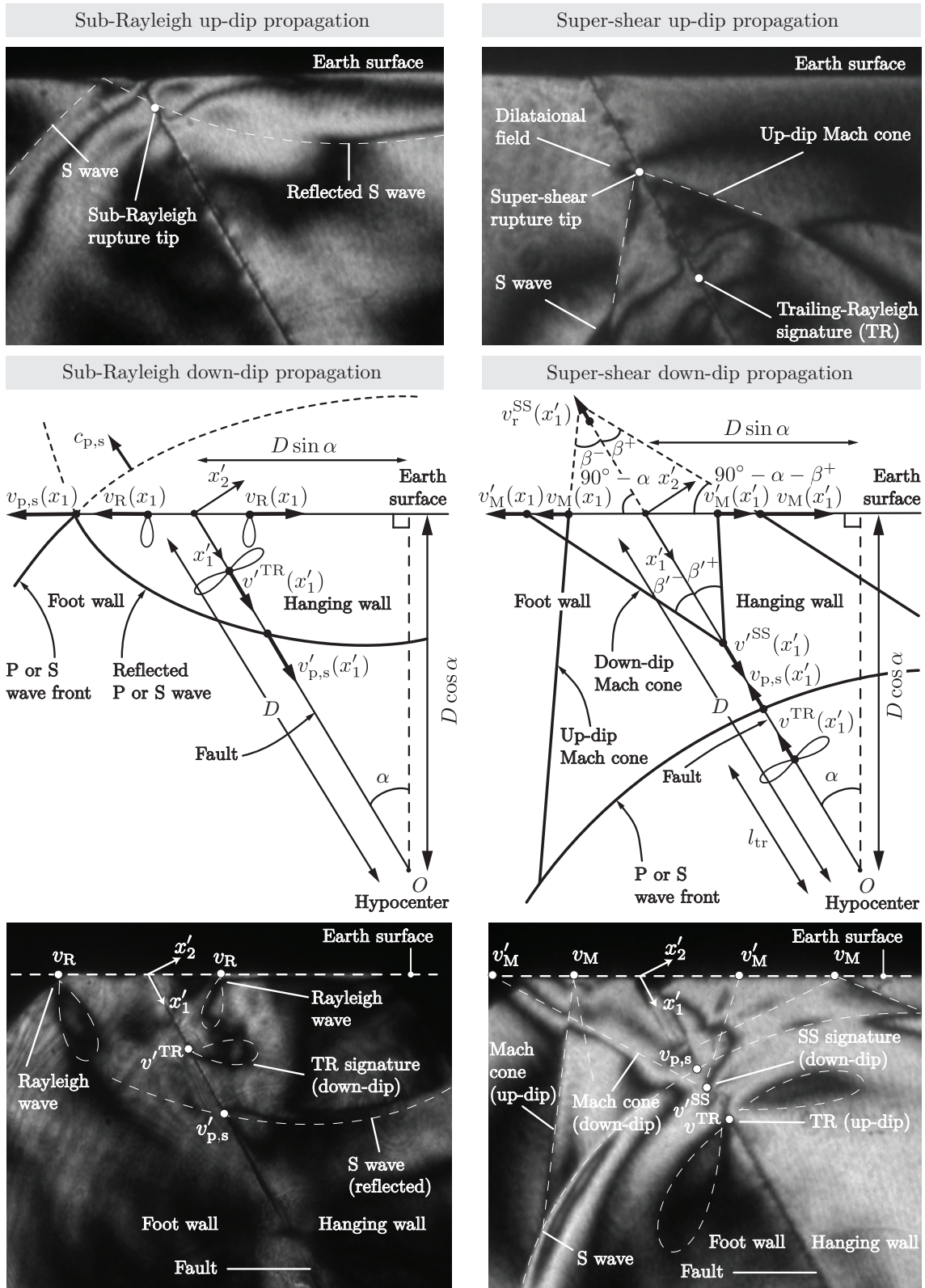
Figure 4.13: Timing analysis of rupture features to stations at-depth along the fault; up-dip and down-dip phases of propagation are shown in the top and bottom panels, respectively.

where D is the rupture track length from hypocenter to the fault trace and α is the fault inclination angle. Inverting Equations 4.9 and 4.10 and differentiating with respect to time gives the phase velocities of the up-dip and reflected P and S waves along the fault, $v_{\mathrm{p,s}}(x_1')$ and $v_{\mathrm{p,s}}'(x_1')$:

$$v_{\mathrm{p,s}}(x_1') = c_{\mathrm{p,s}} \qquad \text{if} \quad t \leq \frac{D}{c_{\mathrm{p,s}}}, \qquad (4.11)$$

$$v_{\mathrm{p,s}}'(x_1') = c_{\mathrm{p,s}} \frac{\sqrt{D^2 + 2(1 - \cos^2 \alpha)Dx_1' + x_1'^2}}{D(1 - \cos^2 \alpha) + x_1'} \qquad \text{if} \quad t > \frac{D}{c_{\mathrm{p,s}}}. \qquad (4.12)$$

While the phase velocity of P and S waves during their up-dip propagation is constant and set by the wave speeds, $c_{\mathrm{p,s}}$, the non-linearity of phase velocities for down-dip propagation (Equation 4.12) is a direct result of the acute angle between the reflected wave fronts and the fault, a fact inherently built into the geometry of thrust faults. For a vertical fault with $\alpha = 0°$, the phase velocity for the up and down-dip segment both degenerate to the wave speeds $c_{\mathrm{p,s}}$, as expected. A critical angle of α exists beyond which the reflected segment of the P and S waves reverse directivity and travel up-dip rather than down-dip; in the limit $\alpha \to 90°$, both up and down-dip phase velocities approach the wave speed and maintain up-dip directivity throughout the dynamic event. Near the fault trace $(x_1' \to 0)$, phase velocities for the down-dip segment are amplified by a factor of $\approx 1/(1 - \cos^2 \alpha)$, thus P and S waves feed back to the fault and achieve SS phase velocities near the free surface.

The SR rupture tip arrival to the free surface generates Rayleigh waves along the earth surface as well as a down-dip propagating TR signature. Rupture tip arrival to the fault trace consistently and simultaneously generates three distinct lobe-like fringe patterns, revealing stress concentrations in the material (Figure 4.13, left column). Two paired Rayleigh waves propagate bi-directionally away from the fault trace along the earth surface $(\pm\hat{x}_1$ directions) and arrive to stations at times $t_{\mathrm{R}}(x_1)$ (Equation 4.6, Section 4.1.1), which is a trivial function since phase velocities are the Rayleigh wave speed, $v_{\mathrm{R}}(x_1) = c_{\mathrm{R}}$. The third generated fringe pattern, the down-dip propagating TR signature (Figure 4.13, bottom left photograph), is confined along the angled fault and travels at a phase velocity, v'^{TR}. Arrival times of the up-dip rupture and the subsequent arrivals of the generated down-dip TR signature are written as:

$$t_{\mathrm{r}}^{\mathrm{SR}}(x_1') = \frac{D - x_1'}{v_{\mathrm{r}}^{\mathrm{SR}}} \qquad \text{if} \quad t \leq t_{\mathrm{r}}^{\mathrm{SR}}(0), \qquad (4.13)$$

$$t'^{\mathrm{SR}}(x_1') = \frac{x_1'}{v'^{\mathrm{TR}}} \qquad \text{if} \quad t > t_{\mathrm{r}}^{\mathrm{SR}}(0). \qquad (4.14)$$

Equation 4.13 is inverted and differentiated to obtain rupture-related phase velocities along the fault:

$$v_{\mathrm{r}}^{\mathrm{SR}}(x_1') = -v_{\mathrm{r}}^{\mathrm{SR}} \qquad \text{if} \quad t \leq t_{\mathrm{r}}^{\mathrm{SR}}(0), \qquad (4.15)$$

$$v'^{\mathrm{SR}}(x_1') = v'^{\mathrm{TR}} \qquad \text{if} \quad t > t_{\mathrm{r}}^{\mathrm{SR}}(0). \qquad (4.16)$$

The functional form of Equations 4.13, 4.14, 4.15, and 4.16 assume that the rupture and signature speeds are constant throughout the up and down-dip segments. Speed measurements of the up-dip SR rupture as well as the up-dip TR signature across all experiments yield well-constrained, constant values for v_r^{SR} and v^{TR}, and moreover, $v_r^{SR} = v^{TR}$ (Section 5.1). Aside from near-source accelerations during nucleation (Section 5.2), there is no measured acceleration of the SR rupture or the TR signature during up-dip propagation towards the free surface. The down-dip TR signature, v'^{TR}, however, experiences different mechanical conditions since the frictional fault has already been processed by the up-dip rupture, and thus its speed requires additional measurements (Section 4.2.2).

SS rupture tip arrival to the fault trace generates additional Mach fronts stemming from a down-dip stress concentration propagating along the fault with a phase velocity $v'^{SS} > c_s$ (Figure 4.13, right column). The up-dip Mach fronts impinge on the free surface and travel bi-directionally away from the fault trace with differing yet constant speeds, with their timing $t_M(x_1)$ (Equation 4.4) and phase velocities $v_M(x_1)$ (Equation 4.5) determined in Section 4.1.1. An additional fringe structure resembling a down-dip Mach cone is observed in the photo-elastic image series upon rupture tip arrival to the fault trace, $t_r^{SS}(x_1' = 0)$: a consistent phenomenon across all SS experiments. While down-dip Mach fronts are clearly visible in the foot wall, wave reflections in the hanging wall obscure the paired down-dip Mach front in the mixed fringe pattern, making it difficult to discern (Figure 4.13, bottom right photograph). Arrival times and phase velocities of these down-dip Mach fronts along the simulated earth surface, $t_M'(x_1)$ (Equation 4.7) and $v_M'(x_1)$ (Equation 4.8), are determined in Section 4.1.5. Up and down-dip SS rupture feature arrival times and phase velocities are:

$$t_r^{SS}(x_1') = \mathcal{H}\left[x_1' - x_1'^{\,tr}\right]\left(\frac{D - x_1'}{v_r^{SR}}\right) + \mathcal{H}\left[x_1'^{\,tr} - x_1'\right]\left(\frac{l_{tr}}{c_s} + \frac{x_1'^{\,tr} - x_1'}{v_r^{SS}}\right) \quad \text{if} \quad t \leq t_r^{SS}(0), \quad (4.17)$$

$$t'^{SS}(x_1') = \mathcal{H}\left[x_1' - x_1'^{\,tr}\right]\left(\frac{x_1'}{v'^{TR}}\right) \quad + \mathcal{H}\left[x_1'^{\,tr} - x_1'\right]\left(\frac{x_1'}{v'^{SS}}\right) \quad \text{if} \quad t > t_r^{SS}(0), \quad (4.18)$$

$$v_r^{SS}(x_1') = \mathcal{H}\left[x_1' - x_1'^{\,tr}\right]\left(-v_r^{SR}\right) \quad + \mathcal{H}\left[x_1'^{\,tr} - x_1'\right]\left(-v_r^{SS}\right) \quad \text{if} \quad t \leq t_r^{SS}(0), \quad (4.19)$$

$$v'^{SS}(x_1') = \mathcal{H}\left[x_1' - x_1'^{\,tr}\right]\left(v'^{TR}\right) \quad + \mathcal{H}\left[x_1'^{\,tr} - x_1'\right]\left(v'^{SS}\right) \quad \text{if} \quad t > t_r^{SS}(0), \quad (4.20)$$

where $x_1'^{\,tr} = D - l_{tr}$ defines the boundary along the fault where the rupture switches speed domains from SR to SS (based on the calculated transition length, l_{tr}). Since transition occurs during the up-dip rupture, Heaviside functions, $\mathcal{H}(\cdot)$, are required to assure correct terms are used to calculate arrivals based on station location $x_1' > l_{tr}$ or $x_1' < l_{tr}$. The functional forms of Equations 4.17, 4.18, 4.19, and 4.20 assume constant up-dip rupture and down-dip signature speeds, v_r^{SS} and v'^{SS}, respectively. Measurements of up-dip rupture speeds (Section 5.1) and lack of Mach front curvature suggest no acceleration of the rupture tip within the resolution of the camera inter-frame times [55]. As discussed in Section 4.1.5, the down-dip Mach fronts have a curved leading front, suggesting a deceleration of the SS signature; however, the entire down-dip fringe structure maintains a SS speed.

4.2.2 Earth surface effects: feedback to the fault

Phase velocities of various rupture features along the fault line are plotted for up-dip propagation in Figure 4.14 (Equations 4.9, 4.11, 4.13, 4.15, 4.17, and 4.19) and down-dip propagation in Figure 4.15 (Equations 4.10, 4.12, 4.14, 4.16, 4.18, and 4.20). Values $x'_1 = 0 - 74.3$ mm are plotted, representing the entire rupture track length from the source at-depth to the fault trace at the earth surface.
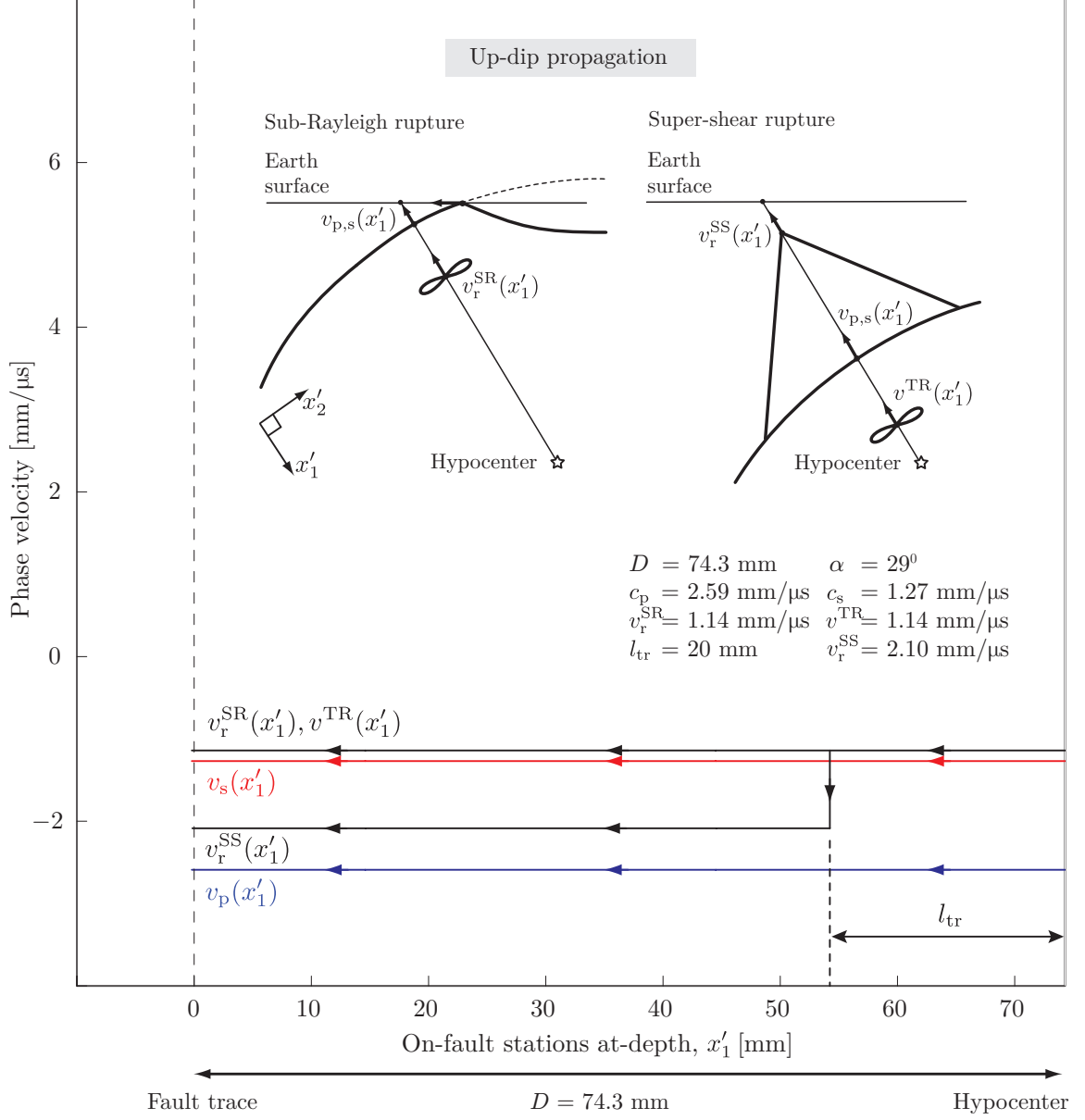
Figure 4.14: Phase velocities of various rupture features along the fault during the up-dip phase.

The phase velocities of the P wave, $v_p(x'_1)$, S wave, $v_s(x'_1)$, and SR rupture tip, $v_r^{SR}(x'_1)$, are all constant during up-dip propagation (Figure 4.14). Negative velocities imply movement towards the fault trace, according to the $\hat{x}'_1 - \hat{x}'_2$ frame. The schematic inserts represent SR and SS events

prior to the rupture tip reaching the fault trace: other than the addition of the Mach cone, the schematics themselves are geometrically identical. The rupture tip accelerates to a SR speed within the nucleation zone and remains constant during up-dip propagation towards the free surface. In case of transition, the rupture tip abruptly accelerates to the SS domain (Figure 4.15, arrow at l_{tr}) and stabilizes to a new constant value for the remainder of the fault length. Note that $v_r^{SR} = v'^{TR}$.
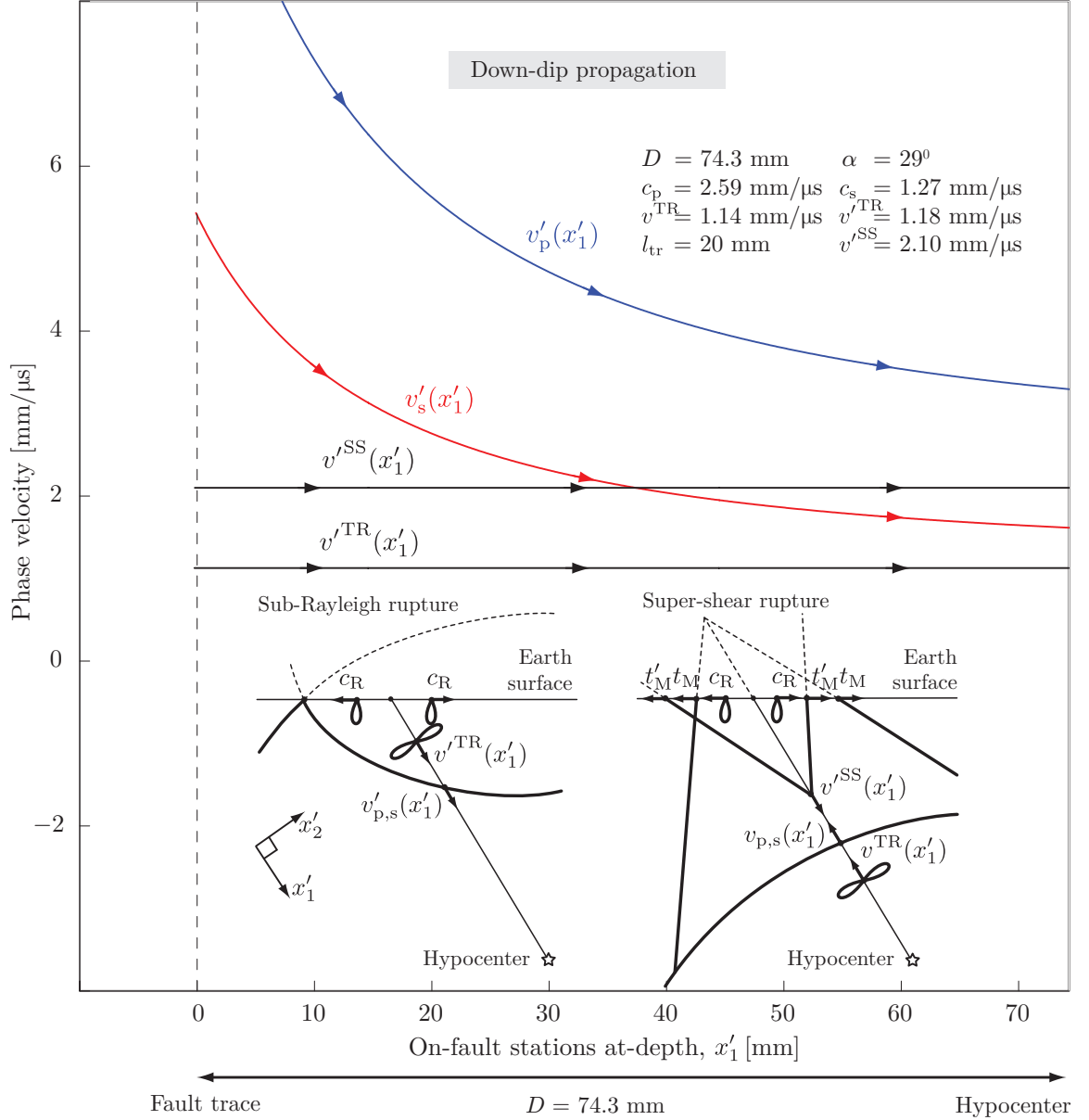
Figure 4.15: Phase velocities of various rupture features along the fault during the down-dip phase.

Phase velocities of down-dip propagation are plotted in Figure 4.15. Schematic inserts represent SR and SS events after the rupture tip has reached the fault trace. The down-dip P and S wave phase velocities $v'_{p,s}(x'_1)$ along the fault decay monotonically due to the asymmetry introduced in

the fault geometry by the angled interface ($\alpha \neq 0°$). Note that the down-dip P and S wave phase velocities are always SS within the experimental time window $T_{\text{exp}} = 120\,\mu$s, with peak magnitudes closest to the fault trace. Features generated with the arrival of the rupture tip to the fault trace travel back down-dip along the fault at nearly constant speeds; a SR event generates a down-dip TR signature, v'^{TR}, with the arrival of the SR rupture tip, while a SS event sequentially generates a down-dip SS signature, v'^{SS}, with the arrival of the SS rupture followed by a down-dip TR signature, v'^{TR}, with the arrival of the up-dip TR signature. In the SR case, stations at depth are first excited by reflected P waves, followed by reflected S waves, and finally the generated TR signature. In the SS case, the leading Mach front reflects from the free surface and mixes with the remaining up-dip features, possibly focusing effects of several dynamic features for stations at critical distances, x'_1. Behind the reflected Mach fronts are the reflected S waves and the generated down-dip TR signature.

4.2.3   Measurements of phase velocities along the fault
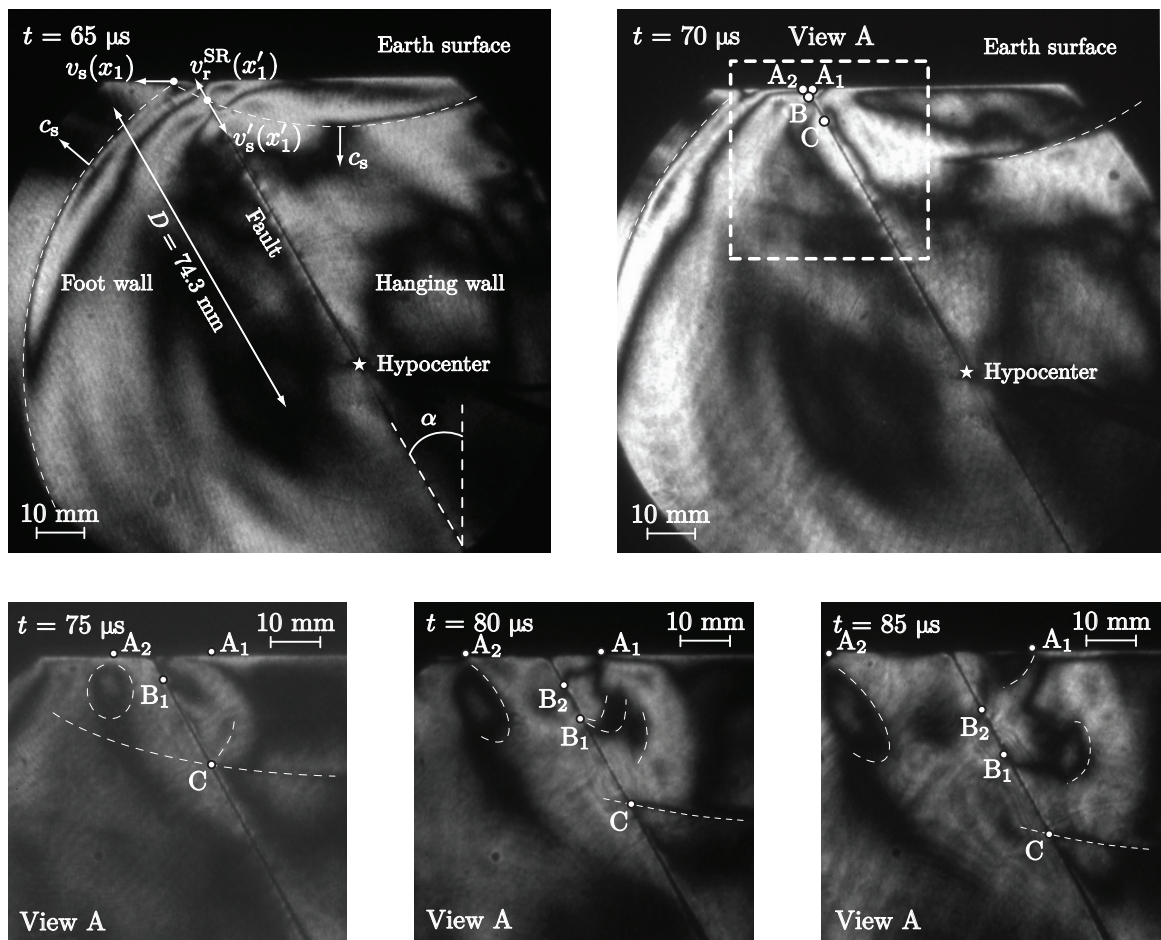
Figure 4.16: SR rupture feature speed measurements from times $t = 65\,\mu$s through $t = 85\,\mu$s. Markers A_1 and A_2 track surface Rayleigh waves (v_R), B tracks a down-dip TR signature (v'^{TR}), and C tracks the intersection of the reflected S wave with the fault (v'_s).
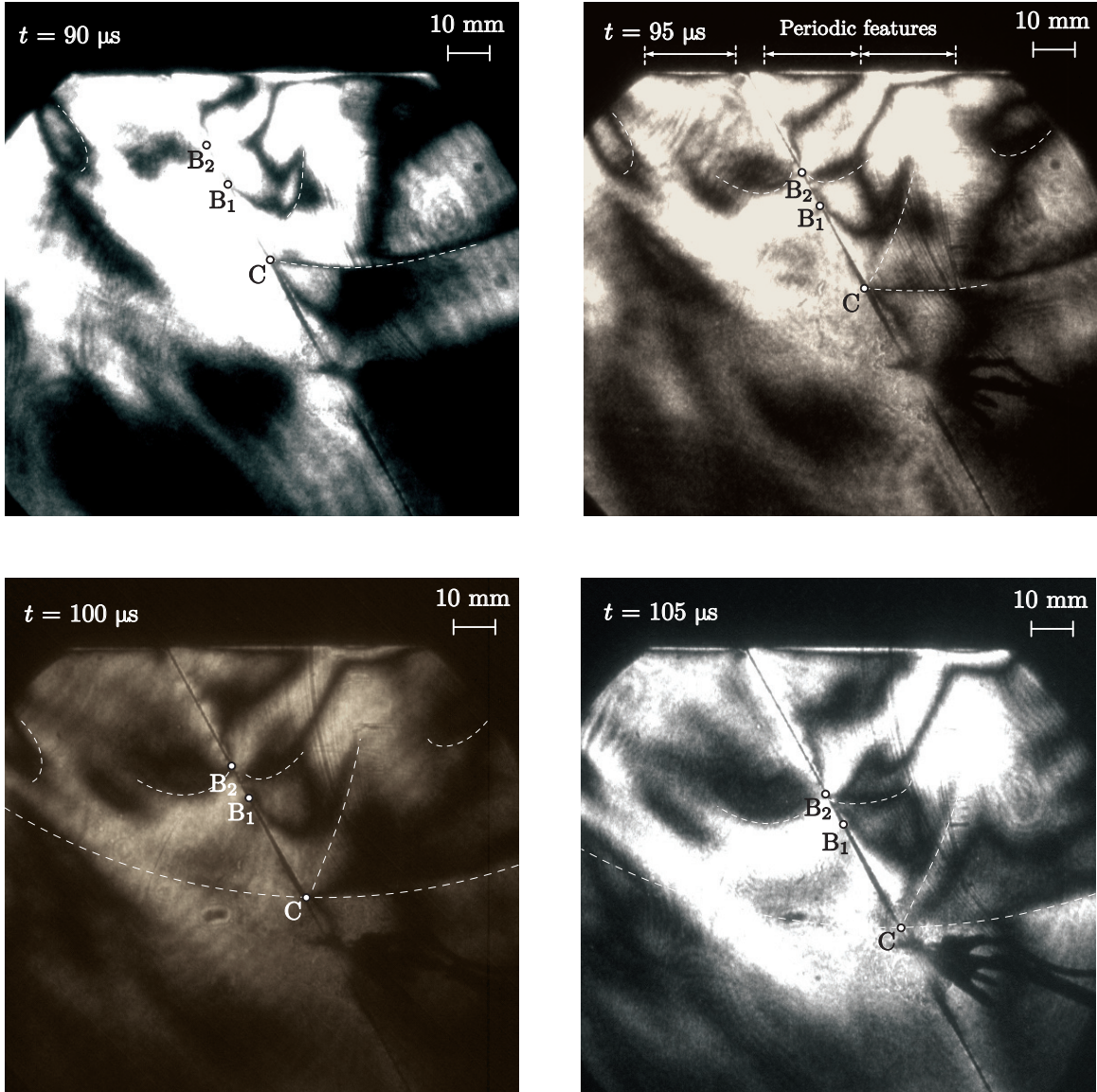
Figure 4.17: SR rupture feature measurements from times $t = 90$ through $t = 105\,\mu s$, continued from Figure 4.16. A linear fringe pattern characteristic of a SS slip feature emerges from marker C.

Digital image sequences are used to validate the proposed timing framework of Section 4.2.1 for both SR and SS ruptures. Figures 4.16 and 4.17 show the evolution of a SR rupture in the experimental thrust fault configuration at $5\,\mu s$ inter-frame times. Markers A_1, A_2, B, and C track two surface Rayleigh waves, the down-dip TR signature, and the intersection of the reflected S wave with the fault, respectively. Dashed curves highlight key fringe patterns representative of each rupture feature. Note the magnified scale of view A. Measurements show that phase velocities $A_1 = 1.20\,mm/\mu s$ and $A_2 = 1.36\,mm/\mu s$ are about the Rayleigh wave speed of Homalite H-100, $c_R = 1.18\,mm/\mu s$. Marker B moves at an average constant speed of $B = 1.40\,mm/\mu s$, while marker C moves at an average speed of $C = 1.60\,mm/\mu s$. A linear fringe pattern characteristic of a Mach
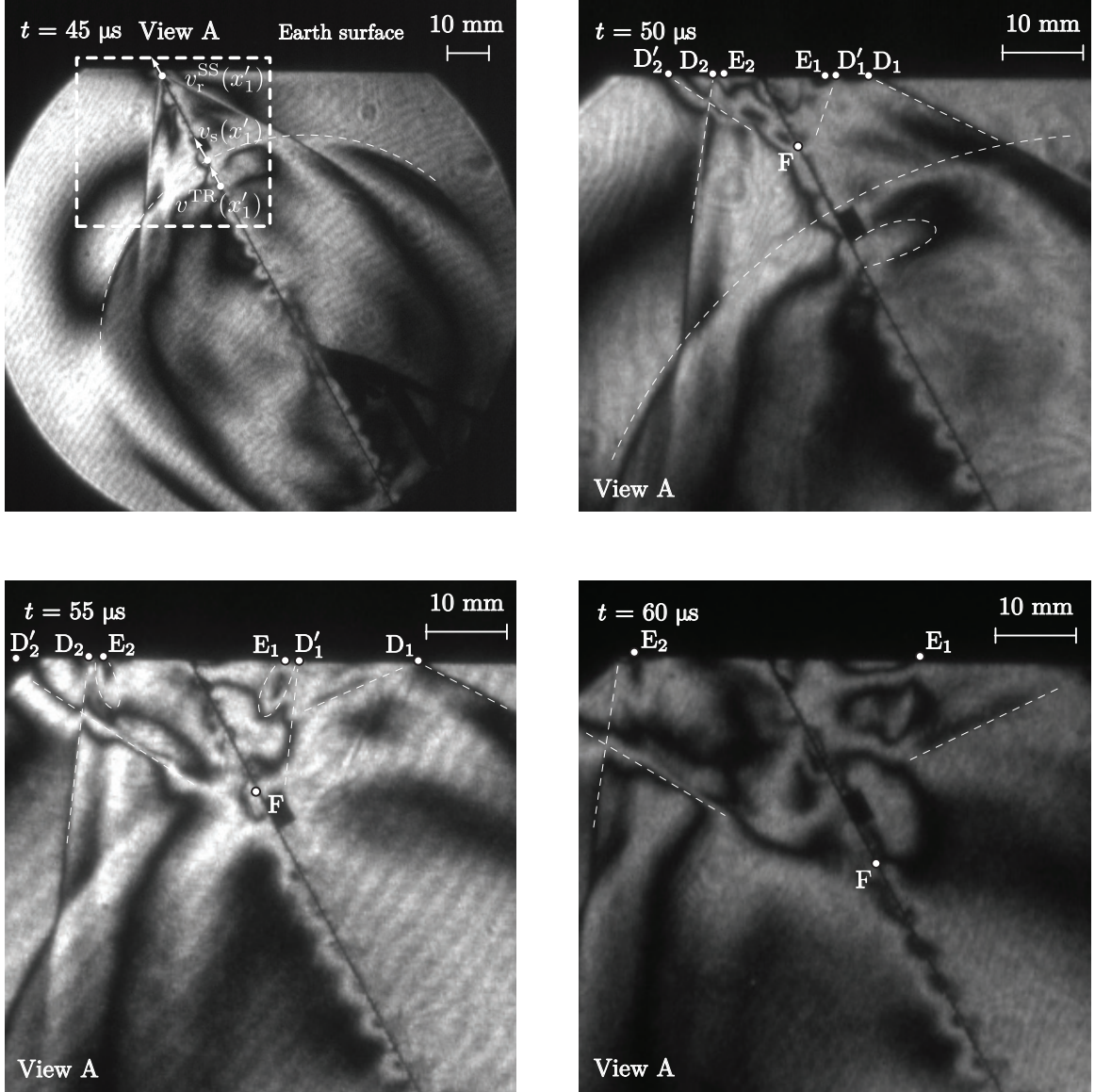
Figure 4.18: SS rupture feature measurements from times $t = 45 - 60\,\mu\text{s}$. Up and down-dip Mach front arrivals to the free surface are tracked with markers D_1, D_2 (v_M), and D'_1, D'_2 (v'_M), respectively. Markers E_1, E_2 track Rayleigh waves (v_R) and marker F tracks the down-dip SS signature (v'^{SS}).

front stems from marker C and is visible in the hanging wall at times $t = (95, 100, 105)\,\mu\text{s}$: this photograph sequence shows evidence of a possible SS down-dip rupture (or slip feature) for an event which was originally SR throughout the entire up-dip propagation towards the free surface.

Figure 4.18 shows the evolution of a SS rupture in the experimental thrust fault configuration at $5\,\mu\text{s}$ inter-frame times. Markers D_1 and D'_1 correspond to up and down-dip Mach front intersections along the earth surface on the hanging wall plate, while markers D_2 and D'_2 correspond to those on the foot wall: primed variables indicate down-dip features. Markers E_1 and E_2 track lobe-like structures characteristic of surface Rayleigh waves. Marker F tracks the location of a down-dip

SS signature (v'^{SS}). Speed measurements of Mach front phase velocities give $D_1 = 2.5\,\text{mm/μs}$, $D'_1 = 0.75\,\text{mm/μs}$ and $D_2 = 1.45\,\text{mm/μs}$, $D'_2 = 2.55\,\text{mm/μs}$. Speeds alternate for up-dip and down-dip Mach front phase velocities, as expected from geometric symmetry (Section 4.1.5). Markers E_1 and E_2 move at speeds $E_1 = 1.36\,\text{mm/μs}$ and $E_2 = 0.80\,\text{mm/μs}$, values close to the Rayleigh wave speed, $c_{\text{R}} = 1.18\,\text{mm/μs}$. Marker F propagates down-dip at SS speeds of $F = 2.42\,\text{mm/μs}$.

4.2.4 Fault parallel and normal velocity records

The image/trace sequence in Figures 4.19-4.20 presents two experiments where fault parallel and fault normal ground motion velocities are recorded just to the right and to the left of the fault at a depth $x'_1 = 40\,\text{mm}$ on the hanging ($x'_2 = +\eta$) and foot wall plates ($x'_2 = -\eta$). The stations are marked by a set of white circles while the paired red and black arrows represent the two fault parallel and two fault normal components measured in each experiment, respectively. The experiment in the left column is conducted at an initial static pre-load $P = 2.5\,\text{MPa}$, while that of the right column is conducted at $P = 7.5\,\text{MPa}$, maintaining all other parameters nominally identical. In both setups, the large shadow in the photographs is the end effector of the velocimeter beam positioned to measure the hanging wall fault normal ground motions; however, the remaining three velocimeter beam end effectors are outside the field-of-view. Note the grazing angle approach discussed in Section 2.2.3.2.

At time $t = 30\,\text{μs}$ (Figure 4.19, top panels), the P wave emitted from nucleation has swept past the measurement stations located a distance $x'_1 = 40\,\text{mm}$ in both experiments. Despite the difference in applied loads, the images look nearly identical between the two cases, suggesting the feature arrival times are independent of the sampled load P (Chapter 5).

At $t = 40\,\text{μs}$ (Figure 4.19, bottom panels), the S wave from nucleation and the rupture tip have swept across the measurement stations, causing peak magnitude ground motions in both loading cases. Fault normal records for the $P = 7.5\,\text{MPa}$ experiment have greater peak magnitudes and move in tandem ($\dot{u}_2^+ = \dot{u}_2^-$) compared to the $P = 2.5\,\text{MPa}$ experiment, where the records are anti-symmetric in nature. Peak magnitudes of fault parallel traces are only slightly greater in the $P = 7.5\,\text{MPa}$ experiment; however, fault parallel motions are close to anti-symmetric in the $P = 7.5\,\text{MPa}$ experiment, $|\dot{u}_1^+| \approx -|\dot{u}_1^-|$, and nearly in tandem for the $P = 2.5\,\text{MPa}$ event. This deepest station $x'_1 = 40\,\text{mm}$ captures rupture ground motions without knowledge of the free surface boundary, as reflected information has not yet arrived from the free surface (reflected P waves, t'_p).

At $t = 60\,\text{μs}$ (Figure 4.20, top panels), the SR rupture tip has passed the station at $x'_1 = 40\,\text{mm}$ and is almost at the free surface. In both experiments, the rupture tip remains SR in speed, noted by the absence of Mach cones in the photographs. Fault normal records oscillate about zero after the rupture tip passes the measurement stations; these oscillations are in tandem for $P = 7.5\,\text{MPa}$ and anti-symmetric for $P = 2.5\,\text{MPa}$ experiments. Fault parallel ground motions also settle about the zero value with anti-symmetric and tandem motion in the $P = 7.5$ and $2.5\,\text{MPa}$ cases, respectively.
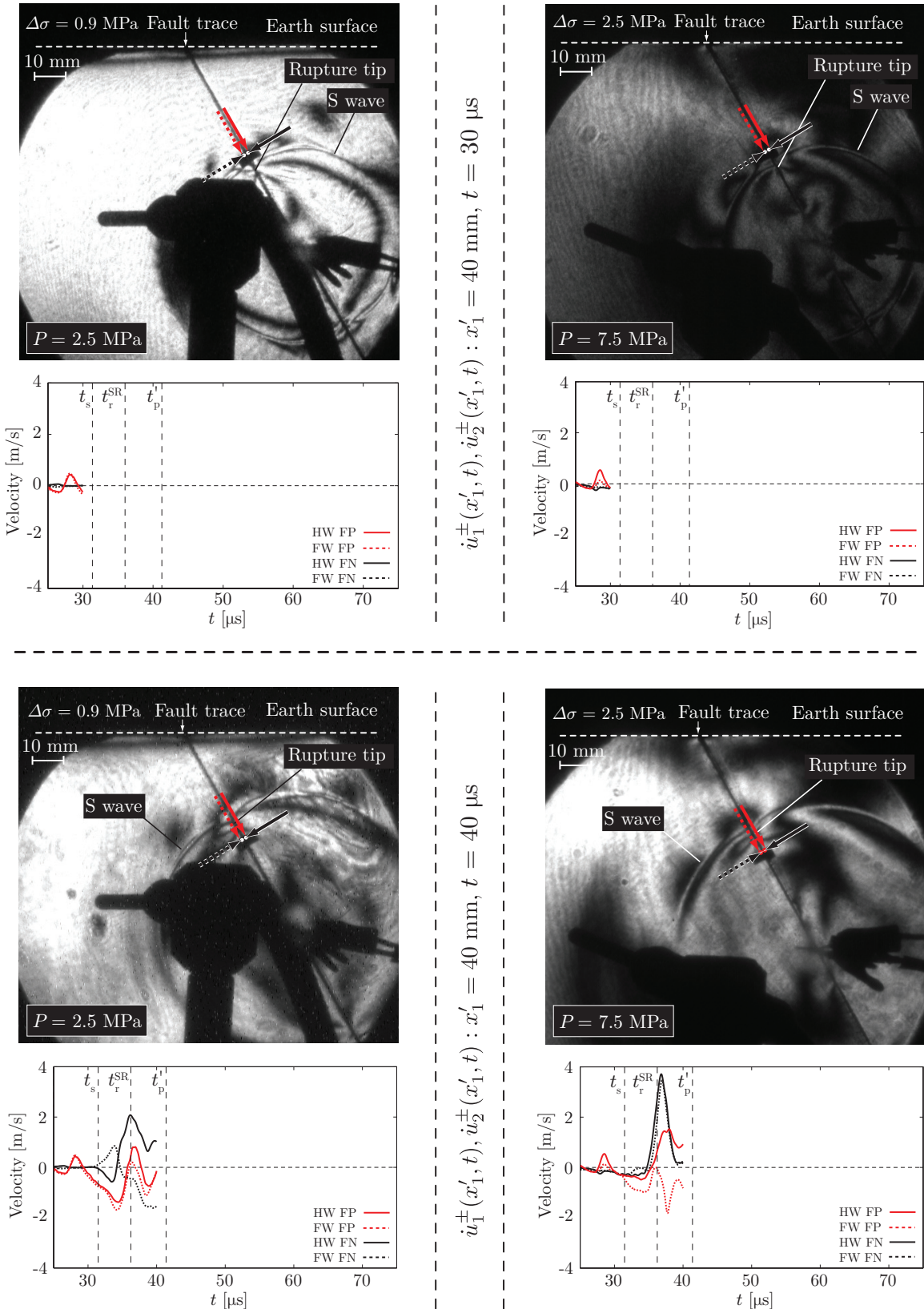
Figure 4.19: SR fault parallel ($\dot{u}_1^{\pm}$) and normal ($\dot{u}_2^{\pm}$) image/trace sequence at $t = 30$ and $t = 40\,\mu\text{s}$.
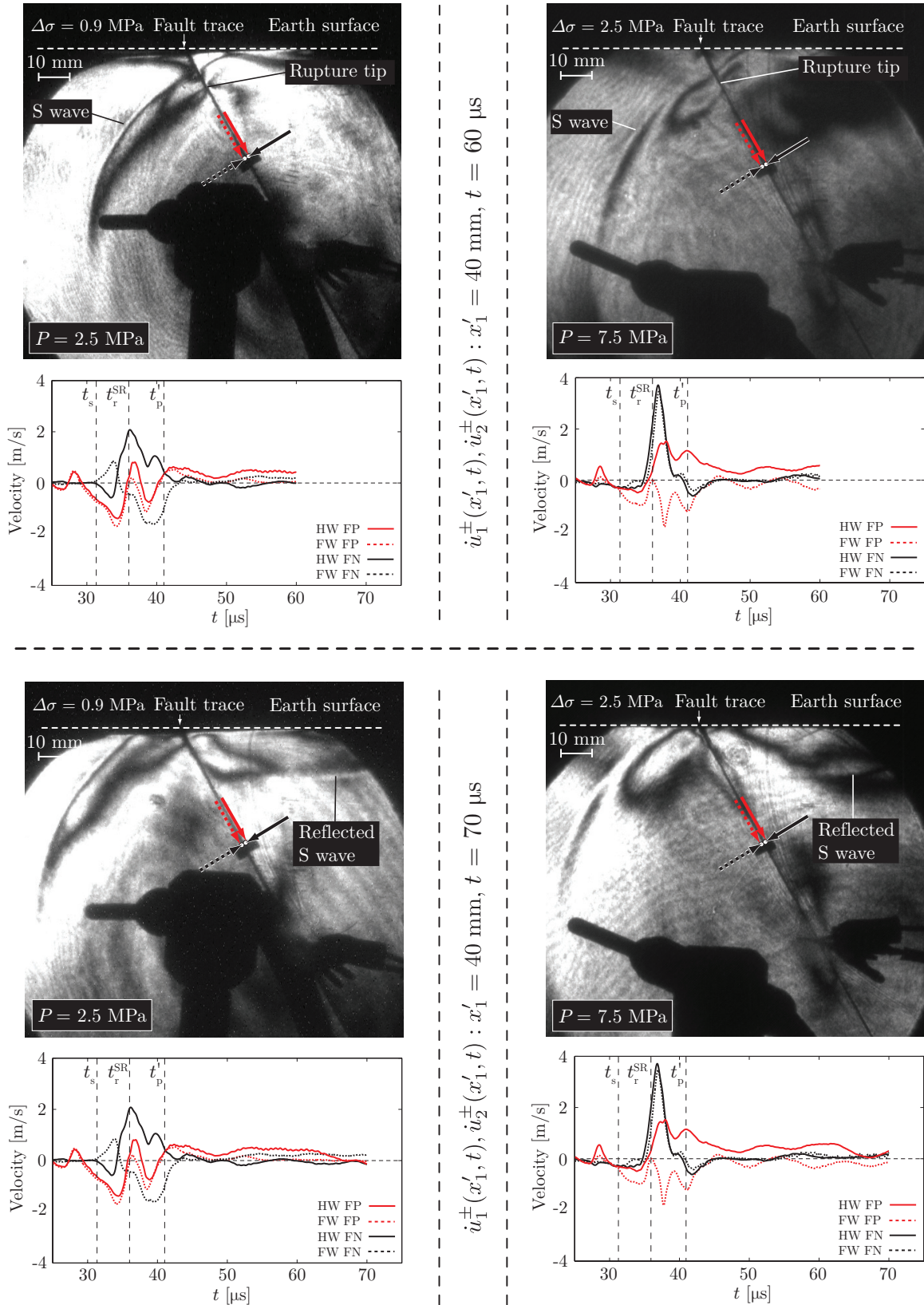
Figure 4.20: SR fault parallel ($\dot{u}_1^{\pm}$) and normal ($\dot{u}_2^{\pm}$) image/trace sequence at $t = 60$ and $t = 70\,\mu$s.

At $t = 70\,\mu$s (bottom panels of Figure 4.20), the SR rupture tip has struck the free surface. A reflected S wave is seen in the hanging wall plate in both experiments.

Figures 4.21, 4.22, and 4.23 summarize the reduced outputs of fault parallel and normal velocity measurements for loads $P = 2.5\,$MPa, $P = 5.0\,$MPa, and 7.5 MPa, respectively. Timing lines bound the arrivals of P waves (t_p), S waves (t_s), and the SR rupture tip (t_r^SR) to the various stations for both up and down-dip propagation (distinguished by primed variables). Note: the phase velocities of both P and S waves along the fault remain SS throughout down-dip propagation (see Section 4.2.2). In some $P = 7.5\,$MPa experiments, transition to SS is observed at $l_\mathrm{tr} \approx 40\,$mm from the hypocenter during the up-dip phase. The down-dip trailing-Rayleigh signature is marked by t'^TR.

Significant ground motions commence with the arrival of the rupture tip. P wave effects are on the order of 0.10 m/s in both components of motion across all loads $P = (2.5, 5.0, 7.5)\,$MPa, a negligible fraction compared to peak ground motion magnitudes up to 6 m/s for fault parallel and 4 m/s for fault normal records associated with the arrival of the rupture tip. Since $c_\mathrm{p} \approx 2c_\mathrm{s}$, effects of the up-dip and down-dip P waves are measured prior to the arrival of the first S wave to all stations with the exception of $x_1' = 40\,$mm, where timing dictates that the reflected P waves arrive after all key up-dip information has swept the station. P wave effects are most apparent in fault parallel records (top panels of Figures 4.21, 4.22, and 4.23) and nearly absent in the fault normal records (bottom panels of Figures 4.21, 4.22, and 4.23). Minor downswings on the order of 1 m/s are measured in the hanging and foot wall fault parallel records with the arrival of the first S wave (t_s). S wave effects on fault parallel motions are most prominent in the lowest load case $P = 2.5\,$MPa (Figure 4.21). The S wave effects in the fault normal records are on the order of 0.1 m/s and are again most prominent in the $P = 2.5\,$MPa experiments. The most significant ground motions commence and persist for roughly 10 µs with the arrival of the SR rupture tip, which trails just behind the S wave at $v_\mathrm{r}^\mathrm{SR} \approx 0.90c_\mathrm{s}$. The arrival of the reflected S wave and the generated down-dip TR signature further enhance both components of ground motion as they propagate back down-dip (further discussed in Section 4.2.5). Up-dip and down-dip signatures are most distinct for stations at depth and coalesce as the measurement stations approach the free surface ($x_1' \to 0\,$mm).

The peak amplitudes of fault parallel and normal ground motions are controlled by the initial static pre-load on the specimen, P, as well as the measurement station proximity to the free surface, x_1'. Figure 4.24 plots the global extrema for fault parallel (left panel) and fault normal (right panel) records presented in Figures 4.21, 4.22, and 4.23. The blue, red, and black colors identify the three static pre-loads, $P = (2.5, 5.0, 7.5)\,$MPa, while the solid and dashed curves distinguish between on-fault stations on the hanging wall ($\dot{u}_1^+$, $\dot{u}_2^+$) and foot wall ($\dot{u}_1^-$, $\dot{u}_2^-$), respectively.

Global extrema in the ground motion records correspond to signatures associated with the rupture tip sweeping past the measurement stations. For any given station x_1', the global extrema of both fault parallel and normal components of ground motion increase with an increase of load from
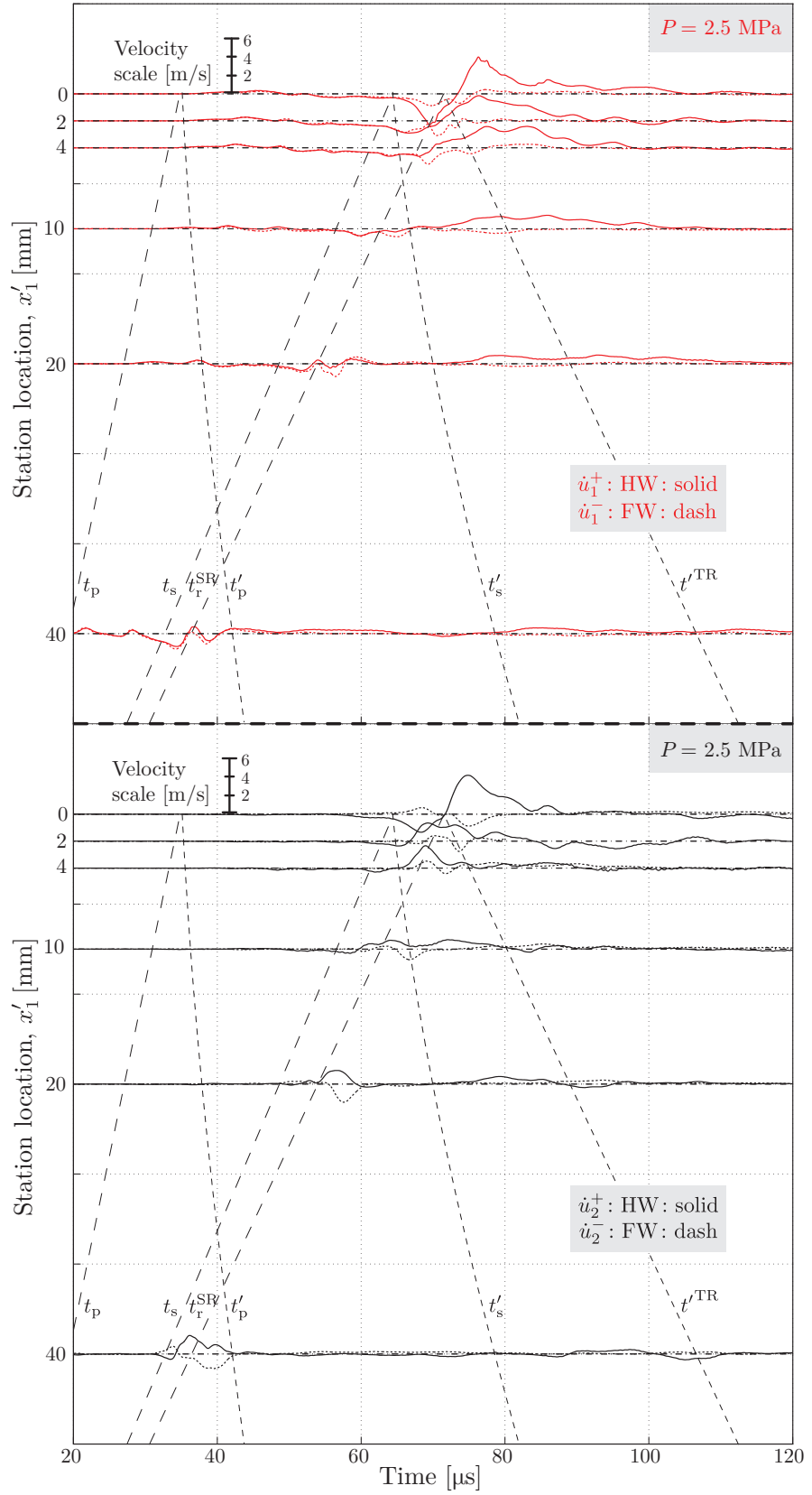
Figure 4.21: Summary of paired fault parallel ($\dot{u}_1^{\pm}$) and normal ($\dot{u}_2^{\pm}$) records for load $P = 2.5\,\mathrm{MPa}$.
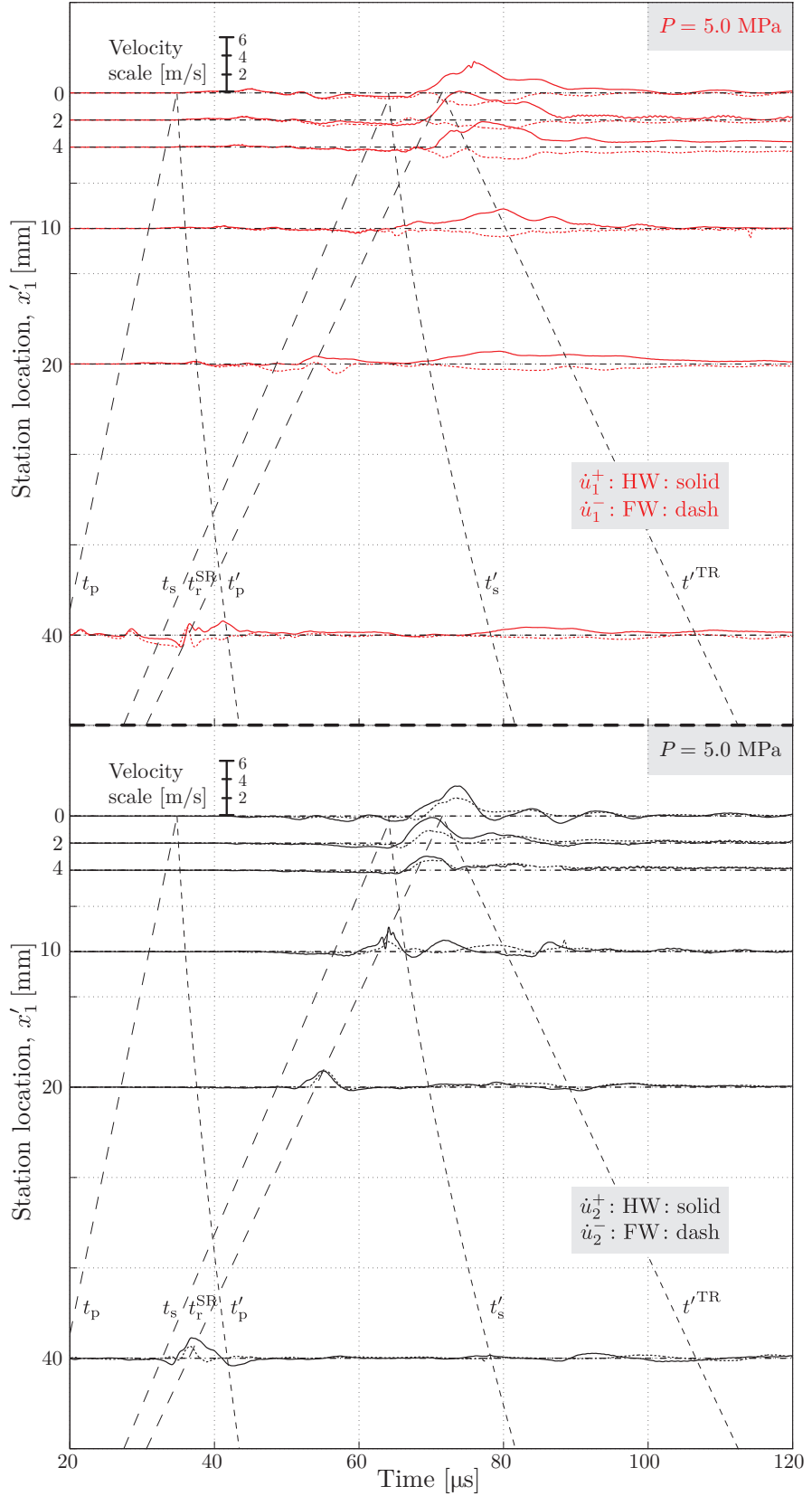
Figure 4.22: Summary of paired fault parallel ($\dot{u}_1^{\pm}$) and normal ($\dot{u}_2^{\pm}$) records for load $P = 5.0\,\mathrm{MPa}$.
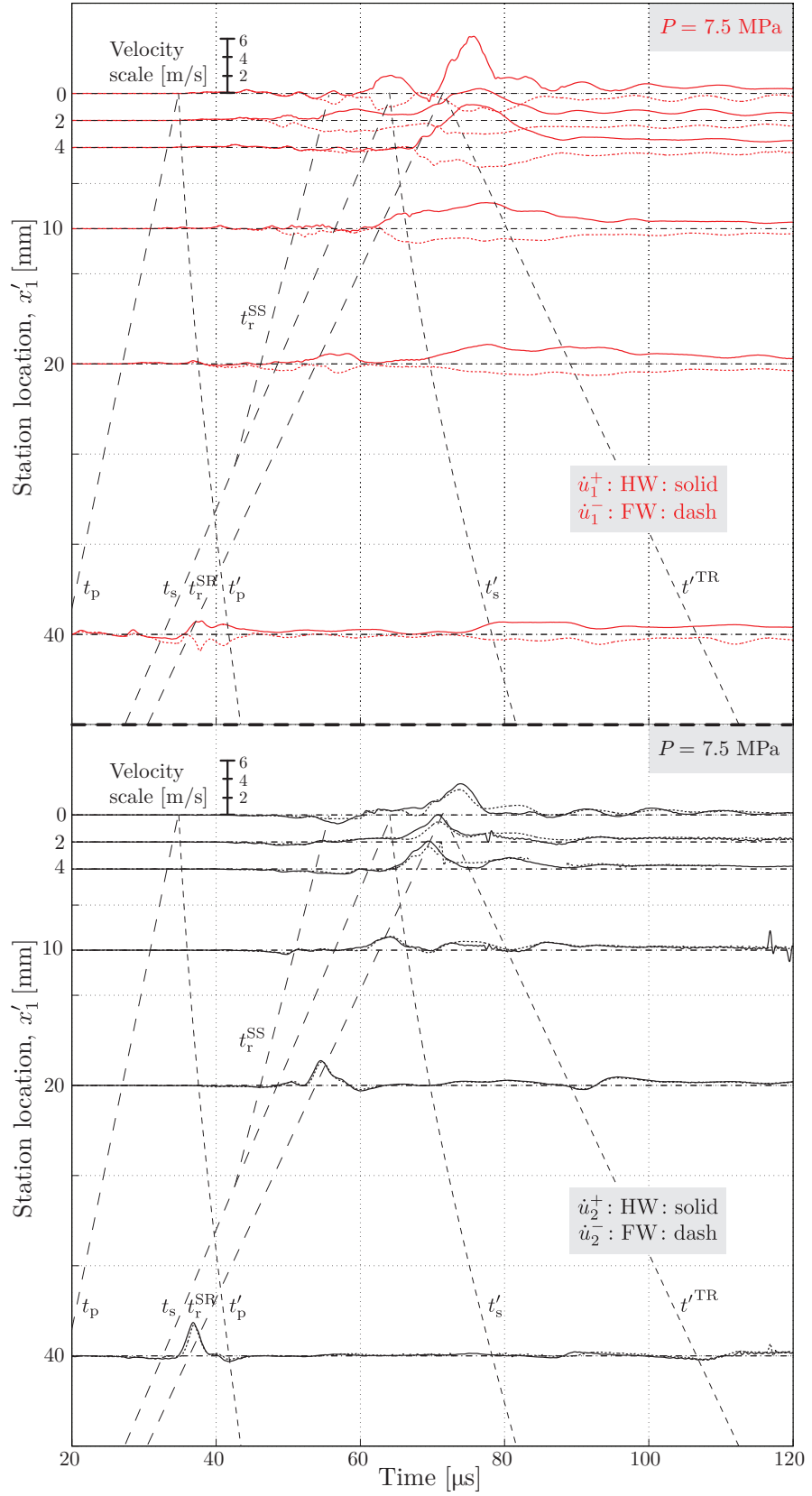
Figure 4.23: Summary of paired fault parallel ($\dot{u}_1^{\pm}$) and normal ($\dot{u}_2^{\pm}$) records for load $P = 7.5\,\text{MPa}$.
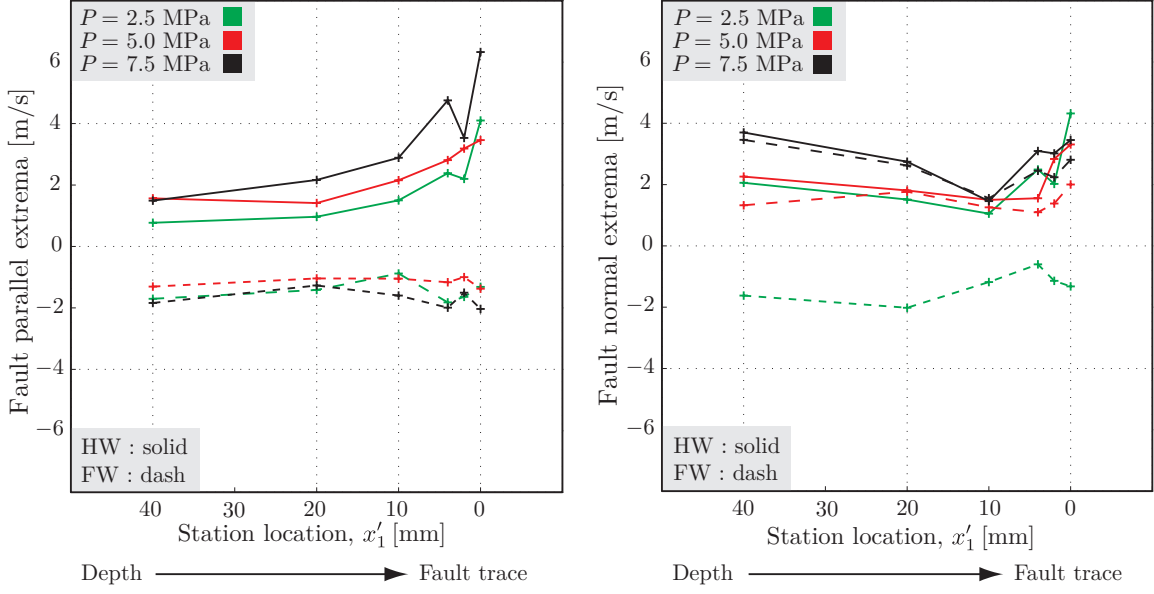
Figure 4.24: Fault parallel and normal peak velocity amplification near the free surface; hanging wall (solid) ground motions are enhanced more than those of the foot wall (dashed).

$P = 2.5$ to $7.5\,\mathrm{MPa}$ (Figure 4.24). The rupture tip signal rise times are nearly identical across all loads for fault parallel and normal components of ground motion, as shown in Figures 4.21, 4.22, and 4.23. Furthermore, the rupture tip speed does not vary for the range of loads tested (Chapter 5), suggesting that the increase in signal amplitude is a direct result of an increase in P. Load dependency of rupture tip signature amplitude has been previously investigated in a similar experimental setup for a strike-slip configuration [37], concluding a similar relation between applied load and peak signal amplitude. Mode-II fracture theory of a dynamic steady-state slip pulse confined to the fault plane states that the slip velocity, $\dot{u}_{\mathrm{slip}} = \dot{u}_1^+ - \dot{u}_1^-$, may be represented as [37, 128, 129]:

$$\dot{u}_{\mathrm{slip}} = \frac{(\tau_{\mathrm{d}} - \tau_{\mathrm{s}})c_{\mathrm{s}}}{\mu} F\left[\frac{v_{\mathrm{r}}}{c_{\mathrm{s}}}, \frac{R}{L}\right], \tag{4.21}$$

where $(\tau_{\mathrm{d}} - \tau_{\mathrm{s}})$ is the material strength drop, μ is the shear modulus, L is the total interface length, and F is a function of non-dimensional rupture tip speed v_{r} and process zone size R. The strength drop is directly related to the static and dynamic friction coefficients f_{s} and f_{d}, as well as the resolved normal stress along the interface, $\sigma_{22} = P \cos^2 \alpha$. The rupture tip field strength increases with an increase of load, P, inducing greater overall accumulated slip along the interface, and ultimately a larger global stress drop, $\Delta\sigma = P_{\mathrm{f}} - P$ (Section 5.2).

Signal amplification occurs in both fault parallel and fault normal components of ground motion as the measurement stations approach the free surface, $x_1' = 0\,\mathrm{mm}$. Figure 4.24 (left panel) shows the increase in global extrema in the fault parallel component in both the hanging ($\dot{u}_1^+$, solid curves) and foot wall ($\dot{u}_1^-$, dashed curves) records as the measurement stations approach the fault trace.

Away from the free surface at stations $x'_1 = (20, 40)$ mm, paired hanging and foot wall fault parallel measurements have roughly identical magnitudes for the fault parallel extrema. Moreover, the fault parallel ground motion signatures should be anti-symmetric for any given paired station in the absence of a free surface, $|\dot{u}_1^+| = -|\dot{u}_1^-|$; this is an expected result from mode-II fracture theory for two semi-infinite plates joined along a linear weak plane [37], i.e., the fault, and is supported by fault parallel measurements of the deepest stations $x'_1 = (20, 40)$ mm for all tested loads $P = (2.5, 5.0, 7.5)$ MPa (Figures 4.21, 4.22, and 4.23). Deviations from anti-symmetry in the records are likely due to the finite distance between the stations and the fault (Section 4.2, $\eta^{\pm}$). Introducing the free surface boundary condition to the system breaks the anti-symmetry between paired fault parallel records; the hanging wall maxima exhibit a higher rate of amplification as $x'_1 \to 0$ mm while the foot wall minima remain banded. The presence of the free surface in itself, however, is insufficient to induce enhanced fault parallel ground motions in the hanging wall plate; the fault line must not be normal to the free surface ($\alpha \neq 0°$) to avoid symmetry between the two plates, in which case both right or left lateral slip will preserve fault parallel asymmetry amongst paired stations.

Similar signal amplification of fault normal component extrema occurs near the free surface, as shown in Figure 4.24 (right panel). For the higher load experiments $P = 5.0$ and 7.5 MPa, the extrema of fault normal records for paired stations are nearly identical in value, with increasing disparity as $x'_1 \to 0$ mm. In the lowest load experiments, $P = 2.5$ MPa, however, the extrema have anti-symmetric values, with a similar increase in disparity as $x'_1 \to 0$ mm; this is a result of the low initial static confinement pressure across the fault. The hanging wall stations experience enhanced fault normal ground motions near the fault trace compared to the foot wall, much like in the fault parallel component. In accordance with mode-II theory, fault normal component continuity is maintained for the higher load experiments $P = (5.0, 7.5)$ MPa, with greatest deviation near the free surface. In the lowest load case, $P = 2.5$ MPa, the dynamic fault normal stresses outweigh the confinement pressure and force paired stations to move away from each other.

Ground motion records of Figures 4.21, 4.22, and 4.23 and the amplification curves of Figure 4.24 show the overall enhanced ground motions in the hanging wall compared to the foot wall, similar to the ground motion enhancement of simulated earth surface-normal measurements of Section 4.1.

4.2.5 Fault slip and opening rates

For any given paired stations at depth x'_1, the slip rate is defined as the difference between the hanging and foot wall fault parallel records, $\dot{u}_{\mathrm{slip}}(x'_1, t) = \dot{u}_1^+(x'_1, t) - \dot{u}_1^-(x'_1, t)$. Similarly, the fault opening rate is defined as the difference between the hanging and foot wall fault normal records, $\dot{u}_{\mathrm{open}}(x_1, t) = \dot{u}_2^+(x'_1, t) - \dot{u}_2^-(x'_1, t)$. Slip and opening rates for the data presented in Section 4.2.4 are plotted in Figures 4.25, 4.26, and 4.27 for loads $P = 2.5$ MPa, $P = 5.0$ MPa, and $P = 7.5$ MPa, respectively; a rupture criterion based on accumulated slip (green dots) is discussed in Section 4.2.6.

Slip commences with the arrival of the up-dip SR (or SS) rupture tip to the measurement stations. Up-dip P wave arrivals induce near-zero slip of the interface across all stations. Reflected P waves feed back to the fault line and increase slip rate to values on the order of $0.1\,\mathrm{m/s}$. Up-dip S wave arrivals also induce no slip in the $P = 2.5$ and $P = 5.0\,\mathrm{MPa}$ experiments (Figures 4.25 and 4.26), with the exception of station $x_1' = 20\,\mathrm{mm}$ in the $P = 5.0\,\mathrm{MPa}$ load, where slip rate increases to about $1\,\mathrm{m/s}$. In the highest load case $P = 7.5\,\mathrm{MPa}$, S wave arrivals are preceded by the SS rupture tip, t_r^SS, which has already initiated slip (Figure 4.27). Peak magnitudes of slip rate across all experiments are indeed associated with the arrival of the SR rupture tip, marked by timing line t_r^SR in Figures 4.25, 4.26, and 4.27. For the deepest station $x_1' = 40\,\mathrm{mm}$, the reflected P waves arrive just at the end of the slip pulse of rise time $\approx 10\,\mathrm{\mu s}$ (marked by squares in Figures 4.25, 4.26, and 4.27). This slip pulse unzips the locked fault during up-dip propagation towards the free surface.

Slip rate data confirms the existence of a down-dip propagating rupture tip. Inspection of slip rate records at deeper stations $x_1' = (20, 40)\,\mathrm{mm}$ indicate that the interface locks after the up-dip slip pulse processes the fault. Arrival of the reflected S waves, marked by stars in Figures 4.25, 4.26, and 4.27, re-ruptures the fault with slip pulses of nearly the same magnitude as their associate up-dip rupture signals. Up-dip and down-dip rupture features coalesce as $x_1' \to 0\,\mathrm{mm}$, causing amplification and broadening of the slip pulse for stations near the free surface, $x_1' \le 10\,\mathrm{mm}$. Trailing behind the reflected S wave is the down-dip TR signature, marked by circles in Figures 4.25, 4.26, and 4.27. This down-dip TR is generated when the rupture tip breaks the free surface, along with the two Rayleigh waves that propagate along the earth surface, as discussed in Section 4.1.2. The down-dip TR propagates at slightly above the Rayleigh wave speed, $v'^\mathrm{TR} = 1.20\,\mathrm{mm/\mu s}$ ($c_\mathrm{R} = 1.18\,\mathrm{mm/\mu s}$), sustaining the slip rate across all stations, especially those within $x_1' \le 10\,\mathrm{mm}$. Slip oscillations of period $\approx 10\,\mathrm{\mu s}$ persist after rupture tip arrival for these stations, however, are absent in the deeper stations $x_1' = (20, 40)\,\mathrm{mm}$, suggesting a local effect likely related to the two surface Rayleigh waves propagating bi-directionally along the earth surface.

Fault opening rates peak with the arrival of the SR rupture tip to the measurement stations. Similar to slip rate, fault opening is nearly dormant to the effects of the up-dip P and S waves. An opening pulse propagates up-dip with the arrival of the SR rupture, marked by t_r^SR in Figures 4.25, 4.26, and 4.27. Comparing the top and bottom panels of Figures 4.25, 4.26, and 4.27, the opening and slip rate signal rise times are nearly identical. The opening pulses similarly amplify and broaden as the up and down-dip features coalesce near the free surface, $x_1' = 0\,\mathrm{mm}$. After the arrival of the rupture tip, fault opening rates remain at zero for the deepest stations $x_1' = (20, 40)\,\mathrm{mm}$ until the arrival of the down-dip TR signature, marked by circles in Figures 4.25, 4.26, and 4.27. These secondary down-dip opening pulses are a small fraction of their up-dip precursors, in contrast to slip rate records, whose up and down-dip signals are nearly equal in magnitude. An interesting finding from the opening rate records are the negative values prior to rupture tip opening pulse, suggesting
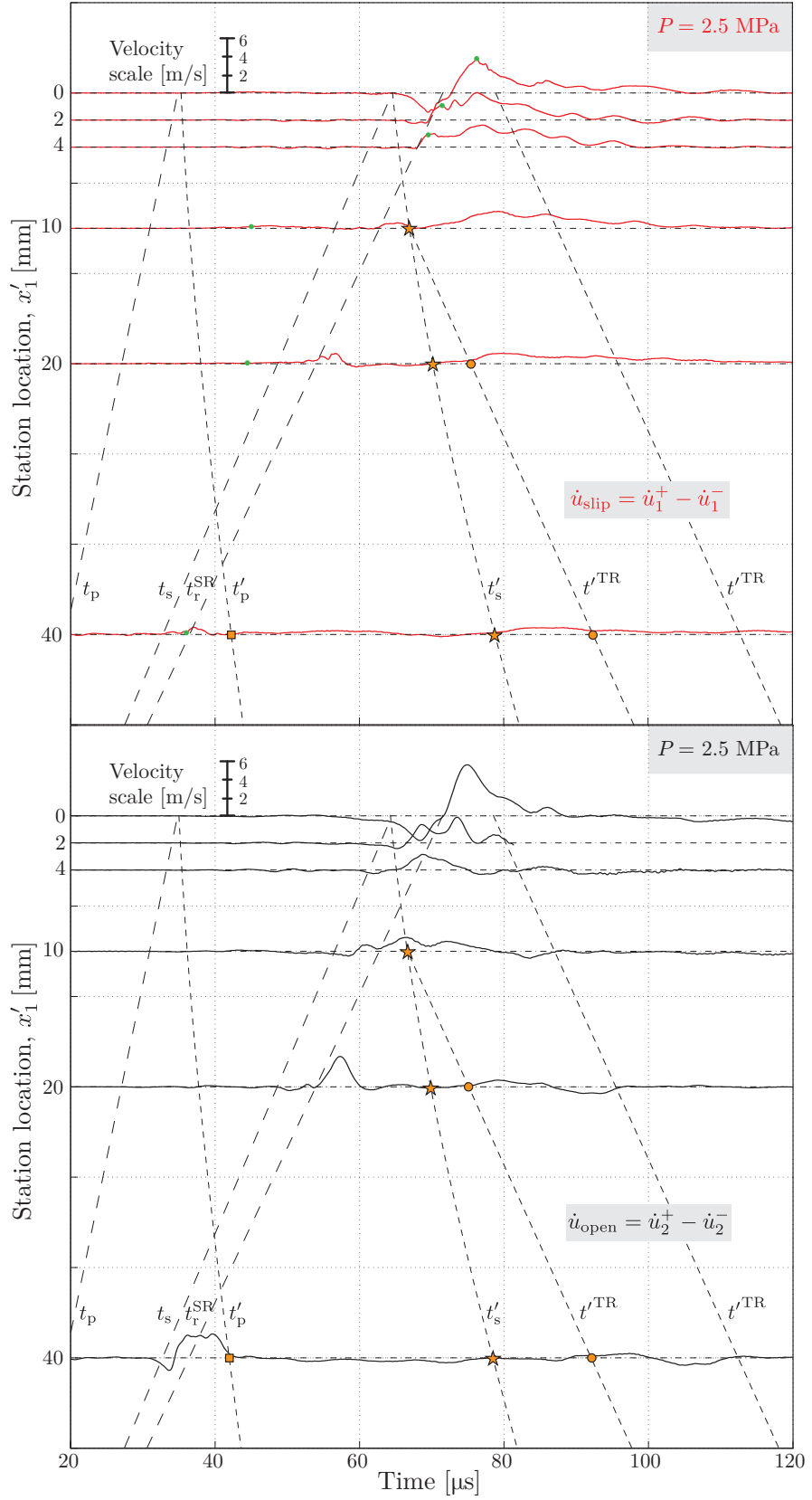
Figure 4.25: Summary of fault slip ($\dot{u}_{\text{slip}}$) and opening ($\dot{u}_{\text{open}}$) rates for load $P = 2.5\,\text{MPa}$.
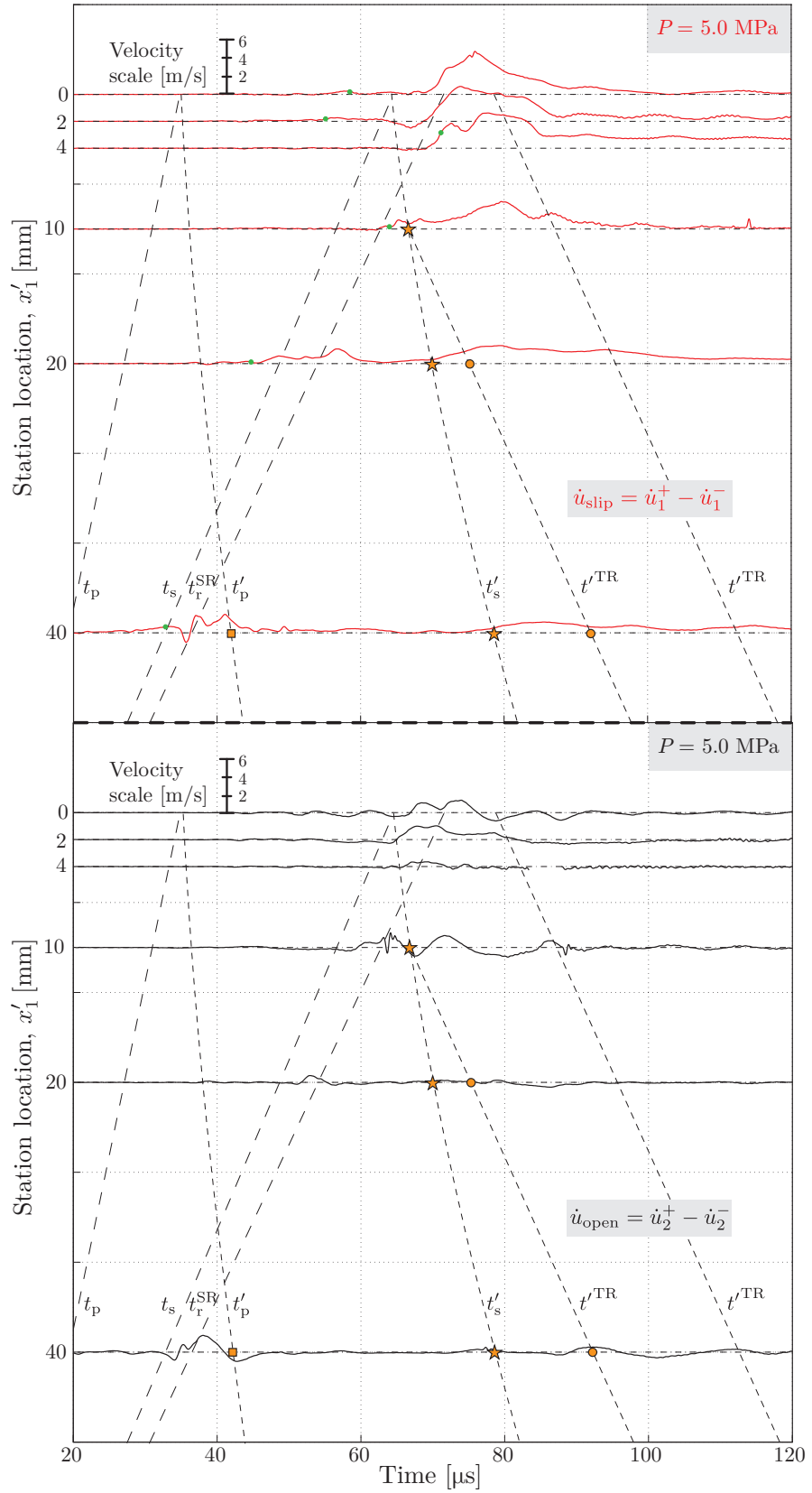
Figure 4.26: Summary of fault slip ($\dot{u}_{\text{slip}}$) and opening ($\dot{u}_{\text{open}}$) rates for load $P = 5.0\,\text{MPa}$.
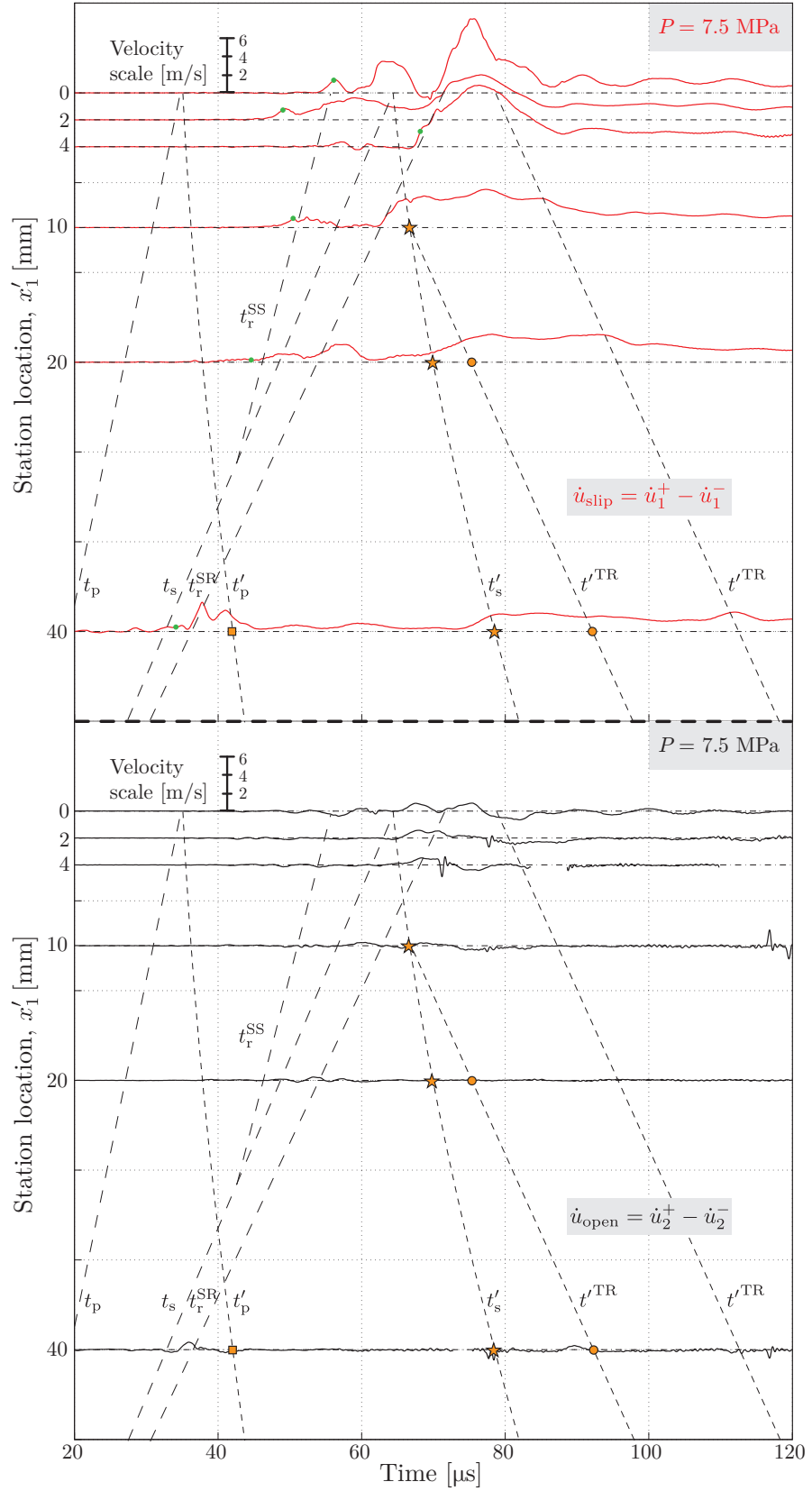
Figure 4.27: Summary of fault slip ($\dot{u}_{\text{slip}}$) and opening ($\dot{u}_{\text{open}}$) rates for load $P = 7.5\,\text{MPa}$.
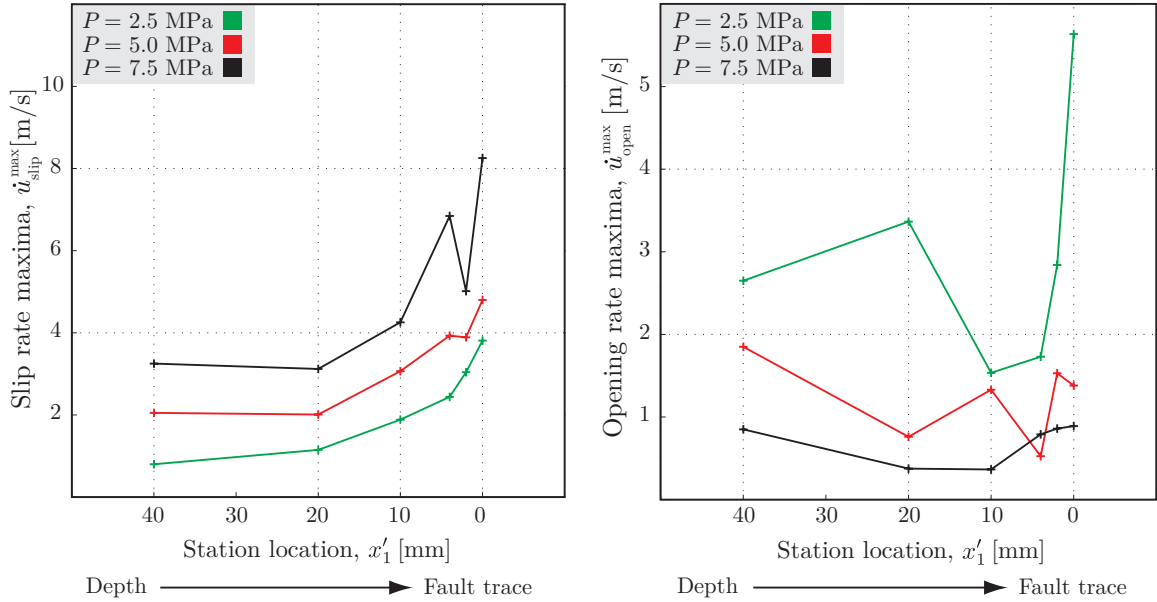
Figure 4.28: Fault slip ($\dot{u}_{\mathrm{slip}}^{\max}$) and opening ($\dot{u}_{\mathrm{open}}^{\max}$) rate peak amplification towards the free surface.

that the stations are being pushed together (pinched) prior to an opening of the fault surfaces. The down-dip TR first induces positive values of opening rates followed by negative values of opening rates in the records as the feature sweeps past paired measurement stations, implying an opening and pinching of the interface. Note that negative values of opening rate are physically viable results, as there is a finite stand-off distance between the interface and the reflective tapes (Section 4.2). Signatures in fault opening records associated with down-dip features are most prominent in lower load experiments, $P = 2.5$ and $5.0\,\mathrm{MPa}$, and are nearly absent for $P = 7.5\,\mathrm{MPa}$ experiments.

Peak magnitudes of slip and opening rates are plotted in the left and right panels of Figure 4.28 for all experimental loads $P = (2.5, 5.0, 7.5)\,\mathrm{MPa}$; note the difference in scale for slip and opening records. For any given station x_1', the slip rate increases with an increase of load from $P = 2.5$ to $7.5\,\mathrm{MPa}$. Peak magnitudes of slip rate also increase towards the free surface and obtain the global maxima at the fault trace station, $x_1' = 0\,\mathrm{mm}$. This trend is monotonic for load $P = 2.5\,\mathrm{MPa}$, however, loads $P = (5.0, 7.5)\,\mathrm{MPa}$ exhibit a dip in magnitude for station $x_1' = 2\,\mathrm{mm}$. For any given station x_1' with the exception of $x_1' = 4\,\mathrm{mm}$, peak opening rate amplitudes increase with a decrease in load, a reversal in trend from slip data due to the load-dependency on fault opening; an increase in confinement pressure along the fault minimizes the effects of the opening phase. The opening rates for $P = 7.5\,\mathrm{MPa}$ are banded between values of about $\dot{u}_{\mathrm{open}}^{\max} = 0.5 - 1.0\,\mathrm{m/s}$, while those of the lowest load, $P = 2.5\,\mathrm{MPa}$, are approximately banded between $\dot{u}_{\mathrm{open}}^{\max} = 1.5 - 5.5\,\mathrm{m/s}$. As $x_1' \to 0\,\mathrm{mm}$, maximum opening rates seem to decrease first before again amplifying near the free surface. In the current setup, stations within $x_1' \leq 10\,\mathrm{mm}$ are subject to continuous enhancement of slip and opening; this critical depth is dependent on the fault geometry and material properties.
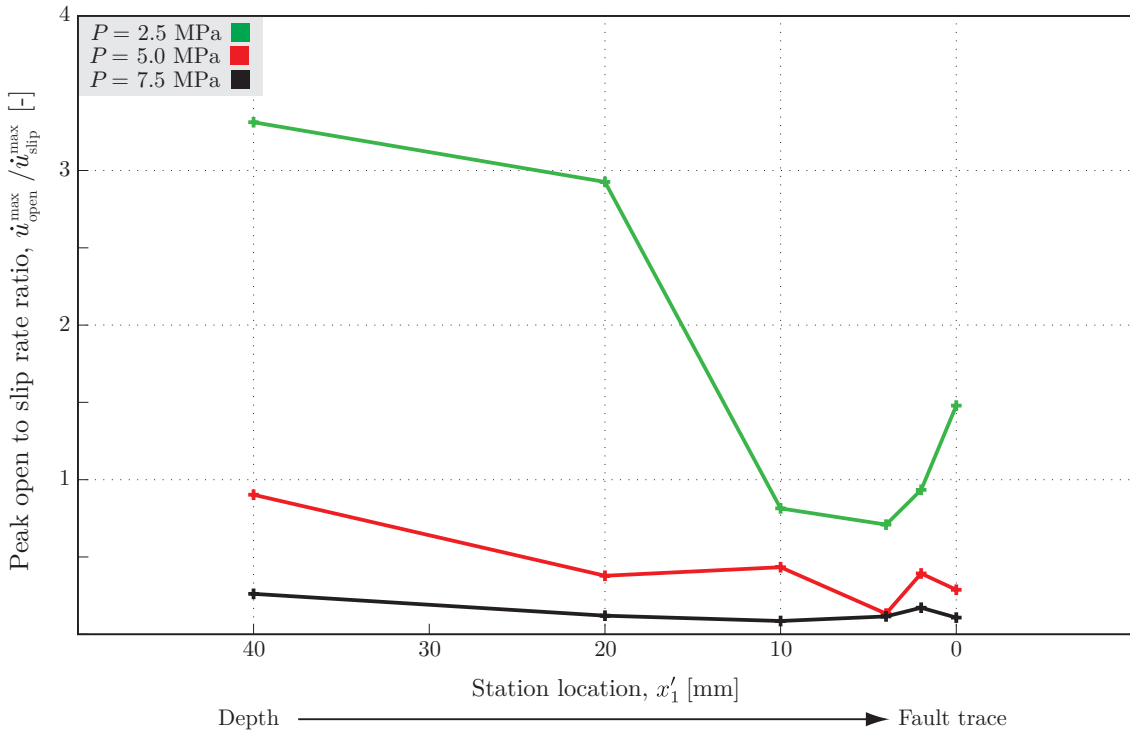
Figure 4.29: Ratio of maximum opening rate to slip rate, $\phi = \dot{u}_{\text{open}}^{\text{max}}/\dot{u}_{\text{slip}}^{\text{min}}$, for various stations, x_1'.

Slip dominant ruptures occur as confinement pressures are increased. Measurements at-depth show that the rupture is mixed-mode with both a slip and opening component. The ratio of opening to slip rate global maxima, $\phi = \dot{u}_{\text{open}}^{\text{max}}/\dot{u}_{\text{slip}}^{\text{max}}$, are plotted in Figure 4.29 for all experimental loads $P = (2.5, 5.0, 7.5)$ MPa: values of ϕ are used to judge the dominant rupture mode. For the highest load experiments $P = 7.5$ MPa (black curve), the opening to slip rate ratio is about $\phi = 1/4$, with very little change as the measurement stations approach the earth surface; this indicates a mode-II dominant rupture process. As the confinement pressure is decreased from $P = 7.5$ to $P = 5.0$ MPa, the ratio ϕ increases across all stations (red curve), indicating a greater mode-I component of the dynamic rupture. The highest values of ϕ occur in the lowest load experiments, $P = 2.5$ MPa (blue curve); in fact, this rupture is mode-I dominant at the deeper stations, $x_1' = (20, 40)$ mm, however, significant mode-II amplification occurs near the earth surface. While Figure 4.29 indicates that all ruptures in the thrust fault configuration are mixed-mode, higher confinement pressures favor a larger mode-II component while low confinement pressures favor a larger mode-I component. The presence of the earth surface greatly amplifies the slip rate for the $P = 2.5$ MPa experiments near the free surface, when otherwise the slip process would be relatively small compared to the concurrent opening. Measurements indicate that two plates sliding past each other in a mode-II dominant rupture also have a mode-I opening component, which is overall enhanced by decreasing the initial applied static load as well as decreased proximity to the earth surface.

4.2.6   Fault slip and opening displacements

Displacement data are obtained through numerical integration of the fault parallel and normal records, as discussed in Section 3.2.3. Accumulated slip is obtained by subtracting the fault parallel displacements from paired stations just to the left (hanging wall) and right (foot wall) of the fault, $u_{\mathrm{slip}}(x_1', t) = u_1^+(x_1', t) - u_1^-(x_1', t)$. Similarly, accumulated fault opening displacements are obtained by subtracting the fault normal displacements of paired stations, $u_{\mathrm{open}}(x_1', t) = u_2^+(x_1', t) - u_2^-(x_1', t)$. Due to the Eulerian nature of the velocimeter measurements, additional corrections to the displacement data are required to obtain u_{open} (Appendix A). Figures 4.30, 4.31, and 4.32 plot u_{slip} (top panels) and u_{open} (bottom panels) for the three experimental loads $P = (2.5, 5.0, 7.5)\,\mathrm{MPa}$. Note the difference in scale between the u_{slip} and u_{open} data, as well as the variable scale within each plot. As in previous sections, timing curves bound arrivals of various rupture features.

Three inflection points in the slip displacement data correspond to the arrival of key rupture features. The first inflection point commences slip accumulation with the arrival of the SR rupture tip (times $t_{\mathrm{r}}^{\mathrm{SR}}$ in Figures 4.30, 4.31, and 4.32), which breaks the locked fault as it sweeps past the measurement stations. Slip accumulation stops for stations $x_1' = (20, 40)\,\mathrm{mm}$ until the arrival of the reflected S waves (marked by stars in Figures 4.30, 4.31, and 4.32). The second inflection point corresponds to the arrival of the reflected S wave, further accumulating slip across paired stations. The third inflection point correspond to the arrival of the down-dip TR signature that is generated at the same time the rupture tip breaks the free surface at the fault trace (marked by circles in Figures 4.30, 4.31, and 4.32). The inflection points become difficult to distinguish as the effects of up and down-dip features coalesce, accumulating slip continuously for stations near the free surface.

Opening displacements commence and peak with the arrival of the rupture tip (times $t_{\mathrm{r}}^{\mathrm{SR}}$ in Figures 4.30, 4.31, and 4.32). The dynamic stresses associated with the rupture tip push the fault surfaces away from each other as they sweep past the paired measurement stations. In the lowest load $P = 2.5\,\mathrm{MPa}$ experiments, the opening pulse spans the arrival of the rupture tip to the arrival of the down-dip TR signature, marked by t'^{TR} and circles in Figure 4.30, respectively. Opening pulse widths decrease as the timing lines coalesce, however, the fault trace station $x_1' = 0\,\mathrm{mm}$ has a longer opening duration than adjacent stations. For higher load experiments $P = 5.0$ and $7.5\,\mathrm{MPa}$, increased confinement pressures significantly reduce the opening displacements across all stations. Effects of the rupture tip ($t_{\mathrm{r}}^{\mathrm{SR}}$), reflected S wave (stars), and down-dip TR signature (circles) on fault opening are most distinguishable for stations at-depth (Figures 4.31 and 4.32) and similarly coalesce into a single pulse near the free surface.

To account for shear deformations due to the finite stand-off distances between paired on-fault stations, a rupture criterion based on total accumulated slip is employed [53]. Fault sliding is assumed to commence when the driving shear stresses overcome the available fault strength. Assuming
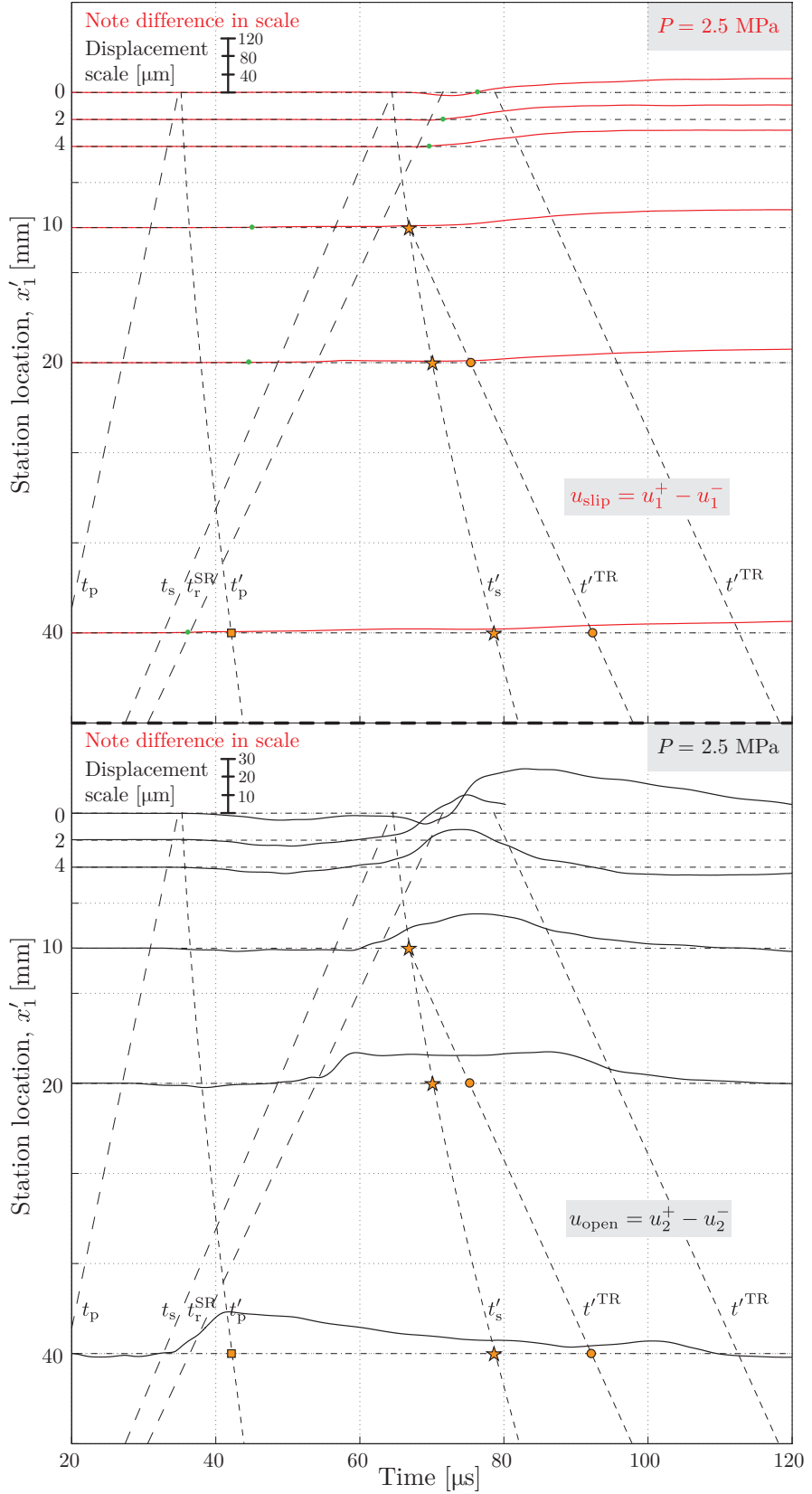
Figure 4.30: Summary of total slip (u_{slip}) and opening displacements (u_{open}) for load $P = 2.5\,\mathrm{MPa}$.
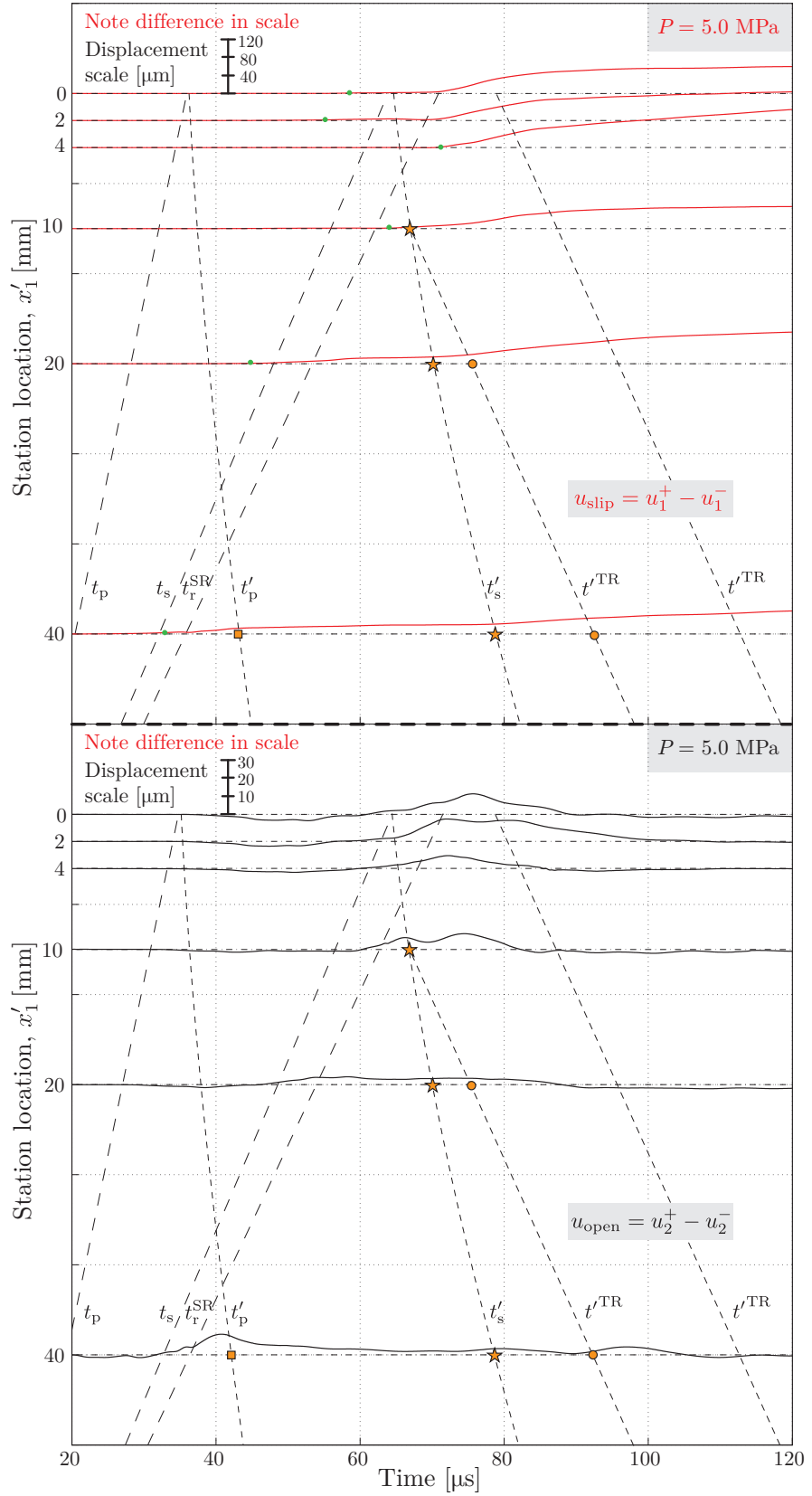
Figure 4.31: Summary of total slip (u_{slip}) and opening displacements (u_{open}) for load $P = 5.0\,\text{MPa}$.
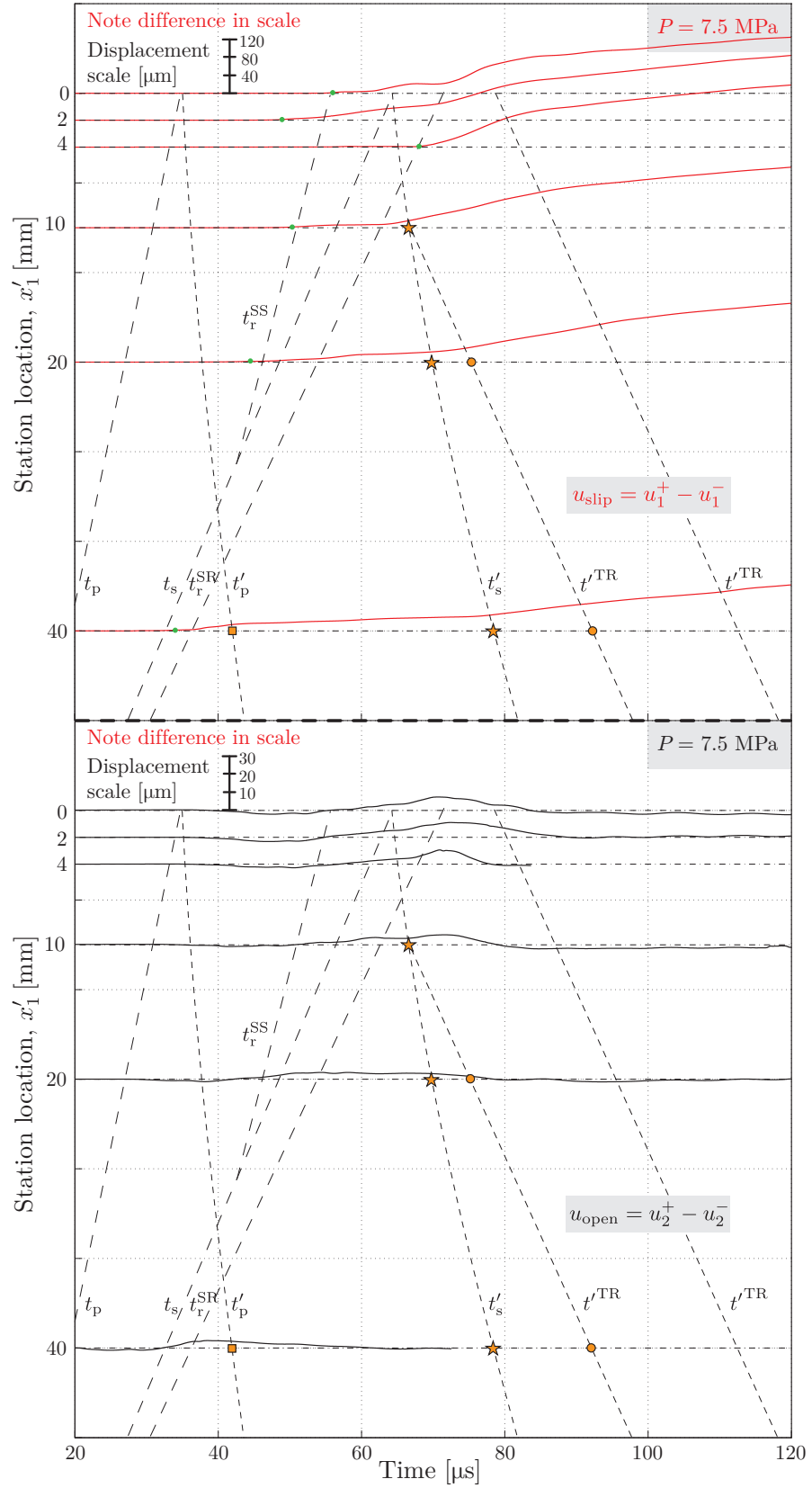
Figure 4.32: Summary of total slip (u_{slip}) and opening displacements (u_{open}) for load $P = 7.5\,\text{MPa}$.
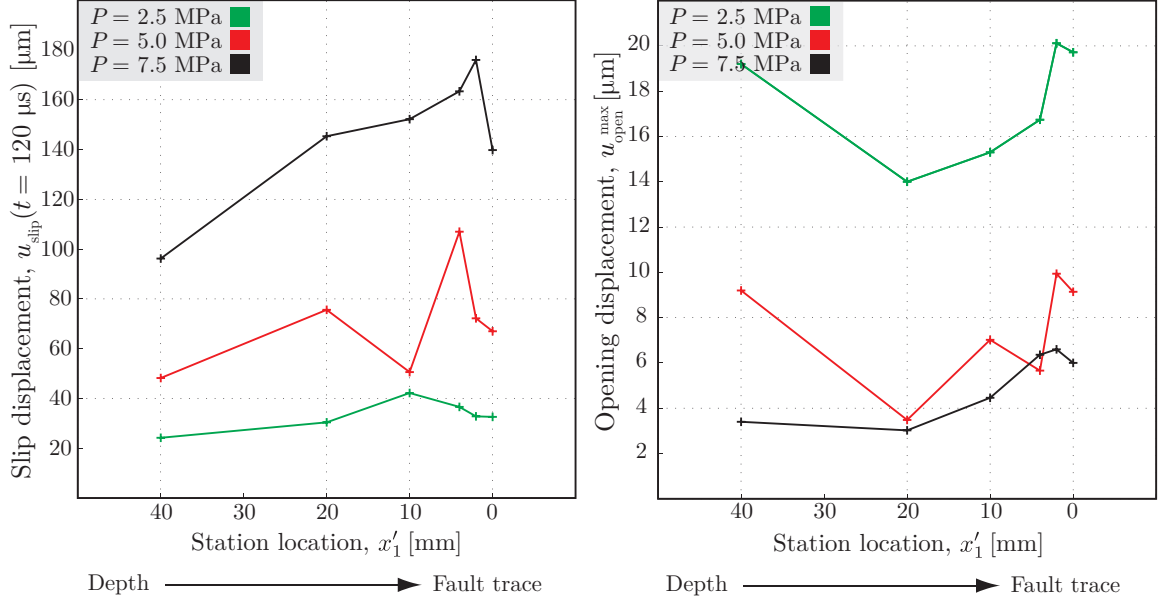
Figure 4.33: Accumulated slip and peak opening displacements are amplified near the free surface.

uniform shear stress between the two stations, the relationship

$$u_{\mathrm{slip}}^{\mathrm{c}} = 2\eta \frac{P\cos^2\alpha(f_{\mathrm{s}} - f_0)}{\mu} \tag{4.22}$$

is used to determined the maximum accumulated slip permissible between paired stations prior to fault rupture, $u_{\mathrm{slip}}^{\mathrm{c}}$, using offset distances $\eta^{\pm} \approx 400 - 600\,\mu\mathrm{m}$. The critical slip distance is evaluated using values $f_{\mathrm{s}} = 0.6$ and $f_0 = 0.2$, giving $u_{\mathrm{slip}}^{\mathrm{c}} = (0.66, 1.31, 1.96)\,\mu\mathrm{m}$ for experimental loads $P = (2.5, 5.0, 7.5)\,\mathrm{MPa}$. These values are found for each experiment and marked with green circles on the traces in Figures 4.30, 4.31, and 4.32; these markers also appear in the slip rate data of Figures 4.25-4.27 (Section 4.2.5). According to the critical slip criterion, there is indeed an up-dip rupture in all experiments. The green markers in $P = 7.5\,\mathrm{MPa}$ experiments align well with the predicted rupture arrival times, indicating how some experiments transitioned to SS while others remained SR. In some $P = 2.5\,\mathrm{MPa}$ and $P = 5.0\,\mathrm{MPa}$ experiments, the green markers underestimate rupture tip arrivals with respect to the timing curve, $t_{\mathrm{r}}^{\mathrm{SR}}$, however, a less conservative estimate of $u_{\mathrm{slip}}^{\mathrm{c}}$ would decrease this disparity while remaining well within bounds to assure fault rupture.

Higher load experiments accumulate more slip for any given station x_1' at any given time t. Increasing the static load P promotes shear-dominant ruptures and impedes the opening mode. Total accumulated slip at the end of the experimental window, $u_{\mathrm{slip}}(t = T_{\mathrm{exp}})$ with $T_{\mathrm{exp}} = 120\,\mu\mathrm{s}$, is reported in Figure 4.33 (left panel); as expected, accumulated slip values increase with load P. Values of total accumulated slip for the highest load experiments are used to estimate offsets $\epsilon^{\pm}$ required for earth surface normal measurements at the fault trace (Section 4.1).

4.2.7 Mechanical behavior near the earth surface of a SR rupture

Ground motion records are used to deduce mechanical behavior near the earth surface of simulated thrust fault earthquakes for both SR and SS up-dip rupture speeds. Earth surface-normal records (Section 4.1) as well as fault parallel and normal records along the the fault (Section 4.2) are summed up with the use of schematics in Figures 4.34 (SR rupture) and 4.39 (SS rupture). Figure 4.34 schematically represents the ground motions near the earth surface of a SR rupture in the thrust fault configuration. Red and green portions represent locked and slipping regions, respectively.

Panel A shows the P and S wave fronts emitted from nucleation propagating along the fault with up-dip phase velocities equal to their wave speeds, $v_\mathrm{p}(x_1') = c_\mathrm{p}$ and $v_\mathrm{s}(x_1') = c_\mathrm{s}$, where $c_\mathrm{p} \approx 2c_\mathrm{s}$. The P wave has reflected from the earth surface and propagates to the left with a phase velocity $v_\mathrm{p}(x_1)$.

Panel B shows a slip rupture pulse propagating up-dip at a SR rupture speed, $c_\mathrm{s} \leq v_\mathrm{r}^\mathrm{SR}(x_1') \leq c_\mathrm{p}$, trailing just behind the S wave front. Reflected P waves feed back onto the fault and propagate down-dip with phase velocities $v_\mathrm{p}'(x_1')$; these arrivals at-depth do not significantly alter the rupture slip and opening processes (square markers in Figures 4.21, 4.22, and 4.23). The double-lobe fringe patterns mark the location of the rupture tip. The right-lateral rupture compresses material ahead in the hanging wall while applying tension in the foot wall, trying to torque the material counterclockwise around the rupture tip. An opening pulse (gap between the fault surfaces) accompanies the up-dip slip pulse. A pinching precursor signal (negative opening rates) arrives prior to the fault opening. The mode-II and mode-I characteristics of the rupture are selected through a choice of load, P: mode-II (slip) is enhanced by an increase of P, while mode-I (opening) is enhanced by a decrease of P. Slip and opening pulses grow in amplitude and pulse-width as they propagate up-dip.

Panel C shows the S wave impinging on the earth surface, generating a disturbance propagating to the left with a phase velocity $v_\mathrm{s}(x_1)$ and feeding back onto the fault with phase velocities $v_\mathrm{s}'(x_1')$: effects of reflected S waves are much more prominent than those of P waves, increasing the slip rates of the already slipping region. A rupture wave is sensed along the earth surface on the hanging wall plate just after the S wave; however, the rupture wave is absent in the foot wall plate (Section 4.1.2, Figure 4.6). Rather than bulk reflected waves informing the rupture process of the free surface boundary, the local stress field of the rupture tip directly interacts with the earth surface. The lack of material above the earth surface renders the system incapable of sustaining a restoring force to counter the local driving stresses; this situation becomes more imminent with proximity of the rupture tip to the fault trace. It is evident that certain stations near the fault trace will experience enhanced durations of ground motions as up-dip rupture and down-dip S wave effects converge; this critical depth is a function of material properties, fault frictional parameters, and asymmetric fault geometry. Absence of the rupture wave in the foot wall plate is confirmed in numerical simulations of similar thrust fault configurations [96]: in the theoretical model, a stopping phase emitted upon rupture tip arrival to the earth surface identically cancels the rupture wave in the foot wall plate.
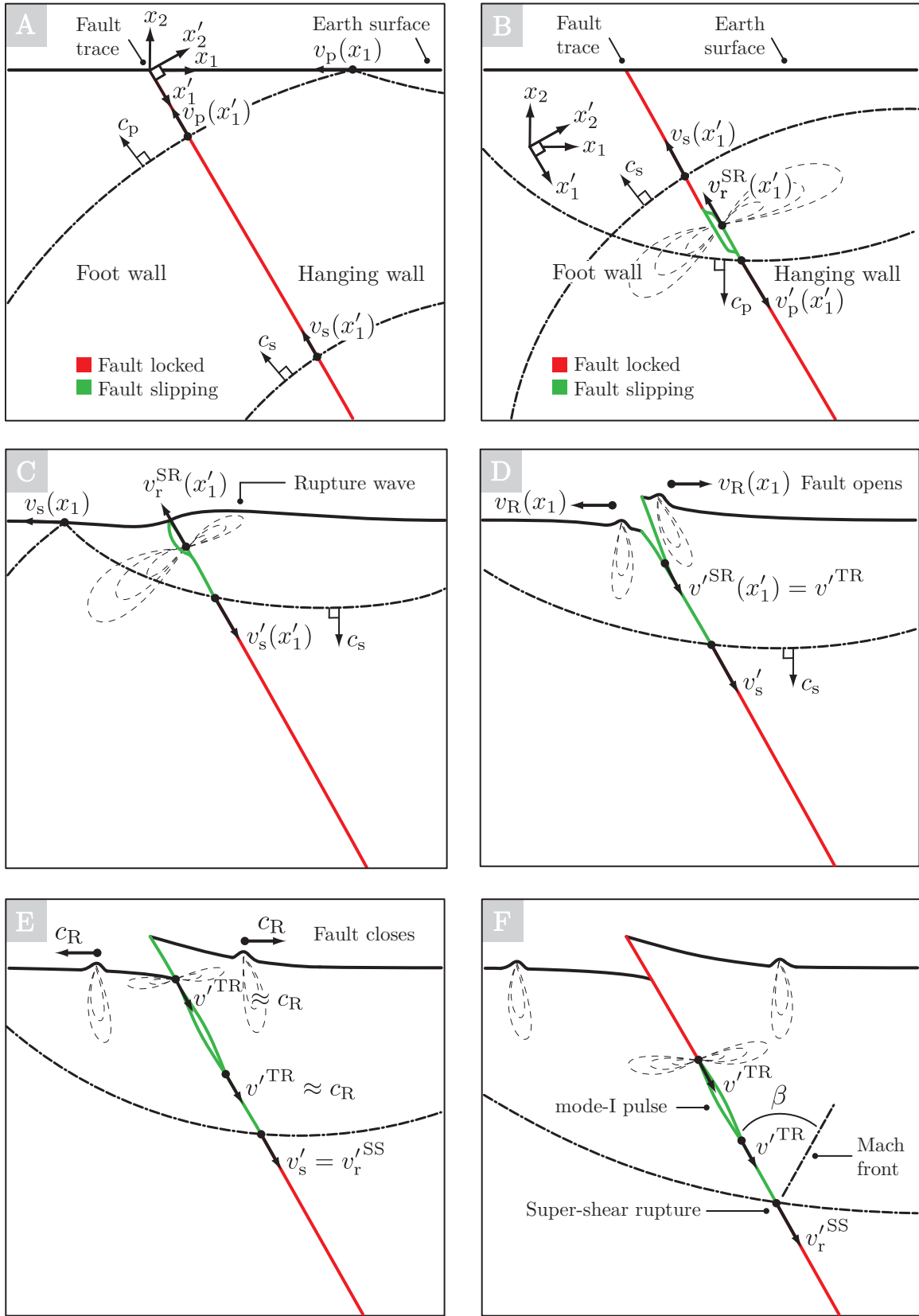
Figure 4.34: Mechanical behavior at the free surface of a SR event in a thrust fault configuration.

Panel D shows the rupture tip breaking the earth surface at the fault trace. Amplified pinching effects are accompanied by similar magnitude negative slip rates. The pinching effect is immediately followed by opening as the hanging wall detaches from the foot wall: to satisfy the (static) force balance at the earth surface, an impulsive restoring force appears at the fault trace upon rupture tip arrival. Rayleigh waves are generated and propagate bi-laterally along the earth surface with phase velocities, $v_R(x_1) = c_R$. Opening of the fault traps waves in the acute hanging wall wedge, while waves are dispersed in the obtuse geometry of the foot wall. Pinching and twisting motions of the fault are corroborated with the SR earth surface-normal records: at the fault trace (black curves, Figure 4.6), the hanging and foot wall surfaces are together pulled towards the earth center, $\dot{u}_2(x_1 = \pm 0\,\mathrm{mm}, t) < 0$, and then begin an upward motion during which the surface breaks as the hanging wall accelerates more than the foot wall. Opening of the fault sends a mode-I opening pulse back down-dip ($v'^{\mathrm{TR}} \approx c_R$), trailing behind $v'_s(x'_1)$.

Panel E shows a second down-dip TR signature propagating at a phase velocity $v'^{\mathrm{TR}} \approx c_R$. The opening and subsequent shutting of the fault at the earth surface generates a down-dip mode-I pulse, which in turn opens and pinches the fault during transit; in the absence of opening, this mode-I pulse would not exist and only the two surface Rayleigh waves would be measured. The reflected S wave leads a down-dip rupture tip (marked by stars in Figures 4.25, 4.26, and 4.27). The asymmetric thrust fault geometry forces the down-dip rupture to propagate at SS speeds, $v'^{\mathrm{SS}}_r(x'_1) = v'_s(x'_1)$.

Panel F shows the slipping region and the down-dip mode-I pulse. Material near the fault trace re-locks for the lower load experiments, however, the fault continues to slip for the highest load experiments $P = 7.5\,\mathrm{MPa}$ (red portion of the fault must extend up to the free surface in panel VI). The appearance of a Mach front emanating from the down-dip rupture verifies SS speeds. Distinct up and down-dip slip pulses become difficult to discern as P is increased and completely coalesce in SS experiments within the observed range $x'_1 \leq 40\,\mathrm{mm}$ ($P = 15\,\mathrm{MPa}$, Figure 4.37, Section 4.2.8), indicating a qualitative mode transition from a pulse-like to a crack-like rupture [104].

A typical sub-Rayleigh earthquake ($P = 2.5$ MPa) is presented in Figure 4.35 at experimental times $t = (50, 65, 70, 100)\,\mathrm{\mu s}$ (rows 1-4). Digital photographs along with pertinent zoomed-in segments of fault slip ($\dot{u}_{\mathrm{slip}}$) and opening rate ($\dot{u}_{\mathrm{open}}$) records are displayed in column A; column B shows select schematics from Figure 4.34; column C shows results of preliminary simulations [130].

At $t = 50\,\mathrm{\mu s}$, the rupture tip, v_r, is about $25\,\mathrm{mm}$ away from the fault trace, trailing behind the S wave front (panel 1A). The P wave, being roughly twice faster than the S, has already struck the free surface, feeding back reflected waves onto the angled fault. Insensitivity of photo-elasticity to dilatation and superposition of S field fringes renders the reflected P wave front invisible in the photograph. Relative motion of paired stations $x'_1 = 20\,\mathrm{mm}$ commences upon arrival of the rupture tip, indicated by a rise in the slip rate record at about $55\,\mathrm{\mu s}$ (red curve); amplified stresses in the local vicinity of the rupture tip are sufficient to overcome the available frictional resistance, inducing
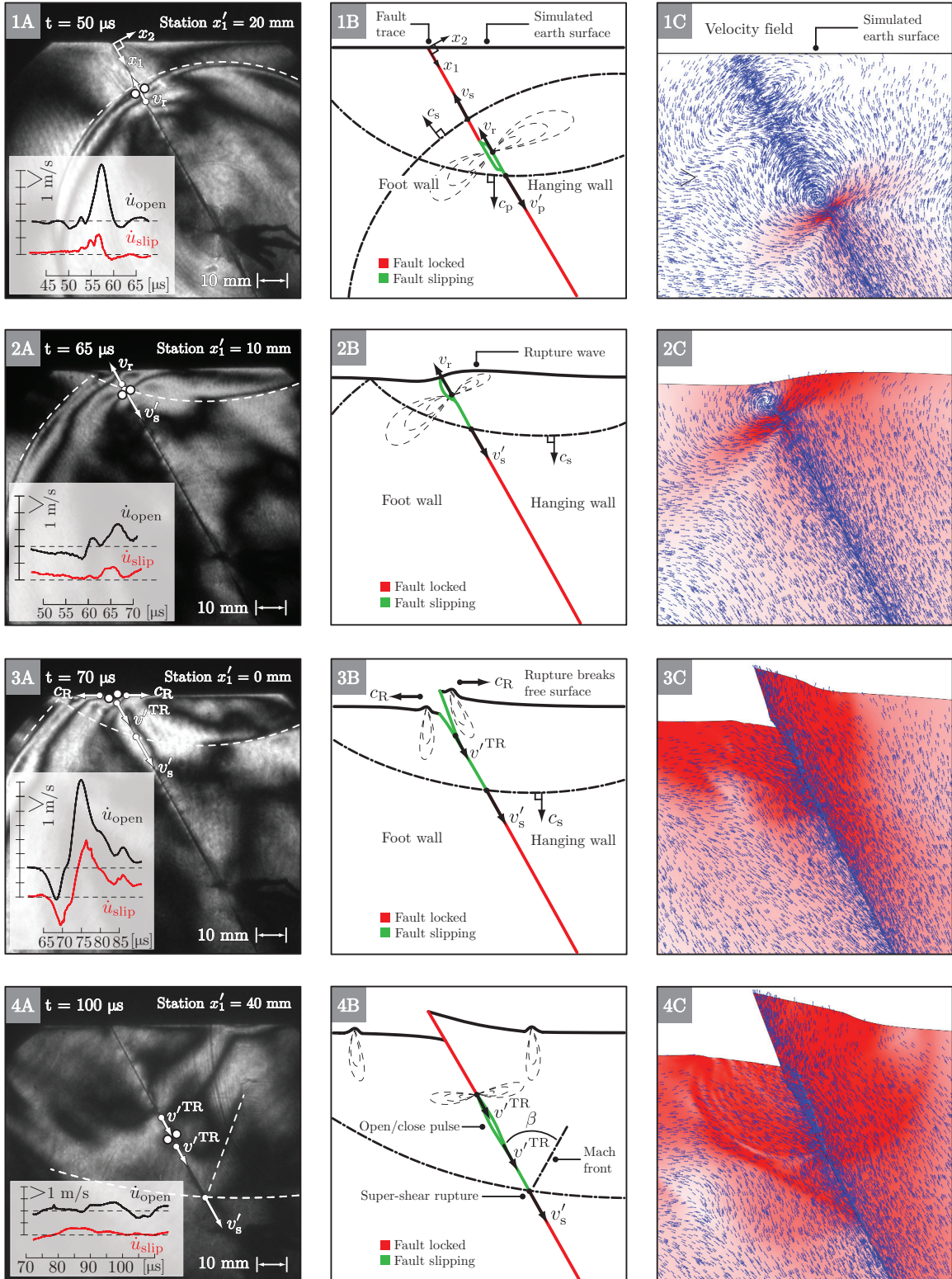
Figure 4.35: A typical SR rupture ($P = 2.5$ MPa) is chronologically portrayed at various experimental times. Experimental results (column A), schematic representations (column B), and numerical results [130] (column C) summarize the up-dip propagation of the rupture tip towards the free surface (v_r). Key phase velocities are annotated in the schematics.

slip of the locked fault. In the rupture tip wake, the fault surfaces cease to slip, resulting in a pulse with a rise time of $\approx 7\,\mu$s. An in-phase pulse of similar duration is observed in the opening rate record (black curve), indicating that the fault also opens and shuts as the rupture tip sweeps past the measurement stations. Negative opening rates measured ahead of the rupture tip imply pinching of the interface prior to the concurrent initiation of both opening and slip. Phase velocities of the up-dip rupture, v_r, S wave, v_s, and down-dip reflected P wave, v'_p, are marked in the complementary schematic (panel 1B). Since the rupture speed is constant and near unity, pulse rise times translate to a process region of $\approx 8\,$mm along the fault, highlighted green in the schematic.

At $t = 65\,\mu$s, the rupture tip has just arrived to station $x'_1 = 10\,$mm (panel 2A). By this time, S waves have impinged on the earth surface and are feeding back reflected stress waves onto the fault, much like their P wave counterparts. Following the pinching precursor, slip and opening events are again initiated by the rupture tip. Additional features in the records appear after the rupture signature, as a direct result of the free surface boundary. The schematic marks the reflected S wave phase velocity, v'_s (panel 2B). Note, while up-dip phase velocities of bulk waves along the fault are constant, $v_p = c_p$, $v_s = c_s$, down-dip phase velocities (distinguished by primed variables) vary with coordinate x'_1: the asymmetric fault geometry is responsible for this dichotomy, mandating that down-dip speeds exceed up-dip values at every station, $|v_p| < |v'_p|$ and $|v_s| < |v'_s|$.

At about $70\,\mu$s, the rupture tip arrives at the fault trace, $x'_1 = 0\,$mm, breaking the earth surface (panel 3A). Slip and opening rate records exhibit significant amplification in peak values at the earth surface ($v_{slip}^{max} \approx 4\,$m/s and $v_{open}^{max} \approx 6\,$m/s). Peak negative values associated with the pinching precursor are also amplified and now accompanied by an in-phase negative slip signature, both $\approx -2\,$m/s. Due to the absence of material above the earth surface, the system is unable to counteract the pinching motion ahead of the rupture, resulting in an immediate compression and release of the material around the fault. Numerical integration reveals a maximum opening displacement of $\approx 20\,\mu$m. Separation of the fault surfaces generates an opening pulse propagating back down-dip, v'^{TR}, and two surface Rayleigh waves along the earth surface, c_R (panel 3B); the latter claim has been verified with previous measurements along the earth surface. The opening pulse trails behind the reflected S wave front and propagates at roughly c_R, and thus the sub-script trailing-Rayleigh. Oscillations in the records persist past the arrival of the rupture tip, extending the slip and opening process durations near the earth surface. Theoretical work on thrust faults discuss the instantaneous emergence of a Boussinesq point force at the fault trace; the sudden inability of the system to sustain a moment upon rupture tip arrival to the free surface is balanced by this solution. The measured fault opening phenomena is strong evidence in support of this claim.

At time $t = 95\,\mu$s, at the deepest station, $x'_1 = 40\,$mm, slip rate records indicate that the reflected S wave front re-ruptures the fault (panel 4A). The photograph at $t = 95\,\mu$s shows a shear Mach front emanating from the intersection of the reflected S wave and the fault, i.e., the rupture tip ($v'^{SS}_r = v'_s$).

Two-point measurements confirm that the average rupture tip speed is indeed SS, $v_{\mathrm{r}}'^{\mathrm{SS}} \approx 1.6\,\mathrm{mm/\mu s}$ $(1.24c_{\mathrm{s}})$, a fact mandated by the asymmetric thrust fault geometry $(c_{\mathrm{s}} < |v_{\mathrm{s}}'|)$. Since the emission source is faster than the shear characteristic speed, S wave effects are necessarily confined to a region bound by the Mach front (panel 4B). The geometric relation $v_{\mathrm{r}}'^{\mathrm{SS}}(\beta) = c_{\mathrm{s}}/\sin\beta$ and Mach angle $\beta = 47°$ verify SS speeds $v_{\mathrm{r}}'(47°) \approx 1.7\,\mathrm{mm/\mu s}$. Trailing behind the down-dip rupture are the pair of fringes corresponding to the opening and shutting of the fault near the earth surface (v'^{TR}), as seen in the opening rate records. Measured speeds of the trailing-Rayleigh signatures are equal to c_{R} within error, $v'^{\mathrm{TR}} = 1.20\,\mathrm{mm/\mu s}$. The down-dip SS slip process is first enhanced by the opening pulse, then ceased by the clamping effect, resulting in larger slipping regions of the fault during down-dip propagation; this situation is schematically summarized in panel 4B.

Preliminary numerical simulation results capture key experimental observations of SR ruptures. Contours and normalized arrows in column C of Figure 4.35 represent velocity magnitude and direction, respectively. Peak ground motion magnitudes near the rupture tip are highlighted red in panel 1C. The rupture breaks the free surface, opens the fault, generates Rayleigh waves along the earth surface as well as a SS rupture propagating back down-dip.

4.2.8   Super-shear fault slip and opening rates

Maintaining all experimental parameters nominally identical and increasing the static load to $P = 15.0\,\mathrm{MPa}$ induces transition of the rupture to the SS regime, $c_{\mathrm{s}} \leq v_{\mathrm{r}}^{\mathrm{SS}} \leq c_{\mathrm{p}}$. The image/trace sequence of Figure 4.36 chronologically represents a single SS experiment where paired measurement stations at depth $x_1' = 34\,\mathrm{mm}$ record on-fault fault parallel velocities for the hanging wall ($\dot{u}_1^+$, red curves) and foot wall plates ($\dot{u}_1^-$, blue curves). Timing lines mark the arrivals of the dilatational field (t_{df}), SS rupture tip ($t_{\mathrm{r}}^{\mathrm{SS}}$), S wave ($t_{\mathrm{s}}$), TR signature ($t^{\mathrm{TR}}$), and down-dip SS signature (t'^{SS}).

At time $t = 30\,\mathrm{\mu s}$ (Figure 4.36, top left panel) the rupture has already transitioned to SS speeds. The initial P wave has already swept past the measurement stations with near-zero contributions to fault parallel ground motions, as in the SR experiments. The effects of the leading dilatational field (t_{df}) are recorded just prior to the arrival of the rupture tip, moving the paired stations in tandem. The rupture tip breaks the fault at $x_1' = 34\,\mathrm{mm}$ and moves the hanging and foot wall plates anti-symmetrically. Peak velocity magnitudes are on the order of $5\,\mathrm{m/s}$, more than twice the maxima of SR experiments measured at stations away from the earth surface (Figure 4.24).

At $t = 42\,\mathrm{\mu s}$, effects of the S waves and the TR signature increase fault parallel ground motion magnitudes as they sweep past the paired stations. The up-dip TR signature is the remnant stress concentration from the original SR rupture prior to SS transition. The anti-symmetry between the hanging and foot wall plates is just broken with the arrivals of reflected P waves (t_{p}') at $t \approx 40\,\mathrm{\mu s}$, though effects in the records are minor. The near-field of the rupture begins to sense the earth surface as the dilatational field approaches the fault trace (top right panel).
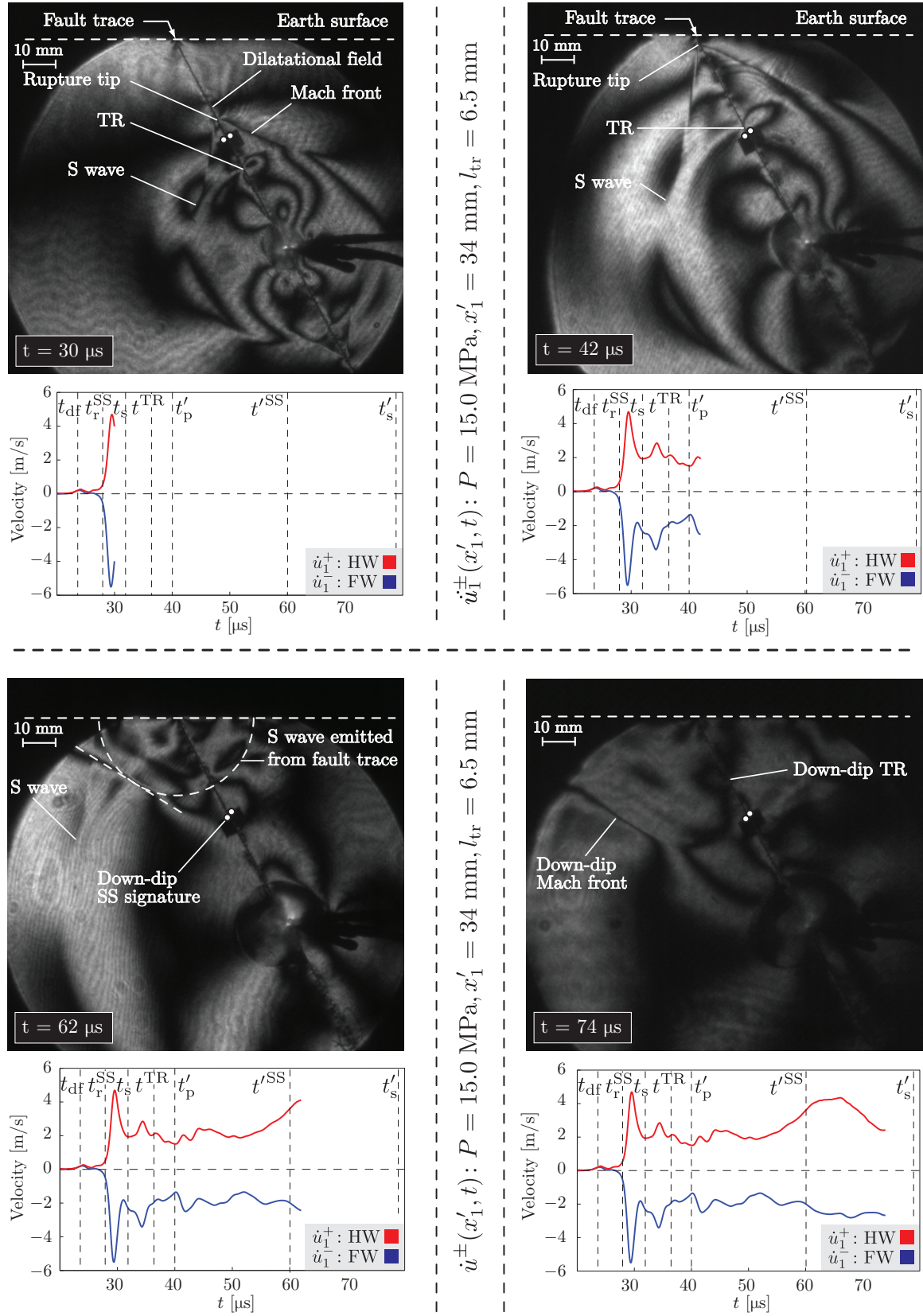
Figure 4.36: SS fault parallel ($\dot{u}_1^\pm$) image/trace sequence at inter-frame times $t = (30, 42, 62, 74)\,\mu\text{s}$.

A down-dip Mach cone is generated once the up-dip rupture tip breaks the earth surface at the fault trace (Figure 4.36, bottom left panel). This Mach cone stems from a stress concentration propagating down-dip at SS speeds, v'^{SS}. The down-dip Mach front is distinct in the foot wall, though more difficult to discern in the hanging wall. At time $t = 62\,\mu\text{s}$, the SS signature just arrives to station $x'_1 = 34\,\text{mm}$ and further enhances fault parallel motions in both stations. Dashed lines outline an S wave emitted from the fault trace when the earth surface was broken; defocused images (not shown here) also capture a P wave envelope emitted from the fault trace. Curvature in the leading edge of the down-dip Mach cone suggest that the SS signature decelerates; however, the entire fringe structure moves back down-dip at SS speeds.

At time $t = 74\,\mu\text{s}$ (Figure 4.36, bottom right panel), the down-dip SS signature has swept past the measurement stations. Trailing behind the SS signature is the down-dip TR signature, generated in turn when the up-dip TR signature reaches the fault trace. While reflected P waves continuously feed back to the fault line, it is only with the arrivals of these down-dip signatures that deviation occurs from the anti-symmetry condition between the hanging and foot wall fault parallel records. In the absence of the free surface boundary condition, the records should remain anti-symmetric for all time. Ground motions are enhanced in the hanging wall station, compared to the paired foot wall station, as a direct result of rupture tip interactions with the earth surface and the angled fault.

A collection of SS fault parallel records for stations $x'_1 = (0, 2, 4, 19, 34)\,\text{mm}$ are presented in the top panel of Figure 4.37. SS content, absent in the SR experiments, is bound between timing lines t_{p} and t_{s}. Similar to SR experiments, fault parallel ground motions are amplified as the earth surface is approached, $x'_1 \to 0\,\text{mm}$. Mode-II anti-symmetry of hanging and foot wall fault parallel records is preserved for the rupture tip signal (t_{r}^{SS}) across all measurement stations, regardless of distance from the fault trace. The anti-symmetry condition is broken once the down-dip SS signature arrives to the paired stations; the hanging wall fault parallel ground motions are enhanced more than those of the foot wall (paired peaks marked by circles in Figure 4.37). The slip record at distance $x'_1 = 34\,\text{mm}$ could also be attained by doubling the hanging wall trace, $\dot{u}_{\text{slip}} \approx 2|\dot{u}_1^+| \approx 2|\dot{u}_1^-|$, until the reflected information arrives at $t = 60\,\mu\text{s}$. Much like SS earth surface-normal records of Section 4.1.3, fault parallel motions of paired hanging and foot wall stations are initially anti-symmetric with rupture tip arrival. Dominant fault parallel motions for SS ruptures propagating above $\sqrt{2}c_{\text{s}}$ and increased applied loads are in contrast to the dominant fault normal motions and lower applied loads typical of SR ruptures; these key differences between SR and SS events may explain the broken symmetry observed in earth surface-normal records at the fault trace (Figure 4.6).

Slip rate records indicate that the down-dip Mach cone stems from a stress concentration rather than a down-dip SS rupture. The bottom panel of Figure 4.37 indicates the crack-like nature of the rupture, sustaining a positive slip rate for the duration of the measurement. Pulse-like to crack-like mode-II rupture transition is observed with an increase of static load from $P = 2.5$ to $P = 15.0\,\text{MPa}$.
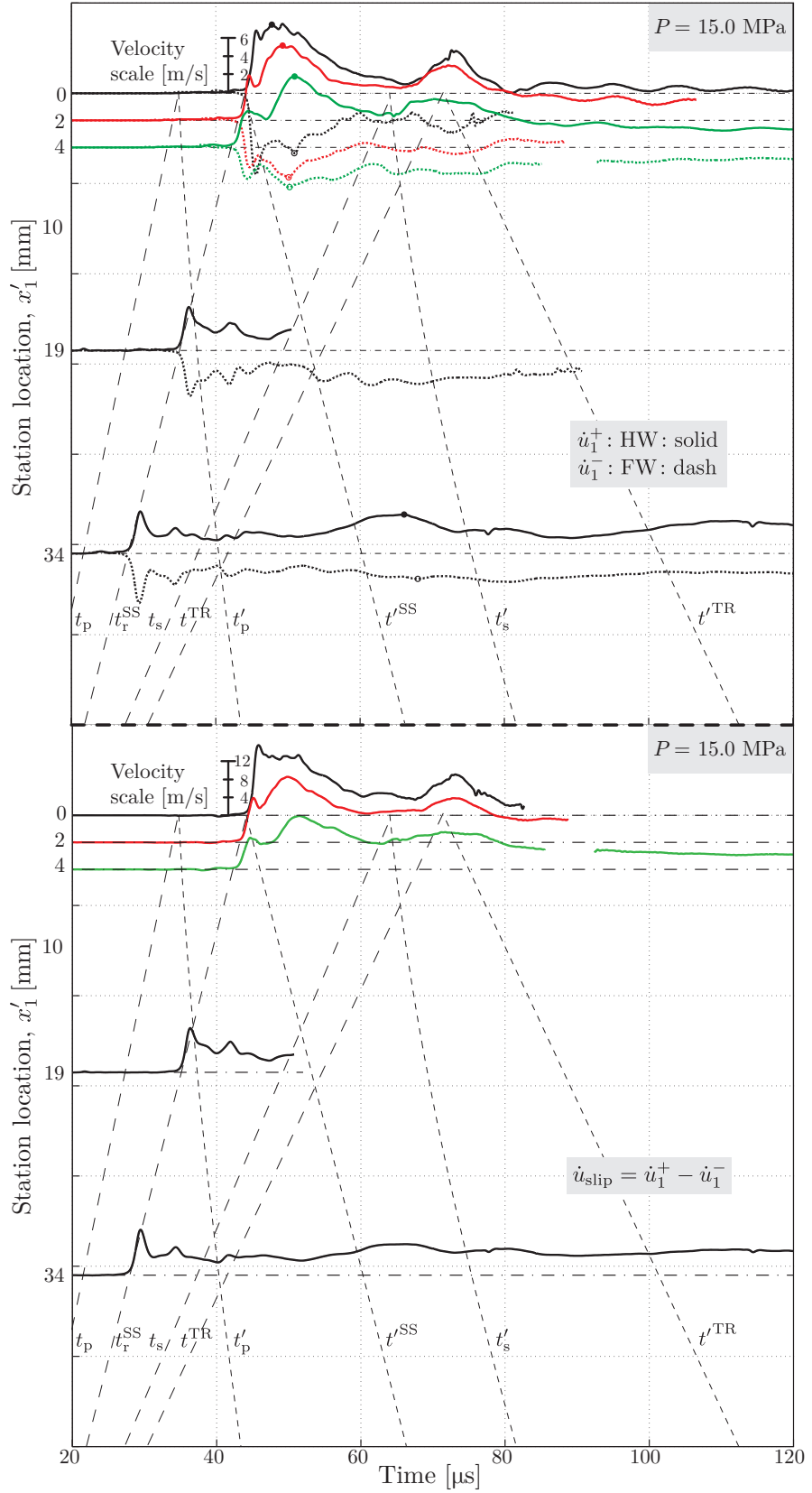
Figure 4.37: Summary of paired fault parallel ($\dot{u}_1^{\pm\epsilon}$) records and slip rate ($\dot{u}_\text{slip}$) for $P = 15.0\,\text{MPa}$.
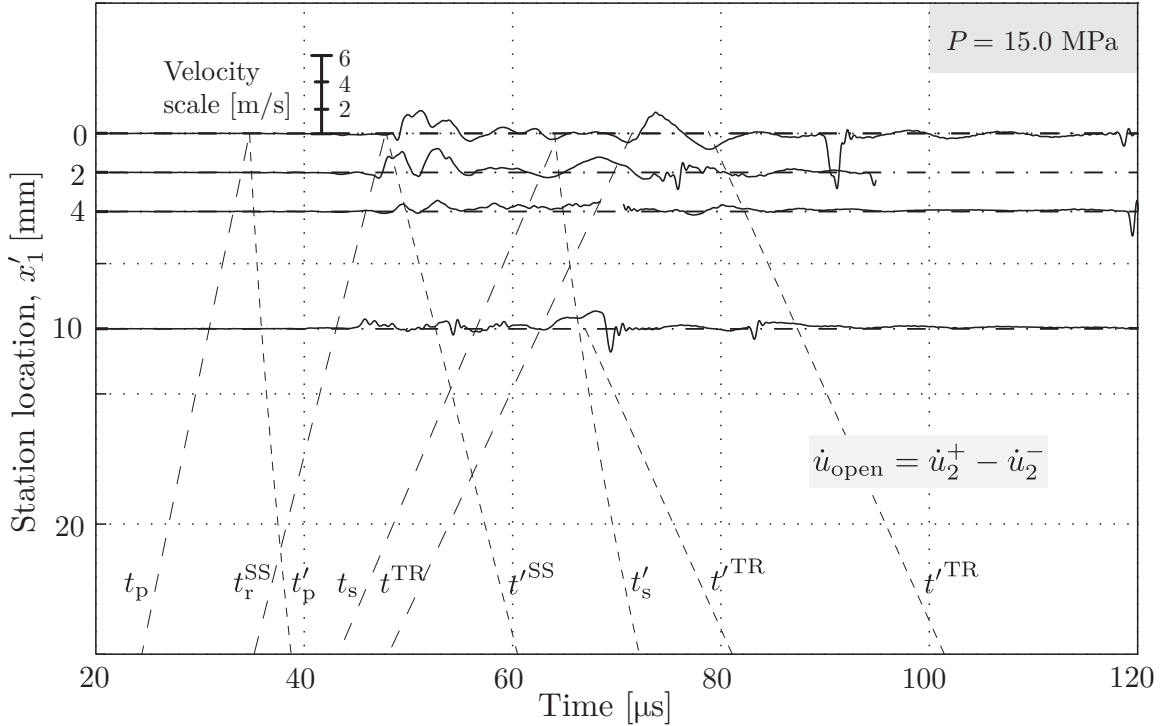
Figure 4.38: A collection of fault opening rates ($\dot{u}_{\mathrm{open}}$) for load $P = 15.0\,\mathrm{MPa}$ SS experiments.

Fault opening rates for SS experiments are reported for stations $x_1' = (0, 2, 4, 10)\,\mathrm{mm}$ in Figure 4.38. Two opening rate pulses are associated with the arrival of the rupture tip ($t_{\mathrm{r}}^{\mathrm{SS}}$), the first from the up-dip rupture and the second from the down-dip SS signature. The up-dip opening rate pulse is nearly absent for station $x_1' = 10\,\mathrm{mm}$ yet is amplified up to $\approx 2\,\mathrm{m/s}$ at the fault trace. Minor fault pinching effects about $\approx -0.5\,\mathrm{m/s}$ are observed ahead of the rupture tip. The third salient signature corresponds to the arrival of the up-dip TR signature, t^{TR}, trailing behind the S wave. While data is sparse and noisy, coherent signal undulations are measured between the two t'^{TR} timing curves: this is analogous to the down-dip mode-I opening pulse generated with the arrival of the rupture tip in SR experiments. Fault opening, while dampened due to the increase in confinement pressure, allows waves to be trapped in the acute geometry of the hanging wall plate, enhancing ground motions.

4.2.9 Mechanical behavior near the earth surface of a SS rupture

Figure 4.39 schematically represents the ground motions near the earth surface of a SS rupture.

In panel A, the P wave is seen ahead of the SS rupture tip and the associated lead dilatational field. Much like the S wave in Figure 4.34, the P wave disturbance propagates along the earth surface at a phase velocity $v_{\mathrm{p}}(x_1)$. The Mach fronts are discontinuities in shear stress caused by the superposition of S waves emitted from the up-dip SS rupture tip propagating at speed $v_{\mathrm{r}}^{\mathrm{SS}}(x_1')$. The fault is locked ahead of the rupture tip, though slipping in its wake.

Panel B shows the SS rupture tip at the fault trace prior to the surface breaking. Slip and opening records of stations near the earth surface indicate that there is nearly negligible negative slip associated with the arrival of the rupture tip (Figure 4.37), unlike in the SR case, e.g., Figure 4.25, where negative slip rates are measured prior to fault opening. An opening pulse is nearly absent at depth but is, however, amplified near the earth surface (Figure 4.38). Anti-symmetry of paired fault parallel records corresponding to the rupture tip is maintained at every depth until the arrival of the reflected P wave, $t'_\mathrm{p}(x'_1)$. The S wave lags behind the Mach cone with an up-dip phase velocity $v_\mathrm{s}(x'_1)$. The rupture is crack-like as the fault continuously slips behind the crack tip.

Panel C shows the earth surface breaking. An opening rate pulse on the order of $2\,\mathrm{m/s}$ pushes the hanging and foot wall away from each other at the fault trace. The breaking of the fault generates a down-dip SS signature, $v'^\mathrm{SS}(x'_1)$, and Rayleigh waves along the earth surface, $v_\mathrm{R} = c_\mathrm{R}$. The down-dip SS signature re-open the interface, resulting in two opening pulses of $\approx 5\,\mathrm{\mu s}$ rise times (Figure 4.38). Temporary opening of the fault allows trapped waves to reflect within the acute wedge of the hanging wall plate. Up-dip Mach fronts impinging on the earth surface propagate with a phase velocity of $v_\mathrm{M}(x_1)$ away from the fault trace, with differing yet constant speeds on the hanging and foot wall plates. Down-dip Mach fronts stemming from the SS travel ahead of the up-dip Mach fronts on the foot wall plate, yet trail behind the up-dip Mach front on the hanging wall plate; phase velocities of the down-dip Mach fronts are marked by $v'_\mathrm{M}(x_1)$. The SS signature immediately breaks the expected fault parallel anti-symmetry condition for stations near the earth surface, selectively enhancing ground motions in the hanging wall plate versus those in the foot wall. The remnant stress concentration of the original SR rupture trails behind the S wave at speeds v^TR; associated with this feature is a finite opening pulse.

Panel D shows the curved front of the down-dip Mach cone, indicating that the stress concentration decelerates with depth; the entire fringe structure, however, propagates down-dip at SS speeds. Since the rupture is crack-like (Figure 4.37), the down-dip Mach cone stems from a stress signature instead of a rupture tip. Down-dip SS signatures mix with up-dip sub-shear content, possibly focusing various rupture effects at critical distances along the fault.

Panel E, aside from the SS content, looks very similar to the schematic for a SR rupture in panel C, Figure 4.34. The effects of the TR signature are sensed on the hanging wall plate along the earth surface, while absent in the foot wall plate. Opening and slip associated with the up-dip TR signature is enhanced towards the earth surface. S waves reflect and feed back onto the fault, propagating down-dip with speeds $v'_\mathrm{s}(x'_1)$; at the same time, S wave perturbations propagate with phase velocities $v_\mathrm{s}(x_1)$ along the earth surface. No perceivable effects from S waves are sensed in the slip or opening rate records, unlike the SR case, where reflected S waves are in fact rupture tips.

Panel F shows the two Rayleigh waves, $v_\mathrm{R}(x_1) = c_\mathrm{R}$, and the down-dip TR signature, $v'^\mathrm{TR}(x'_1)$, generated when the up-dip TR signature opens the fault near the earth surface.
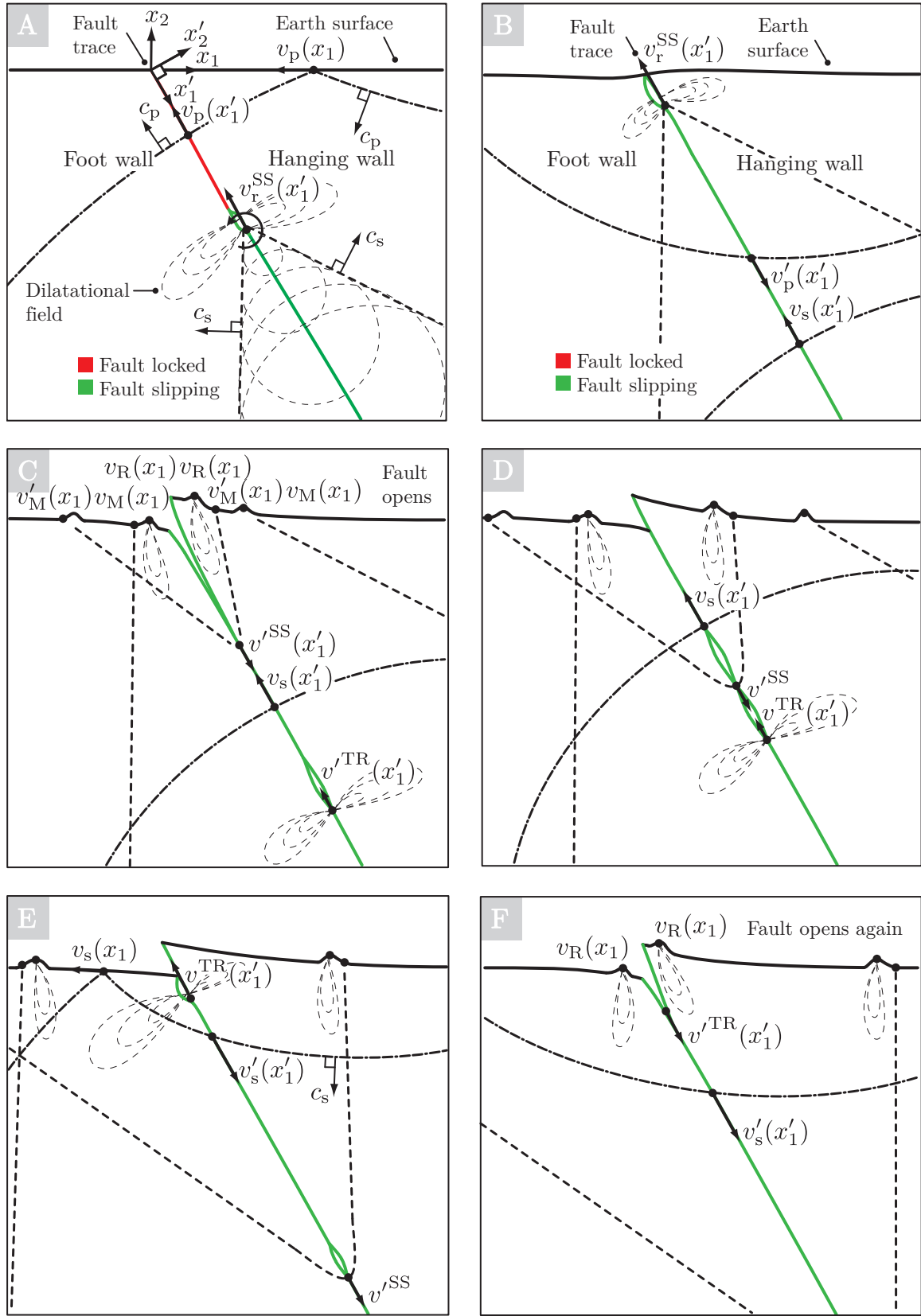
Figure 4.39: Mechanical behavior at the free surface of a SS event in a thrust fault configuration.

The anti-symmetric nature of the up-dip SS rupture signal stems from the dominant fault parallel velocity component near the shear-dominant crack tip. SR ruptures, on the other hand, have dominant fault normal velocity components near the crack tip and are more likely to open the fault near the earth surface. In a SR rupture, the paired hanging and foot wall stations at the fault trace move in tandem (Figures 4.6) as the fault pinches just prior to the hanging wall detaching and opening the fault (Figure 4.25). The whipping motion motion of the hanging wall wedge during opening contributes a large component to the earth surface-normal hanging wall velocity record, accounting for the asymmetric peak ground motion velocities measured at the fault trace (Figure 4.10). For SR ruptures, the salient ground motions on the foot wall are indeed from Rayleigh waves generated during fault opening. In SS ruptures, the fault ruptures nearly anti-symmetrically with minimal opening and weaker fault normal velocity components; the fault motion is shear-dominant.

4.3   Earth surface-normal ground motions with heterogeneity

Results of this section lead to no clear conclusions, however, are presented here for completeness.
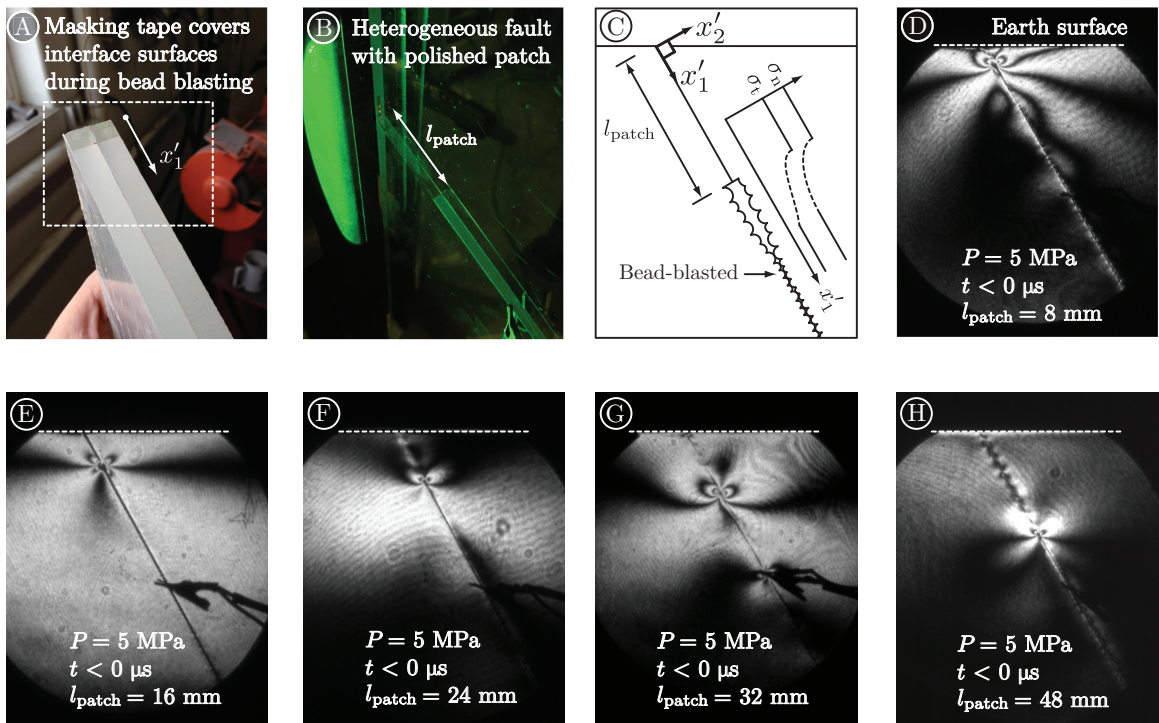
Figure 4.40: A polished patch along the interfacial surfaces of the hanging and foot wall plates remains near the fault trace by masking the region with layers of tape during bead blasting. Photographs of the specimen interface surfaces show the change in reflective properties between the polished patches and the roughened bead-blasted segments. A series of static initial photographs of $P = 5\,\text{MPa}$ experiments with varying patch lengths shows the stress concentration associated with the boundary of the heterogeneous patch traveling down-dip with increasing patch length, l_{patch}.

Ruptures of Sections 4.1 and 4.2 all break the earth surface at the fault trace. One method of preventing surface breaking is to subject the rupture tip to a sudden increase in fault strength. In an attempt to arrest the rupture, a polished patch is introduced by covering sections of the mating interface surfaces with multiple layers of masking tape during the bead blasting procedure (Section 2.2.1.3). This results in two uniform, distinct segments on the fault surfaces, demarcated by the boundary $x'_1 = l_{\text{patch}}$, where l_{patch} is the length of the polished patch (Figure 4.40, A); under load, the polished segment is optically transparent while the bead-blasted segment is translucent (B). Based on average roughness measurements of polished and bead-blasted surfaces [55], removal of material during bead blasting will introduce a height offset on the order of 2 µm; assuming increased frictional resistance in the polished segment, an increase in local shear and compressive fault stresses is expected as the rupture traverses across the boundary $x'_1 = l_{\text{patch}}$ into the polished patch (C). At the patch boundary, it is uncertain whether a gap exists or if contact is enforced; a state dependent on the far-field load, P. Static images of specimens with various patch lengths, $l_{\text{patch}} = (8, 16, 24, 32, 48)\,\text{mm}$ (D-H), for a compressive load $P = 5.0\,\text{MPa}$ are taken prior to nucleation; the fringe concentration at the patch boundary indicates large local gradients in shear stress magnitude, as expected near $x'_1 = l_{\text{patch}}$. Ruptures generated with loads $P = 5.0\,\text{MPa}$ and $P = 15.0\,\text{MPa}$ in standard, uniformly bead-blasted faults consistently generate SR and SS up-dip ruptures, respectively (Sections 4.1 and 4.2); to isolate effects of the heterogeneity on ground motions, reference is maintained to these measurements by generating ruptures with $l_{\text{patch}} = (8, 16, 24, 32, 48)\,\text{mm}$ for identical loads, $P = 5.0\,\text{MPa}$ and $P = 15.0\,\text{MPa}$. For a given load P, the difference in fault strength across the boundary is invariant of l_{patch} due to uniform loading, however, the boundary experiences different local rupture fields since the hypocenter remains fixed across all specimens.

Several observations indicate that the fault strength is greater in the polished patch than the bead-blasted segment. Two SS earthquakes are generated ($P = 15.0\,\text{MPa}$) and earth surface-normal velocities ($\dot{u}_2$) are measured at hanging wall stations $x_1 = +(0, 2, 4)\,\text{mm}$ (Figure 4.41); the left photograph and the solid records correspond to a fully bead-blasted fault ($l_{\text{patch}} = 0\,\text{mm}$), while the right photograph and dashed records correspond to a fully polished fault ($l_{\text{patch}} = \infty$), the two experiments are otherwise nominally identical. The optically polished surfaces mate very well and seem to have additional cohesion under load, likely due to the larger available contact area. Inspection of the bead-blasted fault surfaces post-experiment show accumulation of fine white powder along the entire interface length (Figure 5.4): since the mating surfaces were thoroughly cleaned prior to sealing the fault, this powder must be generated from the rupture tip processing the roughened surfaces. The fine powder is absent in the polished surface, instead, scratches whose lengths are aligned along the interface with the rupture directivity can be seen with the naked eye (Section 5.2). Fault trace records (black curves) indicate that the earth surface was broken in both events upon rupture tip arrival (t_r^{SS}). The stress drop for the polished fault is less than half of the bead-blasted
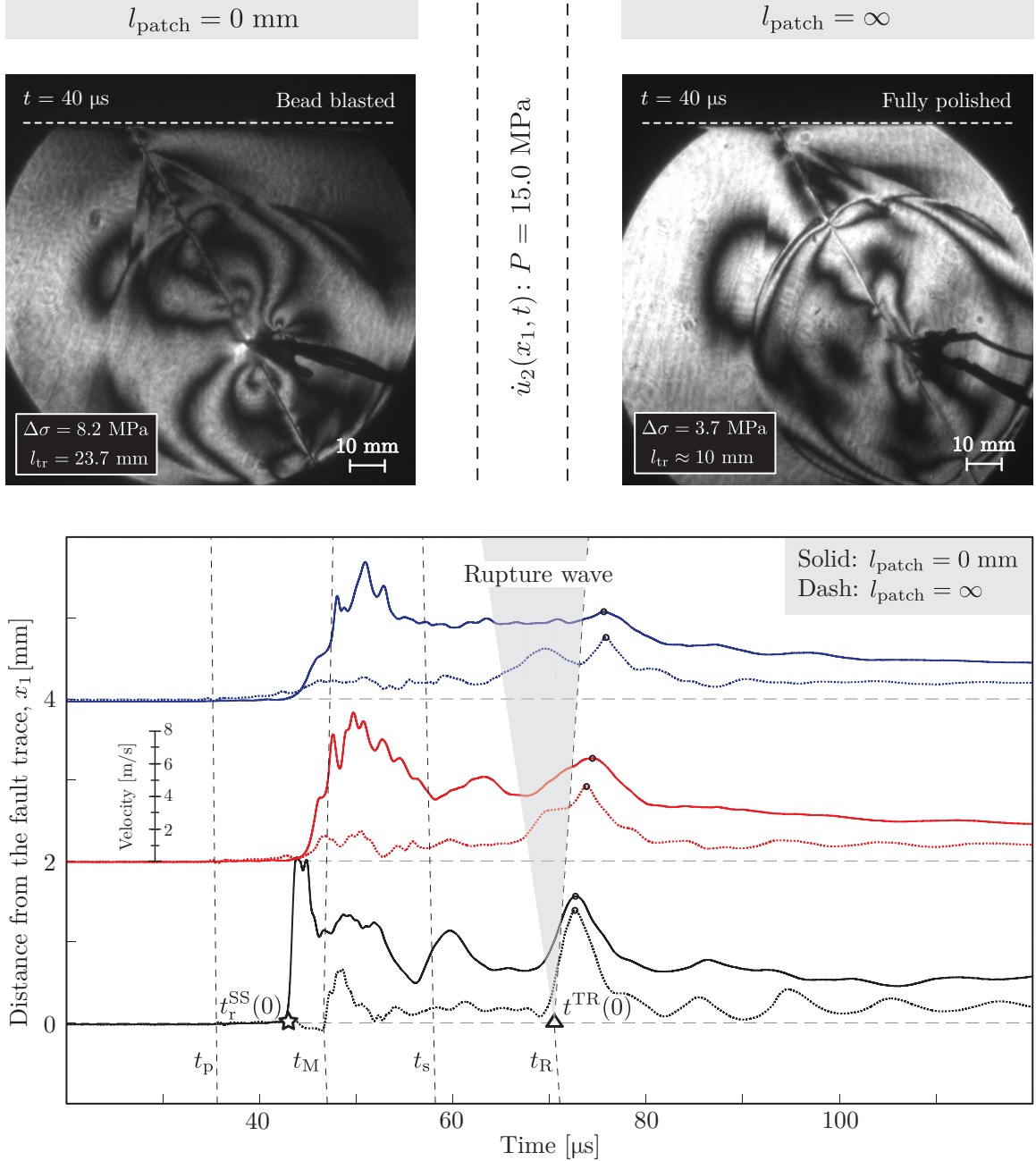
Figure 4.41: SS rupture ($P = 15.0\,\mathrm{MPa}$) along a bead-blasted ($l_{\mathrm{patch}} = 0\,\mathrm{mm}$) and polished fault ($l_{\mathrm{patch}} = \infty\mathrm{mm}$). Earth surface-normal records ($\dot{u}_2$) are recorded at hanging wall stations $x_1 = +(0, 2, 4)\,\mathrm{mm}$ for bead-blasted (solid) and polished (dashed) faults.

($\Delta\sigma = 3.7\,\mathrm{MPa}$ and $\Delta\sigma = 8.2\,\mathrm{MPa}$), indicating an overall deficit in total accumulated slip; the polished fault has a greater tendency to hinder slip. Rupture and trailing-Rayleigh signature speeds are nearly identical in bead-blasted and polished experiments ($v_{\mathrm{r}}^{\mathrm{SS}} = 2.15\,\mathrm{mm/\mu s}$, $v_{\mathrm{r}}^{\mathrm{SS}} = 2.01\,\mathrm{mm/\mu s}$ and $v^{\mathrm{TR}} = 1.13\,\mathrm{mm/\mu s}$, $v^{\mathrm{TR}} = 1.19\,\mathrm{mm/\mu s}$), however, the transition length is much shorter for the polished fault ($l_{\mathrm{tr}} = 23.7\,\mathrm{mm}$ and $l_{\mathrm{tr}} \approx 10\,\mathrm{mm}$). Mach front signals are significantly attenuated in

the polished system (dashed curves), about $\approx 35\%$ of peak values in the bead-blasted system at the fault trace; the fault trace, in fact, is nearly dormant between $t_{\mathrm{r}}^{\mathrm{SS}}$ and t^{TR}, in contrast to the bead-blasted records (solid curves), which tend to sustain ground motions throughout the entire experimental window, $T_{\mathrm{exp}} = 120\,\mu\mathrm{s}$. A distinct rupture wave is observed in stations $x_1 = (2, 4)\,\mathrm{mm}$ for the polished experiment, a signal which is difficult to discern in the bead-blasted experiment. Note that the TR signal attenuates much less than the Mach front, $\approx 0.88\%$ from $8\,\mathrm{m/s}$ to $7\,\mathrm{m/s}$. The Mach and TR signals are also much more distinct with shorter pulse-widths, supporting the notion that the polished fault has the tendency to re-lock more than the bead-blasted fault, perhaps related to presence of the crushed powder. Distinct, sharp oscillations in the fault trace records after the TR signature are easier to discern in the polished system, however, are difficult to discern in the bead-blasted system, where minute oscillations are overlain onto a constant velocity of $\approx 4\,\mathrm{m/s}$.

4.3.1   Earth surface-normal records of high-load ruptures with patches

A series of experiments are conducted with an applied load of $P = 15.0\,\mathrm{MPa}$ for patch lengths $l_{\mathrm{patch}} = (0, 8, 16, 24, 32, 48)\,\mathrm{mm}$. Each column in Figures 4.42-4.44 corresponds to a given l_{patch}, containing two photographs from a single event pre and post-rupture tip interaction with the patched boundary, $x_1' = l_{\mathrm{patch}}$, and a collection of earth surface-normal velocity records measured on the hanging and foot wall plates in two nominally identical experiments at distances $x_1 = \pm(0, 2, 4)\,\mathrm{mm}$. The experiment of Section 4.1.3 ($l_{\mathrm{patch}} = 0\,\mathrm{mm}$, fully bead-blasted), is reproduced here for reference. At these loads, SS transition is expected within the total rupture track length, D.

The SS ruptures easily pass through the patch barrier and eventually break the earth surface at the fault trace. Unfortunately, the increase of fault strength from the polished patch was insufficient to cease the rupture tip, as is the case for short patches; for longer patches, however, the standard SS transition observed in fully bead-blasted interfaces is absent as the patch barrier disrupts the transition process which happens to coincide with the barrier location. The Mach fronts are rendered invisible during slip in the polished region for large patches. Fringe patterns propagate up-dip ahead of the TR signature in the polished patch segment; ground motions bound between t_{p} and t_{s} represent SS rupture signatures, inducing ground motions prior to arrivals of shear information. In general, patched experiments have distinct SS and TR signature pulses, unlike the case of $l_{\mathrm{patch}} = 0\,\mathrm{mm}$, where ground motions are sustained after rupture tip arrival. The rupture wave is also more distinct with sharper peaks in patched experiments. Shear arrest waves are captured in photographs of some experiments when the rupture tip interacts with the polished barrier. While strong conclusions may not be drawn from the data, two trends seem apparent: the SS and TR signals dampen with an increase in patch length and ground motion pulses are more easily generated in a fault system with a patched heterogeneity (Figure 4.45). While SS signatures dampen with the presence of a patch, the TR signatures seem less affected; from previous measurements, the large asymmetry of ground

$$\dot{u}_2(l_{\mathrm{patch}}:x_1,t) = \pm[0,2,4]\ \mathrm{mm},\ P = 15.0\ \mathrm{MPa},\ \alpha = 29°$$
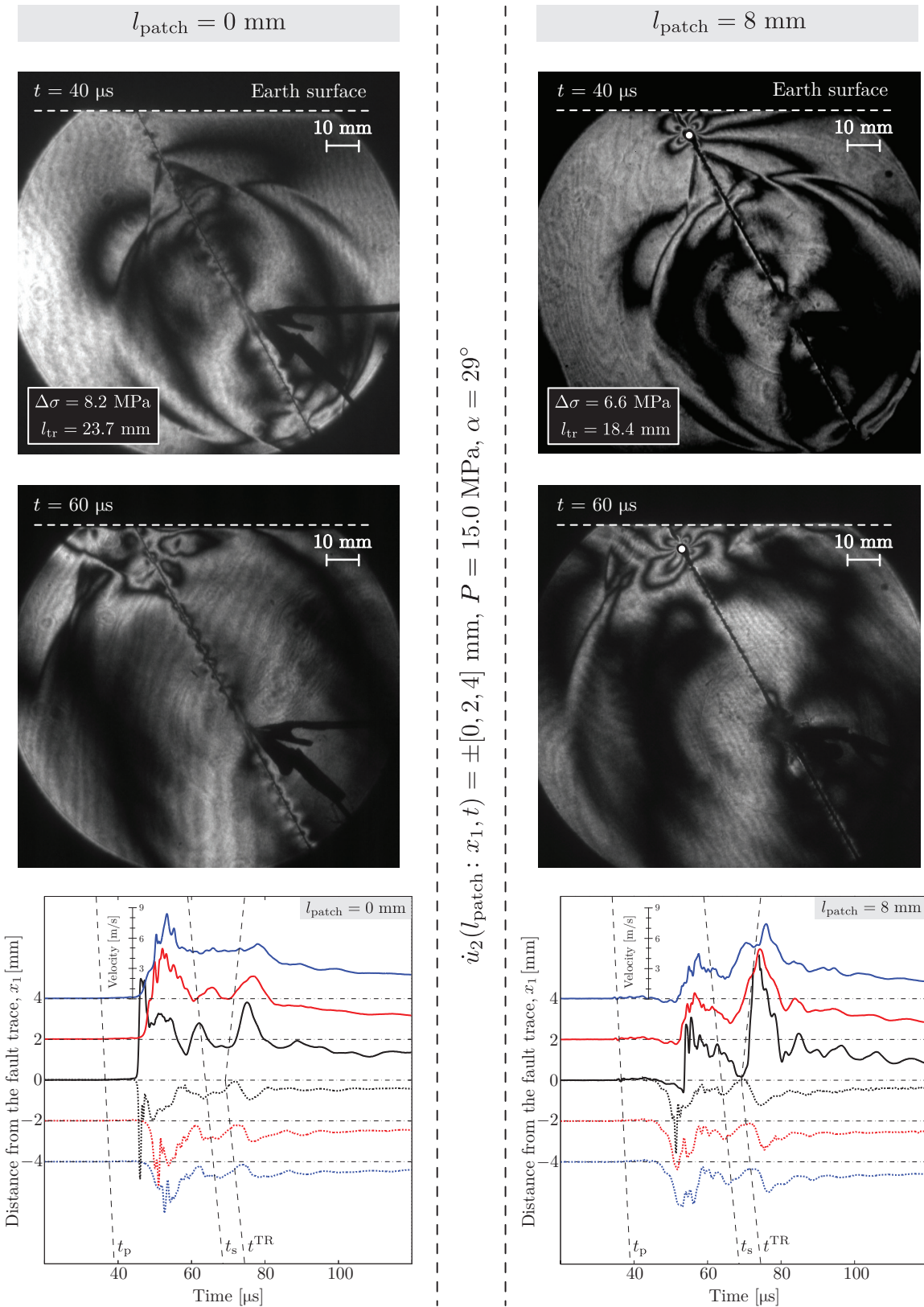
Figure 4.42: Earth surface-normal records ($P = 15.0\,\mathrm{MPa}$) with $l_{\mathrm{patch}} = 0\,\mathrm{mm}$ and $l_{\mathrm{patch}} = 8\,\mathrm{mm}$.
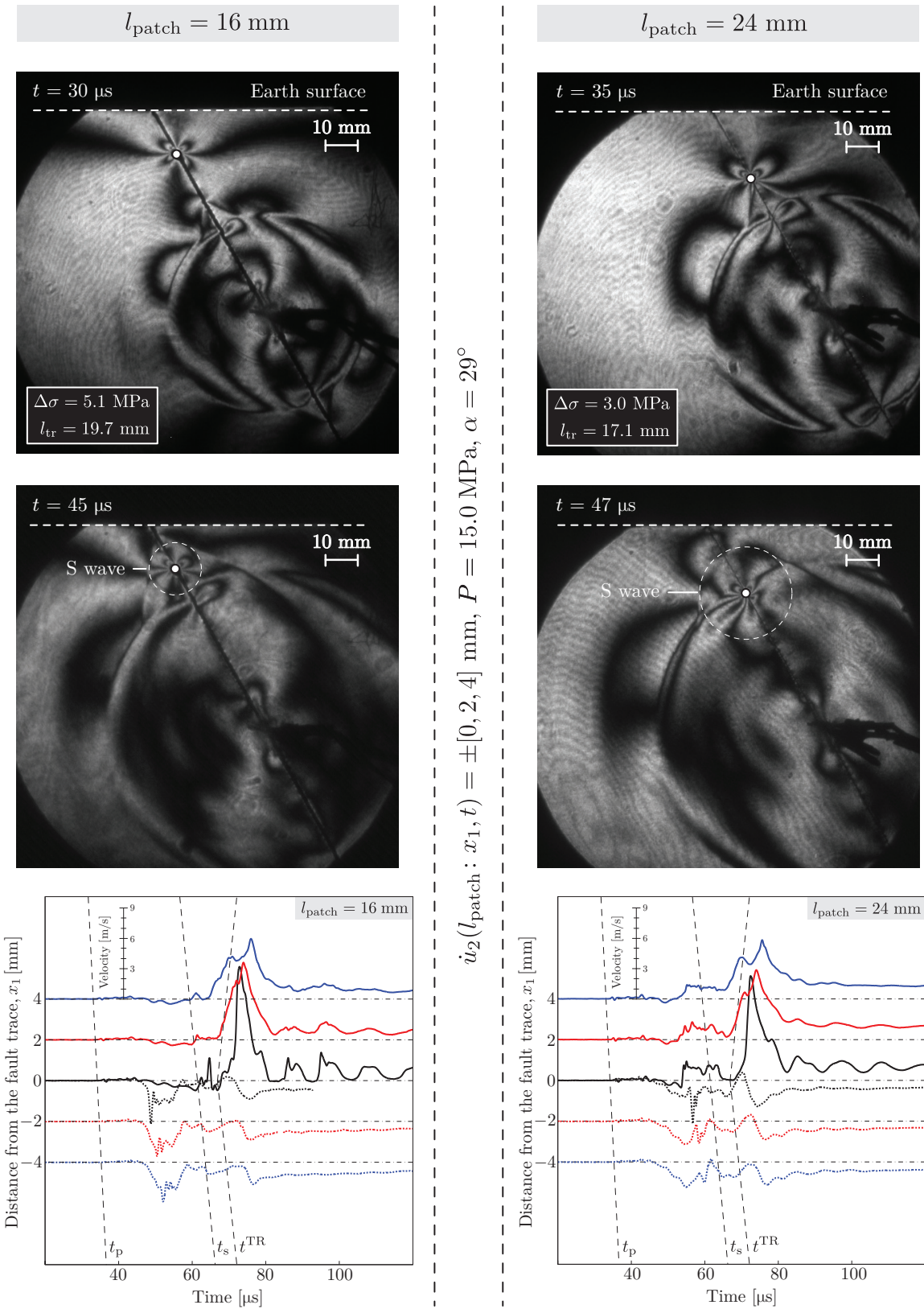
Figure 4.43: Earth surface-normal records ($P = 15.0\,\text{MPa}$) with $l_{\text{patch}} = 16\,\text{mm}$ and $l_{\text{patch}} = 24\,\text{mm}$.
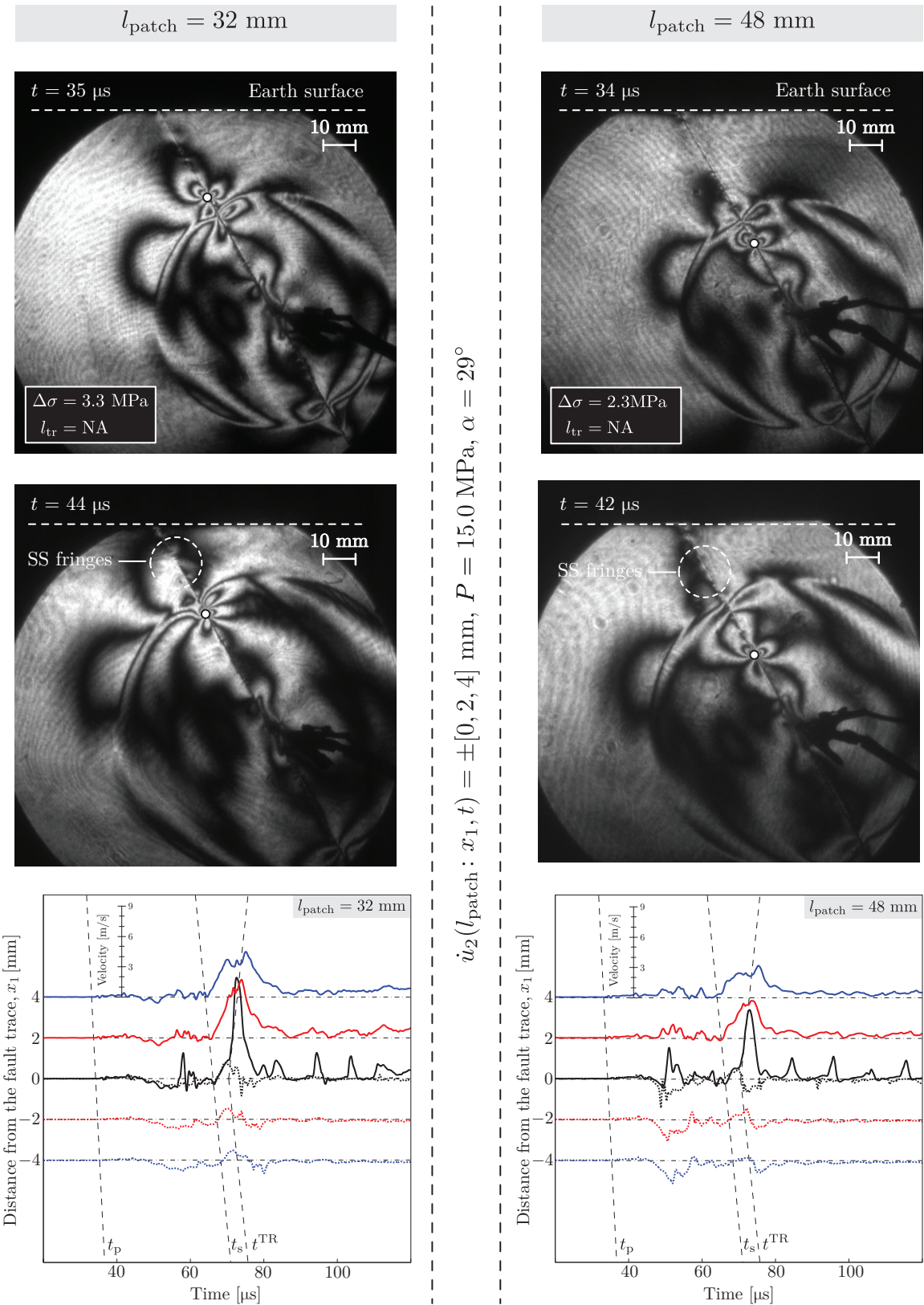
Figure 4.44: Earth surface-normal records ($P = 15.0\,\mathrm{MPa}$) with $l_{\mathrm{patch}} = 32\,\mathrm{mm}$ and $l_{\mathrm{patch}} = 48\,\mathrm{mm}$.
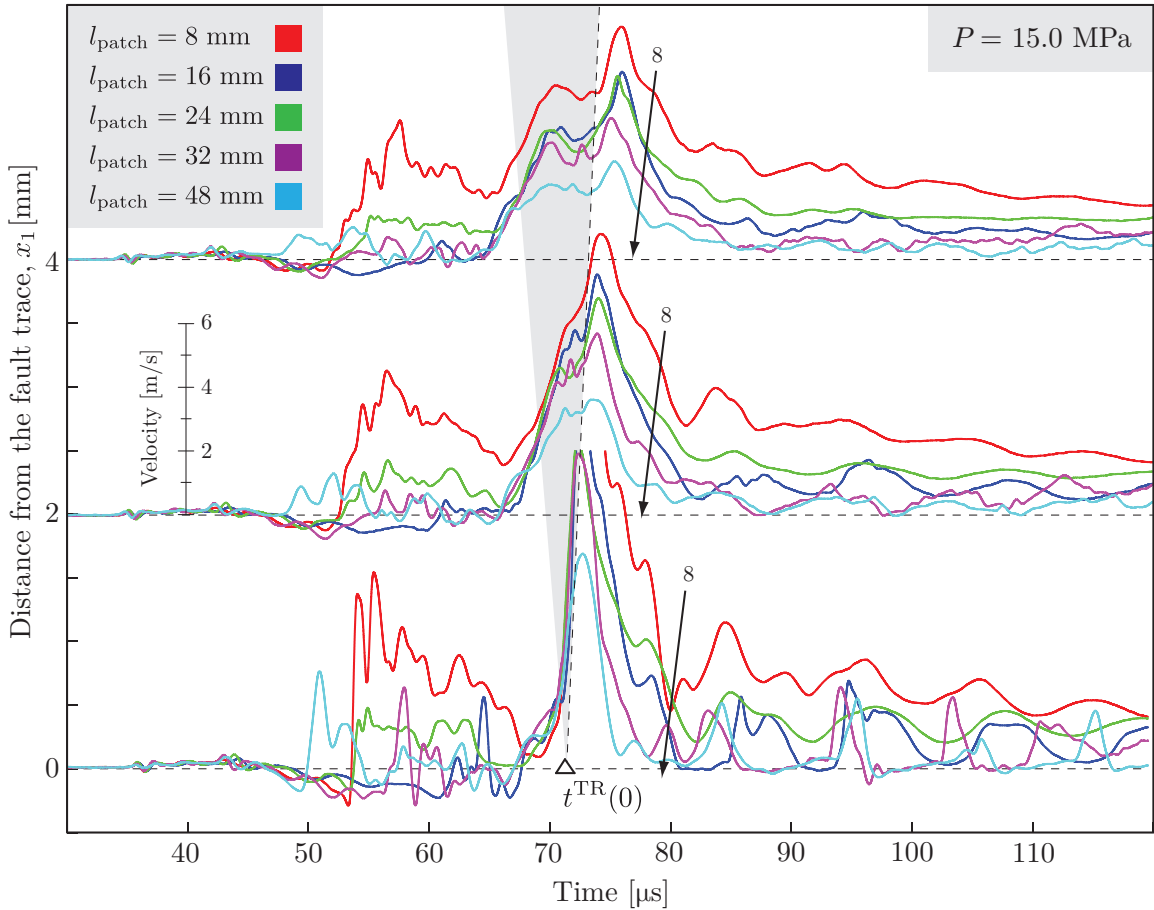
Figure 4.45: Collection of hanging wall earth surface-normal records ($P = 15.0\,\text{MPa}$) for all l_{patch}.

motions at the fault trace implies fault opening, and may explain why the TR signature dampens less than the shear-dominant rupture tip. The study is inconclusive since the hypocenter location does not change while the patch lengths do; the patch barrier will sense different rupture tip fields according to how long the rupture has propagated along the interface.

4.3.2 Earth surface-normal records of low-load ruptures with patches

Dropping the load to $P = 5\,\text{MPa}$ generates ruptures along faults with $l_{\text{patch}} = (0, 8, 16, 24, 32, 48)\,\text{mm}$. Much like the previous section, Figures 4.46-4.47 summarize the results of patched experiments, with each column corresponding to a single l_{patch}. The additional fault strength from the patched segment was again insufficient to cease the rupture tip at the patch boundary. One event transitioned to SS speeds (Figure 4.47, $l_{\text{patch}} = 24\,\text{mm}$), which would have remained SR in the absence of the patch. Arrest waves are again generated with rupture tip arrival to the patch boundary, indicating abrupt deceleration. Typical ground motion records of SR ruptures are observed with additional leading signals between curves t_{p} and t_{s}, as well as amplification of the TR signature with increase in l_{patch}.
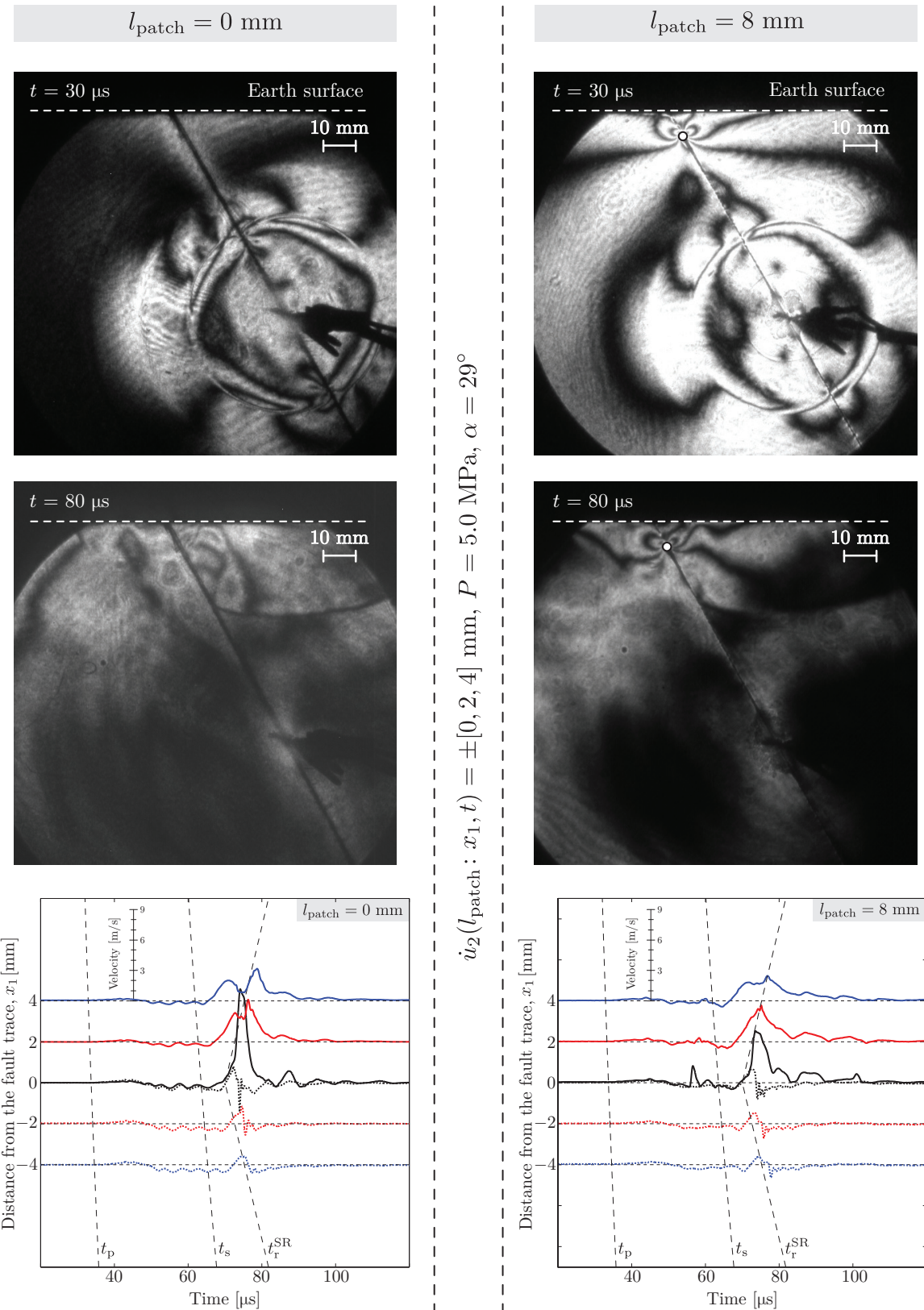
Figure 4.46: Earth surface-normal records ($P = 5.0\,\mathrm{MPa}$) with $l_{\mathrm{patch}} = 0\,\mathrm{mm}$ and $l_{\mathrm{patch}} = 8\,\mathrm{mm}$.
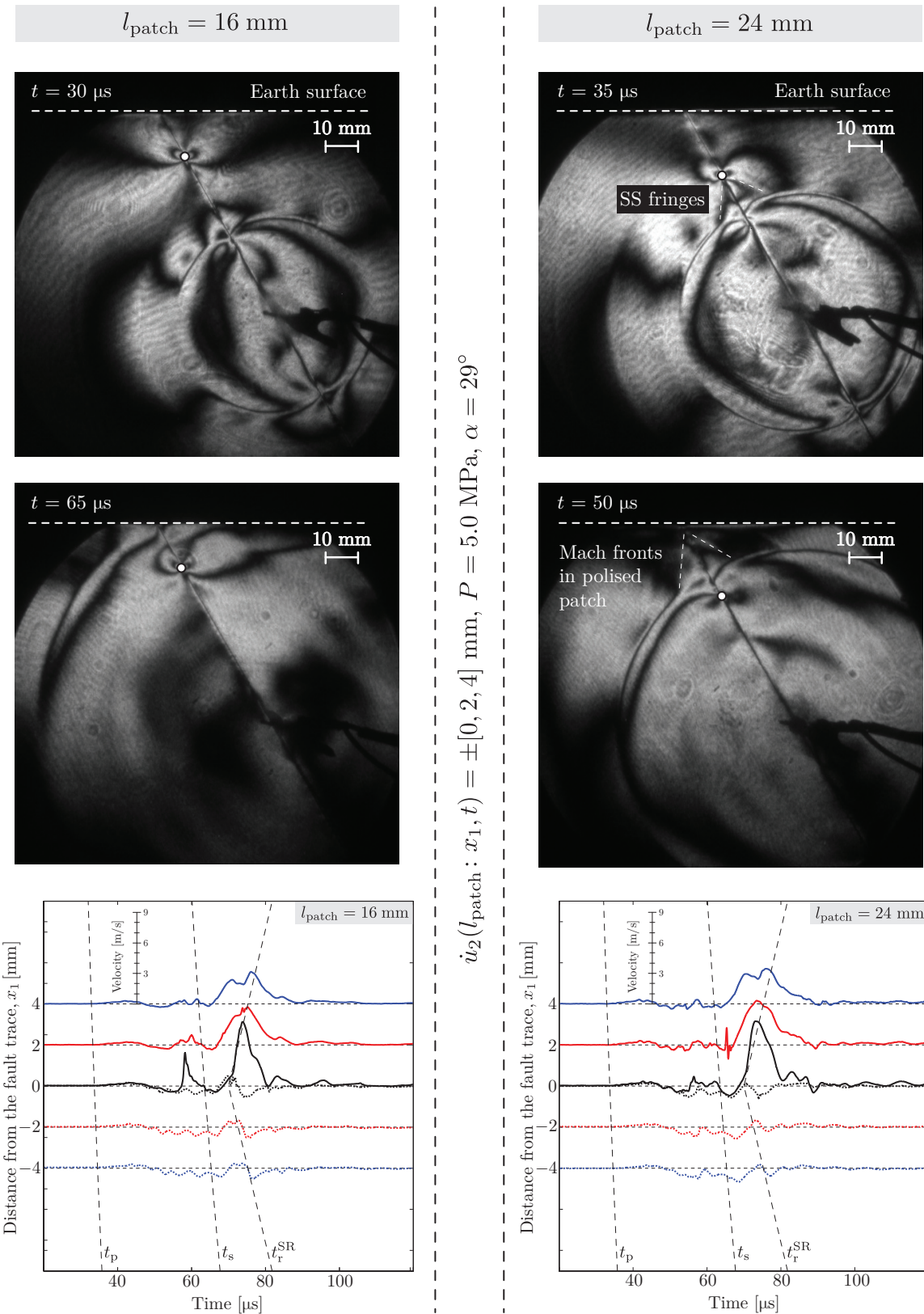
Figure 4.47: Earth surface-normal records ($P = 5.0$ MPa) with $l_{\text{patch}} = 16$ mm and $l_{\text{patch}} = 24$ mm.
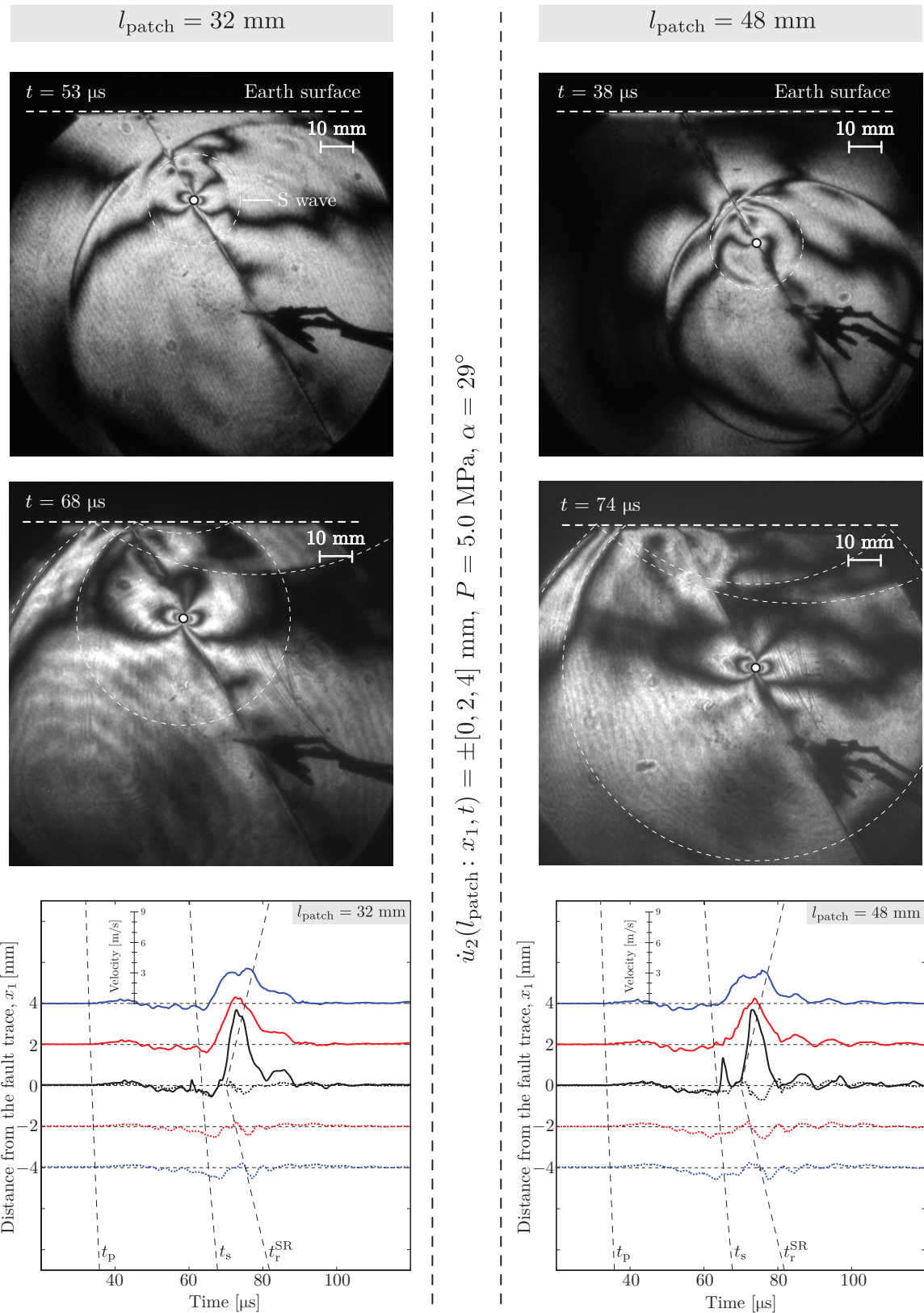
Figure 4.48: Earth surface-normal records ($P = 5.0\,\mathrm{MPa}$) with $l_{\mathrm{patch}} = 32\,\mathrm{mm}$ and $l_{\mathrm{patch}} = 48\,\mathrm{mm}$.
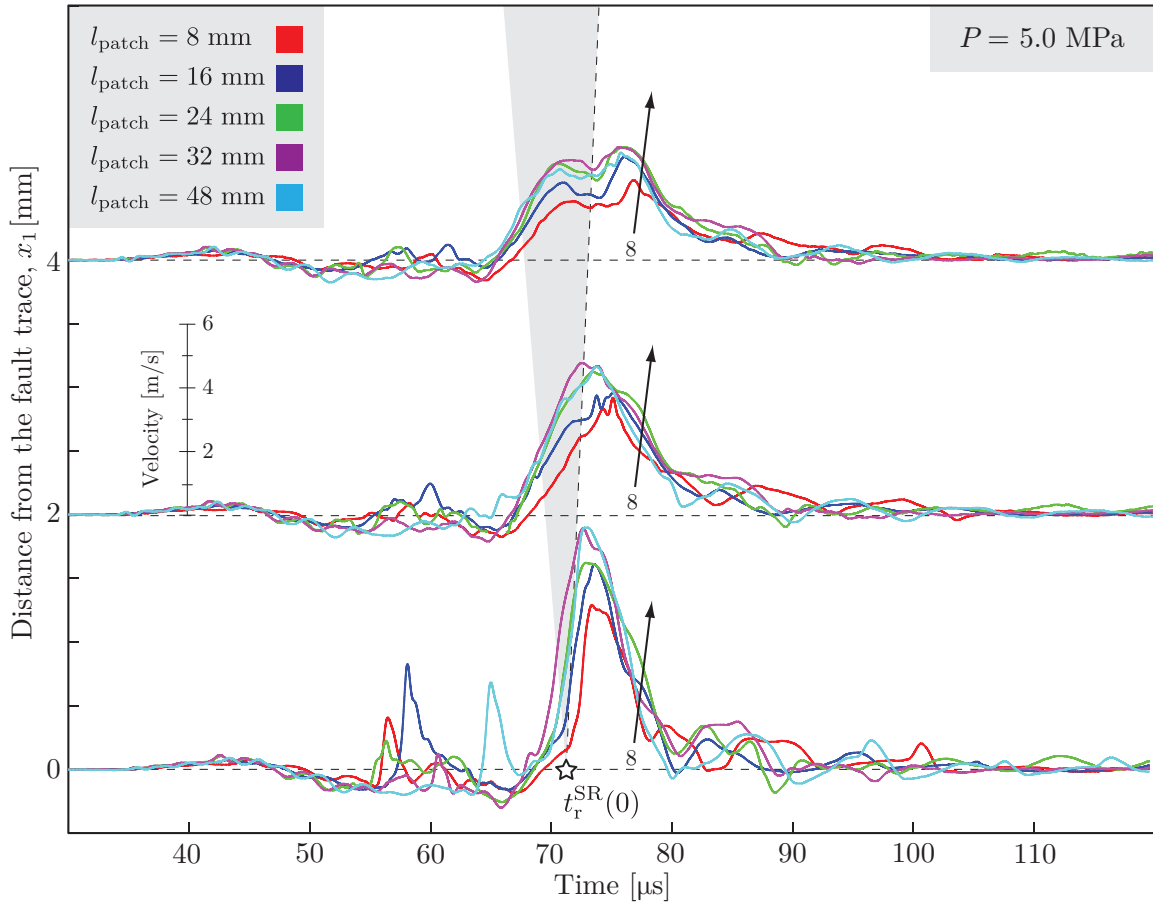
Figure 4.49: Collection of hanging wall earth surface-normal records ($P = 5.0\,\mathrm{MPa}$) for all l_{patch}.

The experiments of this section need modification to allow comparisons of resulting ground motions from buried and surface-breaking thrust fault ruptures; a glued patch or another solution may be needed to completely arrest the rupture and isolate effects of the surface-breaking phenomenon.

Chapter 5

Reproducibility of Ruptures

The question of reproducibility of different, yet nominally identical, experiments needs to be addressed in every experimental data set where comparisons are made across such experiments, e.g., Figure 4.6. Geared with the mindset of experimental reproducibility, a discussion of measurable data sets and qualitative observations is presented in the following sections.

5.1 Speed measurements and transition

Speed measurements are well-banded, suggesting consistency in material manufacturing (properties) and uniformity of loading and surface conditions at the interface. Measured values of P (S) waves, SR and SS rupture tip speeds are presented in Figure 5.1 for 59 experiments. Open and closed markers indicate nominally identical experiments conducted at $P = 5\,\mathrm{MPa}$ and $P = 15\,\mathrm{MPa}$, respectively.

The S wave is the most accurate rupture feature measured from the photo-elastic images, since the method is sensitive to shear (Appendix B). Figure 5.1 shows well-banded values of $c_\mathrm{s} = 1.27(2)\,\mathrm{mm/\mu s}$, P wave measurements are less precise, $c_\mathrm{p} = 2.59(5)\,\mathrm{mm/\mu s}$, due to the faint nature of the wave fronts and fewer frames available for measurement ($c_\mathrm{p} \approx 2c_\mathrm{s}$). Accuracy of wave speeds are verified using dilatational and shear transducers (Section 3.1.1), yielding results within $0.05\,\mathrm{mm/\mu s}$ of the mean values. The banded wave speeds indicate consistency of material properties.

Uniformity and repeatability of interface conditions drive the spread in values for rupture tip speeds, v_r^SR and v_r^SS, as well as transition length, l_tr. Measurements of the SR rupture tip speeds (Figure 5.1, open stars) yield values $v_\mathrm{r}^\mathrm{SR} = 1.14(3)\,\mathrm{mm/\mu s}$. Aside from the nucleation zone where accelerations are greatest, SR rupture tip speeds are nearly constant throughout up-dip propagation towards the fault trace and are about $89-92\,\%$ of the Rayleigh wave speed, $c_\mathrm{R} = 1.18\,\mathrm{mm/\mu s}$. Up-dip trailing-Rayleigh (TR) signature speeds are measured similarly for experiments where SS transition occurs and yield values $v^\mathrm{TR} = 1.14(3)\,\mathrm{mm/\mu s}$, identical to v_r^SR; the remnant stress concentration of the original SR rupture is insensitive to changes of interface properties and loading introduced by the lead SS rupture. The SS rupture tip speeds are much less constrained with values $v_\mathrm{r}^\mathrm{SS} =$
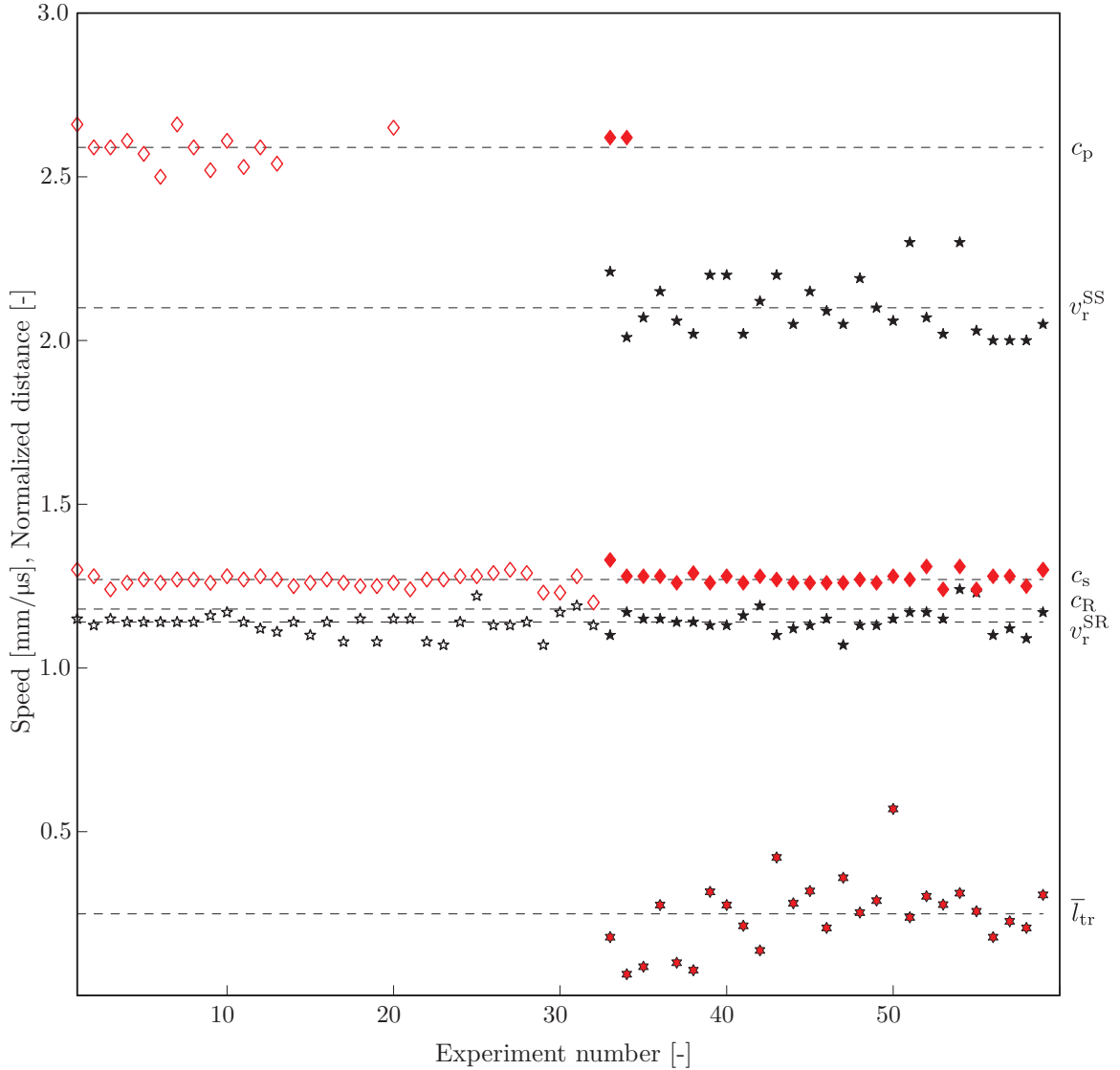
Figure 5.1: Speed measurements from nominally identical experiments of loads $P = 5\,\text{MPa}$ (empty markers) and $P = 15\,\text{MPa}$ (solid markers). Average speeds are marked with lines $c_{\text{p,s}}$ (P and S waves, diamonds) and $v_{\text{r}}^{\text{SR,SS}}$ (SR and SS rupture tips, stars). Transition lengths for SS experiments are normalized by rupture tip track length, $\bar{l}_{\text{tr}} = l_{\text{tr}}/D$, where $D = 74.3\,\text{mm}$ (red starburst). The average trailing-Rayleigh signature speed, v^{TR}, is indistinguishable from v_{r}^{SR}.

$2.10(10)\,\text{mm/µs}$. Even less constrained are transition lengths, normalized by rupture track length $\bar{l}_{\text{tr}} = l_{\text{tr}}/D$. Transition lengths are found to be $l_{\text{tr}} = 18.5(80)\,\text{mm}$, corresponding to about $25\,\%$ of the rupture track length from the hypocenter. Spread in v_{r}^{SS} and l_{tr} suggests that the transition mechanism is much more sensitive to interface conditions than v_{r}^{SR} and v^{TR}.

Specimen preparation processes and plate alignment during loading contribute to non-uniform interface conditions. Manufacturing of the specimen may introduce geometrical errors in the specimen, causing non-uniform loading conditions at the interface. Loss of planarity of the specimen load-
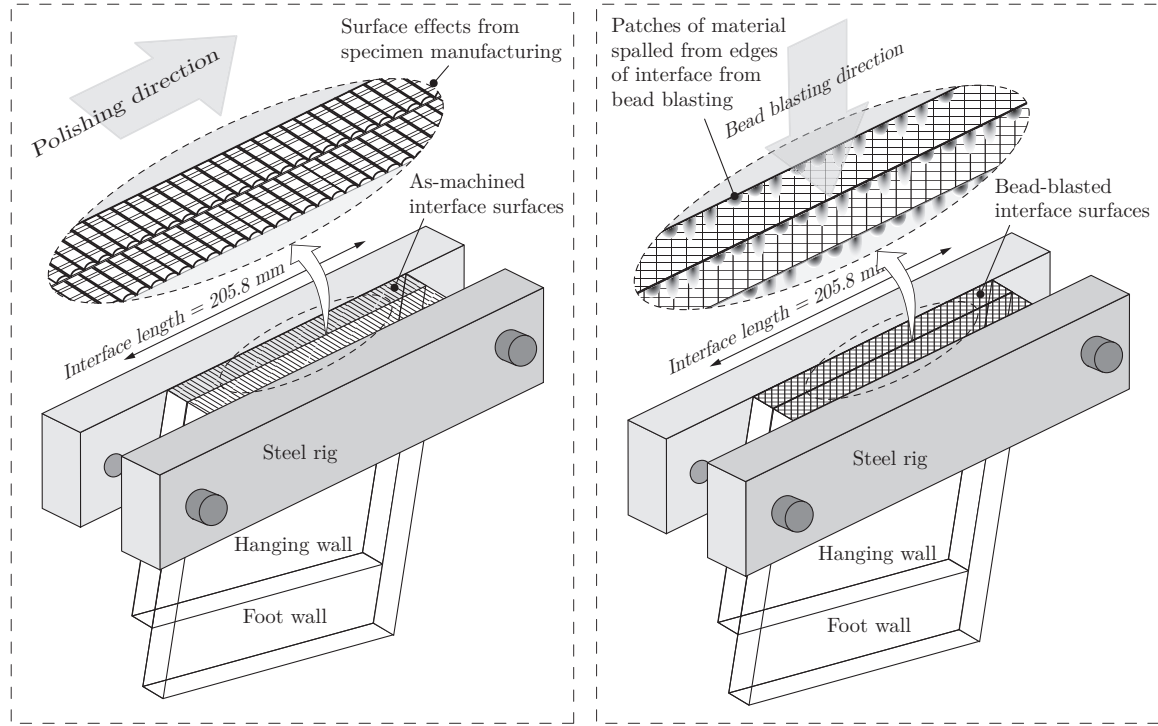
Figure 5.2: Surface effects from specimen machining process and bead blasting procedure. Short and long-wavelength features are removed with the polishing process (left panel). Bead blasting may introduce edge effects due to improper alignment of plates in the steel rig, insufficient confinement, loss of protective cover, or bowed plates, allowing the glass beads to penetrate the gaps (right panel).

ing surfaces causes a gradient in resolved stresses along the interface, $\sigma_{\mathrm{n}} = \sigma_{\mathrm{n}}(x_1')$ and $\sigma_{\mathrm{t}} = \sigma_{\mathrm{t}}(x_1')$. Moreover, uniaxial loading of the specimen in the hydraulic press is not guaranteed (Section 2.2.2.2). An experiment with fully polished interface surfaces exemplifies this effect: the mated, optically coherent surfaces change reflective properties during loading, but not at all points at the same time. Repeated loading cycles assure uniform load distribution along the interface with the shadow technique, an additional step which may be omitted if the press platens have gimbal arms.

The polishing and bead blasting processes in themselves contribute to irregularities: two surface features on the mating surfaces are eliminated with the polishing process (Figure 5.2, left panel), including through-thickness short-wavelength ridges and long-wavelength striations along the entire interface length caused by the milling process. Both of these features are visible with the naked eye and disappear after the polishing process: long-wavelength effects, however, are impossible to sense and must be avoided during specimen manufacturing (Section 2.2.1.1). Uneven or over-polishing may introduce imperceivable long-wavelength effects; a systematic polishing process should be established to eliminate user bias. Bead blasting the polished interfaces may damage the imaging surfaces if insufficient clamping force is used to position the hanging and foot wall plates in the steel rig (Figure 5.2, right panel), allowing glass beads to enter gaps between the specimen and the rig.

SR and SS rupture tip speeds depend on geometry, loading, and interface frictional parameters, $v_{\mathrm{r}}^{\mathrm{SR}} = v_{\mathrm{r}}^{\mathrm{SR}}(P, \alpha, f_{\mathrm{s}}, f_{\mathrm{d}})$ and $v_{\mathrm{r}}^{\mathrm{SS}} = v_{\mathrm{r}}^{\mathrm{SS}}(P, \alpha, f_{\mathrm{s}}, f_{\mathrm{d}})$. Transition lengths are dependent on identical parameters, $l_{\mathrm{tr}} = l_{tr}(P, \alpha, f_{\mathrm{s}}, f_{\mathrm{d}})$, however, SS rupture tip speeds are much more banded than corresponding transition lengths, suggesting that SS rupture tip speeds tend to accelerate to a constant, steady-state value irrespective of the transition length. Rupture tip speeds are much more reproducible than transition lengths, thus suggesting a finer length scale dependency for transition lengths. Experimental evidence of non-symmetric transition lengths for the bilateral rupture further corroborate the sensitivity of transition lengths to the driving parameters; numerical studies predict that heterogeneities along the interface may induce premature SS transition [119].

5.2 Nucleation and post-dynamics

Dynamic rupture delay times (t_{dyn}) and wire soot deposit lengths (L_{soot}) indicate that the nucleation process is repeatable for nominally identical experiments. A schematic summary of the experimental nucleation process is shown in Figure 5.3 along with a photograph of typical soot deposit patterns.

Nucleation of rupture can be achieved with a drop in fault frictional strength or a sudden local increase in stressing conditions at the hypocenter. The wire-notch mechanism decreases the fault
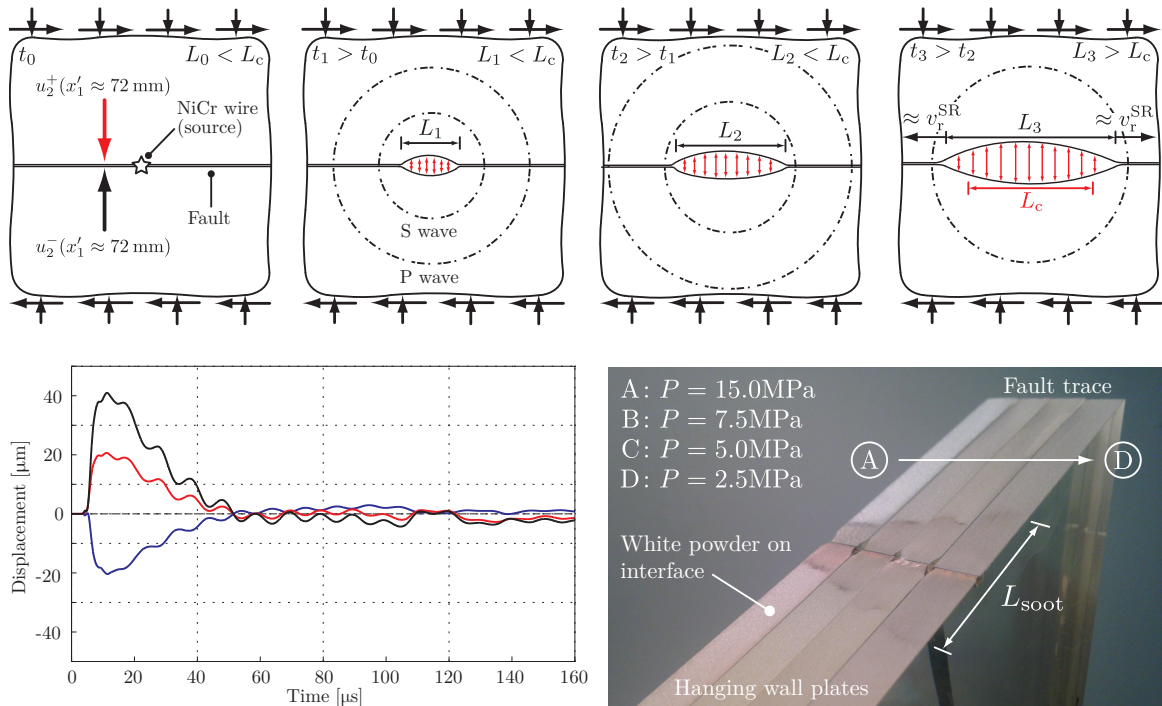
Figure 5.3: Nucleation process for the dynamic rupture. A schematic representation of the nucleation process shows interface opening near the notch and a post-experiment soot deposit of length L_{soot} at the nucleation site (top panel). Fault opening displacement measurements at the notch (black curve) and soot deposits from the wire phase transformation corroborate this physical model.
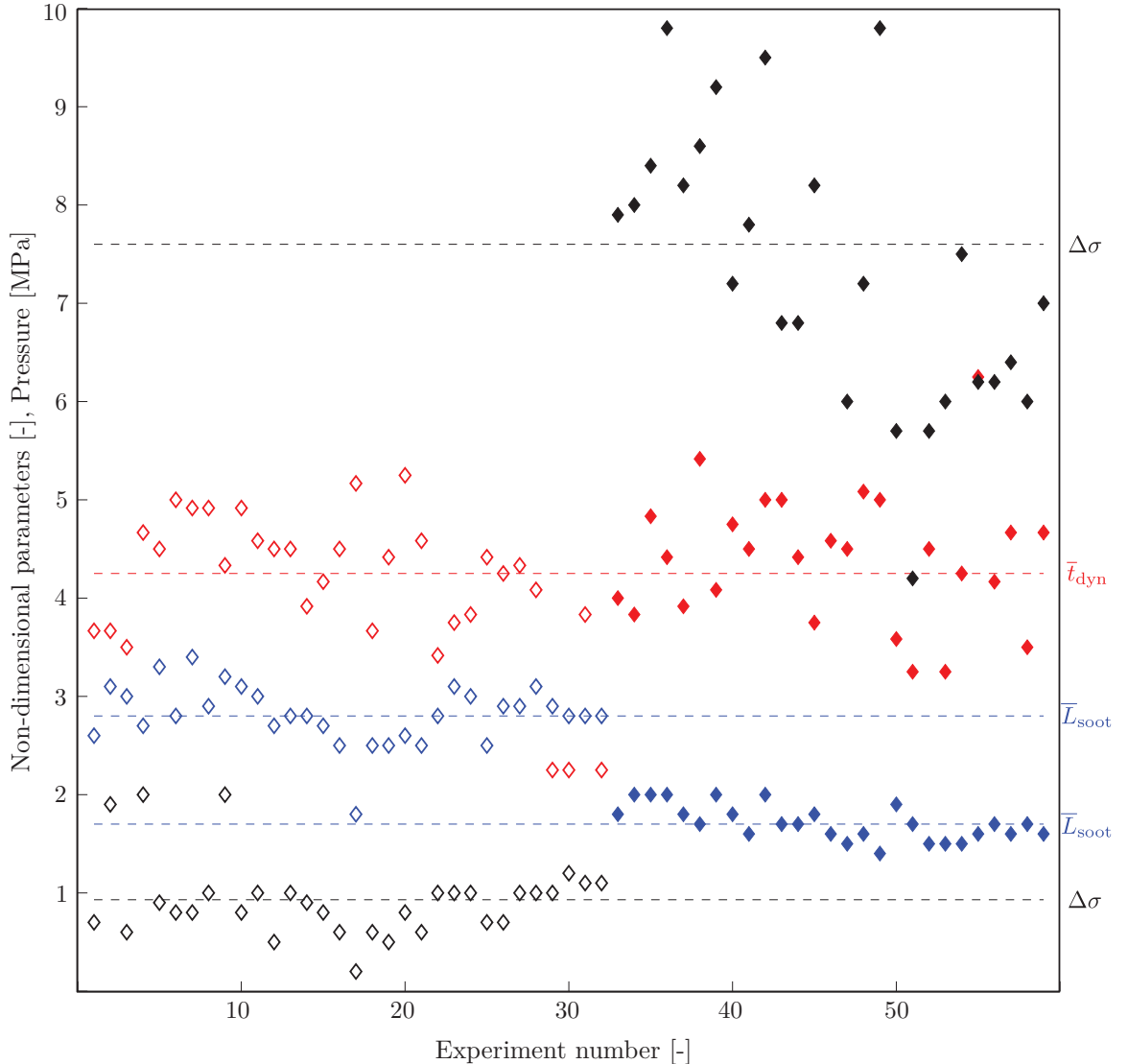
Figure 5.4: Global stress drop, $\Delta\sigma$, non-dimensional dynamic event lag time, $\bar{t}_{\mathrm{dyn}} = 100 t_{\mathrm{dyn}}/T_{\mathrm{exp}}$ ($T_{\mathrm{exp}} = 120\,\mu\mathrm{s}$), and non-dimensional soot deposit length, $\overline{L}_{\mathrm{soot}} = L_{\mathrm{soot}}/t$ ($t = 10\,\mathrm{mm}$), are presented for $P = 5.0\,\mathrm{MPa}$ (empty) and $P = 15.0\,\mathrm{MPa}$ (solid) experiments.

strength by temporarily opening the interface; the discharge of $1.6\,\mathrm{kV}$ from a capacitor bank across the embedded wire rapidly transforms the filament to plasma, generating large pressures [46]. The pressure increase is sufficient to locally open the fault at the interface, as shown by fault opening displacement measurements u_{open} at a station $\approx 2\,\mathrm{mm}$ from the hypocenter ($x'_1 = 72.3\,\mathrm{mm}$) in the bottom panel of Figure 5.3 (black curve). Opening persists for about $50\,\mu\mathrm{s}$ near the hypocenter, increasing its spatial extent up to the wire soot deposit length, L_{soot}; the photograph insert of Figure 5.3 shows post-experiment soot deposit patterns on the hanging wall plates for events generated with initial static loads of $P = (2.5, 5.0, 7.5, 15.0)\,\mathrm{MPa}$. Dynamic rupture propagation is roughly achieved once the critical crack length is exceeded by the nucleation patch length, $L_{\mathrm{soot}} > L_{\mathrm{c}}$. Graphical

determination of t_{dyn} (Section 3.1) shows that the best-fit lines for S waves, P waves, and SR rupture tips cross the ordinate at nearly the same time: this implies large accelerations of rupture tip speeds from zero to $\approx v_{\mathrm{r}}^{\mathrm{SR}}$ during the forced opening of the interface (t_0 to t_3 in Figure 5.3, top panel).

The dynamic rupture delay times, t_{dyn} (red markers), total far-field stress drop, $\Delta\sigma = P_{\mathrm{f}} - P$ (black markers), and soot deposit lengths, L_{soot} (blue markers), are plotted in Figure 5.4 for a total of 59 experiments, similar to Figure 5.1. The dynamic event lag times range from $t_{\mathrm{dyn}} \approx 4 - 6\,\mu\mathrm{s}$ across both SR and SS experiments with no bias based on initial applied load; coupling of the wire to the surrounding material seems consistent across notch fabrication. The overall stress drops encapsulate total slip accumulated from the transient rupture process and cannot be used directly to infer about local rupture mechanics, however, consistency in values does provide another measure of reproducibility. Soot deposit lengths tend to decrease with an increase of applied load P, a direct consequence of increased background stresses impeding opening near the hypocenter.

5.3   Ground motion reproducibility

The top of Figure 5.5 displays a collection of three nominally identical experiments corresponding to the far-field load $P = 15\,\mathrm{MPa}$ and angle $\alpha = 29°$. In all of these experiments, transition of the rupture to SS has been observed through dynamic photo-elasticity. The bottom of Figure 5.5 displays a second set of three nominally identical experiments for which the far field load is $P = 5\,\mathrm{MPa}$ while the angle is kept at $\alpha = 29°$. The up-dip ruptures in these three cases remained SR.

The experimental results are quite repeatable. In the three SS experiments, Mach front peaks are well aligned and arrive at the theoretically estimated time t_{M}. As already discussed in relation to Figure 4.9, the arrival times t_{s} of the S wave result in a local amplitude increase, as does the arrival of the effect associated with the TR signature. The amplitudes of all traces are remarkably similar throughout the duration of the recordings for both hanging and foot walls. The only significant difference between the experiments is in the arrival times of the maxima following t^{TR}. These time differences are due to variations in the transition length calculated from the photo-elastic images; the transition lengths of the three experiments are $29.3\,\mathrm{mm}$, $27.6\,\mathrm{mm}$, and $22.7\,\mathrm{mm}$. The experiment with the transition length of $22.7\,\mathrm{mm}$ results in the largest time delay between the Mach peak and the TR peak. Numerical work has shown that the transition length is very sensitive to the frictional parameters of the interface as well as the exact nucleation conditions [54]; measured differences in the transition length are attributed to small variations in surface preparation and nucleation conditions.

The bottom of Figure 5.5 compares three SR experiments. A small upswing in all traces is first observed just after the arrival of the P wave at times t_{p}. Just after the arrival of the S waves, a small downswing is observed, while the major ground shaking only becomes evident after the time $t_{\mathrm{r}}^{\mathrm{SR}}$ when the SR rupture reaches the fault trace. Note that, in this particular experiment,
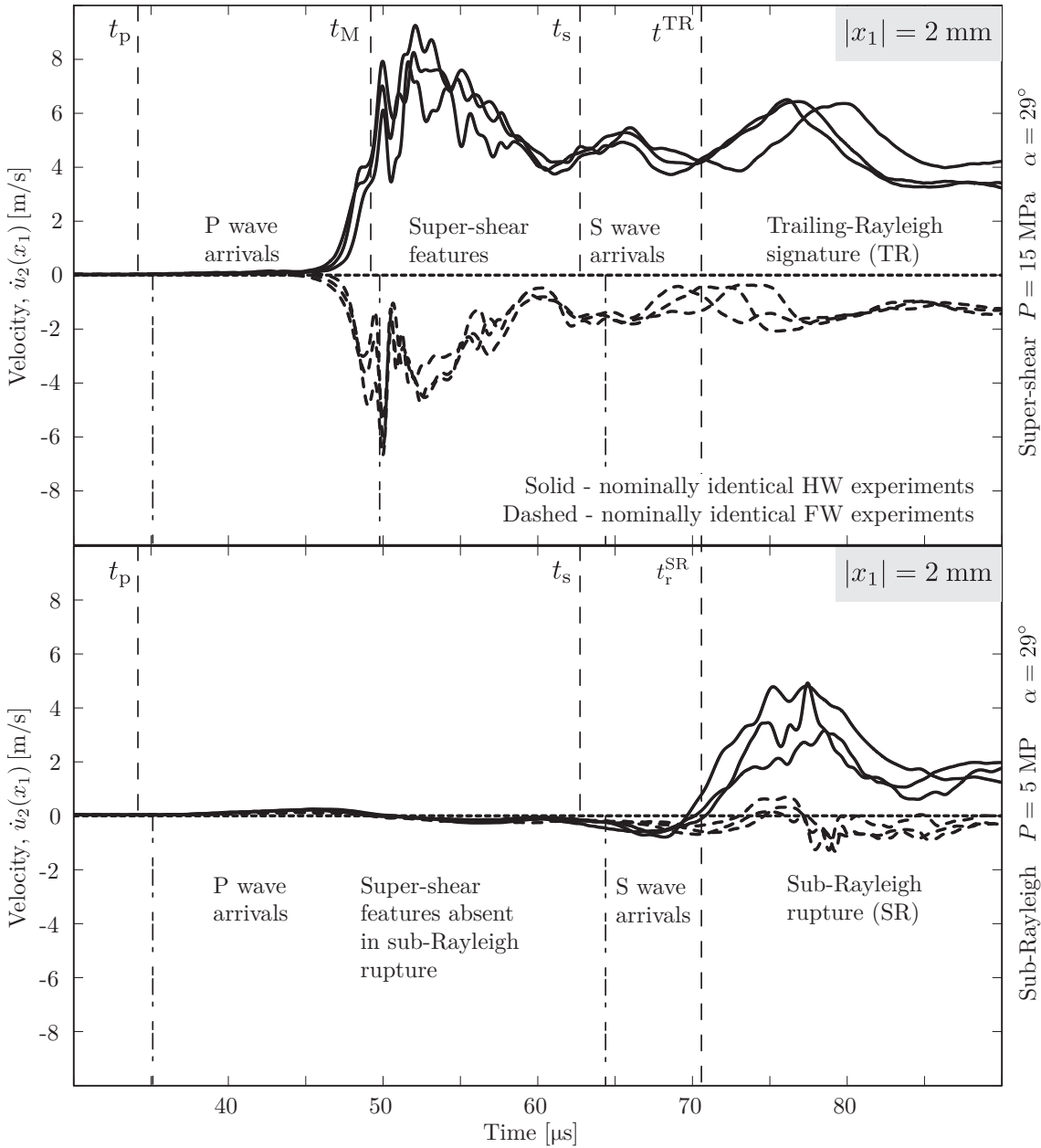
Figure 5.5: Experimental reproducibility illustrated through velocimeter traces measured at a symmetric distance $|x_1| = 2$ mm on the hanging (solid) and foot (dashed) walls, for SS (top) and SR (bottom) experiments. The experiments have nominally the same conditions, with the SR set conducted at a load of $P = 5$ MPa and the SS set at $P = 15$ MPa. The pairs of vertical lines t_p, t_M, t_s, t^TR, and t_r^SR indicate the arrivals of the initial P wave, Mach fronts, initial S wave, TR signature, and the SR rupture tip to the stations at the hanging and foot wall plates.

the rupture tip propagates at $v_\mathrm{r}^\mathrm{SR} = 1.14$ mm/µs, nearly at the Rayleigh wave speed of Homalite, $c_\mathrm{R} = 1.18(3)$ mm/µs. The three experiments exhibit similarities in the timing of feature arrivals and the wavelengths of various signatures. The variation in signal amplitudes is likely due to the same reasons as for SS experiments, namely variations in surface preparation and nucleation procedure.

5.4   Specimen thickness effects

Finite thickness of the specimen introduces measurable three-dimensional effects in the ground motion records with no loss of generality to the interpretation of results. Figure 5.6 shows two earth surface-normal records, $\dot{u}_2(x_1, x_2, x_3)$, measured at stations $(x_1, x_2, x_3) = (2, 0, \pm 4.8)$ mm: the origin of $\hat{x}_3$ is mid-thickness of the specimen ($t = 9.52$ mm), and thus the stations measure ground motions on opposing edges of the plate the same distance away from the fault trace.
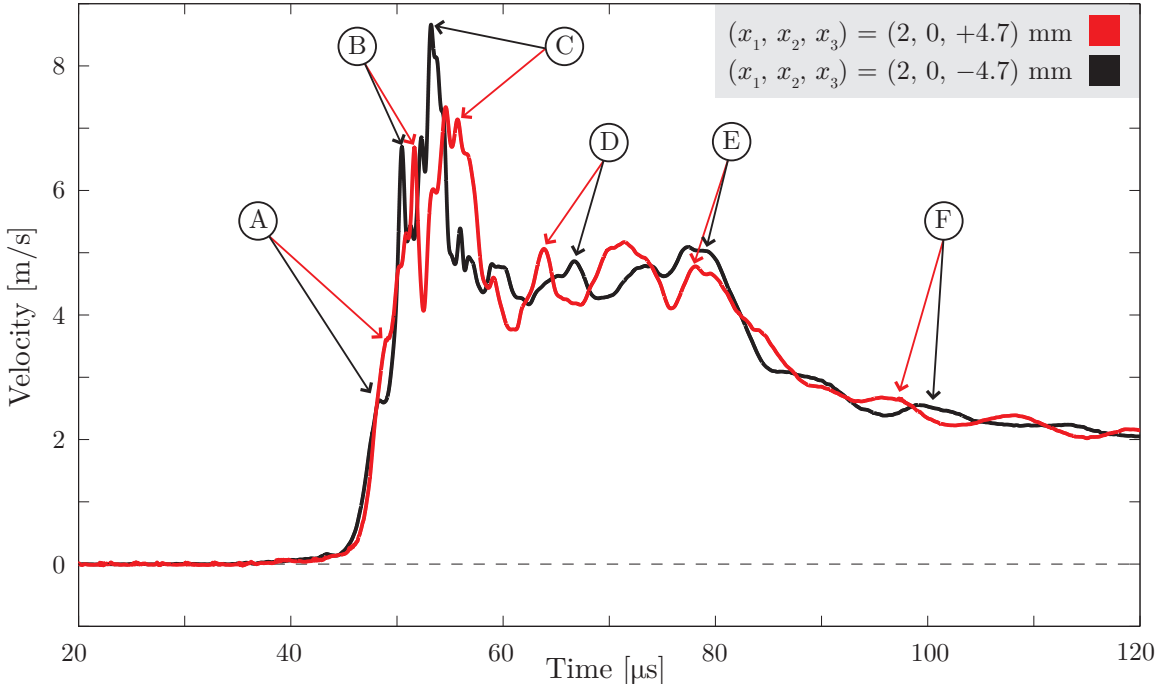
Figure 5.6: Finite thickness effects of the plate; simulated earth surface-normal records, $\dot{u}_2$, at $(x_1, x_2, x_3) = (2, 0, \pm 4.8)$ mm measure the ground motion records on opposite edges of the plate, $x_3 = \pm t/2$, where $t = 9.52$ mm. Note: origin of $\hat{x}_3$ is mid-thickness of plate.

If $t \to 0$ mm, the records are expected to converge; however, inspection of the black and red curves indicate a phase-lag as well as an amplitude mismatch. Dilatational field effects (A) are nearly in-phase yet with a disparity of ≈ 1 m/s. Up-dip Mach fronts (B) arrive with a time delay of ≈ 1 µs with identical amplitudes; the phase lag is much too short for any rupture feature to transverse across the specimen thickness, indicating an oblique or curved rupture front. Down-dip Mach fronts (C) similarly arrive ≈ 1 µs apart, yet with a greater amplitude disparity (≈ 1.5 m/s). Surface Rayleigh wave effects (D) and arrivals of the TR signature (E) are nearly identical in amplitude, but the oscillations following the TR are off-sync by ≈ 5 µs; rupture features propagating with sub-Rayleigh speeds may not transverse the specimen thickness in such a short time span. These records show the consistency of the observable physics across the specimen thickness; this fact is important when comparing records measured along the simulated earth surface (Section 4.1) and records at-depth

(Section 4.2), as the former is conducted mid-thickness ($x_3 = 0$ mm), while the latter is conducted on the imaging surface of the specimen ($x_3 = 4.8$ mm, see Figure 4.12).

5.5   Velocimeter beam placement accuracy

Laser light from the velocimeter systems are focused on reflective tapes attached to the experimental specimen (Section 2.2.3). Glass beads attached to the tape diffusely reflect the beam, making it difficult to accurately visualize the focal point. Switching the beam emission iteratively on/off allows a better judgement of where the focal point lies. Relative placement of stations becomes increasingly important when difference of two signals is required, such as fault slip and opening rate records $\dot{u}_{\mathrm{slip}}(x_1', t) = \dot{u}_1^+(x_1', t) - \dot{u}_1^-(x_1', t)$ and $\dot{u}_{\mathrm{open}}(x_1', t) = \dot{u}_2^+(x_1', t) - \dot{u}_2^-(x_1', t)$. Disparity in coordinate x_1 of paired stations may lead to false interpretation of physics.

Initial placement of paired reflective tapes along the fault on the hanging and foot wall plates is controlled with a micrometer and magnifying lens, however, uniaxial loading of the specimen introduces elastic deformation, leading to an initial fault parallel displacement, $\Delta x_1'$, between the paired measurement stations. Estimations of offsets are based on strain calculations using the greatest difference in load, $P = 15.0$ MPa, showing that paired stations will displace by about 3 µm with respect to each other (assuming no slip along the fault during loading). At times, displacements of about 500 µm are observed, and are either caused by loss in plate alignment or some settling process at the interface during loading. Experimental rupture speeds are roughly 1 mm/µs (constant) with pulse widths of about 10 µs, translating to slipping regions of about 10 mm, a length much greater than the largest disparity in initial placement of paired stations: errors from placement are minor.

5.6   Initial alignment: image optimization

Proper initial alignment of optics is the source of quality opto-mechanical measurements. When laser light is utilized, the general philosophy of checking back-reflections during setup will assure that the incident beam enters the imaging solution with proper orientation.

The source beam must first be guided to a predetermined spot of the selected imaging solution. Optical quality mirrors and multi-degree-of-freedom actuators guide the emitted beam towards this spot. Directivity of the beam requires collinearity between the laser axis and that of the imaging solution. A mirror placed normal to the imaging solution axis will reflect the beam back into the emission point if properly aligned. Once the spot is focused and the laser axis is aligned, the remaining optical components are sequentially installed along the beam path. Back-reflections are checked with every subsequent addition of component; this is similarly done during placement of the specimen in the test section to avoid skewing of images (Section 2.2.2.2).

Chapter 6

Concluding Remarks

Sub-Rayleigh (SR) and super-shear (SS) thrust fault earthquakes are studied in the laboratory with the use of high-speed digital photography and laser velocimetry. The experiment has been redesigned from previous setups used to study analog strike-slip earthquakes [69], namely, the plate dimensions have been enlarged and optimized to avoid corruption of ground motion velocity records from unnatural specimen boundaries. The enlarged plate of dimensions $w = 180\,\mathrm{mm}$, $h = 360\,\mathrm{mm}$, and $t = 9.52\,\mathrm{mm}$ provides a sufficiently long time window to capture both up and down-dip phases of the simulated earthquakes. Linear fault surfaces are manufactured to sustain uniform shearing and normal prestress conditions prior to rupture, resolved according to the $61°$ dip angle. Ruptures are nucleated at-depth and are guided up-dip towards the simulated earth surface. Timing analyses bound the arrivals of various rupture features, identifying key signatures in ground motion records.

Earth surface-normal records of both SR and SS ruptures show substantial asymmetry between the hanging and foot wall ground motions. Comparing stations placed an equal distance from the fault trace on the hanging and foot wall plates, peak ground motion amplitudes are consistently greater for the hanging wall station; this finding is in agreement with both field observations, e.g., [86, 87, 88, 89], and numerical models, e.g., [91, 92, 93, 94]. During SR up-dip propagation, a rupture wave is sensed in the hanging wall but is absent in the foot wall plate [96]; this is a direct consequence of broken geometric symmetry between the two plates and the earth surface, i.e., a non-vertical fault. During SS up-dip propagation, similar rupture wave disturbances are observed with arrivals of the trailing-Rayleigh (TR) signature (stress concentration remnant of the original SR rupture prior to transition), however, these are difficult to discern since the effects are preceded by those of the leading SS rupture. The earth surface breaks with the arrival of the rupture tip, generating Rayleigh waves that propagate bi-directionally away from the fault along the earth surface; in SS events, similar Rayleigh waves are observed later in time with arrival of the TR signature. The presence of strong Rayleigh waves radiated by the breakout of rupture to the surface match kinematic numerical results [96]. Global maxima of ground motion magnitudes are measured at the fault trace and are outcomes of the surface breaking phenomenon associated with the arrival of the rupture tip.

Signatures attenuate and broaden with distance from the fault trace. P and S wave contributions to ground motions are a minor fraction of the local rupture tip effects. SS earthquakes feature greater amplitudes of ground shaking profiles than SR earthquakes, as expected from the increased tectonic pressures required to induce transition. Features generated from rupture tip interactions with the earth surface are observed propagating back down-dip, in particular, a down-dip SS signature which emits its own shear Mach front; combined effects of the up and down-dip Mach fronts are sequentially sensed in surface-normal records. Inspection of fault trace data reveals an interesting distinction between SR and SS ruptures; in the SR case, peak velocity magnitudes show a large asymmetry ($6\,\mathrm{m/s}$ on the hanging wall and $1.5\,\mathrm{m/s}$ on the foot wall), while SS magnitudes are nearly identical at about $10\,\mathrm{m/s}$. Such extreme asymmetry in the SR case may have been observed in the 1971 San Fernando earthquake, where an asphalt road surface right on the toe of the hanging wall is believed to have flipped into the air [131]; SR results are also consistent with vertical motion in numerical models [127]. Overall, the dynamic nature of hanging wall surface-normal records indicates erratic motion of the acute wedge when compared to the foot wall, whose records are relatively banded.

On-fault measurements at-depth track the rupture evolution towards the earth surface. Peak fault slip and opening rates associated with the rupture tip amplify with proximity to the fault trace, a result of selective ground motion amplification in the hanging wall. Integrated displacements are utilized in a critical slip criterion, assuring that the fault indeed ruptures instead of deforming elastically. The fault heals behind the up-dip SR rupture, creating a finite slip pulse of period $\approx 10\,\mathrm{\mu s}$; the pulse-like ruptures broaden and transition to crack-like with increased tectonic loads. An opening pulse of the same period accompanies the rupture, led by a pinching precursor just ahead of the rupture tip; pinching and opening rates are significantly amplified at the fault trace, implying the fault surfaces pinch, then detach. The subsequent shutting of the fault sends an opening pulse propagating back down-dip at about the Rayleigh speed. Increased tectonic pressures suppress fault opening and enhance slip; for any given depth, opening rates decrease with an increase of load. Peak opening displacements of $\approx 20\,\mathrm{\mu m}$ and $\approx 8\,\mathrm{\mu m}$ are measured at the fault trace for loads $P = 2.5\,\mathrm{MPa}$ and $P = 7.5\,\mathrm{MPa}$, respectively. Fault parallel records of paired stations are much more anti-symmetric for deeper stations where longer times are required to communicate presence of the earth surface. For stations within $\approx 10\,\mathrm{mm}$ from the fault trace, up and down-dip segments of the rupture coalesce, broadening the slip and opening pulses. The fault parallel dominant ground motions near SS rupture tips maintain anti-symmetry of fault parallel records at all depths, however, this is immediately broken at the fault trace where opening rates of $\approx 2\,\mathrm{m/s}$ are measured. Dominant fault parallel ground motion component and suppressed opening of SS ruptures together reconcile the difference in polarity of earth surface-normal fault trace records between SR and SS ruptures. In SR ruptures, the reflected S wave feeds back and re-ruptures the fault; this rupture is necessarily SS from the fault geometry, emitting a shear Mach front captured in the photographs.

Chapter 7

Future Research Directions

The current section is a summary of the mental meanderings during the course of the research, as summarized in Figure 7.1. Above the familiar experimental specimen is a water cell, used to study tsunami mechanics; time-dependent loading permits a natural nucleation mechanism; advances and addition of diagnostics, e.g., S.P.S.I. (Section 7.7), further elucidate thrust fault rupture dynamics.
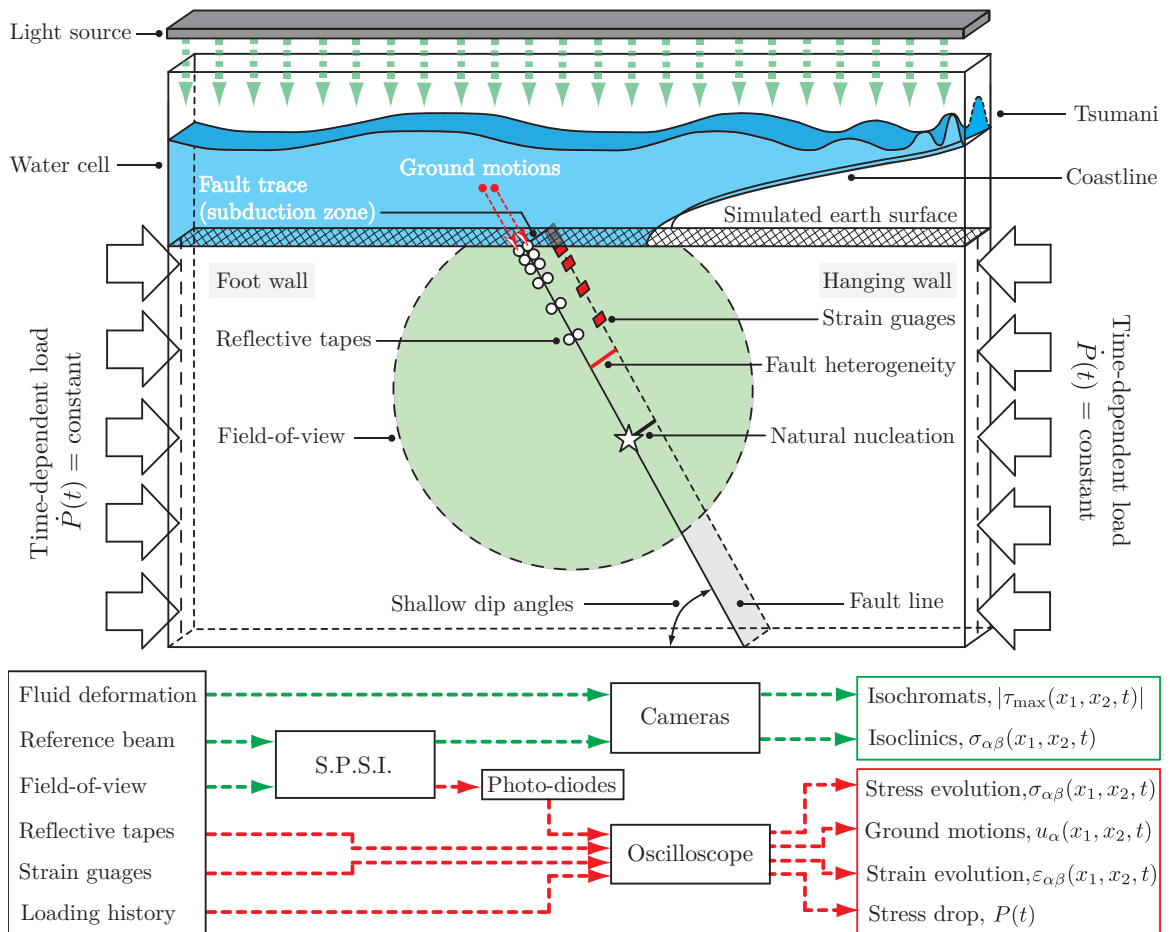
Figure 7.1: Future research directions are summarized both in schematic form and as a workflow.

7.1 Natural nucleation: time-dependent loading

Dynamic ruptures are nucleated by the discharge of a capacitor bank across a wire embedded along the fault a depth $D = 74.3\,\mathrm{mm}$ from the fault trace. The phase transformation of the wire generates high pressures, locally opening the interface until conditions permit the dynamic propagation of a rupture. The abrupt phase transformation is confined to the nucleation site and does not affect the rupture dynamics [126]; however, this mechanism is less natural, as it would imply an "explosion" as the source of the earthquake. Periods of aseismic loading slowly increase the mechanical driving stresses along the fault until a rupture nucleates; a press capable of time-dependent loading, $P(t)$, would be capable of simulating such conditions. A constant, quasi-static load rate, $\dot{P}(t) \approx 0$, would uniformly increase the resolved shear stress along the fault. To control the hypocenter location, a notch is fabricated through-thickness at a given location on either the hanging or foot wall fault surface. This heterogeneity locally amplifies the far-field loads, promoting rupture nucleation at that point. Numerical modeling of this mechanism requires fewer physics and avoids the more difficult problem of modeling the mechanical coupling between the expanding plasma and the surrounding material. While the hydraulic press in the experiments may only provide the initial and final static loads, the dynamic press would be capable of filling in the transient stress drop behavior as a function of time, $\Delta\sigma(t\colon P)$. Correlations may be drawn between rupture tip location and stress drop during the dynamic event: an interesting measure would be the ratio of accumulated stress drops when the earth surface is broken to the global stress drop once all dynamics have ceased.

7.2 Forcing SS transition: fault heterogeneity

Rupture tip speed and stability analyses along with experimental evidence show that a mode-II rupture is unstable in the sub-Rayleigh (SR) regime, $0 < v_\mathrm{r} < c_\mathrm{R}$, accelerating and stabilizing at the Rayleigh wave speed, $v_\mathrm{r} \to c_\mathrm{R}$. Indeed, measured SR rupture tip speeds are $v_\mathrm{r}^\mathrm{SR} = 1.14(4)\,\mathrm{mm/\mu s}$, which is 97 % of the Rayleigh wave speed, $c_\mathrm{R} = 1.18(4)\,\mathrm{mm/\mu s}$. In certain circumstances, the rupture tip transitions to super-shear (SS) speeds, $c_\mathrm{s} < v_\mathrm{r} < c_\mathrm{p}$, at a distance l_tr away from the event source. The Burridge-Andrews mechanism surpasses the energetically forbidden sub-domain, $c_\mathrm{R} < v_\mathrm{r} < c_\mathrm{s}$, by nucleating a secondary rupture tip at a shear stress peak ahead of the crack tip [66, 123]: this secondary rupture is born SS, accelerating away from the original crack tip. Instead of increasing the driving shear force along the fault to generate SS ruptures, alternatively, transition may occur by introducing a second flaw along the fault or by increasing/decreasing the available frictional resistance, e.g., a heterogeneity. Numerical work indicates that appropriately sized heterogeneities are sufficient to induce SS transition if placed in the proper position along the fault [119]; a notch fabricated either along the hanging or foot wall plate is one such example. If the notch is placed

a distance within the predicted transition length, $l_{\rm tr}$, then SS transition may occur sooner than expected. Transition lengths have the largest spread in experimental values (Section 5.1), while rupture speeds tend to be well-banded: experimental work on forced transitions may validate the hypothesis that transition lengths are much more sensitive to fault frictional conditions, and thus are operating on a smaller characteristic length scale than processes selecting rupture speeds.

7.3   Water cell: tsunami generation

Underwater earthquakes in thrust fault configurations generate dynamic disturbances along the ocean floor. Once the rupture tip breaks the surface of the ocean bed, a subduction zone where material is entrained into the earth is created at the fault trace. The water resting above the ocean floor must compensate for the sudden dynamic motion, in turn generating surface waves above the waterline. As the coastline is approached, surface waves must grow in amplitude in response to topography changes; these wave amplifications are called tsunamis [132, 133, 134]. This situation is modeled by a water cell resting above the thrust fault experimental specimen, as shown in Figure 7.1. An accurate diagnostic must be implemented to measure expected surface deformations along the surface of the water. One method would be to utilize the reflective properties of the water surface and the method of caustics, which relates surface deformations directly to interference patterns of incident and reflected wave fields. Various parameters could be studied, such as the geometry and distance of the coastline from the fault trace. An interesting observation should be made if such experiments are conducted: are the fault surfaces wet at-depth after the event? Results show that the fault surfaces open at the fault trace, consequently generating a mode-I opening pulse propagating back down-dip along the fault; if water was to rest above the simulated ocean floor, the generated opening pulse should entrain water from the ocean into the earth, wetting the fault surfaces.

7.4   Shallow dip angles: cohesion along the fault

Thrust faults in the earth tend to occur in shallow dip angle configurations [97, 98, 93], which correspond to steep interface angles, α. For the fault surface conditioning of the experimental specimens, configurations with angles above $30°$ cannot sustain static equilibrium as the frictional resistance is always less than the self-weight driving stresses. Cohesively bonding the fault surfaces increases the resistive shear strength and permits the loading of specimens with steeper interface angles, α (shallow dip angles). As predicted by past numerical work [91, 124], increasing geometrical asymmetry in turn increases the asymmetry of ground motion records between the hanging and foot wall plates. Below a critical fault angle, no down-dip phase velocity of P and S waves exists as up and down-dip directionality converge (Section 4.1.1): the angle $\alpha = 29°$ is well below this limit.

7.5 Station density and digital image correlation

Two major limitations exists in the velocimeter measurements. The fist is the allocation of instrument space, the second are limitations of the instrumentation. A single component of velocity requires a full laser velocimeter system. In order to increase the resolution of the seismometer array, additional systems would be required, one for each component of motion being measured. A multibeam system with multiple termini would reduce the required laboratory real estate for instruments and make the advancement possible. A custom mounting arm will likely be required to arrange, focus, and direct the various beams to their required stations on the interface; herein would lie some thought. Of course, a continuous array of beams would be the ultimate diagnostic for this system. The second limitation stems from the capabilities of the instruments used to capture the velocity records. The bandwidth of the instruments are limited to $1.5\,\mathrm{MHz}$, which are on the order of the frequencies in the records corresponding to the SS rupture tip signature rise-times; the peak velocity values are $\pm 10\,\mathrm{m/s}$, which are on the order of the peak velocity values in the records associated with the SS rupture tip signature. As there is a trade-off amongst bandwidth and peak velocities, it is difficult to dual-optimize such interferometer systems [135]. Digital image correlation (D.I.C.) is a full-field technique for obtaining the in-plane velocity field, $u_\alpha(\mathbf{x}, t)$, by tracking displacements of material points at set inter-frame times [136, 137]. Current difficulties in D.I.C. are the unique recognition of speckle patterns and high-speed camera resolution and inter-frame limitations. The scale at which material points are unique sets the resolution limit within the field-of-view. High-speed cameras must capture at these resolutions at shutter speeds sufficiently lower than the slowest dynamic feature speed: this is practically difficult to achieve as there is a trade-off between resolution and inter-frame times. At high-enough resolution and short enough inter-frame times, the full velocity field evolution may be obtained. D.I.C. is by nature a reflective technique, while photo-elasticity is transmissive; it is unclear if both may be implemented within a single experiment of a similar setup.

7.6 Strain gauges and coherent gradient sensing

Strain gauges output principle strain values, $\varepsilon_1(\mathbf{x}, t)$ and $\varepsilon_2(\mathbf{x}, t)$, at a given material point, $\mathbf{x}$. An array of strain gauges placed along the fault line at various distances from the fault trace will output the evolution of in-plane strain values during the dynamic event. Since reflective tapes will likely be placed along the fault line, the opposite specimen surface must be used to align the strain gauges. Coherent gradient sensing (C.G.S.) is a reflective opto-mechanical technique capable of outputting full-field values of $\varepsilon(\mathbf{x}, t)$ [138, 139] by directly measuring gradients of out-of-plane displacements, then differentiating to obtain in-plane strain components. C.G.S., much like photo-elasticity and D.I.C., suffers the same spatio-temporal resolution limitations set by the current state of the art.

7.7 Spatial phase-shifting interferometer (S.P.S.I.)

Opto-mechanical techniques relate interference patterns of light to mechanical field quantities at material points within the field-of-view. Photo-elasticity relates the beam intensity to contours of maximum shear stress magnitudes, $|\tau_{\max}(\mathbf{x}, t)|$ [51, 140], digital image correlation yields the velocity field, $u_\alpha(\mathbf{x}, t)$ [141, 142], coherent gradient sensing yields the principle strains, ε_1 and ε_2 [143, 144], and Mach-Zehnder interferometry yields directions of the principle stresses, σ_1 and σ_2 [145].

Spatial phase-shifting interferometer (S.P.S.I.)

A custom module simultaneously utilizing two interferometry techniques to extract mechanical measurements in a single test

GALCIT

To camera or photo-diodes

Mach-Zehnder mosaic module

To camera or photo-diodes

Photo-elasticity mosaic module

Blazed grating (master) module

F-theta lensmodule (downstream)

Filter screen module

F-theta lens module (upstream)

Master 2-D grating module

Compensator module

Beamsplitter module #2

Beamsplitter module #1

$l = 58$ inches

Breadboard (system)

Specimen beam

Reference beam

Reference beam module

$l = 16$ inches

Designed by: Vahe Gabuchian Based on the opto-mechanical configuration of Michael Mello

Figure 7.2: Spatial phase-shifting interferometer (S.P.S.I.) module overview. The instrument accepts a reference beam from the light source and the perturbed wave field beam emerging from the specimen plane. Optical components operate on the light and perform both dynamic photo-elastic and Mach-Zehnder interferometry concurrently in a single experiment, outputting two sets of data.

The spatial phase-shifting interferometer module (S.P.S.I.), shown in Figure 7.2, utilizes both photo-elasticity and Mach-Zehnder interferometry to obtain the full-field, in-plane stress tensor, $\sigma_{\alpha\beta}(\mathbf{x}, t)$. The S.P.S.I. accepts two inputs, a reference beam from the light source (laser) and the perturbed beam transmitted through-thickness of the specimen. By making four physical copies of the specimen beam and appropriately interfering the wave fields, two sets of wave fields containing both isochromatic and isopachic fringe patterns are sent to either cameras for full-field imaging or

Expanded beam
through specimen

Photo-elasticity
interferometry

To cameras or photo-diodes

Mach-Zehnder
interferometry

Collected beam
to S.P.S.I.

Light source

Reference beam (expanded)

Reference beam
to S.P.S.I.

Plexiglass
casing
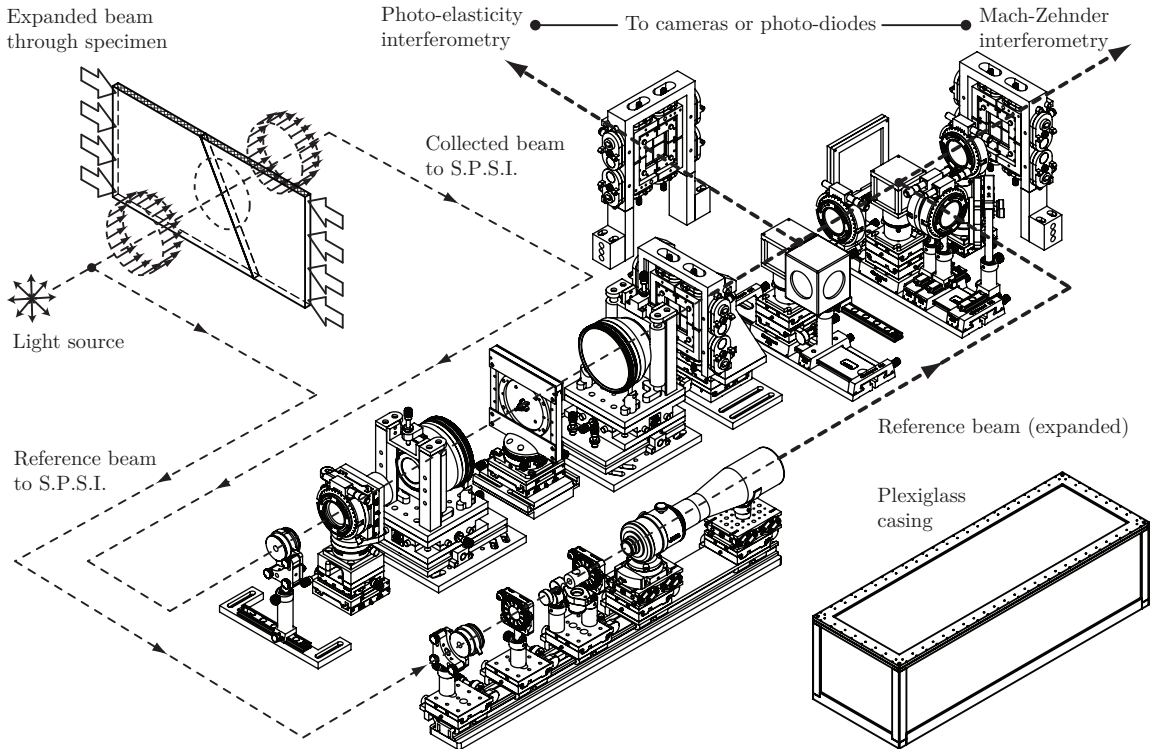
Figure 7.3: S.P.S.I. module schematic: an exploded view. The system accepts two inputs: an unperturbed reference beam from the source and the collected beam transmitted through the specimen. Dashed lines schematically represent the optical pathways of the set of beams. The system physically copies and interferes the specimen beams with the techniques of both photo-elasticity and Mach-Zehnder interferometry, outputting a set of interference patterns to cameras or photo-diodes.

to photo-diodes for temporally-resolved values of $\sigma_{\alpha\beta}(\mathbf{x}, t)$ at a given material point. The S.P.S.I. contains numerous modules (Figure 7.3), each housing the necessary optical components of the system; dashed lines show the optical paths of both the reference and the perturbed beams, placing the system appropriately in relation to the experimental setup discussed in Chapter 2. The short focal lengths mandate a compact design; pushing further in this direction, all optical components are mounted on a single breadboard, making the system mobile and easy to transport. The perturbed beam gets physically copied four-fold (Figure 7.4) and spatially interfered with a set of mosaic structures (Figure 7.5) to output isochromatic (photo-elastic) and isopachic (Mach-Zehnder) fringe patterns. Single and double-headed red arrows in Figures 7.4-7.5 represent translational and rotational (tilt) degrees-of-freedom, respectively: set screws fix the alignment of each available motion. Once initial alignment is complete, a Plexiglass case covers the system to prevent dust accumulation and accidental tampering. Note: due to multiple operations on the beam, a high-power laser is required to avoid dim images and low signal-to-noise ratios.

The specimen beam is physically copied, emerging as a set of four expanded, collimated beams parallel to the laser axis (Figure 7.4). A compensator module accepts the incident beam and is

Compensator module

F-theta lens module (down-stream)

Filter screen eliminates k_0 and passes $k_1^\pm$ beams

A

$k_1^\pm$

k_0

$k_1^\pm$

Perturbed beam from specimen (elliptically-polarized)

$k_0, k_1^\pm$

$k_1^\pm$

k_0

$k_0, k_1^\pm$

F-theta lens module (up-stream)

Master 2-D grating module diffracts beams in orthogonal planes

Master mosaic module

Mosaic arm (x4)

$k_1^\pm$

B

45^0 gratings recollimate beams

Mosaic orients 4 square optical components

$k_1^\pm$

A

Figure 7.4: S.P.S.I. beam duplication segment. Green paths and red arrows represent the laser beam and available degrees-of-freedom for system alignment. Inserts show details of the mosaic assembly.

used as an overall adjustment to system-introduced perturbations (used during alignment) [146]. A custom-made two-dimensional grating copies the beam through diffraction in two normal planes: by etching two sets of linear gratings on a single glass such that lines of each set are always normal, two $\pm k_1$ beams are emitted in one plane at an angle θ to the laser axis (k_0) while another two $\pm k_1$ beams are emitted in the plane normal to the first set: higher diffraction orders, $\pm k_2, \pm k_3, ...$, are captured and eliminated by a black-anodized telescoping cylindrical shroud. The four k_1 beams enter the rear aperture of a scanning lens; scanning lenses have the ability to accept light from a range of angles and focus them to a single point at the focal distance f from the lens exit plane, displaced from the axis-of-rotation by an amount $f\theta$ (hence the common name, f-theta lens). A filter screen allows the focused k_1 beams to pass through while eliminating the zeroth order beam, k_0. The screen is placed at a distance f from the scanning lens so than an array of holes will allow the focused k_1 beams to pass through the filter plane, while the non-displaced k_0 beam is captured and eliminated in the center of the screen. As initial alignment may require re-design in the screen hole pattern, the screen itself is replaceable. A second f-theta lens, in reverse orientation to the first, accepts the k_1 beams and sends the four copies to a (master) mosaic structure containing four custom-made $45°$ gratings; proper alignment of these four optics assures the beam copies are collimated and parallel to each other on exit, thus demanding full control of spatial orientation at micro-scale resolutions; manual actuation with a minimum resolution of 120 t.p.i. is utilized.

Spatially phase-shifting the copied beams with unique angles provides a fully-defined system of equations for the intensity pattern. The copied beams enter a $90°$ non-polarizing beamsplitter cube, which splits the information into two directions: the first is sent to a photo-elasticity mosaic and the second is sent to additional optics required for Mach-Zehnder interferometry. To complete the Mach-Zehnder configuration, the copied beams are interfered with an expanded reference beam in a second, polarizing beamsplitter: the resulting wave field enters the Mach-Zehnder mosaic. Both photo-elasticity and Mach-Zehnder mosaics contain four custom-made, sandwiched optics, which perform the final spatial interference necessary to generate isochromatic and isopachic fringe patterns; in each case, the optics are manufactured to introduce a unique spatial phase-shift. Collecting the outputs of the two mosaics and capturing with high-speed cameras will generate four copies of the same full-field information, shifted in space with unique phase-angles, in each frame for both photo-elasticity and Mach-Zehnder interferometers. The full-field intensity patterns for photo-elasticity, $I_1^{\mathrm{PE}}(\mathbf{x},t), I_2^{\mathrm{PE}}(\mathbf{x},t), I_3^{\mathrm{PE}}(\mathbf{x},t), I_4^{\mathrm{PE}}(\mathbf{x},t)$, and Mach-Zehnder interferometers, $I_1^{\mathrm{MZ}}(\mathbf{x},t), I_2^{\mathrm{MZ}}(\mathbf{x},t), I_3^{\mathrm{MZ}}(\mathbf{x},t), I_4^{\mathrm{MZ}}(\mathbf{x},t)$, provide a fully-defined system of four independent equations which may be used to extract mechanical information from both diagnostics, namely, the magnitudes and directions of the principle stresses averaged through-thickness of the test specimen.

Instead of cameras, photo-diodes may be used to capture the interfered wave fields exiting the S.P.S.I. module. Rather than expanding the source laser beam prior to transmission through the
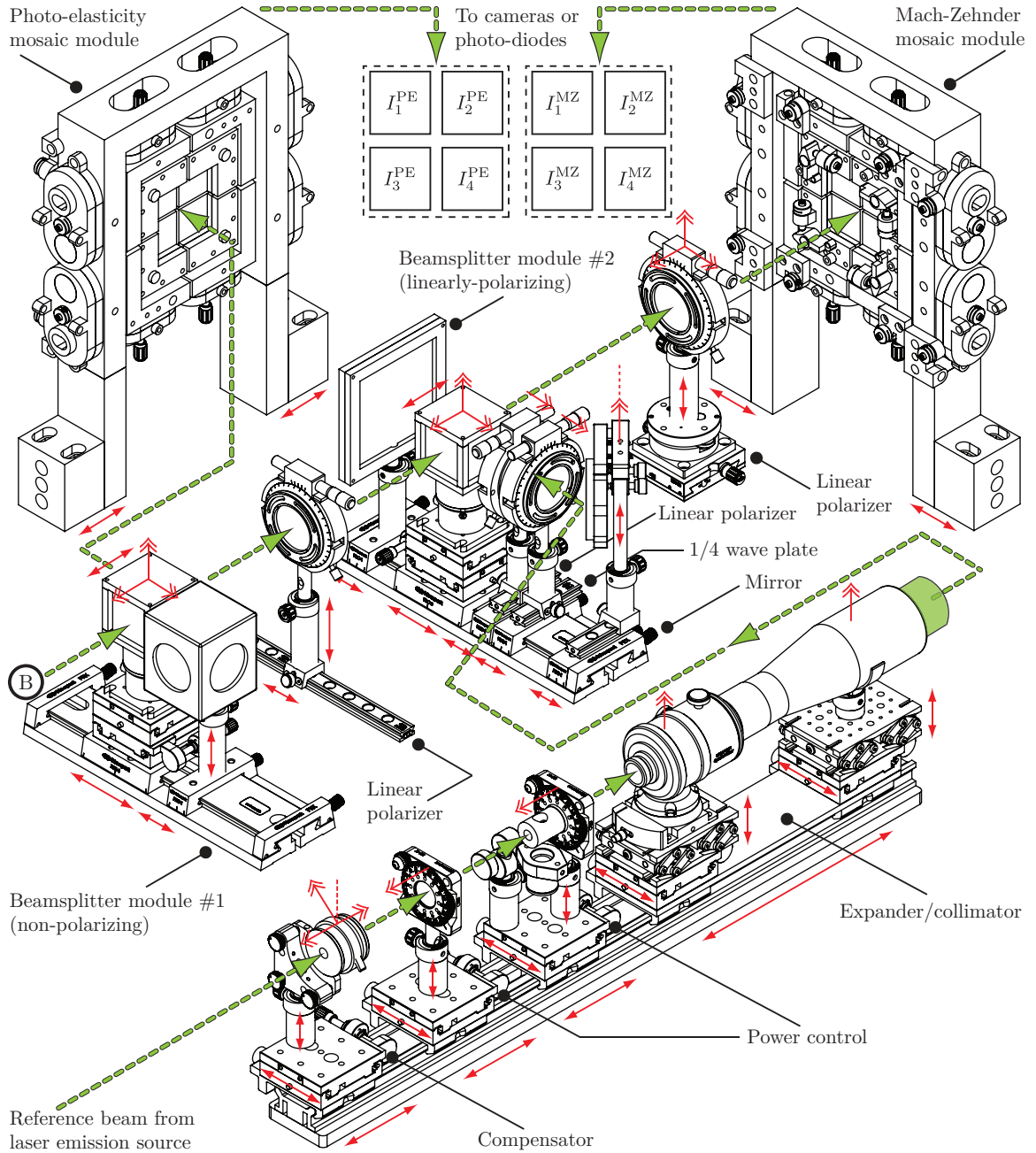
Figure 7.5: S.P.S.I. interference and output segment. Beamsplitters distribute the four duplicate beams and direct them towards a photo-elasticity mosaic and a Mach-Zehnder mosaic (additional reference beam required as shown), where custom optics perform the spatial phase-shift and output two beams towards cameras for full-field imaging or towards photo-diodes for temporally resolved stress values at single select material point.

test specimen, a point measurement is conducted by passing the laser through a specific point. Eight photo-diodes record a temporally-resolved intensity pattern from each of the optics in the photo-elasticity and Mach-Zehnder mosaics; similarly, a set of four equations may be used to extract mechanical information at a single point as a time series from both interferometer techniques.

Appendix A

Corrections to Displacement Data

The grazing angle measurements require an offset distance of $\eta^{\pm} \approx 400 - 600\,\mu\text{m}$ between the reflective tape edge and the interface surface for a total of $\approx 400 - 600\,\mu\text{m}$ between hanging $(+)$ and foot wall $(-)$ paired stations, which is the culprit for measuring apparent material interpenetration in the fault opening velocity and displacement records. The beam orientation and position are adjusted with manual actuators (Section 2.2.3.2) to focus the beam at the corner of the reflective tapes. The center of the beam diameter $(\approx 150\,\mu\text{m})$ is placed at the tape corner by moving the beams into the tapes an additional $\approx 100\,\mu\text{m}$ (half-turn of 100 t.p.i. manual actuator) past the point of initial measured back-reflectance (Figure A.1, left panel). Based on hanging and foot wall fault parallel displacement records, the fixed beams must remain on the tapes for expected peak fault parallel displacement of $\approx 380\,\mu\text{m}$ within the experimental time window $T_{\text{exp}} = 120\,\mu\text{s}$ (Figure A.1, right panel). Pushing initial beam placement further into the tapes will increase the probability
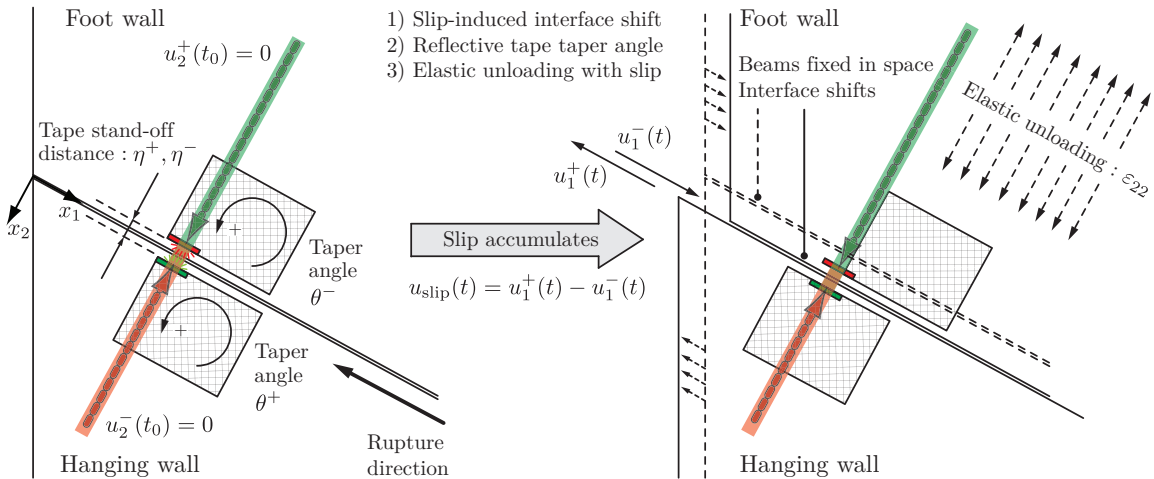
Figure A.1: Eulerian nature of measurements requires several corrections to the velocimeter displacement traces. Slip-induced interface shift, reflective tape taper angle with respect to the interface, and elastic unloading of the specimen are considered. Fault parallel displacements correct paired fault normal records at all given times to satisfy closed fault conditions after the window $T_{\text{exp}} = 120\,\mu\text{s}$.

of a clean record, but also increase the timing disparity between the fault parallel and fault normal measurements at the corner of the tape for experiments measuring both components simultaneously. Internal reflections within the specimen are used to assure that the beams are indeed parallel and perpendicular to the interface for accurate measurement of the two velocity components, defining the orientation of the beams (photographs in Figure 4.12). The fault normal beams approach the tapes in a crossed pattern at grazing angles (less than $\approx 5°$) to utilize the thickness of the tapes for back-reflections into the sensors. The crossed pattern requires one of the fault normal records to be inverted to match the sign convention of the $\hat{x}'_1 - \hat{x}'_2$ frame; the hanging wall record is selected.

In addition to data reduction of velocimeter traces described in Section 3.2, slip displacements are used to correct for interface shifts in the fault normal displacements due to slip accumulation along the interface. The interface plane shifts as the plates slip (Figure A.1), causing a baseline shift in the fault normal displacement records. Moreover, the asymmetry in the hanging and foot wall slip magnitudes increases as stations get closer to the free surface. Fault parallel displacements correct their paired fault normal displacements to account for this slip-induced shift as:

$$u_2^{\pm}(x'_1, t)^{\dagger} = u_2^{\pm}(x'_1, t) + u_1^{\pm}(x'_1, t) \tan \alpha. \tag{A.1}$$

The corrected fault opening displacements are obtained as $u_{\mathrm{open}}(x'_1, t)^{\dagger} = u_2^{+}(x'_1, t)^{\dagger} - u_2^{-}(x'_1, t)^{\dagger}$.

The taper angle of the tape edge with the interface is another source of error and is similarly treated as the slip-induced interface shift. Though the tapes are nominally placed at zero taper angles on both hanging and foot walls for all experiments, edge imperfections on the scale of $\approx 100\,\mu\mathrm{m}$ near the tape corner may compound taper effects. Fault parallel displacements are again used to correct their paired fault normal records for taper angle errors as:

$$u_2^{\pm}(x'_1, t)^{\ddagger} = u_2^{\pm}(x'_1, t)^{\dagger} + u_1^{\pm}(x'_1, t)^{\dagger} \tan \theta^{\pm}. \tag{A.2}$$

Allowing adjustments of up to $\pm 8°$ for both θ^{+} and θ^{-} enforces fault closing for times beyond $T_{\mathrm{exp}} = 120\,\mu\mathrm{s}$. Corrected displacement records in Figures 4.30-4.32 follow Equations A.1-A.2.

The effects of elastic unloading from a global stress drop are negligible and are not factored into the corrections. The pre and post-rupture global loads are used to obtain the global stress drop, $\Delta\sigma = P_{\mathrm{f}} - P$. Stress drops increase with initial applied load, with average values $\overline{\Delta\sigma}|_{P=2.5\,\mathrm{MPa}} = 0.8\,\mathrm{MPa}$, $\overline{\Delta\sigma}|_{P=5.0\,\mathrm{MPa}} = 1.0\,\mathrm{MPa}$, $\overline{\Delta\sigma}|_{P=7.5\,\mathrm{MPa}} = 2.5\,\mathrm{MPa}$, and $\overline{\Delta\sigma}|_{P=15.0\,\mathrm{MPa}} = 7.8\,\mathrm{MPa}$. Since slip accumulates past the clean experimental time window, $T_{\mathrm{exp}} = 120\,\mu\mathrm{s}$, these global stress drops would be overestimates of errors due to unloading. Using the highest stress drop and obtaining ϵ_{22} shows that the paired stations displace away from each other less than $\approx 0.5\,\mu\mathrm{m}$. Peak fault opening displacements are $\approx 20\,\mu\mathrm{m}$ at the fault trace; for this reason, elastic unloading effects are neglected.

Appendix B

Principles of Photo-elasticity

Photo-elasticity is an opto-mechanical technique where the polarization state of light is utilized to determine information about the stress state in a material, namely contours of maximum shear stress magnitudes, $|\tau_{\max}|$. The physical phenomenon operates on the principle of temporary stress-induced optical birefringence (i.e., the photo-elastic effect). The index of refraction response is anisotropic to applied stresses, generating a perturbed wave field whose intensity is related to the three principle stresses, σ_1, σ_2, and σ_3. Contours of constant intensity are related to the maximum shear stresses.

Polarization state of light
 I : Light source
 II : Liearly-polarized light
 III: Circularly-polarized light
 IV: Polarization state altered by principle stresses
 V : Reverse circular polarization from III
 VI: Linearly-polarized, phase-shifted light

A_3 represents specimen
Homalite H-100 is a stress-induced
optically birefringent material

To imaging solution

Photo-elasticity optical components
A_1: Linear polarizer
A_2: Quarter-wave plate
A_3: Optically-birefringent plate
A_4: Quarter-wave plate
A_5: Linear polarizer

Figure B.1: Principles of photo-elasticity. The series of plates represent various optical components of a standard light/dark field photo-elasticity setup. Effects on the polarization state of light are tracked with red arrows and schematically represented with the single transmitting beam. [107]

The relation between light intensity and stress state at any given material point is derived to further understand the nature of isochromatic patterns [107, 45]. The light beam in Figure B.1

passes perpendicularly through each optical component. The light from the source passes through the plane-polarizer (Figure B.1, A_1), emerging as:

$$A^{II} = a \sin(\omega t). \tag{B.1}$$

This beam enters a quarter-wave plate (A_2), a fabricated crystal with permanent optical anisotropy ($n_1 \neq n_2$), whose fast and slow optical planes are oriented at $45°$ with the horizontal and vertical axes. The incoming beam is resolved into components

$$A_f^{II} = a \sin(\omega t) \cos(45°) = b \sin(\omega t), \tag{B.2}$$

$$A_s^{II} = a \sin(\omega t) \sin(45°) = b \sin(\omega t), \tag{B.3}$$

which experience selective retardation in phase as they propagate along the fast and slow axes. This selective retardation introduces a phase difference, R, between the emerging beam components:

$$R = \frac{d}{\lambda}(n_1 - n_2), \tag{B.4}$$

where d is the thickness of the circular polarizer and λ is the wavelength of the light source. For a quarter-wave plate, thickness and orientation of the locked-in principle optical planes are chosen such that a relative phase difference of $90°$ is introduced between components A_f^{II} and A_s^{II}. The components of the beam exiting the quarter-wave plate are given by:

$$A_f^{III} = b \cos(\omega t), \tag{B.5}$$

$$A_s^{III} = b \sin(\omega t), \tag{B.6}$$

which are parametric equations for a circle (Figure B.1, III). The circularly polarized light enters an arbitrarily oriented specimen (A_3) with permanent or stress-induced optical birefringence and emerges with an additional angular phase difference between the two components; with the principle directions of the plate oriented at an angle β with respect to A_s^{III}, the components are

$$A_f^{III} = b \cos(\beta) \cos(\omega t) - b \sin(\beta) \sin(\omega t) = b \cos(\omega t + \beta), \tag{B.7}$$

$$A_s^{III} = b \sin(\beta) \cos(\omega t) + b \cos(\beta) \sin(\omega t) = b \sin(\omega t + \beta). \tag{B.8}$$

Optical anisotropy of the specimen introduces an angular phase difference α in emerging components:

$$A_f^{IV} = b \cos(\omega t + \beta - \alpha), \tag{B.9}$$

$$A_s^{IV} = b \sin(\omega t + \beta). \tag{B.10}$$

The circularly polarized beam, now with an additional angular phase difference, represents an equation of an ellipse. Whether the specimen is permanently anisotropic or experiences temporary stress-induced anisotropy, the entering circularly polarized light will become elliptically polarized. The elliptically polarized light enters the second quarter-wave plate (A_4), whose fast and slow axes are crossed with respect to the first quarter-wave plate. The beam components are resolved and emerge from the second quarter wave plate with an additional angular phase difference of $90°$:

$$A_f^V = b \cos(\beta) \cos(\omega t + \beta - \alpha) + b \sin(\beta) \sin(\omega t + \beta), \tag{B.11}$$

$$A_s^V = b \sin(\beta) \sin(\omega t + \beta - \alpha) + b \cos(\beta) \cos(\omega t + \beta). \tag{B.12}$$

The final optical component is the plane polarizer (i.e., analyzer), oriented perpendicular to the axis of vibration of the first plane polarizer. The final emerging beam is resolved into a single plane:

$$A^{VI} = \frac{1}{\sqrt{2}}(A_{12} - A_{13}) = a \sin\left(\frac{\alpha}{2} \sin \omega t + 2\beta - \frac{\alpha}{2}\right). \tag{B.13}$$

The intensity of the emerging light, A^{VI}, is given as twice the square of the amplitude of the beam,

$$I = 2a^2 \sin^2 \frac{\alpha}{2} = 2a^2 \sin^2 \left[\frac{\pi d}{\lambda}(n_1 - n_2)\right], \tag{B.14}$$

indicating that the only condition where light may be extinguished is $\alpha = 2n\pi$, where n is an integer. The maximum intensity is obtained when $\alpha = (2n+1)\pi$. When this point-wise analysis is extended to the entire specimen, contours of constant intensity patterns will form, representing all points whose difference in refractive indices are the same, e.g., fringe patterns.

The vibration planes of the temporary crystal coincide with the planes of the principle stresses and allow a relation to be drawn between the intensity patterns and shear stresses within the material. As shown by Maxwell, the principle optical axes coincide with the principle stress axes, and thus both the stress and index ellipsoids coincide in direction but not necessarily in magnitude. The stress-optic relations are written in common form as:

$$n_a - n_b = (C_1 + C_2)(\sigma_1 - \sigma_2), \tag{B.15}$$

$$n_b - n_c = (C_1 + C_2)(\sigma_2 - \sigma_3), \tag{B.16}$$

$$n_c - n_a = (C_1 + C_2)(\sigma_3 - \sigma_1), \tag{B.17}$$

where constants C_1 and C_2 are the stress-optic coefficients and n_a, n_b, n_c are the perturbed principle values of the refraction index with respect to an unstressed reference, n_0. For plane-stress ($\sigma_3 = 0$):

$$n_2 - n_1 = (C_1 + C_2)(\sigma_2 - \sigma_1). \tag{B.18}$$

In general, the retardation of light in one direction only depends on the principle stresses in the orthogonal plane. For two-dimensions, the retardation in optical path is related to stresses as

$$R = \frac{d}{\lambda}(n_2 - n_1) = \frac{Ct}{\lambda}(\sigma_2 - \sigma_1), \tag{B.19}$$

where $C = C_1 - C_2$. The application of stress to the specimen introduces optical anisotropy, whose index ellipsoid aligns with the stress ellipsoid [107]; this alignment is elucidated by Equation B.19, which shows that the difference between the two principle stresses at any given point in the specimen is linearly related to the relative retardation of the beam components, which in turn determine the beam intensity, I. Maximum shear stress, $\tau_{max} \approx \sigma_1 - \sigma_2$, and beam intensity, I, are related through C, drawing a relation between isochromatic fringe patterns and maximum shear stress, $I \approx |\tau_{max}|$.

A laser beam is a suitable candidate of light source for dynamic photo-elasticity due to its continuous, coherent (uniform polarization state), and directive characteristics. A monochromatic laser beam assures full extinction, as no other wavelengths of source light exist. A flash system may also be utilized, but it requires synchronization and sustained, uniform intensity for the duration of data capture. Circularly polarizing the input beam, while strictly not necessary for photo-elasticity, removes the ambiguity of finding the material principle direction, β (Figure B.1), by removing the parameter from the governing equations; this greatly simplifies experimental procedures. Since photo-elasticity averages effects through-thickness of the specimen, alignment of the plate in the test section must be normal to the incident beam to avoid skewing of images. Dilatational information is difficult to capture with this technique, as photo-elasticity is sensitive to shear deformations; the finite thickness of the plate, however, activates transverse three-dimensional stresses, which make it possible to visualize the P wave front, though faint, and captured only in early experimental times.

Appendix C

Manufacturing Drawing Files

Thrust fault experimental specimen manufacturing

1. The experimental region of interest is circled on the right. Surfaces C and D must be as parallel as possible when halves are mated together (no offset acceptable).

2. 40 specimens total should be machined (40 hanging wall and 40 foot wall sample halves).

3. Please keep the mating pairs (foot wall/hanging wall sample halves) together.

4. The angle (29 degrees) must be kept to as high a tolerance as possible.

5. The top and bottom surfaces (surface A and B on the right) should be as parallel as possible when halves as assembled.

6. The interface (labeled on right) must mate as good as possible (i.e. the interface cut should be a straight line on both halves and the angles must be 29 degrees).

7. Notch is placed only on the hanging wall sample half: samples are machined first, polished and bead-blasted (not Aero shop), then the notch is placed. The interface of the hanging wall sample half will be covered in tape with the notch location exposed. Please take care not to touch the interface after polishing and bead blasting.

Thrust fault specimen

Draft: Vahe Gabuchian
Date: January 5, 2011
Advisor: Ares J. Rosakis
Manufacture: Aero Shop
Material: Homalite H-100
Dimensions: mm [inches]

Figure C.1: Experimental specimen drawing file: assembly of hanging wall and foot wall plates.

Thrust fault specimen holder

New specimen holder for thrust fault experiments: hole array used for simply-supporting one side of sample while other side remains free. Samples may be up to 15 mm thick.

Ares J. Rosakis, G.A.L.C.I.T.

Vahe Gabuchian, 12/14/09
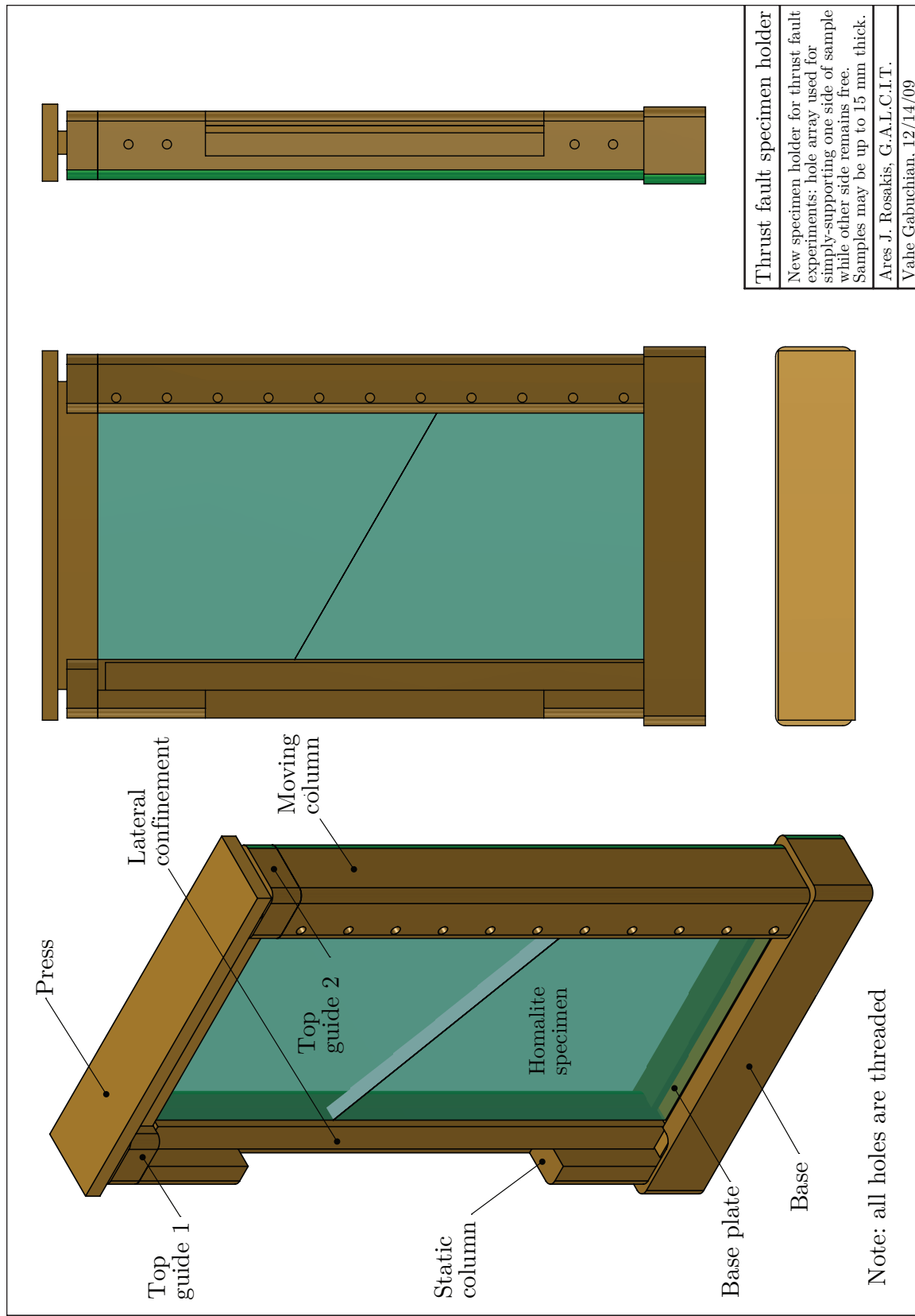
Figure C.2: Specimen holder drawing file: assembly overview with specimen aligned in the holder.

246.200
241.200
231.200
203.100
43.100
15
5

2.775
15
20
35
36
47.225
50

∅14
∅10
∅14
∅10

8
15
40

Base
All dimensions in mm
Material: Steel
M10 counterbore holes
Ares J. Rosakis, G.A.L.C.I.T.
Vahe Gabuchian, 12/14/09

199
180
19
20

21
23
27

Base plate
All dimensions in mm
Material: Aluminum
Ares J. Rosakis, G.A.L.C.I.T.
Vahe Gabuchian, 12/14/09
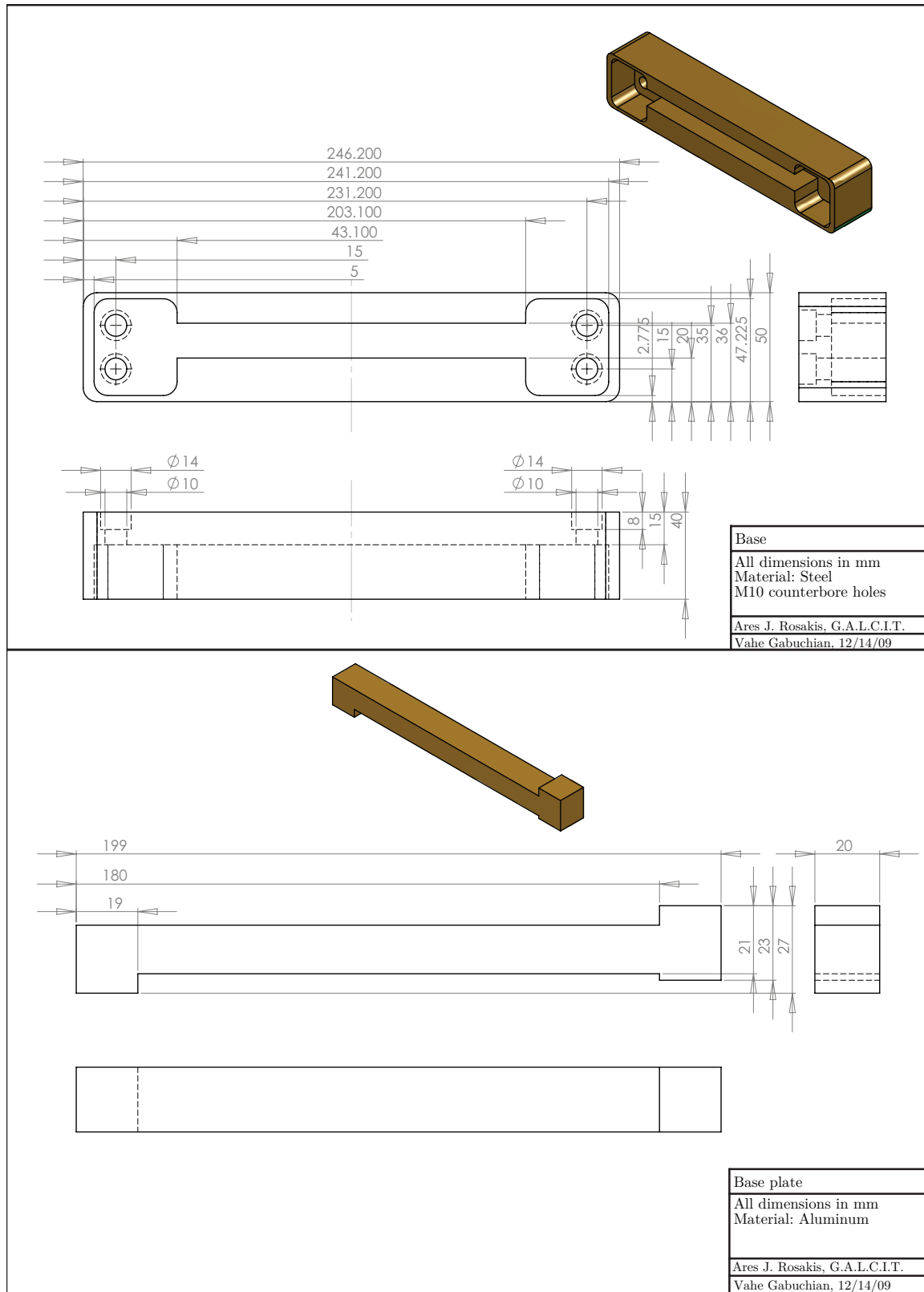
Figure C.3: Specimen holder drawing file: remainder of parts attach to the base and base plate.
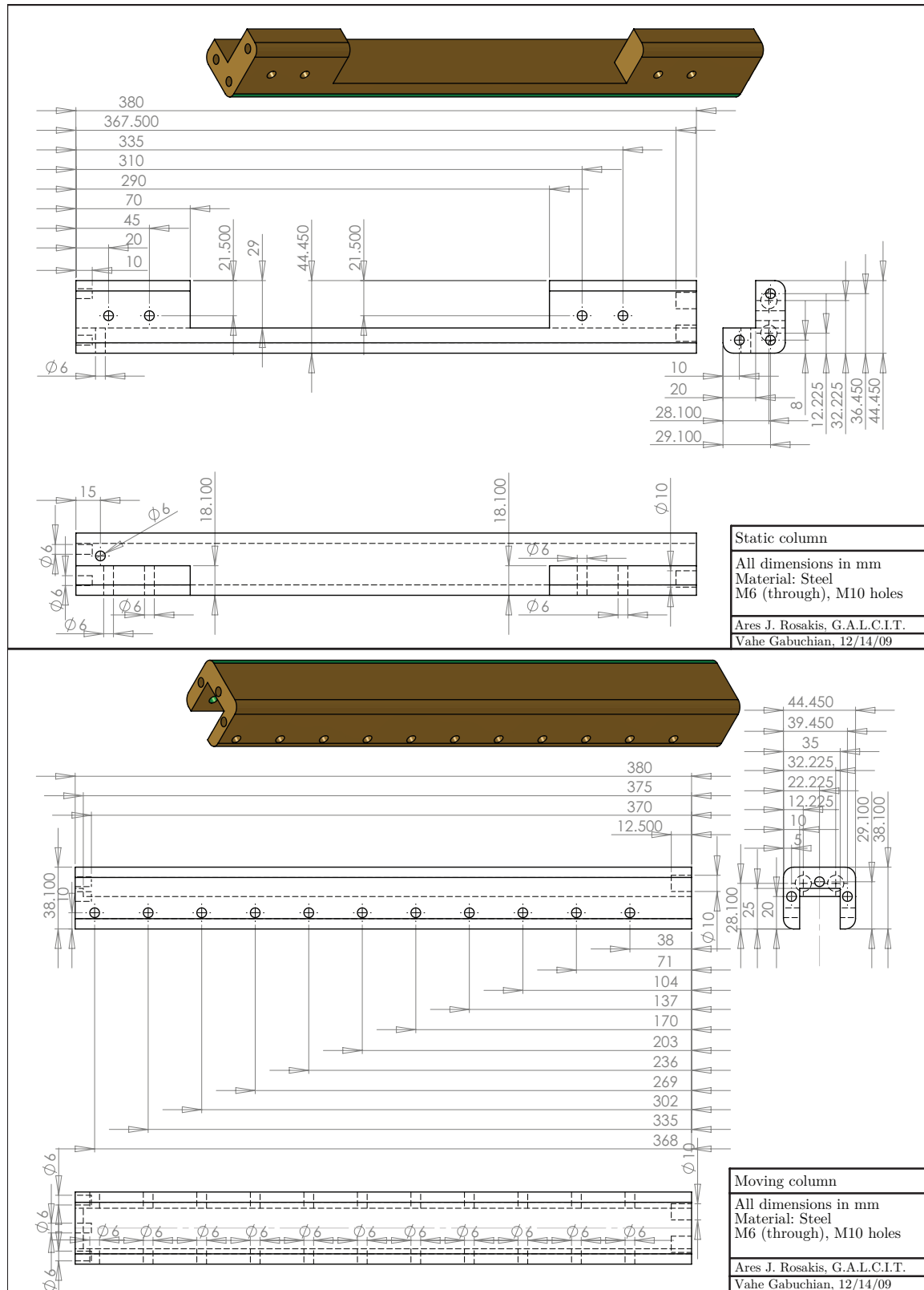
Figure C.4: Specimen holder drawing file: static/moving columns guide and support the specimen.
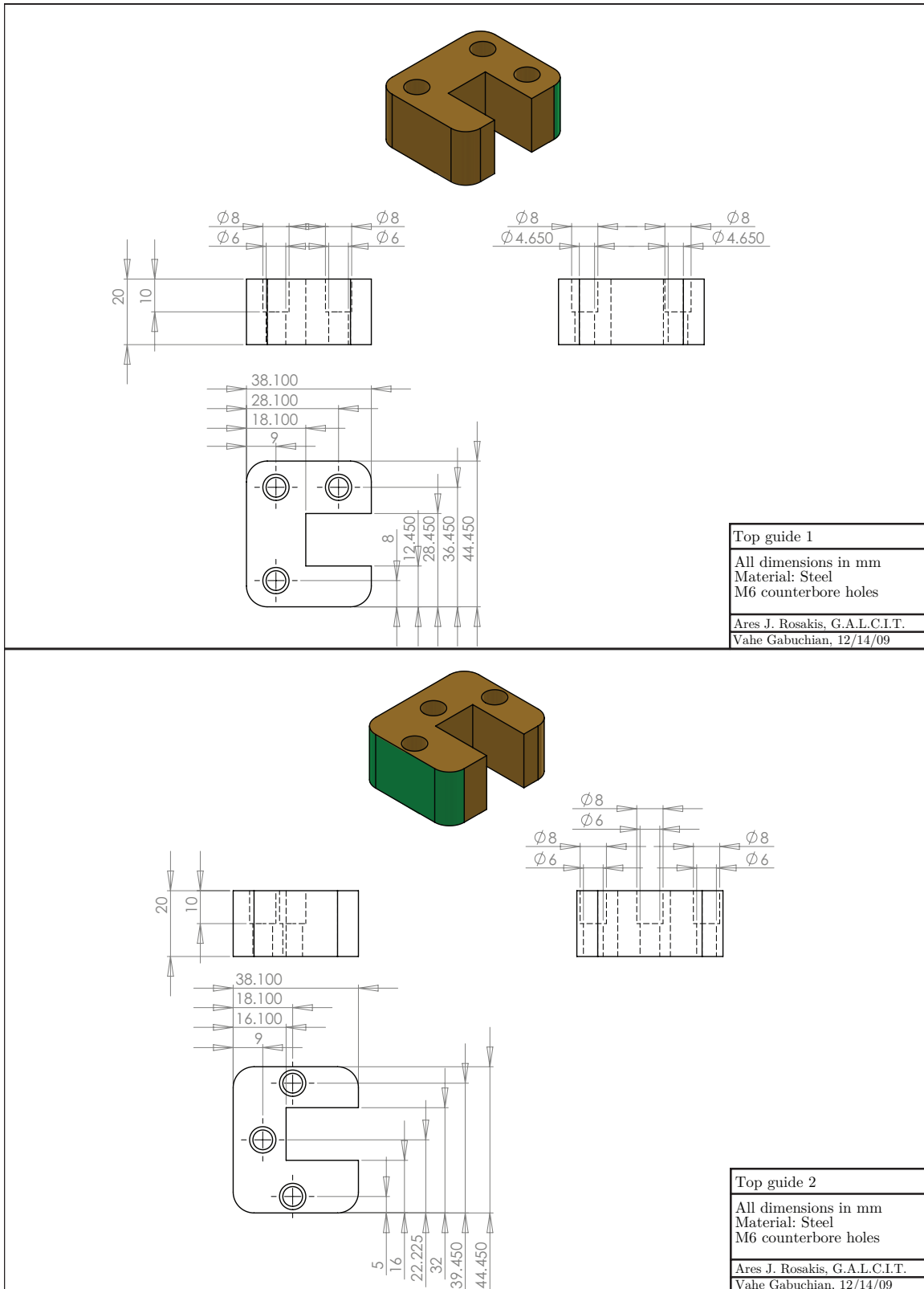
Figure C.5: Specimen holder drawing file: a pair of top guides provide slots for plate insertion.

355

18

15

Lateral confinement

All dimensions in mm
Material: Aluminum

Ares J. Rosakis, G.A.L.C.I.T.
Vahe Gabuchian, 12/14/09

20

220

240

17.500

32.500

50

Press

All dimensions in mm
Material: Steel

Ares J. Rosakis, G.A.L.C.I.T.
Vahe Gabuchian, 12/14/09
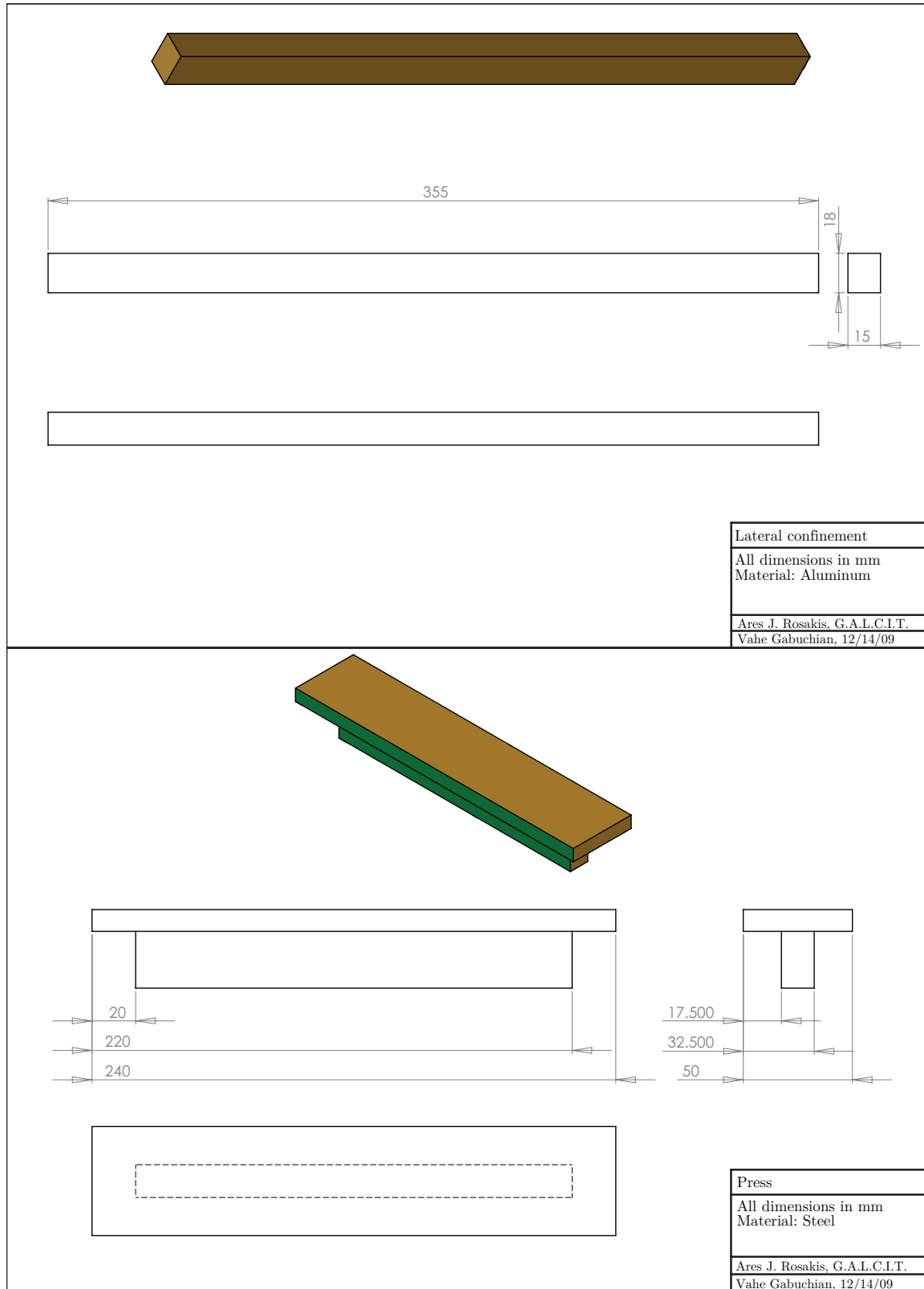
Figure C.6: Specimen holder drawing file: lateral confinement and press bars are used for loading.

Appendix D

Table of Values

Table D.1: Homalite$^{\text{TM}}$ H-100 material properties; a division of Brandywine Investment Group.

E [GPa]	μ [GPa]	ρ [kg/m^3]	ν [-]	C [m^2/N]
5.2	1.4	1200	0.35	23.1×10^{-12}

Table D.2: Mean experimental speeds as measured from the sequences of digital photographs for P (S) waves, $c_{\text{p,s}}$, sub-Rayleigh and super-shear up-dip rupture tip speeds, $v_{\text{r}}^{\text{SR/SS}}$, and the up-dip trailing-Rayleigh signature speeds, v^{TR}. The plane-stress Rayleigh wave speed, c_{R}, is determined from these mean values.

c_{p} [mm/µs]	c_{s} [mm/µs]	v_{r}^{SR} [mm/µs]	v_{r}^{TR} [mm/µs]	v_{r}^{SS} [mm/µs]	c_{R} [mm/µs]
2.59(8)	1.27(2)	1.14(3)	1.14(3)	2.10(10)	1.18(3)

Table D.3: Bill of materials used in the experiment. Item manufacturer information is followed by a description of its usage and the pertinent sections for reference.

Item	Usage (Section)
Homalite$^{\text{TM}}$ H-100	Surrogate material used in all experimentation (2.1.1).
Fadal$^{©}$ VCM 40 CNC machine	Used to manufacture hanging and foot wall plates (2.2.1.1).
12 inch polishing wheel	Used to polish the mating interface surfaces (2.2.1.2).
Polishing cloth (Buehler$^{©}$ #407222)	Cloth for polishing mating interface surfaces (2.2.1.2).
CeO suspension (Buehler$^{©}$ #406355006)	1 µm cerium oxide polishing compound (2.2.1.2).
Steel rig (custom)	Custom rig used to hold mating plates (2.2.1.2, 2.2.1.3).
Kim Wipes (small) (KimTech$^{©}$ #06666A)	Cleans various specimen surfaces (2.2.1.2, 2.2.1.5, 2.2.2.2).
Kim Wipes (large) (KimTech$^{©}$ #34133)	Used to offset plate alignment in steel rig (2.2.1.2).

Item	Usage (Section)
Econoline© Sandblasting Cabinet DP 36-1	Chamber to roughen polished interface surfaces (2.2.1.3).
Glass beads (McMaster Carr© #3386K73)	Roughen interface surfaces through impact (2.2.1.3).
Lagun Engineering© FTV-2 mill	Fabricates notch on hanging wall interface surface (2.2.1.4).
Reflective tape (Polytec© #A-RET-S001)	Record ground motion velocities on specimen (2.2.1.6).
Xacto© knife	Removes excess film and places reflective tapes (2.2.1.6).
Razor blade	Used to cut $90°$ corner of reflective tape marker (2.2.1.6).
Mitutoyo© calipers #500-465	Reflective tape position and linear measurements (2.2.1.6).
Magnifying glass	Reflective tape position and embedded wire (2.2.1.5).
Gimbal arm	Fixes plate during NiCr wire embedding (2.2.1.5).
NiCr wire (McMaster Carr© #8880K87)	Nucleation mechanism of ruptures (2.2.1.5, 5.2).
Scotch® tape	Holds wire in place during alignment (2.2.1.5).
Methanol (solvent grade)	Wipes difficult to remove stains from specimen.
Acetone (solvent grade)	Solvent to keep specimen clean during preparation.
Specimen holder	Houses hanging and foot wall plates (2.1.4, 2.2.1.7).
Carver© hydraulic unit #3925	Apply uniaxial load to specimen (2.2.2.2).
Coherent® Verdi V-5	Continuous green light (532 nm) laser source (2.2.2.1).
Coherent Verdi V-5 laser head	Emits the laser beam (2.2.2.1).
Laser chiller (Verdi #T255P)	Maintains constant laser head temperature (2.2.2.1).
Linear polarizer	Auxiliary power control (2.2.2.1).
Glan-laser polarizer	Auxiliary power control (2.2.2.1).
Reflective mirrors	Guide the laser beam (2.2.2.1).
Microscope objective (60x)	Spatial filtering of high frequencies (2.2.2.1).
Microscope 15 µm pinhole	Spatial filtering of high frequencies (2.2.2.1).
Canon® EF 400 mm telephoto	Expands and collimates laser beam (2.2.2.1).
Circular polarizers	Custom-made circular polarizers (2.2.2.2).
Plano-convex lens	Collects and focuses specimen beam to cameras (2.2.2.2).
Cordin model 220 digital camera	High-speed cameras used to capture images (2.2.2.3)
Field lenses (SMC Pentax 6×7)	Direct collected light towards cameras (2.2.2.3).
Polytec© OFV-511 and 551†	Decodes and outputs a velocity signal (2.2.3).
Polytec© OFV-5000 VD-02 and 09†	Interferes Doppler-shifted light (2.2.3).
Polytec© fiber-optic terminus	Emits and captures Doppler-shifted light (2.2.3.2).
Polytec© $90°$ corner turn	Used to bend the emitted light by $90°$ (2.2.3.2).
Tektronix© DPO 3034	Capture velocimeter data and trigger cameras (2.2.4).
Capacitor bank (custom)	Custom capacitor bank for rupture trigger (2.2.4.1).
BNC cables (20AWG RG58/U VW-1)	Used to connect various components of the experiment.

† A delay time of $t = 4.9\,\mu s$ exists between the different decoders in the laser velocimeter systems.

Table D.4: Earth surface-normal mean peak velocity magnitudes, $|\dot{u}_2(x_1, t)|$, measured at stations a distance x_1 from the fault trace on the hanging $(+)$ and foot wall $(-)$ plates. Tested loads $P = 5.0\,\mathrm{MPa}$ and $P = 15.0\,\mathrm{MPa}$ generate sub-Rayleigh and super-shear up-dip ruptures, respectively.

$x_1\,[\mathrm{mm}]$	-8	-4	-2	-0	+0	+2	+4	+8
$P = 5.0\,\mathrm{MPa}$	0.62	0.84	1.14	1.55	6.19	4.93	3.48	2.24
$P = 15.0\,\mathrm{MPa}$	3.97	4.94	5.90	10.02	10.30	6.98	6.26	5.06

Table D.5: Peak fault parallel (1)/normal (2) velocities at stations x_1' on the hanging $(+)$ and foot wall $(-)$.

$x_1'\,[\mathrm{mm}]$		40	20	10	4	2	0
$P = 2.5\,\mathrm{MPa}$	$\dot{u}_1^+$	0.77	0.97	1.50	2.39	2.80	4.10
	$\dot{u}_1^-$	-1.70	-1.42	-0.88	-1.82	-1.64	-1.32
	$\dot{u}_2^+$	2.05	1.51	1.05	2.49	2.03	4.32
	$\dot{u}_2^-$	-1.60	-2.02	-1.18	-0.60	-1.14	-1.32
$P = 5.0\,\mathrm{MPa}$	$\dot{u}_1^+$	1.55	1.42	2.16	2.81	3.19	3.46
	$\dot{u}_1^-$	-1.30	-1.04	-0.95	-1.32	-1.00	-1.38
	$\dot{u}_2^+$	2.25	1.81	2.71	1.56	2.83	3.29
	$\dot{u}_2^-$	1.35	1.77	1.11	1.10	1.38	2.01
$P = 7.5\,\mathrm{MPa}$	$\dot{u}_1^+$	1.50	2.17	2.89	4.76	3.53	6.33
	$\dot{u}_1^-$	-1.85	-1.27	-1.60	-2.18	-1.50	-2.04
	$\dot{u}_2^+$	3.70	2.75	1.46	3.10	3.02	3.46
	$\dot{u}_2^-$	3.45	2.63	1.56	2.45	2.24	2.81

Table D.6: Peak fault slip and opening rate magnitudes for $P = (2.5, 5.0, 7.5)\,\mathrm{MPa}$ at various stations x_1'.

$x_1'\,[\mathrm{mm}]$		40	20	10	4	2	0
$P = 2.5\,\mathrm{MPa}$	$\dot{u}_{\mathrm{slip}}$	0.80	1.15	1.89	2.44	3.04	3.81
	$\dot{u}_{\mathrm{open}}$	2.65	3.37	1.54	1.73	2.84	5.64
$P = 5.0\,\mathrm{MPa}$	$\dot{u}_{\mathrm{slip}}$	2.05	2.01	3.07	3.93	3.89	4.80
	$\dot{u}_{\mathrm{open}}$	1.85	0.76	1.33	0.53	1.53	1.38
$P = 7.5\,\mathrm{MPa}$	$\dot{u}_{\mathrm{slip}}$	3.25	3.12	4.26	6.85	5.02	8.26
	$\dot{u}_{\mathrm{open}}$	0.85	0.38	0.37	0.79	0.86	0.89

Table D.7: Measured values from experiments with uniform interface conditions. Column 1 is the initial uni-axial static (tectonic) load applied with the hydraulic press, P; column 2 is the stress drop, $\Delta\sigma = P_{\mathrm{f}} - P$, the difference between final and initial static loads after dynamics have ceased; P and S wave speeds c_{p} and c_{s} are measured in each experiment and presented together in column 3; sub-Rayleigh (SR) rupture tip speeds, $v_{\mathrm{r}}^{\mathrm{SR}}$ (or trailing-Rayleigh signature, v^{TR}, in case of transition to super-shear) are presented in column 5; column 6 reports the super-shear (SS) rupture tip speed, $v_{\mathrm{r}}^{\mathrm{SS}}$; column 7 reports the SS transition length along the fault measured from the hypocenter at depth, l_{tr}; the lag time between capacitor discharge and initiation of dynamic event, t_{dyn}, and the total length of soot deposit from the nucleation process measured along the interface , L_{soot}, are reported in columns 7 and 8, respectively.

P [MPa]	$\Delta\sigma$ [MPa]	$c_{\mathrm{p,s}}$ [mm/µs]	$v_{\mathrm{r}}^{\mathrm{SR}}$ [mm/µs]	$v_{\mathrm{r}}^{\mathrm{SS}}$ [mm/µs]	l_{tr} [mm]	t_{dyn} [µs]	L_{soot} [mm]
5.0	0.8	2.68/1.26	1.15	-	-	6.3	26
5.0	1.0	2.56/1.27	1.14	-	-	5.5	30
5.0	1.0	2.57/1.27	1.12	-	-	5.4	28
5.0	0.5	2.62/1.28	1.12	-	-	5.4	27
5.0	1.0	2.62/1.27	1.14	-	-	5.9	29
5.0	0.6	- /1.24	1.15	-	-	5.5	25
5.0	1.0	- /1.28	1.14	-	-	4.6	30
5.0	0.8	- /1.26	1.10	-	-	5.0	27
5.0	0.5	- /1.25	1.08	-	-	5.3	25
5.0	0.6	- /1.25	1.15	-	-	4.4	25
15.0	6.8	- /1.26	1.12	2.05	20.9	5.3	17
15.0	8.2	- /1.26	1.13	2.15	23.7	4.5	18
15.0	6.8	- /1.27	1.10	2.20	31.3	6.0	17
15.0	15.0†	- /1.26	1.15	2.09	15.3	5.5	16
15.0	6.0	- /1.26	1.07	2.05	26.7	5.4	15
15.0	9.5	- /1.28	1.19	2.12	10.2	6.0	20
15.0	7.8	- /1.26	1.16	2.02	15.8	5.4	16
15.0	5.7	- /1.31	1.17	2.07	22.5	5.4	18
15.0	6.0	- /1.24	1.15	2.02	20.6	3.9	15
15.0	7.5	- /1.31	1.24	2.30	23.2	5.1	15
15.0	6.2	- /1.24	1.23	2.03	19.1	7.5	15
15.0	6.2	- /1.28	1.10	2.00	13.2	5.0	16
15.0	6.4	- /1.28	1.12	2.00	16.8	5.6	17
15.0	6.0	- /1.25	1.09	2.00	15.3	4.2	16
15.0	7.0	- /1.30	1.17	2.05	22.8	5.6	16

† On rare occasion, bowed specimens may fly out of the holder, fully unloading the hydraulic press.

Bibliography

[1] R. A. Serway and J. W. Jewett. *Physics for Scientists and Engineers*. Brooks/Cole Publication Company, 6 edition, 1961.

[2] Y. C. Fung. *A First Course in Continuum Mechanics*. Prentice Hall, 3 edition, 1993.

[3] I. S. Sokolnikoff. *Mathematical Theory of Elasticity*. McGraw-Hill Inc., 2 edition, 1956.

[4] K. F. Graff. *Wave Motion in Elastic Solids*. Dover Books on Physics. Dover Publications, Inc., 1 edition, 1991.

[5] J. D. Achenbach. *Wave Propagation in Solids*. Elsevier Science, 1 edition, 1973.

[6] L. D. Landau and E. M. Lifshitz. *Theory of Elasticity*, volume 7 of *Course of Theoretical Physics*. Butterworth-Heinemann, 3 edition, 1986.

[7] K. Aki and P. G. Richards. *Quantitative Seismology: Theory and Methods*. University Science Books, 2 edition, 2002.

[8] H. W. Liepmann and A. Roshko. *Elements of Gas Dynamics*. John Wiley and Sons, Inc., 1 edition, 1957.

[9] J. D. Anderson. *Modern Compressible Flow: with Historical Perspective*. McGraw-Hill Series in Aeronautical and Aerospace Engineering. McGraw-Hill Inc., 3 edition, 2002.

[10] K. Ravi-Chandar. *Dynamic Fracture*. Elsevier Science, 1 edition, 2004.

[11] A. T. Zehnder. *Fracture Mechanics*. Lecture Notes in Applied and Computational Mechanics. Springer, 1 edition, 2012.

[12] J. N. Reddy. *An Introduction to Continuum Mechanics: with Applications*. Cambridge University Press, 1 edition, 2007.

[13] A. J. Rosakis and Y. Huang. Intersonic debonding. In *Comprehensive Structural Integrity Handbook, Fracture of Materials from Nano to Macro*, volume 8, pages 137–179. Elsevier, 8 edition, 2003.

[14] D. Gross and T. Seelig. *Fracture Mechanics: with an Introduction to Micromechanics*. Mechanical Engineering Series. Springer, 1 edition, 2006.

[15] M. H. Sadd. *Elasticity: Theory, Application, and Numerics*. Academic Press, 2 edition, 2009.

[16] M. J. Ablowitz and A. S. Fokas. *Complex Variables: Introduction and Applications*. Cambridge Texts in Applied Mathematics. Cambridge University Press, 2 edition, 2003.

[17] J. Chakrabarty. *Theory of Plasticity*. Butterworth-Heinemann, 3 edition, 2006.

[18] A. Saxena. *Nonlinear Fracture Mechanics for Engineers*. CRC Press, 1 edition, 1998.

[19] T. L. Anderson. *Fracture Mechanics: Fundamentals and Applications*. CRC Press, 3 edition, 2005.

[20] M. Janssen, J. Zuiderma, and J. H. Wanhill. *Theory of Plasticity*. VSSD, 2 edition, 2006.

[21] R. D. Hiscocks. *A Case Study in Aircraft Design: the De Havilland Family of STOL Commuter Aircraft*, volume 19 of *Case Studies*. American Institute of Aeronautics and Astronautics, 1980.

[22] E. E. Gdoutos. *Fracture Mechanics: an Introduction*. Solid Mechanics and its Applications. Springer, 2 edition, 2011.

[23] L. B. Freund. *Dynamic Fracture Mechanics*. Cambridge Monographs on Mechanics and Applied Mathematics. Cambridge University Press, 1 edition, 1990.

[24] K. B. Broberg. *Cracks and Fracture*. Academic Press, 1 edition, 1999.

[25] K. V. Ravi-Chandar and W. G. Knauss. An experimental investigation into dynamic fracture II: microstructural aspects. *Int. J. Fracture*, 26(1):65–80, 1984.

[26] K. V. Ravi-Chandar and W. G. Knauss. An experimental investigation into dynamic fracture III: on steady state crack propagation and crack branching. *Int. J. Fracture*, 26(2):141–154, 1984.

[27] M. Ramulu and A. S. Kobayashi. Mechanics of crack curving and branching: a dynamic fracture analysis. *Int. J. Fracture*, 27(3-4):187–201, 1985.

[28] H. Gao. Surface roughening and branching instabilities in dynamic fracture. *J. Mech. Phys. Solids*, 41:457–486, 1993.

[29] E. Johnson. Process region changes for rapidly propagating cracks. *Int. J. Fracture*, 55(1):47–63, 1992.

[30] K. V. Ravi-Chandar and W. G. Knauss. Processes controlling fast fracture of brittle solids. *Comput. Sci. Eng.*, 1(5):24–31, 1999.

[31] J. Fineberg and M. Marder. Instability in dynamic fracture. *Phys. Rep.*, 313:1–108, 1999.

[32] P. D. Washabaugh and W. G. Knauss. A reconciliation of dynamic crack velocity and Rayleigh wave speed in isotopic brittle solids. *Int. J. Fracture*, 65(2):97–114, 1994.

[33] K. B. Broberg. How fast can a crack go? *Mater. Sci+*, 32(1):80–86, 1996.

[34] B. Cotterell and J. R. Rice. Slightly curved or kinked cracks. *Int. J. Fracture*, 16(2):155–169, 1980.

[35] S. Nemat-Nasser and H. Horii. Compression-induced nonplanar crack extension with application to splitting, exfoliation, and rockburst. *J. Geophys. Res.*, 87(B8):6805–6821, 1982.

[36] W. Hutchinson and Z. Suo. Mixed-mode cracking in layered materials. *Adv. Appl. Mech.*, 29:63–191, 1992.

[37] M. Mello, H. S. Bhat, A. J. Rosakis, and H. Kanamori. Identifying the unique ground motion signatures of supershear earthquakes: theory and experiments. *Tectonophysics*, 493(3-4):297–326, 2010.

[38] R. Haberman. *Applied Partial Differential Equations: with Fourier Series and Boundary Value Problems.* Prentice Hall, 4 edition, 2003.

[39] O. Samudrala, Y. Huang, and A. J. Rosakis. Subsonic and intersonic shear rupture of weak planes with a velocity weakening cohesive zone. *J. Geophys. Res.*, 107(B8):1–32, 2002.

[40] S. P. Timoshenko and J. N. Goodier. *Theory of Elasticity.* Engineering Mechanics Series. McGraw-Hill, Inc., 3 edition, 1970.

[41] B. R. Munson, D. F. Young, and T. H. Okiishi. *Fundamentals of Fluid Mechanics.* John Wiley and Sons, Inc., 5 edition, 2005.

[42] A. J. Rosakis. Intersonic shear cracks and fault ruptures. *Advances in Physics*, 51(4):1189–1257, 2002.

[43] A. J. Rosakis, H. Kanamori, and K. Xia. Laboratory earthquakes. In A. Carpinteri, Y. Mai, and R. O. Ritchie, editors, *Advances in Fracture Research*, volume 138, pages 211–218. Springer, 2006.

[44] J. W. Dally and W. F. Riley. *Experimental Stress Analysis.* McGraw-Hill Inc., 2 edition, 1978.

[45] E. G. Coker and L.N. G. Filon. *A Treatise on Photoelasticity.* Cambridge University Press, 2 edition, 1957.

[46] Kaiwen Xia. *Laboratory Investigation of Earthquake Dynamics*. PhD thesis, California Institute of Technology, 2005. Geological and Planetary Sciences.

[47] K. Xia, A. J. Rosakis, and H. Kanamori. Laboratory earthquakes: the sub-Rayleigh-to-supershear rupture transition. *Science*, 303(5665):1859–1861, 2004.

[48] L. B. Freund. The mechanics of dynamic shear crack propagation. *J. Geophys. Res.*, 84(B5):2199–2209, 1979.

[49] G. Lykotrafitis, A. J. Rosakis, and G. Ravichandran. Particle velocimetry and photoelasticity applied to the study of dynamic sliding along frictionally-held bimaterial interfaces: techniques and feasibility. *Exp. Mech.*, 46(2):205–216, 2006.

[50] George Lykotrafitis. *Experimental Study of Dynamic Frictional Sliding Modes Along Incoherent Interfaces*. PhD thesis, California Institute of Technology, 2006. Engineering and Applied Science.

[51] G. Lykotrafitis, A. J. Rosakis, and G. Ravichandran. Self-healing, pulse-like, shear ruptures in the laboratory. *Science*, 313(5794):1765–1768, 2006.

[52] G. Zheng and J. R. Rice. Conditions under which velocity-weakening friction allows a self-healing versus crack-like mode of rupture. *B. Seismol. Soc. Am.*, 88(6):1466–1483, 1998.

[53] X. Lu, N. Lapusta, and A. J. Rosakis. Pulse and crack-like ruptures in experiments mimicking crustal earthquakes. *P. Natl. Acad. Sci. USA*, 104(48):18931–18936, 2007.

[54] X. Lu, N. Lapusta, and A. J. Rosakis. Analysis of supershear transition regimes in rupture experiments: the effect of nucleation conditions and friction parameters. *Geophys. J. Int.*, 177:717–732, 2009.

[55] Michael Mello. *Identifying the Unique Ground Motion Signatures of Supershear Earthquakes: Theory and Experiments*. PhD thesis, California Institute of Technology, 2012. Engineering and Applied Science.

[56] Y. Ida. Cohesive force across the tip of a longitudinal-shear crack and Griffith's specific surface energy. *J. Geophys. Res.*, 77(20):3796–3805, 1972.

[57] O. Samudrala, Y. Huang, and A. J. Rosakis. Subsonic and intersonic mode-II crack propagation with a rate-dependent cohesive zone. *J. Mech. Phys. Solids*, 50:1231–1268, 2002.

[58] R. Summers and J. Byerlee. Summary of results of frictional sliding studies, at confining pressures up to 6.98 kb, in selected rock materials. Open-file report 77-142, U.S.G.S., 1977.

[59] J. H. Dieterich. Time-dependent friction and the mechanics of stick-slip. *Pure Appl. Geophys.*, 116(4-5):790–806, 1978.

[60] J. H. Dieterich. Modeling of rock friction I. experimental results and constitutive equations. *J. Geophys. Res.*, 84(B5):2169–2175, 1979.

[61] J. H. Dieterich. Experimental and model study of fault constitutive properties. In S. Nemat-Nasser, editor, *Solid Earth Geophysics and Geotechnology*, volume 42 of *Applied Mechanics Division*, pages 21–30. American Society of Mechanical Engineers, 1980.

[62] J. H. Dieterich and B. D. Kilgore. Direct observation of frictional contacts - new insights for state-dependent properties. *Pure Appl. Geophys.*, 143(1-3):283–302, 1994.

[63] J. H. Dieterich. Applications of rate-and-state-dependent friction to models of fault slip and earthquake occurence. In H. Kanamori, editor, *Treatise in Geophysics*, chapter 4, pages 107–129. Elsevier Science, 2007.

[64] T. H. Heaton. Evidence for and implications of self-healing pulses of slip in earthquake rupture. *Phys. Earth Planet In.*, 64:1–20, 1990.

[65] A. J. Rosakis, O. Samudrala, and D. Coker. Intersonic shear crack growth along weak planes. *Mater. Res. Innov.*, 3:236–243, 2000.

[66] R. Burridge. Admissible speeds for plane-strain self-similar shear cracks with friction but lacking cohesion. *Geophys. J. Roy. Astr. S.*, 35(4):439–455, 1973.

[67] D. J. Andrews. Rupture velocity of plane-strain shear cracks. *J. Geophys. Res.*, 81(32):5679–5687, 1976.

[68] W. F. Brace and J. D. Byerlee. Stick-slip as a mechanism for earthquakes. *Science*, 153(3739):990–992, 1966.

[69] M. Mello, H. S. Bhat, A. J. Rosakis, and H. Kanamori. Reproducing the supershear portion of the 2002 Denali earthquake rupture in laboratory. *Earth Planet. Sc. Lett.*, 387:89–96, 2014.

[70] M. Ohnaka, Y. Kuwahara, K. Yamamoto, and T. Hirasawa. Dynamic breakdown processes and the generating mechanism for high-frequency elastic radiation during stick-slip instabilities. In S. Das, J. Boatwright, and C. H. Scholz, editors, *Earthquake Source Mechanics*, volume 6 of *Maurice Ewing*, pages 12–24. American Geophysical Union, 1986.

[71] Rowena B. Lohman. *The Inversion of Geodetic Data for Earthquake Parameters*. PhD thesis, California Institute of Technology, 2004. Geological and Planetary Sciences.

[72] E. M. Dunham and R. J. Archuleta. Evidence for a supershear transient during the 2002 Denali Fault earthquake. *B. Seismol. Soc. Am.*, 94(6B):S256–S268, 2004.

[73] R. J. Archuleta. A faulting model for the 1979 Imperial Valley earthquake. *J. Geophys. Res.*, 89(B6):4559–4585, 1984.

[74] M. Bouchon and M. Vallée. Observation of long supershear rupture during the magnitude 8.1 Kunlunshan earthquake. *Science*, 301(5634):824–826, 2003.

[75] A. J. Rosakis, M. Mello, H. Bhat, and H. Kanamori. Identifying the unique ground motion signatures of supershear earthquakes: the one-two punch effect on high-rise buildings. *AGU Fall Meeting Abstracts*, 2011.

[76] Eric M. Dunham. *The Dynamics and Near-Source Ground Motion of Supershear Earthquakes*. PhD thesis, University of California, Santa Barbara, 2005. Engineering and Applied Science.

[77] S. Krishnan, C. Ji, D. Komatitsch, and J. Tromp. Case studies of damage to tall steel moment-frame buildings in southern California during large San Andreas earthquakes. *B. Seismol. Soc. Am.*, 96(4A):1523–1537, 2006.

[78] B. T. Aagard and T. H. Heaton. Near-source ground motions from simulations of sustained intersonic and supersonic fault ruptures. *B. Seismol. Soc. Am.*, 94(6):2064–2078, 2004.

[79] S. Song, G. C. Beroza, and P. Segall. Evidence of supershear rupture during the 1906 San Francisco earthquake. *AGU Fall Meeting Abstracts*, 2005.

[80] Pillsbury Photo Company. The burning of San Francisco, April 18, 1906, view from St. Francis Hotel. Library of Congress Prints and Photographs Division, April 1906.

[81] Unknown. Aerial photo of March 11 tsunami hitting the Sendai Plain in northern Japan. California Geological Survey, 2011.

[82] R. E. Wallace. The San Andreas fault system, California. Professional paper 1515, United States Geological Survey, 1990.

[83] J. W. Wallace. Building performance in the 17 August 1999 Izmit (Kocaeli), Turkey earthquake. Paper presented at Los Angeles Tall Buildings Conference.

[84] C. J. Langer. Partially collapsed five-story masonry building in Spitak. United States Geological Survey, December 1988.

[85] W. Chen, B. Huang, Y. Chen, Y. Lee, C. Yang, C. Lo, H. Chang, Q. Sung, N. Huang, C. Lin, S. Sung, and K. Lee. 1999 Chi-Chi earthquake: a case study on the role of thrust-ramp structures for generating earthquakes. *B. Seismol. Soc. Am.*, 91(5):986–994, 2001.

[86] R. Nason. Increased seismic shaking above a thrust fault. In L. M. Murphy, editor, *San Fernando, California, Earthquake of February 9, 1971, Vol. III: Geological and Geophysical Studies*, pages 123–126. U.S. Government Printing Office, 1973.

[87] K. V. Steinbrugge, E. E. Schader, and D. F. Moran. Building damage in San Fernando Valley. *CDMG Bulletin*, 196:323–353, 1975.

[88] N. A. Abrahamson and P. G. Somerville. Effects of the hanging wall and footwall on ground motions recorded during the Northridge earthquake. *B. Seismol. Soc. Am.*, 86(1B):593–599, 1996.

[89] T.-C. Shin and T.-L. Teng. An overview of the 1999 Chi-Chi, Taiwan, earthquake. *B. Seismol. Soc. Am.*, 91(5):895–913, 2001.

[90] J. N. Brune. Particle motions in a physical model of shallow angle thrust faulting. *P. Indian As. - Earth*, 105(2):L197–L206, 1996.

[91] D. D. Oglesby, R. J. Archuleta, and S. B. Nielsen. Earthquakes on dipping faults: the effects of broken symmetry. *Science*, 280(5366):1055–1059, 1998.

[92] B. Shi, A. Anooshehpoor, J. N. Brune, and Y. Zeng. Dynamics of thrust faulting: 2D lattice model. *B. Seismol. Soc. Am.*, 88(6):1484–1494, 1998.

[93] D. D. Oglesby, R. J. Archuleta, and S. B. Nielsen. The three-dimensional dynamics of dipping faults. *B. Seismol. Soc. Am.*, 90(3):616–628, 2000.

[94] S. Ma and G. C. Beroza. Rupture dynamics on a bimaterial interface for dipping faults. *B. Seismol. Soc. Am.*, 98(4):1642–1658, 2008.

[95] S. B. Nielsen. Free surface effects on the propagation of dynamic rupture. *Geophys. Res. Lett.*, 25(1):125–128, 1998.

[96] R. Madariaga. Radiation from a finite reverse fault in half space. *Pure Appl. Geophys.*, 160(3):555–577, 2003.

[97] D. D. Oglesby and S. M. Day. Fault geometry and the dynamics of the 1999 Chi-Chi (Taiwan) earthquake. *B. Seismol. Soc. Am.*, 91(5):1099–1111, 2001.

[98] D. D. Oglesby and S. M. Day. The effect of fault geometry on the 1999 Chi-Chi (Taiwan) earthquake. *Geophys. Res. Lett.*, 28(9):1831–1834, 2001.

[99] B. Duan. Role of initial stress rotations in rupture dynamics and ground motion: a case study with implications for the Wenchuan earthquake. *P. Indian As. - Earth*, 115(B5), 2010.

[100] A. J. Rosakis, O. Samudrala, and D. Coker. Cracks faster than the shear wave speed. *Science*, 284(5418):1337–1340, 1999.

[101] K. Xia, A. J. Rosakis, H. Kanamori, and J. R. Rice. Laboratory earthquakes along inhomogeneous faults: directionality and supershear. *Science*, 308(5722):681–684, 2005.

[102] R. L. Biegel, H. S. Bhat, C. G. Sammis, and A. J. Rosakis. The effect of asymmetric damage on dynamic shear rupture propagation I: no mismatch in bulk elasticity. *Tectonophysics*, 493(3-4):254–262, 2010.

[103] H. S. Bhat, R. L. Biegel, A. J. Rosakis, and C. G. Sammis. The effect of asymmetric damage on dynamic shear rupture propagation II: with mismatch in bulk elasticity. *Tectonophysics*, 493(3-4):263–271, 2010.

[104] X. Lu, A. J. Rosakis, and N. Lapusta. Rupture modes in laboratory earthquakes: effect of fault prestress and nucleation conditions. *J. Geophys. Res.*, 115(B12), 2010.

[105] Polytec. *User Manual: Fiber-Optic Vibrometer Sensor Head OFV-551/-552*, 2005.

[106] A. W. Hendry. *Elements of Experimental Stress Analysis*. Structures and Solid Body Mechanics Division. Pergamon Press, 1 edition, 1964.

[107] A. J. Durelli. *Introduction to Photomechanics*. Prentice-Hall International Series in Theoretical and Applied Mechanics. Prentice Hall, 1 edition, 1965.

[108] W. N. Sharpe, editor. *Springer Handbook of Experimental Solid Mechanics*. Springer, 2008 edition, 2008.

[109] A. S. Kobayashi, editor. *Handbook on Experimental Mechanics*. VCH, 2 edition, 1993.

[110] A. J. Rosakis and A. T. Zehnder. On the method of caustics: an exact analysis based on geometrical optics. Technical report, California Institute of Technology, 1985.

[111] G. Lykotrafitis and A. J. Rosakis. Sliding along frictionally held incoherent interfaces in homogeneous systems subjected to dynamic shear loading: a photoelastic study. *Int. J. Fracture*, 140(1-4):213–233, 2006.

[112] S. P. Timoshenko and S. Woinowsky-Krieger. *Theory of Plates and Shells*. Engineering Mechanics Series. McGraw-Hill Inc., 2 edition, 1959.

[113] S. P. Timoshenko and J. M. Gere. *Theory of Elastic Stability*. Engineering Mechanics Series. McGraw-Hill Inc., 2 edition, 1961.

[114] J. E. Stewart. *Optical Principles and Technology for Engineers*, volume 104 of *Mechanical Engineering*. CRC Press, 1 edition, 1996.

[115] Polytec. *Data Sheet: OFV-5000 Vibrometer Controller.*

[116] Polytec. *User Manual: Vibrometer Controller OFV-5000*, 2005.

[117] Polytec. *Data Sheet: VD/DD Decoder Guideline*, 2005.

[118] Polytec. *Data Sheet: OFV-551/552 Fiber-Optic Interferometer.*

[119] Y. Liu and N. Lapusta. Transition of mode-II cracks from sub-Rayleigh to intersonic speeds in the presence of favorable heterogeneity. *J. Mech. Phys. Solids*, 56(1):25–50, 2008.

[120] L. Thede. *Practical Analog and Digital Filter Design.* Artech House Microwave Library. Artech House Publishers, 2 edition, 2004.

[121] A. V. Oppenheim, R. W. Schafer, and J. R. Buck. *Discrete-Time Signal Processing.* Prentice-Hall signal Processing Series. Prentice Hall, 2 edition, 1999.

[122] J. Schell and D. Oliver. *Application Note: Influence of Lateral Motion on Vibrometer Measurement.* Polytec, 2009.

[123] R. Burridge, G. Conn, and L. B. Freund. The stability of rapid mode-II shear crack with finite cohesive traction. *J. Geophys. Res.*, 84(B5):2210–2222, 1979.

[124] D. D. Oglesby, R. J. Archuleta, and S. B. Nielsen. Dynamics of dip-slip faulting: explorations in two dimensions. *J. Geophys. Res. - Sol. Ea.*, 105(B6):13643–13653, 2000.

[125] A. J. Rosakis, G. Lykotrafitis, K. Xia, and H. Kanamori. Dynamic shear rupture in frictional interfaces: speeds, directionality, and modes. In H. Kanamori, editor, *Treatise in Geophysics*, volume 4 of *Earthquake Seismology: Fracture and Frictional Mechanics - Experimental Study I.* Elsevier Science, 2007.

[126] Xiao Lu. *Combined Experimental and Numerical Study of Spontaneous Dynamic Rupture on Frictional Interfaces.* PhD thesis, California Institute of Technology, 2009. Engineering and Applied Science.

[127] B. Duan and D. D. Oglesby. The dynamics of thrust and normal faults over multiple earthquake cycles: effects of dipping fault geometry. *B. Seismol. Soc. Am.*, 95(5):1623–1636, 2005.

[128] J. R. Rice, C. G. Sammis, and R. Parsons. Off-fault secondary failure induced by a dynamic slip-pulse. *B. Seismol. Soc. Am.*, 95(1):109–134, 2005.

[129] E. M. Dunham and R. J. Archuleta. Near-source ground motion from steady state dynamic rupture pulses. *Geophys. Res. Lett.*, 32, 2005.

[130] H. S. Bhat. Work in progress, 2015. This is a note.

[131] C. R. Allen, L. S. Brune, L. S. Cluff, and A. G. Barrows. Evidence for unusually strong near-field ground motion on the hanging wall of the San Fernando fault during the 1971 earthquake. *Seismol. Res. Lett.*, 69(6):524–531, 1998.

[132] H. Kanamori. Mechanism of tsunami earthquakes. *Phys. Earth Planet In.*, 6(5):346–359, 1972.

[133] E. A. Okal. Seismic parameters controlling far-field tsunami amplitudes: a review. *Nat. Hazards*, 1:67–96, 1988.

[134] H. Kanamori and M. Kikuchi. The 1992 Nicaragua earthquake: a slow tsunami earthquake associated with subducted sediments. *Nature*, 361:714–716, 1993.

[135] T. O. H. Charrett, S. W. James, and R. P. Tatam. Optical fibre laser velocimetry: a review. *Meas. Sci. Technol.*, 23(3), 2012.

[136] H. Jin and H. A. Bruck. Theoretical development for pointwise digital image correlation. *Opt. Eng.*, 44(6):067003–067014, 2005.

[137] M. A. Sutton, J. Orteu, and Schreier H. W. *Image Correlation for Shape, Motion, and Deformation Measurements: Basic Concepts, Theory and Applications*. Springer, 1 edition, 2009.

[138] T. C. Chu, W. F. Ranson, M. A. Sutton, and W. H. Peters. Application of digital-image correlation techniques to experimental mechanics. *Exp. Mech.*, 25(3):232–244, 1985.

[139] A. J. Rosakis. Two optical techniques sensitive to gradients of optical path difference: the method of caustics and the coherent gradient sensor (CGS). In J. Epstein, editor, *Experimental Techniques in Fracture*, chapter 10, pages 327–425. Wiley-VCH, 1993.

[140] J. Lim and K. Ravi-Chandar. Photomechanics in dynamic fracture and friction studies. *Strain*, 43(3):151–165, 2007.

[141] M. Mello, S. Hong, and A. J. Rosakis. Extension of the coherent gradient sensor (CGS) to the combined measurement of in-plane and out-of-plane displacement field gradients. *Exp. Mech.*, 49(2):277–289, 2009.

[142] V. Rubino, N. Lapusta, A. J. Rosakis, S. Leprince, and J. P. Avouac. Static laboratory earthquake measurements with digital image correlation method. *Exp. Mech.*, 2014.

[143] A. J. Rosakis. Application of coherent gradient sensing (CGS) to the investigation of dynamic fracture problems. In A. Shukla, editor, *Optics and Lasers in Engineering*, chapter 19, pages 3–41. Elsevier Science, 1993.

[144] R. Singh, J. Lambros, A. Shukla, and A. J. Rosakis. Investigation of the mechanics of intersonic crack propagation along a bimaterial interface using coherent gradient sensing and photoelasticity. *P. R. Soc. A*, 453:2649–2667, 1997.

[145] L. H. Tanner. The optics of the Mach-Zehnder interferometer. Technical Report 3069, National Physical Laboratory, 1959.

[146] CVI Melles Griot. *All Things Photonic: the CVI Melles Griot Technical Guide.*